University of Nottingham
UK | CHINA | MALAYSIA

Understanding the relationship between synthetic conditions, porosity and CO_2 uptake capacity of turbostratic carbons

Thesis submitted to the University of Nottingham for the degree of **Doctor of Philosophy, August 2022.**

L. Scott Blankenship

4343286

Supervised by

Professor Robert Mokaya
Dr Begum Tokay

Abstract

As of 2021, the atmospheric concentration of CO_2 is 412 ppm and continues to rise. It is well established that these concentrations are resulting in rising temperatures, an increased incidence of extreme weather, and thus unspeakably disastrous consequences for all life. It follows then that CO_2 capture and removal technologies must be rapidly developed to ensure the longevity of human society. One area of research is CO_2 capture *via* physisorption onto porous materials and in particular on the easily synthesised turbostratic carbons. This application requires fine control over porosity (surface area, pore volume, pore size) according to conditions of sorption, and it therefore follows that both the ability to precisely measure pore sizes, as well as a definitive knowledge of the relationship between CO_2 uptake capacity and pore size is needed. This thesis attempts to address all three of these issues.

In terms of routes to activated carbons, this work investigates two principal synthetic methods. Firstly in chapter 4 - developing on the author's previous work - a simplification of the production of turbostratic carbons from unwrapped Used Cigarette Filters (UCFs) was attempted by activation of whole Used Cigarette Butts (UCBs) with KOH. The simplified method resulted in much less porosity as compared to the previous work (maximal A_{BET} of 4300 compared with 1960 $m^2\ g^{-1}$) and the samples derived by this

method possess a hierarchical - as opposed to narrow, microporous - Pore Size Distribution (PSD). Nevertheless, these new materials may perform well for CO_2 capture in Pressure Swing Adsorption (PSA) applications. Pyrolysis of UCBs in the absence of a porogen created minimal porosity, perhaps as a result of contaminants present from the UCB wrapping paper.

The other approach to activation used (chapter 5) is a set of methods which have been collectively coined as impregnation routes, i.e. methods which attempt to achieve close contact between precursor and the activating species whilst maintaining a homogeneous distribution of the latter throughout the former. Impregnation was achieved through (i) the hydrothermal carbonisation of sawdust (SD) with KOH prior to pyrolysis, as well as (ii) direct activation of a polymeric sodium salt, sodium carboxymethyl cellulose (NC). In both cases, PSDs achieved were generally narrow and situated principally in the small micropore region, making the products potential candidates for low pressure CO_2 capture. Both sets of materials also showed unexpected features, SD-derived samples having extremely low bulk density, and those obtained from NC exhibiting reduction in porosity at surprisingly low porogen:precursor ratios. The latter of these suggests pore formation effects outside of the caustic nature of porogenesis with Na compounds, and is a potential route for further investigation of activation mechanisms.

For materials derived through the synthetic routes mentioned above, reliable, accurate, and efficient isothermal porosimetry proved difficult due to poor diffusion of N_2 into the materials' pores. As such, alternative porosimetric techniques were investigated in chapter 6. It was found that dual isotherm porosimetry using O_2 and H_2 isotherms measured at -196 °C results not only in more expedient equilibration of the sorptive-sorbent system, but allows the measurement of sub-angstrom level developments

in porosity associated with changes in quantity of porogen used. These subtle developments in porosity are not measurable through traditional porosimetry using N_2.

As for improving the understanding of the relationship between CO_2 uptake as a function of pressure and pore size, chapter 7 details the development and deployment of the python Porosity Uptake Correlator (pyPUC) which, using experimental PSDs and gravimetric gas uptake isotherms applies a brute force approach to determine the correlation between porosity within some pore width range and CO_2 uptake at a given pressure. This is performed for all user-defined pore width ranges and pressures, and correlation coefficients are compared to give optimum pore size ranges, Ω at each pressure. When applied to CO_2 uptake on turbostratic carbons, it was confirmed that Ω broadens with increasing pressure. In addition, the relationship between Ω and pressure-dependent CO_2 uptake was calculated to a more granular level of detail than has been previously reported. Furthermore, following on from findings in chapter 6 it was found that these relationships at low pressures are best described using dual isotherm O_2/H_2 porosimetry.

Statutory Declaration

I hereby declare that this thesis with the title "***Understanding the relationship between synthetic conditions, porosity and CO_2 uptake capacity of turbostratic carbons***" has been written by myself without any external unauthorised help, that it has been neither presented to any institution for evaluation nor previously published in its entirety. Any parts, words or ideas, of the thesis however limited and including tables, graphs and schemes, which are quoted from or based on other sources have been acknowledged as such without exception.

Signature _____

Date _____ / _____ / _____

Acknowledgements

It has been a long and unusual journey to finally come to submitting my thesis. As with anything such as this, it would not have been possible without the help of a hoard of disparate delightful humans. The first I'd like to acknowledge of course is my supervisor, Robert Mokaya. From the beginning (prior to my master's research) you have accepted and encouraged every half-planned route of investigation I've decided to go down. I look forward to continuing to work with you. I'm also grateful to all current and former members of the Mokaya group, but in particular Alison Taylor who trained me on many synthetic and analytical techniques as well as Thria Alkhaldi with whom it is always fun to discuss ideas for experiments. I'd like to thank the technical staff in the School of Chemistry, in particular Mark Guyler and Neil Barnes for their essentially help and calm heads when things (frequently!) break, or indeed when I break them even worse than they were originally broken. Neil also provided a vital listening ear when I was extremely stressed and frustrated in my second year. On that topic, thanks to everyone who frequents the school smoking area for allowing me to vent when needed.

Outside of the University of Nottingham, I'd like to thank Jacek Jagiello for taking an avid interest in my work and the many chats we had about adsorption theory. In a similar vein, discussions with Paul Iacomi have

always been so insightful. He alongside Hassan Akhtar have been a great help in improving my infantile computer code at times. More recently, abstract mathematical discussions with my dear Ηρώ have been great fun and helped me look at my work in a different way. Two broad groups of friends that may not have donated technical knowledge but lent more emotional support are those at Kunsthaus and its extended universe, and the Whitchurch OGs - you know who you are. From the latter group I'd like to single out my best mate Jonnie Felton, and from the former Raffa and Mattia who have patiently listened to me babble about some incoherent abstract concept for which I have not armed them adequately with the prerequisite knowledge.

I'd further like to acknowledge Alexandra Elbakyan for her work in liberating scientific literature with sci-hub. This work, and indeed my research in general would be much more difficult if not impossible without her persistent fight against the greed of the scientific publishing industry. Similarly I thank all who have laid groundwork, and worked tirelessly with the goal of a more open scientific ecosystem including such figures as Mike Morrison and the late Aaron Swartz.

I suppose that just leaves my family. My younger sisters have all served as cheerleaders in their own right and I'm thankful for all three of you. Aunt Mimi and Grandma Joy you've always told me I can be anything I want to be and that has inspired (an at times dangerous) amount of self-confidence which has pushed me through this PhD. But the biggest thanks goes to my mother Cheryl. Apart from preventing me from dying at various points before I was five and being a great Mom in general you literally taught me how to read and write, so none of this would be possible without you. You inspired and encouraged a lifelong love of learning in me and that is truly something that money cannot buy.

Glossary

activated carbon Turbostratic carbon that has porosity produced during pyrolysis, aided by some external porogen. This contrasts with biochar.

activating agent Reagent used to develop porosity in a material. Also known as a porogen.

activation The process of producing porosity in a material, typically *via* pyrolysis and frequently using an activating agent.

adsorbate The substance being adsorbed onto a surface.

adsorbent The material onto which a substance is adsorbed.

adsorption The process by which molecules adhere onto a solid surface through chemical or physical bonds.

ash content Amount of ash, i.e. non-combustible oxides left following thermal decomposition of a sample in air. Used to determine to what degree a sample is carbonaceous, typically performed using Thermogravimetric Analysis (TGA).

biochar The product of pyrolysis, generally produced in the absence of added porogen.

hydrochar The solid, carbonaceous product of hydrothermal carbonisation, composed of microspheres having a hydrophilic shell and hydrophobic core.

hydrothermal carbonisation Carbonisation in water in a sealed container, typically of biomass.

macropore Pore of width > 500 Å.

mesopore Pore of width $20 - 500$ Å.

micropore Pore of width < 20 Å.

physisorption Adsorption that occurs due to Van der Waals forces between adsorbent surface and adsorbate, as opposed to due to chemical bonding.

porogen See activating agent.

porogenesis See activation.

pyrolysis Thermal decomposition of material in an inert atmosphere.

self-activation Activation that occurs due to some inherent properties of the precursor. This could be a result of oxidising agents (e.g. alkali metals) present in the precursor, or volatiles (CO_2 etc.) released upon pyrolysis.

supermicropore A micropore of width $7 - 20$ Å.

turbostratic carbon Carbons having a partially disordered structure with some ordered, graphitic domains.

ultramicropore A micropore of width < 7 Å.

Acronyms

BED backscatter electron detection.

BET Brunauer, Emmet and Teller theory.

BSE backscatter electrons.

CA Cellulose Acetate.

CB Cigarette Butt.

DAC Direct Air Capture.

DFT Density Functional Theory.

DS degree of substitution.

EDX Electron-Dispersive X-ray Analysis.

GAB Guggenheim-Anderson-de Boer.

GCMC Grand Canonical Monte Carlo.

ICP-OES Inductively Coupled Plasma-Optical Emission Spectrometry.

IUPAC International Union of Pure and Applied Chemistry.

MOF Metal Organic Framework.

NC sodium carboxymethyl cellulose.

NLDFT Non-Local Density Functional Theory.

P-XRD Powder X-ray Diffraction.

PSA Pressure Swing Adsorption.

PSD Pore Size Distribution.

pyPUC python Porosity Uptake Correlator.

SD sawdust.

SE secondary electrons.

SEI secondary electron images.

SEM Scanning Electron Microscopy.

TEM Tunneling Electron Microscopy.

TGA Thermogravimetric Analysis.

TSA Temperature Swing Adsorption.

UCB Used Cigarette Butt.

UCF Used Cigarette Filter.

VSA Vaccuum Swing Adsorption.

XPS X-ray Photoelectron Spectroscopy.

List of Publications

This thesis resulted in the following publications;

I L. Scott Blankenship, Jacek Jagiello and Robert Mokaya, **Confirmation of pore formation mechanisms in biochars and activated carbons by dual isotherm analysis**, *Materials Advances*, 2022, (3), 3961-3971, 10.1039/D2MA00141A

II L. Scott Blankenship, Nawaf Albeladi, Thria Alkhaldi, Asma Madkhali and Robert Mokaya, **Brute force determination of the optimum pore sizes for CO_2 uptake**, *Energy Advances*, 2022 (1), 1009-1020, 10.1039/D2YA00149G

III L. Scott Blankenship and Robert Mokaya, **Modulating the porosity of carbons for improved adsorption of hydrogen, carbon dioxide, and methane: a review**, *Materials Advances*, 2022 (3), 1905-1930, 10.1039/D1MA00911G

The author's contribution to these publications; In all cases, the author wrote the manuscript. In the case of **Publication I** the author did all experimental work and conceptualised the project and performed the majority of data analysis. For **Publication II** the author contributed to the synthesis of some of the samples and measurement of some isotherms.

In addition the author conceptualised and designed the software needed to perform the analyses, and performed all data analysis. For **Publication III** the author performed the literature review; while it does not represent original experimental work it is a useful supplement to the introduction (chapter 1) and thus has been provided as appendix A.

In addition to this thesis, the author has contributed porosimetric analyses to the following publication;

IV Ryan R Larder, Thomas M Bennett, L. Scott Blankenship, Jesum A Fernandes, Bethany K Husband, Rachel L Atkinson, Matthew J Derry, Daniel TW Toolan, Higor A Centurion, Paul D Topham, Renato V Gonçalves, Vincenzo Taresco, Steven M Howdle, **Porous hollow TiO_2 microparticles for photocatalysis: exploiting novel ABC triblock terpolymer templates synthesised in supercritical CO_2**, *Polymer Chemistry*, 2021 (12), 19, 2904-2913, 10.1039/D1PY00334H

The following publications were produced from the author's MSc, and form the basis of work in chapter 4.

V L. Scott Blankenship, Norah Balahmar and Robert Mokaya, **Oxygen-rich microporous carbons with exceptional hydrogen storage capacity**, *Nature Communications*, 2017 (8), 1–12, 10.1038/s41467-017-01633-x

VI L. Scott Blankenship and Robert Mokaya, **Cigarette butt-derived carbons have ultra-high surface area and unprecedented hydrogen storage capacity**, *Energy & Environmental Science*, 2017 (10), 2552–2562, 10.1039/C7EE02616A

Notes on the text

Terminology: The plethora of porous carbon materials are referred to by various terms in the literature. The focus of this work are turbostratic carbons, which are defined as possessing some regions of graphitic ordering, but are not ordered on the large scale. Within this group are activated carbons and biochars which are distinguished only by the former having a porogen added in their synthesis in order to aid pore formation. Because many carbons in this work may be considered to lay at the boundary of these two materials, in general the term turbostratic carbon is used. Occasionally, the terms biochar or activated carbon may appear in the text to explicitly distinguish two materials or sets thereof derived without and with a porogen.

Navigation: In the electronic version of this thesis there are various hyperlinked words. This includes chapter, section, figure and table numbers, as well as words and abbreviations defined in the glossary. The presence of a hyperlink is shown by the word(s) being highlighted when hovered over, and clicking will take you to the appropriate page or part thereof.

Contents

Chapter 1

Introduction

The current climate crisis necessitates the rapid development of technologies for CO_2 capture. Ideally these technologies should be simple and cheap to deploy. Exploitation of the phenomenon of physical adsorption of CO_2 onto porous materials may comprise a viable solution for both point source and Direct Air Capture (DAC), and turbostratic carbons provides a cheap, simple route to a viable material for such purposes. The following sections provide the essential background of the concepts and applications of the experimental, analytical, and computational work employed in this thesis in order to understand how to develop porosity, measure the developed porosity, and understand the relationship between CO_2 capture and porosity. In addition the author provides for convenience his published review on the modulation of the porosity of carbons for uptake of various gases (**Publication III**) as appendix A. This provides much broader information regarding the synthesis of porous carbons outside of just the turbostratic carbons which are examined in this work, methods to measure and control porosity in such materials, as well as the relationship between porosity and uptake of different sorbents in porous carbons.

1.1 Synthesis of turbostratic carbons

Turbostratic carbons are semi-ordered carbonaceous materials characterised as having high surface area due to an extensively porous structure. Gases such as CO_2 can be physisorbed onto the surface of the material making for facile regeneration.[1,2] These characteristics make the material attractive for CO_2 capture. In addition, these materials are chemically and thermally robust, meaning that they are suitable for industrial applications.[1,3,4] As the only requirement for a material to be suitable for use as a precursor to turbostratic carbon is that it have a high carbon content, these materials can be synthesized from a range of cheap, and even renewable or waste-derived precursors.[5–9]

The porosity of a carbonaceous material is typically developed *via* a pyrolysis process wherein at first, a semi-graphitic structure is established; the voids between layers forming pores. Pores are then further constructed *via* intercalation of species between the graphitic layers for example by gases,[10] or metal ions such as Na or K.[5,11–13] Both of these intercalating agents can come from the raw precursor itself or be added to improve pore development. Further pore development comes as the result of chemical reactions, including the oxidation of carbon to form carbonates, or condensing processes including dehydration reactions which form cross-links between graphitic layers.[5,12,14] All of these processes tend to yield pores of a slit-like geometry, whose width is defined by the distance between two adjacent carbon walls, while the other dimensions are not usually defined (or assumed to be infinite).[15,16]

In order to facilitate high levels of porosity development, polymeric carbohydrates and sugars are often hydrothermally carbonised prior to activation with oxidative chemical porogens such as KOH, by heating in water under

high pressure to form hydrochar. Hydrochar is a low-surface area material ($\sim$30 $m^2\,g^{-1}$) composed of microspheres with hydrophilic reactive oxygen moieties at the surface. The overall overall oxygen concentration of the material is also increased relative to that of the precursor.[7,17] Dried hydrochar is then more susceptible to KOH-activation due to the improved reactivity between K and the oxygen-rich outer layer of the material.[17,18] In some cases, hydrothermal carbonisation forms a necessary step in the activation of a precursor, as some carbohydrates will not activate unless they have been first hydrothermally carbonised.[19]

The following subsections detail background and rationale for the synthesis routes towards turbostratic carbons employed in this thesis.

1.1.1 From Cigarette Butts

Used Cigarette Butts (UCBs) pose a large environmental hazard as a result of (i) being made of non-biodegradable Cellulose Acetate (CA) as well as (ii) containing a myriad of toxic chemicals.[20–22] As they are the most common waste material worldwide, there have been attempts to reduce their environmental presence, initially *via* anti-littering campaigns.[23,24] More promising however is the prospect of valorising UCBs by various means, including conversion to activated carbons as reported by the author in **Publication VI** as well as many other researchers - a summary of preparation conditions and properties of resultant turbostratic carbons is given in table 1.1.[25–34]

The reported porosity of carbons derived from UCBs is highly varied depending on synthetic conditions - see table 1.1. In the absence of an activating agent, and without pre-carbonisation steps, A_{BET} typically does not exceed 700 $m^2\,g^{-1}$.[26,29,30,33,35] Whereas using a porogen, and/or pre-

Table 1.1: Details of preparation, activation conditions, porosity and composition of selected UCB-derived turbostratic carbons reported in the literature. For simplicity, any materials derived using a non-inert atmosphere[29] or *via* microwave activation[30] are excluded. For the porogen, number in brackets indicates the mass ratio, if reported. The number in brackets following the BET area, A_{BET} is the micropore surface area, where reported. The average pore width, w_{avg} is taken as reported without any further analysis. O/C ratio is the atomic ratio.

Preparation	**Pyrolysis**		$\mathbf{A_{BET}}$ / $\mathbf{m^2\,g^{-1}}$		$\mathbf{w_{avg}}$ / **Å**	**O/C**	**Elements**	**Ref.**
	T / °C	**Porogen**						
-	900	KOH (1)	224		32	0.34	K, Na, Si, Cl, Ti	[25]
-	900	-	637		33	0.085	Si, K, Ti	[35]
Formation of polypyrrole composite	800	KOH (1.5)	3420		46	0.12		[36]
-	900	-	573	(395)	25		Ti, N	[29]
Soaked in $NH_4VO_{3(aq)}$ then dried. Heated to 270 °C in a NH_3/N_2 atmosphere	800	-	164		>100			[32]
Soaked in $NaOH_{(aq)}$ (48 vol.%), then carbonised at 400 °C	800	NaOH	1083		22	0.23	Na	[33]
-	800	-	571		27	0.29		[33]
-	800	-	262		45			[37]
Washed in ethanol and water, carbonised at 600 °C	800	KOH (5)	2751		<20			[6]
Hydrothermal carbonisation	600	KOH (4)	4310	(3867)	<20	0.53	N	[8]
Hydrothermal carbonisation	800	KOH (4)	1012					[34]

carbonising in air or hydothermally can improve surface areas to around $3000\,m^2\,g^{-1}$.[6,33,34,36] The author's reports of ultrahigh porosity from KOH-activated hydrothermally carbonised UCBs in **Publication VI** (BET surface area (A_{BET}) $>4000\,m^2\,g^{-1}$, pore volume $>2.00\,cm^3\,g^{-1}$) and high degree of microporosity ($>90\,\%$) are partially corroborated by the similar results using hydrochar derived from pure CA in **Publication V**, suggesting that CA is an ideal precursor for activation to yield high surface area carbons. The structure of CA (see figure 1.1) - especially the labile acetyl groups - is likely a large contributor to the high porosities reported in derived activated carbons. Xiong *et al.* also report a nitrogen-doped UCB-derived activated carbon with hierarchical porosity and A_{BET} of $3420\,m^2\,g^{-1}$, though this result is dubious as (i) the N_2 isotherm does not include ultralow pressure data, (ii) freespace appears to be incorrectly measured and (iii) isotherm measurement is not described in the text.[28] It was suggested in **Publication VI** that the unusually high porosity of UCB-derived carbons may be contributed to by the action of so-called contaminant-porogens, i.e. trace elements found in cigarette butts that can act as activating agents because carbons from UCBs had greater porosity than unused, i.e. 'fresh' CBs. However, another factor may be the specific treatment of the UCBs prior to any carbonisation - that is the removal of any paper, residual ash and tobacco.

The trace element composition of UCBs has been studied by various means, including neutron activation analysis of the intact butts,[38–41] adsorption and emission spectroscopy of various aqueous extracts,[42–47] voltammetry experiments,[48,49] and mixed methods according to environmental contaminant quantification standards.[50] The reported concentrations of different elements in UCBs has a great degree of variability depending on collection site, method, and brand. For example, work by Iskander *et al.* indicates

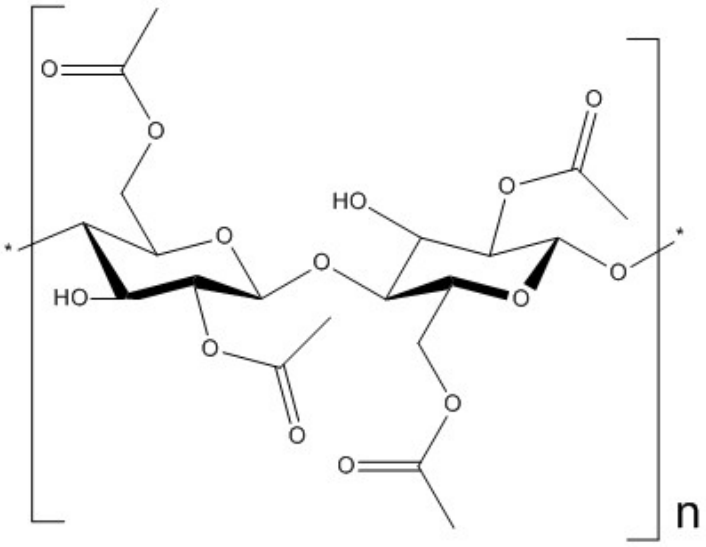

Figure 1.1: Structure of cellulose acetate.

that Al can be present in concentrations as low as 59, and as high as 2200 µg g^{-1}, depending on the country of origin of the smoked cigarette butt. Similarly, UCB samples collected from the environment [22,44,45,51] may have lower quantities of some elements due to leaching, but simultaneously may absorb some elements from the environment (for example from sea water). Trace elements have been identified in UCBs from almost every region of the periodic table, including alkali and alkaline earth metals; [38–42,50] transition metals, post transition metals and metalloids; [22,39–42,44–47,50–52] lanthanides; [38] and halogens. [38–41] Cigarette butt derived carbons have been also been found to contain various metals in trace quantities (see table 1.1, [25,26,35] although Ti, K, and Na have also been reported at quantities above 1 wt.%. [25–27,29,35] In addition the presence of Ca, K, Mg, Na, and Al were identified in UCB-derived hydrochar reported in **Publication VI**.

1.1.2 Impregnation Methods

Most commonly in the synthesis of activated carbons porogens are added to precursors by physical mixing with the precursor - i.e. some combination

of grinding and stirring.[8,53–55] An alternative technique is to impregnate the precursor with a (typically aqeuous) solution of porogen.[56–60] While there is scant evidence that solution impregnation has better outcomes over physical mixing in terms of porosity development, the rationale of the former technique is that the activating agent will be more evenly distributed throughout the precursor thus providing more homogenous porosity in the product however there is as yet no study to support this.

A further method using oxidative chemical activation is so-called organic salt carbonisation wherein the metal cation of an organic salt activates the carbonised precursor during pyrolysis. Reports, in particular from Sevilla *et al.* show that this method allows for a high degree of tunability in carbon PSDs by changing the identity of the activating cation.[61–68] The majority of anions used in organic salt carbonisation are small molecules such as gluconate or citrate,[61–65,69–72] however polymers have also been employed.[66,67,73,74]

The philosophy of these two emergent techniques (solution impregnation and organic salt carbonisation) for porogen-precursor mixing is that (i) the process can be simplified, (ii) porosity can be more readily controlled, and (iii) porosity is more homogeneous throughout the product. These effects are supposedly a result of both improved porogen-precursor contact, and more homogeneous porogen distribution. For the purposes of this work, mixing techniques with such goals are collectively termed 'impregnation' methods. In terms of solution impregnation, thus far syntheses have only been reported wherein the precursor is mixed with the porogen directly prior to pyrolysis.[56–60,75] That is, it has not been attempted to impregnate the porogen at the hydrothermal carbonisation step. The observation made by Zhang *et al.* that the formation of K salts with oxygen-rich moieties on the surface of calcined glucose is associated with improvements in ul-

tramicroporosity,[76] is notable and provides scope for further control over porosity in turbostratic carbons.

On the other hand, while the porosity of carbons derived through organic salt carbonisation has been exploited through changing the cation,[61–68] the capacity for more precise control over porosity by changing the degree of substitution of a cation on a polymer chain has not yet been explored. In studies using physical mixing, the porogen:precursor weight ratio is typically reported.[8,54,77–82] Oxidative chemical activation primarily relies on redox reactions between C and the porogen, thus knowing the exact stoichiometric porogen:C ratio may provide a route to understanding the precise effects of porogen concentration on carbon porosity.

1.2 Physisorption & porosity

Porous materials possess an interconnected pore system where pores are defined as voids which are deeper than they are wide.[83,84] Additionally, pores are defined as being able to contain fluid, which indirectly gives a minimum width for voids to be considered pores of 2.6 Å, as this is the kinetic diameter of the smallest practical fluid specie, He.[84,85] The ability of porous materials to contain fluids has led to the use of the phenomenon of adsorption being used to characterise their porosity. That is, knowledge of the behaviour of the system when the material is enriched with a fluid is utilised to understand pore size, shape and interconnectivity. In particular, so-called physisorption is exploited wherein adsorbate-adsorbent interactions do not include any sort of chemical attraction but instead rely on non-bonding forces[84] - thus hypothetically (although not always in practice), structure ought not be significantly conflated with surface chemistry.

What follows is a discussion of the various types of pore structures and associated adsorption phenomena, and thus an overview of methods to determine porosity from an isotherm.

1.2.1 Pore characteristics & filling mechanisms

The International Union of Pure and Applied Chemistry (IUPAC) defines ranges of pore sizes according to the mechanisms of pore filling by an adsorbate.[84] The three main mechanisms; micropore filing; monolayer adsorption; and multilayer adsorption are illustrated in figure 1.2. Specifically, micropores (<20 Å)[83] are filled at ultralow relative pressures, and are characterised by strong heats of adsorption due to complementary adsorbate-adsorbent interactions from all pore walls.[86] The subdivision into ultramicropores (<7 Å) and supermicropores (7 to 20 Å)[83] is derived from the fact that pores narrower than 7 Å can fit two adjacent rows of N_2 molecules,[84] and thus have the highest degree of pore wall potential overlap. Mesopores (20 to 500 Å)[83] are characterised by being large enough to allow monolayer adsorption. That is, all adsorbed molecules are in contact with the surface and are not significantly influenced by attraction to the adjacent or opposite pore wall.[87,88] As pressure increases, repulsive adsorbate-adsorbate interactions are overcome so that additional adsorbate molecules adsorb on top of the monolayer - this process is known as multilayer adsorption. The widest pore size classification is macropores which are larger than 500 Å[83] and are not easily characterised by isothermal gas adsorption experiments, instead necessitating the use of mercury intrusion porosimetry for determination of porosity.[87,89,90] In addition to these principal adsorption processes, in mesopores capillary condensation can occur at relative pressures greater than ∼0.2 wherein the adsorbate enters a liquid-like state

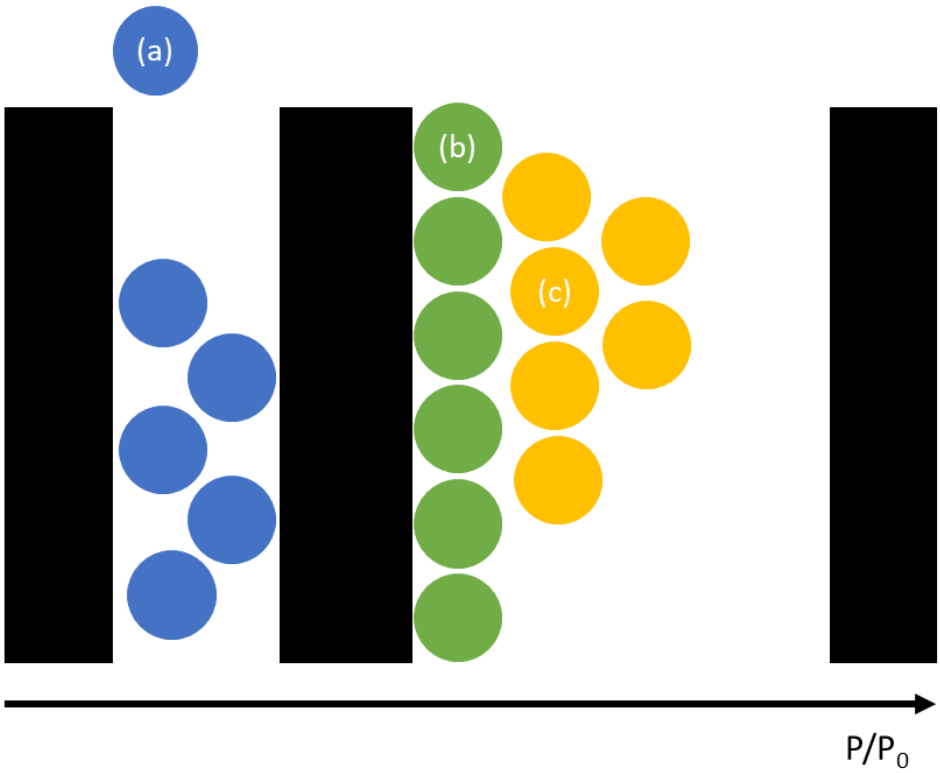

Figure 1.2: The three principle pore filling mechanisms, in order of their occurence with increasing relative pressure; (a) micropore filling; (b) completion of the monlayer in mesopores; and (c) multilayer adsorption.

despite being below saturation pressure. This can lead to hysteresis in the resultant isotherm[84,91] which is discussed in more depth in section 1.2.2.

While few materials show uniform pore shape, idealised shape is defined by IUPAC according to five characteristic shapes; cylindrical, slit, funnel, sphere, and ink-bottle.[92–94] For example while aluminium oxides typically have cylindrical pores,[94] turbostratic carbons are usually assumed to have slit-shaped pores,[16,95,96] although carbide-derived carbons have been shown to possess cylindrical or spherical pores.[97] Zeolites have a broad range of pore shapes.[98]

In addition to shape and size, pores are also defined by their degree of accessibility. Figure 1.3 illustrates this type of pore classification. In general, pores can be termed as 'closed' or 'open', based on whether or not they have

an accessible entrance. In the case of open pores, these are further subdivided into 'through' pores wherein both ends of the pore are accessible, and 'blind' pores wherein only one end of the pore is accessible. In addition, porosity can be formed through undulations on the surface, provided that the depth of these undulations is greater than the width. These are known as 'external pores'. However open pores are not necessarily accessible to an adsorptive, that is there entrance may be smaller than the adsorptive molecule - these pores are termed as 'chemically closed'. This can occur for ink-bottle pores with a narrow neck, or for very narrow slit or cylindrical pores.[92–94] Porosimetry is only able to quantify apparent porosity as defined by 'true' open pores (i.e. not chemically closed) and indeed for gravimetric adsorption applications this is the the only kind of meaningful porosity. However, closed pores nonetheless contribute to a materials bulk density and thus can influence *volumetric* uptake capacity for an adsorptive.

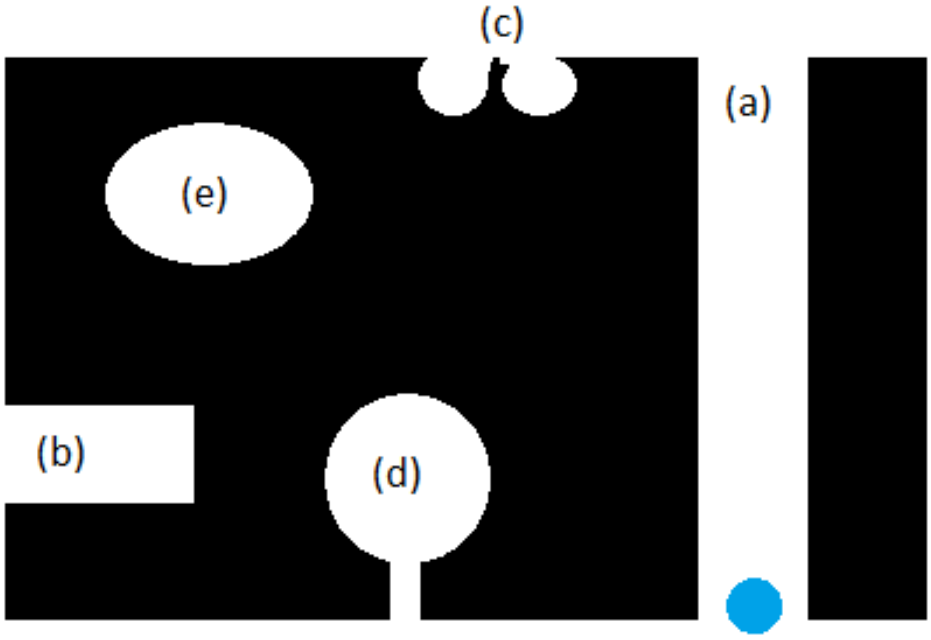

Figure 1.3: The different types of pores classified according to their accessibility; (a) an open, through pore; (b) an open, blind pore; (c) external pores; (d) a chemically closed pore; and (e) a closed pore. The small blue dot indicates the probe molecule size.

The final characteristic of porous structures is porosity hierarchy. Materials like MOFs and zeolites typically possess uniform or unimodal porosity,[99–102] whereas turbostratic carbons typically have multiple- or even a continuous range of (i.e. hierarchical) pore widths.[5,103–105] The pore hierarchy or lack thereof can play an important role in which applications the material is best suited to - for example a uniform Pore Size Distribution (PSD) can be used to exclude molecules above a certain size.[106–108]

1.2.2 Isotherm classification & interpretation

The various adsorption behaviours of a porous material discussed in the previous section result in distinct and interpretable forms of the resultant isotherms. As a general rule, the relative amount of gas adsorbed in different pressure ranges gives an indication of the amount of porosity in the internal micropore and mesopore regions as well as the amount of external surface area. To demonstrate, a labelled isotherm is shown in figure 1.4. High adsorption in the low pressure region indicates the presence of micropores, while an increase in uptake at pressures around the midpoint of the isotherm indicate mesoporosity. If there is a plateau in the middle of the isotherm, this typically indicates that a monolayer has formed. The curvature of the isotherm prior to the plateau (the adsorption 'knee') is indicative of the breadth of the PSD; a gentle knee shows a broad PSD, while a sharp knee indicates that pore sizes are narrowly distributed. Finally, high uptake as relative pressure approaches 1 is indicative of adsorption on the external surface, showing that the material is non-porous or macroporous.[84] IUPAC has designated eight distinct isotherm types.[84,109] These need not be discussed in full detail here - it is sufficient to state that types I(a) and (b) isotherms are indicative of microporosity, while IV(a), IV(b) and V are

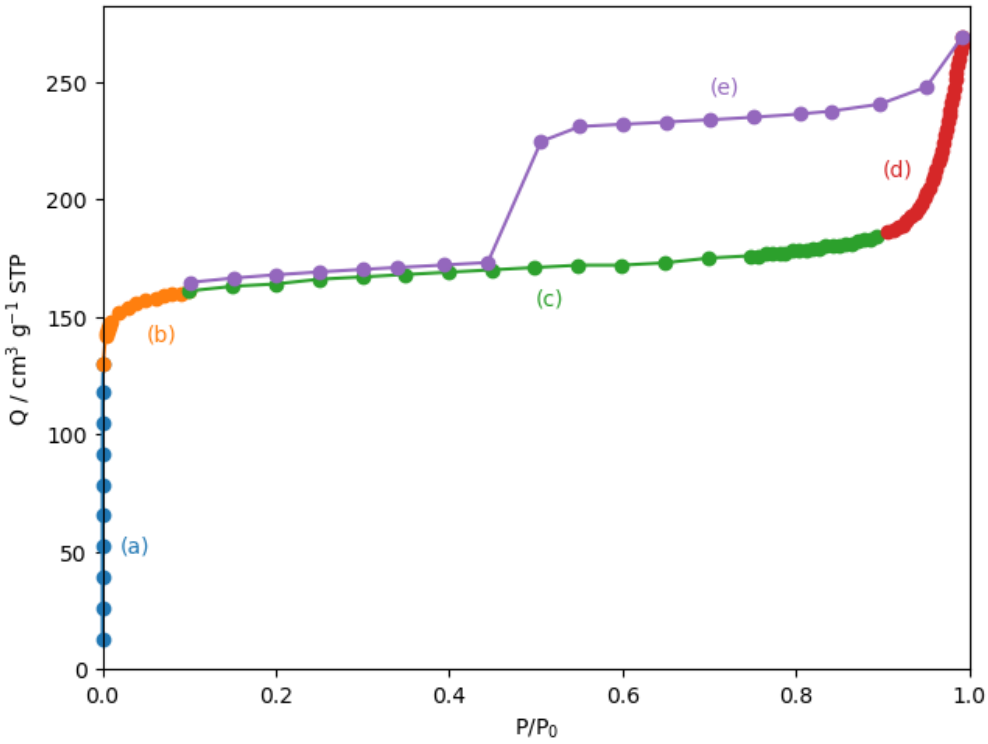

Figure 1.4: An isotherm of N_2 on a turbostratic carbon. The isotherm possesses (a) high uptake in the micropore region, indicating microporosity; (b) a sharp knee due to a narrow PSD; (c) a plateau in the medium pressure region due to formation of a monolayer this remains flat in the middle of the isotherm due to lack of mesoporosity; (d) high uptake as relative pressure approaches 1 showing external surface adsorption; and (e) a hysteresis loop due to capillary condensation.

seen on isotherms with high mesoporosity. Nonporous samples typically exhibit type II, III or VI isotherms. The variation in shapes can be indicative of surface chemistry and/or pore size hierarchy.[91,110] Of course as a lot of materials exhibit multiple types of porosity, many materials exhibit characteristics of multiple isotherm types.[84]

Apart from the general isotherm types, the presence of hysteresis - i.e. desorption releasing less adsorbate than is taken up during adsorption at an identical relative pressure - is indicative of capillary condensation.[91,110,111] As with characteristic isotherm types, IUPAC has defined six distinct forms of hysteresis loop. Depending on the type of hysteresis loop, its presence may indicate adsorption metastability in an 'open' pore, pore network ef-

fects and/or other forms of pore blocking.[84] Each of the six hysteresis loops are associated with specific kinds of materials - for example H4 loops are frequently found in micro-mesoporous carbons, whereas H1 is typically associated with materials possessing uniform open mesopores.[84,91]

1.2.3 Isotherm models

The theory of adsorption on a surface can be described mathematically, that is loading of adsorbate on an adsorbent, Q can be described as a function of pressure, P. In the simplest instance, Henry's law[112] (equation 1.1) describes a linear increase in Q with increasing P.

$$Q(P) = K_H P \tag{1.1}$$

Of course, a linear relationship is unrealistic as saturation eventually occurs. Nonetheless the Henry constant, K_H an be used as an approximation of the strength of interaction between adsorbate and adsorbent. Improvements can be attained through treating the isotherm as a quadratic or virial function, or by the Freundlich approach which modifies the Henry equation to account for the unavailability of adsorption sites by with increase in loading by using the exponent $\frac{1}{m}$, but this still does not account for saturation. Furthermore, neither of these approaches consider the specific case of adsorption of gases onto solid surfaces, instead being more suited to absorption of gas into a liquid. Such a theory was first introduced by Langmuir using kinetics. This assumes a reversible reaction between an ideal adsorbate, A_g and an adsorption site, S to form the adsorbed complex, A_{ad}. The reaction proceeds until it reaches equilibrium with constant K;

$$\mathrm{A}_g + \mathrm{S} \overset{\mathrm{K}}{\rightleftharpoons} \mathrm{A}_{\mathrm{ad}} \tag{1.2}$$

From this can be derived the Langmuir isotherm (equation 1.3), which also accounts for the formation of the monolayer which under this theory is the maximum possible loading, by including the monolayer capacity, Q_m.

$$Q(P) = Q_m \frac{KP}{1 + KP} \tag{1.3}$$

This can then be adapted to account for adsorbent heterogeneity by considering multiple adsorption sites, each with their own equilibrium constants, K_i and monolayer capacities Q_{m_i}. Thus the isotherm is modelled as a summation of Langmuir isotherms as in equation 1.4. Alternatively, as in the Tóth model, a heteroegeneity factor, t can be used - see equation 1.5.

$$Q(P) = \sum_1 Q_{m_i} \frac{K_i P}{1 + K_i P} \tag{1.4}$$

$$Q(P) = Q_m \frac{KP}{\sqrt[t]{1 + (KP)^t}} \tag{1.5}$$

Thus, surface heterogeneity can be quantified by t (equation 1.5) or the number of adsorption sites (equation 1.4). In addition, it has been recently shown that equilibrium constant(s) can be use to approximate the potential energy of adsorption, ε as a function of surface coverage (i.e. fractional loading).[113] On the other hand, the Dubinin-Radushkevitch and later the Dubinin-Astakhov (see equation 1.6) models explicitly considers the thermodynamics of adsorption and so ε is included in such a treatment.

$$Q(P) = Q_m \exp\left[-\left(\frac{-RT\ln\left(\frac{P}{P_0}\right)}{\varepsilon}\right)\right]^m \tag{1.6}$$

What is lacking in all of the models discussed above is a description of multilayer adsorption. Stephen Brunauer, Paul Emmet, and Edward Teller expanded Langmuir theory to account for multilayer adsorption, which occurs at higher pressures and temperatures. The following assumptions are made;[114]

(1) Gas molecules adsorb on solid layers infinitely,

(2) Gas molecules only interact with adjacent layers,

(3) The Langmuir theory can be applied to each layer,

(4) The enthalpy of adsorption for the first layer is constant and greater than that for subsequent layers,

(5) After monolayer adsorption, the enthalpy of adsorption is the same as that of liquefaction.

The total quantity of gas adsorbed, Q and thus the proportional surface coverage, θ is related the quantity of the monolayer, Q_m by equation 1.7. This contains the constant c which describes (see equation 1.8) the difference in heats of adsorption, λ between the first and subsequent layers. The latter is assumed to be the heat of liquefaction λ_L.

$$\theta(P) = \frac{Q}{Q_m} = Q_m \frac{cP}{\left(1 - \frac{Q}{Q_0}\right)\left(P_0 + P\left(c - 1\right)\right)} \tag{1.7}$$

$$c = \exp\frac{\lambda_1 - \lambda_L}{RT} \tag{1.8}$$

Equation 1.7 can be rearranged to give equation 1.9, which yields a linear relationship. When applied to an iostherm both the thermodynamic constant c and the monolayer loading, Q_m can be derived. From the former the enthalpy of monolayer adsorption can be calculated. The latter gives a simple method (equation 1.10) to quantify the specific surface area of the adsorbent if the cross-sectional area of the adsorbate, σ is known.

$$\frac{1}{Q\left(\frac{P_0}{P}-1\right)} = \frac{c-1}{Q_m\, c}\left(\frac{P}{P_0}\right) + \frac{1}{Q_m\, c} \tag{1.9}$$

$$A_{BET} = \frac{Q_m\, N_A\, \sigma}{a} \tag{1.10}$$

Where N_A is the Avogadro constant and a is the mass of the adsorbent.[114] In equation 1.10, calculation of the BET area per unit mass of adsorbent is shown. It can also be written in terms of total area, or adsorbent volume given the density of the adsorbent.

For microporous materials, using the BET method to calculate surface area is problematic for two reasons;

(1) The initial step in the adsorption mechanism is not the formation of the monolayer, but the filling of micropores. This renders BET theory inaccurate for microporous materials.

(2) Following the BET transform, there are often multiple linear regions of the plot. This means that report values of A_{BET} will differ depending on which linear region is used.

Despite these problems, A_{BET} continues to be the dominant measure of surface area used for microporous materials. As yet, there is no widespread

alternative or extension of BET theory that solves (1), however the standardisation required according to (2) is most commonly achieved according to a method described by Rouquerol et al, where the BET plot is transformed by changing the term on the y-axis to $Q\left(1-\frac{P}{P_0}\right)$. This yields a roughly parabolic graph known as the Rouquerol transform. A pressure range of the BET transform can then be selected to yield a consistent calculation of A_{BET} according to the following principles;

(1) The intercept of the original BET transform must be positive, as a negative intercept would yield a negative value for c.

(2) The range selected must correspond to a region of the Rouquerol transform where $Q\left(1-\frac{P}{P_0}\right)$ constantly increases with $\frac{P}{P_0}$.

(3) Q_m as determined from (1) and (2) can be found in the region of the isotherm selected.[115]

There have been further modifications to the BET theory including Guggenheim-Anderson-de Boer (GAB), which attempts to account for the differences in enthalpies of adsorption and liquefaction.[116] Other extensions to BET theory have been developed to give a more realistic model of adsorption for example by including the fact that number of layers adsorbed ought to be finite, or by substitution of relative pressure for relative density of the adsorbed phase which is useful in the case of for supercritical isotherms.[117,118]

1.2.4 Pore size distributions

As detailed in section 1.2.2, isothermal porosimetry can be used to determine a general qualitative definition of the porosity of a sample. Due to the development of models of adsorption, this can further be expanded

to quantify porosity. In the first instance, scalar quantities such as pore volume or surface area can be determined.[84] The simplest example of the former is the single point pore volume which relies simply on the amount adsorbed at the isothermal plateau for a subcritical adsorbent as saturation is approached. As for surface area, this is most commonly determined from BET theory and/or Langmuir theory.[114,119] Further theoretical manipulations such as t-plot or Dubinin treatments can be used to determine porosity within some range, i.e. within micropores or mesopores.[120,121] Alternatively a supercritical isotherm can be used to find pore volume below a certain maximum pore width, with the adsorbate and conditions selected to exclude pores larger than some maximum. A common example of this is CO_2 at 0 °C to find pore volume in pores smaller than 10 Å.[84,122,123] Porosity can also be defined using a vector, namely the Pore Size Distribution (PSD) which is essentially the porosity of the sample as a function of pore width typically represented as $f(w)$. Typically porosity is defined as pore volume but can easily be converted to be in terms of surface area. The resulting relationship can be used in the form of an incremental or cumulative PSD. While incremental PSDs can be used to determine discreet pore widths, its cumulative counterpart is useful for finding the volume of pores within some range of widths such as micropores. By this token, the PSD can also be used to determine total pore volume or surface area.[84,124,125]

Classical models used for determining Pore Size Distributions (PSDs) rely on parameters including the monolayer capacity of the adsorbent, as well as the adsorbate-adsorbent interaction. Additionally, they make use of false assumptions such as that the adsorbate behaves as a two-dimensional ideal gas (in the case of the Horvath-Kawazoe model).[125,126] A more recent development method is the kernel fit PSD, wherein the experimental isotherm is fit to a library (the kernel) of model isotherms that vary only accord-

ing to the single pore width of the adsorbent.[84,127–129] The determination of isotherms in the kernel relies on statistical modelling of adsorbate-adsorbate and adsorbate-adsorbent interactions specific to a system defined by pore size, pore geometry, the adsorptive and temperature. As a result, the PSDs determined this way are much more accurate. The determination of the kernel is most commonly performed using Density Functional Theory (DFT) or Grand Canonical Monte Carlo (GCMC) computational methods. Currently, DFT methods are preferred and are discussed below.

In the simplest method to calculate a kernel, a system is described by a surface with single width, slit shaped pores under vacuum. This is then dosed with argon at a specified pressure. As this occurs argon atoms will begin to fill the pore, causing pressure in the bulk adsorbate to decrease until an equilibrium is reached between the bulk argon and that adsorbed within the pore. According to the theory of dispersion interactions, the argon should be most concentrated at the surface at equilibrium – this concentration is the amount of gas adsorbed at the given pressure, i.e. one point on an isotherm. The amount of gas adsorbed can be calculated by minimising the free energy of the system as given by the Lennard-Jones potential, $U(s)$;

$$U(s) = 4\varepsilon \left[\left(\frac{\sigma}{s}\right)^{12} - \left(\frac{\sigma}{s}\right)^{6} \right] \tag{1.11}$$

Where s is the distance between the adsorbate and surface, ε is the energy of the adsorbate; and σ is the molecular diameter of the adsorbate. Thus, by varying the pressure from ultra-low to saturation, the amount of gas adsorbed at defined pressures can be calculated, and from this a model isotherm of this simple theoretical system can be built.

In practice, the equilibrium density profile is built up by minimising the grand potential energy of the system as a function of density, $\Omega[\rho(r)]$ - which is calculated for a point r in the system as follows;

$$\Omega[\rho(r)] = F[\rho(r)] + \int \rho(r)\,(V(r) - \mu)\ \mathrm{dr} \tag{1.12}$$

The rightmost, integral term defines the gas properties via the ideal gas equations according to the potential acting on the molecule $V(r)$, while $F[\rho(r)]$ is the Helmholtz free energy of the gas at equilibrium density at point r. $F[\rho(r)]$ is defined by the sum of repulsive (hard sphere) and attractive interactions between gas molecules. This treatment results in the local density approximation, which assumes that a local part of an inhomogeneous system has the same free energy density as a bulk homogeneous system of the same density. The inaccuracy of this treatment has led to further development of the theory via non-localised methods (Non-Local Density Functional Theory (NLDFT)),[111,129,130] and further extended using a corrugated pore model to account for energetic heterogeneity, as developed by Jagiello et al.[95] These adaptations are discussed in greater depth below.

Regardless of the method, the computational generation of an isotherm is repeated across a range of pore widths to generate a library of isotherms for a specific adsorbate-adsorbent system known as the kernel, $N\left(\frac{P}{P_0}, W\right)$. The general adsorption integral equation (equation 1.13) is then used to correlate the experimental isotherm, $N\left(\frac{P}{P_0}\right)$ with the kernel resulting in the pore size distribution as a function of pore width, $f(w)$.[84]

$$N\left(\frac{P}{P_0}\right) = \int_{w_{min}}^{w_{max}} N\left(\frac{P}{P_0}, w\right) f(w)\,\mathrm{d}w \tag{1.13}$$

This data can be displayed in terms of differential or cumulative pore volume and surface area, and as such can be used to determine textural quantities which prior to the development of kernel-fit PSDs had been calculated *via* classical methods.

The earliest kernels for adsorption of N_2 on porous carbon used a one-dimensional, homogeneous, semi-infinte model of the pore wall surface.[131] That is, the pore wall is completely flat and its length extends to infinity. This simplified kernel determination as pore space was only characterised by the pore width, and used a local density approximation to account for repulsive forces; short-range interactions are omitted for simplicity. Unfortunately this results in a poor description of the density profile of adsorbate molecules near the pore walls. Tarazona and co-workers improved on this model by considering these short-range interactions, producing the so-called Non-Local Density Functional Theory (NLDFT) kernel.[129,132] This nonetheless does not consider the energetic and chemical heterogeneity of pore walls within real porous carbons. Not only is this inaccurate, but the use of these kernels leads to poor fitting to the experimental isotherm and consistent artefacts in the resultant PSD.[95,133–135] Olivier suggested improvements such as applying weightings to the model isotherms before fitting to the experimental data, as well as using a finite pore model.[133] Nguyen and Bhatia found some improvements by taking the approach of accounting for pore wall heterogeneity by varying the pore wall thickness.[135] Jagiello *et al.*, however consider the pore wall to be a two-dimensional surface, having regular sinusoidal corrugations. This accounts for both chemical and energetic heterogeneity[95] and the eponymous 2D-NLDFT-HS (2-dimensional NLDFT heterogeneous surface) approach results in a better fit to the experimental isotherm.[95,136,137] Thus far, the 2D-NLDFT-HS kernel has been developed for N_2, O_2, H_2, CO_2, and Ar.[95,138–140]

The general adsorption integral equation was shown in equation 1.13. For convenience, it is reproduced in equation 1.14 in a form closer to that used by Jagielllo. $V(p_i)$ and $K(p_i,\, w)$ are the experimental isotherm and kernel respectively, and $f(w)$ is the differential PSD to be calculated.

$$V(p_i) = \int_{w_{min}}^{w_{max}} K(p_i, w) f(w)\, \mathrm{d}w \tag{1.14}$$

The solution to this equation is quite involved, but is achievable using a method developed by Jagiello.[141] In short, a stable PSD can be determined by using the regularization approach to determine an appropriate fitting parameter, λ[142–144] and the discrete result is interpolated using the B-spline approach.[145–147] This method is automated in the SAIEUS (Solution to the Adsorption Integral Equation Using Splines) program.[141] The λ variable is added to the expression in equation 1.14 to produce 1.15;

$$V(p_i) = \int_{w_{min}}^{w_{max}} K(p_i, w) f(w)\, \mathrm{d}w + \lambda \int_{w_{min}}^{w_{max}} \left[f''(w)\right]^2\, \mathrm{d}w \tag{1.15}$$

It is useful to be able to derive a single PSD from multiple isotherms in order to span the full breadth of pore sizes. When considering M multiple isotherms, a summative approach is needed.[148] Minimisation of the multi-isotherm, multi-kernel expression in equation 1.16 for each adsorbate, m will yield a single PSD for all M isotherms.*

$$\min \sum_{m}^{M} \sum_{i}^{N_m} \left[V_m(p_i) - \int_{w_{min}}^{w_{max}} K_m(p_i,\, w) f(w)\, \mathrm{d}w \right]^2 + \lambda \int_{w_{min}}^{w_{max}} \left[f''(w)\right]^2\, \mathrm{d}w \tag{1.16}$$

*The summative expression in equation 1.16 is a result of the solution to the single isotherm general adsorption integral equation described in equation 1.15. Its derivation is discussed by Jagiello in the original paper,[141] but is outside the scope of this work.

Where $V_m(p_i)$ and $K_m(p_i, w)$ are the mth experimental isotherm and mth kernel respectively.[149–151]

1.3 CO_2 capture

Methods for CO_2 capture as an add-on to industrial processes can be divided into three principal, broad groups; (i) oxy-fuel combustion, (ii) pre-combustion capture and (iii) post-combustion capture.[152] Oxy-fuel combustion is not a true CO_2 capture method, but provides a means to more facile CO_2 capture by producing a highly pure stream of CO_2 meaning that gas separation is not necessary priory to capture.[153,154] Pre-combustion capture on the other hand involves the gasification of the fuel source using steam and oxygen, forming a mixture of H_2 and CO which is known as syngas. The H_2 can be used as a fuel, while in a similar manner to oxy-fuel combustion, the CO is converted to pure CO_2 for ease of capture.[155] Post-combustion capture does not require any of these complex treatments - CO_2 is simply separated and captured from existing flue streams.[156,157] Thus, this method may be considered the the most versatile of the three.

The principal commercial mode of post-combustion CO_2 capture is *via* chemical capture using liquid amines. This process is plagued by high costs due to the degradation of the amine solvent as well as corrosion of equipment.[158–160] Membrane-based CO_2 capture and separation doesn't rely on chemical regeneration as the requisite membrane material simply selectively allows CO_2 to travel through it while excluding other molecules due to their size.[161,162] The (theoretically) pure stream of CO_2 is then captured at the other side. In order for this to work, high pressures must be use to force CO_2 through the membrane; this can often lead to membrane degra-

dation.[163] As a result of these problems, a third category of CO_2 capture materials is under a lot of investigation - that is, solid porous sorbents which are not plagued by high regeneration costs or degradation. These include MOFs,[101,106] zeolites,[100,164] and of course porous carbons.[55,165–167]

Candidates for solid adsorbents applied to CO_2 capture are typically exploited for swing adsorption processes such as Pressure Swing Adsorption (PSA), Vaccuum Swing Adsorption (VSA) or Temperature Swing Adsorption (TSA). Such processes rely on adsorption taking place at some pressure (PSA, VSA) or temperature (TSA) after which CO_2 can be regenerated by changing the condition; typically this means reducing the pressure or increasing the temperature to facilitate desorption.[161,168–171] PSA and VSA only differ in that the former captures CO_2 at very high pressure and regenerates by reducing to atmospheric pressure whereas the latter performs capture at atmospheric pressure and release occurs at vaccuum. Thus VSA is more cost effective, however both of these pressure-based solutions are more desirable than TSA as they can be performed at the elevated temperatures present in flue gases.[161,171,172] Due to the different physical conditions used to capture and regenerate CO_2 in each of these processes, selection of solid sorbent is based on porosity. For example, materials for PSA should have a high specific surface area and possess minimal microprosity while for VSA pore size is more important than overall surface area.[171,173,174] Physisorbents such as MOFs and zeolites have also been recently applied to the newer field of Direct Air Capture (DAC), which may prove a necessary, complementary technology to post-combustion capture.[175–177] Selectivity for CO_2 over N_2 is particularly important in DAC due to CO_2's low partial pressure in the air. The selectivity is usually facilitated *via* moieties with high chemical affinity for CO_2, but nonetheless porosity is likely to play a role in the performance of these materials.[175,178,179]

While surface chemistry may play a role in the suitability of a porous carbon to capture CO_2 and indeed the applicability of a porous material in general to adsorb a gas,[56,180–185] for turbostratic carbons, porosity is the defining variable for CO_2 capture performance.[5,123,174,186–189] Increasing overall surface area and pore volume does improve gas uptake,[8,190] but the magnitudes of the effects of increasing these parameters are limited by pore size[5,123,187,191–194] - that is, it is important to maximise the porosity contained within pores of some specific width in order to optimise CO_2 uptake capacity. This so-called optimum pore width is dependent on the surface chemistry[180,183,185] and pore geometry[195–197] of the adsorbent. With all of these factors controlled for, at a given temperature, optimum pore size also appears to be highly variable with pressure.[174,198] Up to now, the optimum pore width is defined either as (i) a single pore width[5,187,191] or (ii) all pores of width less than some maximum.[174,192,199] Thus far, the values of both (i) and (ii) are estimated through computational modelling,[192,197,199] and then attempts have been made to confirm these results through experiment.[174,187] For CO_2 capture carbons with pores of width <5 Å are optimal at 0.1 bar, while this increases to <8 Å at 1.0 bar.[174] Larger micropores and mesopores have been shown to have far greater importance at high pressure.[123,200,201] It also appears that the *exact* size of these pores may not be as important under high pressure regimes.[202] As such, design of turbostratic carbons for specific CO_2 capture regimes relies on tailoring porosity. For example carbons for PSA ought to have minimal porosity below 8 Å and high porosity in larger pores. On the other hand, DAC physisorbents may rely on pores smaller than 5 Å. However, a rigorous analysis of the relationship between porosity within some range of pore widths and CO_2 uptake as a function of pressure does not yet exist in the literature.

References

1. T. Kuramochi, A. Ramírez, W. Turkenburg and A. Faaij, *Progress in Energy and Combustion Science*, 2012, **38**, 87–112.
2. S. Ghosh, M. Sevilla, A. B. Fuertes, E. Andreoli, J. Ho and A. R. Barron, *Journal of Materials Chemistry A*, 2016, **4**, 14739–14751.
3. H. M. Coromina, D. A. Walsh and R. Mokaya, *Journal of Materials Chemistry A*, 2016, **4**, 280–289.
4. E. Haffner-Staton, N. Balahmar and R. Mokaya, *Journal of Materials Chemistry A*, 2016, **4**, 13324–13335.
5. M. Sevilla and R. Mokaya, *Energy & Environmental Science*, 2014, **7**, 1250–1280.
6. H. Sun, P. La, R. Yang, Z. Zhu, W. Liang, B. Yang, A. Li and W. Deng, *Journal of Hazardous Materials*, 2017, **321**, 210–217.
7. M.-M. Titirici and M. Antonietti, *Chemical Society Reviews*, 2010, **39**, 103–116.
8. L. S. Blankenship and R. Mokaya, *Energy & Environmental Science*, 2017, **10**, 2552–2562.
9. A. Ariharan and V. Balasubramanian, *Indian Journal of Chemical Technology*, 2018, **25**, 140–149.
10. J. F. González, S. Román, C. M. González-García, J. V. Nabais and A. L. Ortiz, *Industrial & engineering chemistry research*, 2009, **48**, 7474–7481.
11. S. Osswald, C. Portet, Y. Gogotsi, G. Laudisio, J. P. Singer, J. E. Fischer, V. V. Sokolov, J. A. Kukushkina and A. E. Kravchik, *Journal of Solid State Chemistry*, 2009, **182**, 1733–1741.
12. J. Wang and S. Kaskel, *Journal of Materials Chemistry*, 2012, **22**, 23710–23725.
13. M. Ruiz-Fernández, M. Alexandre-Franco, C. Fernández-González

and V. Gómez-Serrano, *Adsorption*, 2011, **17**, 621–629.

14. D. Prahas, Y. Kartika, N. Indraswati and S. Ismadji, *Chemical Engineering Journal*, 2008, **140**, 32–42.
15. M. Sevilla, G. A. Ferrero and A. B. Fuertes, in *CO 2 Storage on Nanoporous Carbons*, Springer, 2019, pp. 287–330.
16. D. H. Everett and J. C. Powl, *Journal of the Chemical Society, Faraday Transactions 1: Physical Chemistry in Condensed Phases*, 1976, **72**, 619–636.
17. M. Sevilla, A. B. Fuertes and R. Mokaya, *Energy & Environmental Science*, 2011, **4**, 1400–1410.
18. M. Sevilla and A. B. Fuertes, *Chemistry–A European Journal*, 2009, **15**, 4195–4203.
19. E. Ares and J. Delebarre, in *Carbon price floor*, 2014.
20. E. Slaughter, R. M. Gersberg, K. Watanabe, J. Rudolph, C. Stransky and T. E. Novotny, *Tobacco Control*, 2011, **20 Suppl 1**, i25–9.
21. J. Puls, S. A. Wilson and D. Hölter, *Journal of Polymers and the Environment*, 2011, **19**, 152–165.
22. Q. Chevalier, H. El Hadri, P. Petitjean, M. Bouhnik-Le Coz, S. Reynaud, B. Grassl and J. Gigault, *Chemosphere*, 2018, **194**, 125–130.
23. B. King, S. Dube, R. Kauffman, L. Shaw and T. Pechacek, *Vital signs: current cigarette smoking among adults aged ≥ 18 year – United States, 2005-2010*, 2011.
24. B. Harris, *Tobacco Control*, 2011, **20**, i10–i16.
25. S. M. Soltani and S. K. Yazdi, 2012 12th IEEE International Conference on Nanotechnology (IEEE-NANO), pp. 1–3.
26. S. M. Soltani, S. K. Yazdi and S. Hosseini, *Applied Nanoscience*, 2013, **4**, 551–569.
27. H. H. Lima, R. S. Maniezzo, V. L. Kupfer, M. R. Guilherme, M. P. Moises, P. A. Arroyo and A. W. Rinaldi, *Journal of Environmental*

Chemical Engineering, 2018.

28. Q. Xiong, Q. Bai, C. Li, D. Li, X. Miao, Y. Shen and H. Uyama, *Journal of the Taiwan Institute of Chemical Engineers*, 2019, **95**, 315–323.
29. M. Lee, G. P. Kim, H. Don Song, S. Park and J. Yi, *Nanotechnology*, 2014, **25**, 345601.
30. Y. Hamzah and L. Umar, *Journal of Physics: Conference Series*, 2017, **853**, 012027.
31. C. Yu, H. Hou, X. Liu, L. Han, Y. Yao, Z. Dai and D. Li, *Frontiers in Materials*, 2018, **5**, 63.
32. Y. Wang, M. Jiang, Y. Yang and F. Ran, *Electrochimica Acta*, 2016, **222**, 1914–1921.
33. C. B. Koochaki, R. Khajavi, A. Rashidi, N. Mansouri and M. E. Yazdanshenas, *Biomass Conversion and Biorefinery*, 2019.
34. S. Bilge, N. K. Bakirhan, Y. Osman Donar, A. Sınağ and S. A. Ozkan, *Sensors and Actuators B: Chemical*, 2019, **296**, 126626.
35. S. K. Yazdi, S. M. Soltani and S. Hosseini, *Advanced Materials Research*, 2012, **587**, 88–92.
36. Y. Xiong, C. Wang, C. Jin, Q. Sun and M. X. Xiong, *Sustainable Chemistry and Engineering*, 2018.
37. S. Polarz, B. Smarsly and J. H. Schattka, *Chemistry of materials*, 2002, **14**, 2940–2945.
38. F. Y. Iskander, *Journal of Radioanalytical and Nuclear Chemistry*, 1992, **159**, 105–110.
39. F. Y. Iskander, *Journal of Radioanalytical and Nuclear Chemistry*, 1985, **91**, 191–196.
40. R. Jenkins, C. Goldey and T. Williamson, *Beiträge zur Tabakforschung International/Contributions to Tobacco Research*, 1985, **13**, 59–65.

41. D. Wu, S. Landsberger and M. S. Larson, *Journal of Radioanalytical and Nuclear Chemistry*, 1997, **217**, 77–82.
42. H. Mussalo-Rauhamaa, A. Leppanen, S. S. Salmela and H. Pyysalo, *Archives of Environmental Health*, 1986, **41**, 49–55.
43. T. Kazi, N. Jalbani, M. Arain, M. Jamali, H. Afridi, R. Sarfraz and A. Shah, *Journal of Hazardous Materials*, 2009, **163**, 302–307.
44. H. Moriwaki, S. Kitajima and K. Katahira, *Waste Management*, 2009, **29**, 1192–1197.
45. J. W. Moerman and G. E. Potts, *Tobacco Control*, 2011, **20**, i30–35.
46. F. O. Pelit, R. E. Demirdöğen and E. Henden, *Environmental monitoring and assessment*, 2013, **185**, 9471–9479.
47. S. Dobaradaran, T. C. Schmidt, I. Nabipour, A. Ostovar, A. Raeisi, R. Saeedi, M. Khorsand, N. Khajeahmadi and M. Keshtkar, *Environmental Science and Pollution Research*, 2018, **25**, 5465–5473.
48. A. Nitsch, K. Kalcher, H. Greschonig and R. Pietsch, *Beiträge zur Tabakforschung International/Contributions to Tobacco Research*, 1991, **15**, 19–32.
49. K. Kalcher, W. Kern and R. Pietsch, *Science of The Total Environment*, 1993, **128**, 21–35.
50. L. S. Cardoso, F. N. Estrela, T. Q. Chagas, W. A. M. da Silva, D. R. de Oliveira Costa, I. Pereira, B. G. Vaz, A. S. de Lima Rodrigues and G. Malafaia, *Environmental Science and Pollution Research*, 2018, **25**, 8592–8607.
51. S. Dobaradaran, I. Nabipour, R. Saeedi, A. Ostovar, M. Khorsand, N. Khajeahmadi, R. Hayati and M. Keshtkar, *Tobacco Control*, 2017, **26**, 461–463.
52. T. Ren, X. Chen, Y. Ge, L. Zhao and R. Zhong, *Analytical Methods*, 2017, **9**, 4033–4043.
53. A. M. Aljumialy and R. Mokaya, *Materials Advances*, 2020, **1**, 3267–

3280.

54. A. Altwala and R. Mokaya, *Energy & Environmental Science*, 2020, **13**, 2967–2978.
55. M. Sevilla, W. Sangchoom, N. Balahmar, A. B. Fuertes and R. Mokaya, *ACS Sustainable Chemistry & Engineering*, 2016, **4**, 4710–4716.
56. M. L. Botome, P. Poletto, J. Junges, D. Perondi, A. Dettmer and M. Godinho, *Chemical Engineering Journal*, 2017, **321**, 614–621.
57. C. Ge, D. Lian, S. Cui, J. Gao and J. Lu, *Processes*, 2019, **7**, 592.
58. K. Adlak, R. Chandra, V. K. Vijay and K. K. Pant, *Journal of Analytical and Applied Pyrolysis*, 2021, 105102.
59. W. Shi, Q. Zhang, S. Liu, S. Su, B. Chang and B. Yang, *Journal of Colloid and Interface Science*, 2021, **600**, 670–680.
60. Z. Han, H. Yu, C. Li and S. Zhou, *Applied Surface Science*, 2021, **544**, 148963.
61. M. Sevilla and A. B. Fuertes, *Journal of Materials Chemistry A*, 2013, **1**, 13738–13741.
62. T. Tsumura, A. Arikawa, T. Kinumoto, Y. Arai, T. Morishita, H. Orikasa, M. Inagaki and M. Toyoda, *Materials Chemistry and Physics*, 2014, **147**, 1175–1182.
63. G. Ferrero, M. Sevilla and A. Fuertes, *Carbon*, 2015, **88**, 239–251.
64. G. A. Ferrero, A. B. Fuertes, M. Sevilla and M.-M. Titirici, *Carbon*, 2016, **106**, 179–187.
65. A. B. Fuertes and M. Sevilla, *ACS Applied Materials & Interfaces*, 2015, **7**, 4344–4353.
66. A. D. Roberts, X. Li and H. Zhang, *Carbon*, 2015, **95**, 268–278.
67. P. Yadav, A. Banerjee, S. Unni, J. Jog, S. Kurungot and S. Ogale, *ChemSusChem*, 2012, **5**, 2159–2164.
68. B. Yang, J. Chen, S. Lei, R. Guo, H. Li, S. Shi and X. Yan, *Advanced*

Energy Materials, 2018, **8**, 1702409.

69. W. Yang, W. Yang, F. Ding, L. Sang, Z. Ma and G. Shao, *Carbon*, 2017, **111**, 419–427.
70. M. Sevilla and A. B. Fuertes, *ACS Nano*, 2014, **8**, 5069–5078.
71. T. Yang, W. Li, M. Su, Y. Liu and M. Liu, *New Journal of Chemistry*, 2020, **44**, 7968–7975.
72. A. Fuertes, G. Ferrero and M. Sevilla, *Journal of Materials Chemistry A*, 2014, **2**, 14439–14448.
73. D. Puthusseri, V. Aravindan, S. Madhavi and S. Ogale, *Energy & Environmental Science*, 2014, **7**, 728–735.
74. D. Hines, A. Bagreev and T. J. Bandosz, *Langmuir*, 2004, **20**, 3388–3397.
75. O. Boujibar, A. Souikny, F. Ghamouss, O. Achak, M. Dahbi and T. Chafik, *Journal of Environmental Chemical Engineering*, 2018, **6**, 1995–2002.
76. Z. Zhang, D. Luo, G. Lui, G. Li, G. Jiang, Z. P. Cano, Y.-P. Deng, X. Du, S. Yin, Y. Chen, M. Zhang, Z. Yan and Z. Chen, *Carbon*, 2019, **143**, 531–541.
77. B. Adeniran and R. Mokaya, *Nano Energy*, 2015, **16**, 173–185.
78. M. Sevilla and A. B. Fuertes, *ChemSusChem*, 2016, **9**, 1880–1888.
79. J. Ludwinowicz and M. Jaroniec, *Carbon*, 2015, **82**, 297–303.
80. J. Deng, T. Xiong, F. Xu, M. Li, C. Han, Y. Gong, H. Wang and Y. Wang, *Green Chemistry*, 2015, **17**, 4053–4060.
81. Y. A. Alhamed, S. U. Rather, A. H. El-Shazly, S. F. Zaman, M. A. Daous and A. A. Al-Zahrani, *Korean Journal of Chemical Engineering*, 2015, **32**, 723–730.
82. Z. Hu, H. Guo, M. Srinivasan and N. Yaming, *Separation and Purification Technology*, 2003, **31**, 47–52.
83. IUPAC, *Compendium of Chemical Terminology*, Blackwell Scientific

Publications, 2nd edn, 1997.

84. M. Thommes, K. Kaneko, A. V. Neimark, J. P. Olivier, F. Rodriguez-Reinoso, J. Rouquerol and K. S. Sing, *Pure and Applied Chemistry*, 2015, **87**, 1051–1069.
85. D. Lide, *Handbook of Chemistry and Physics, volume 88th edition*, CRC Press, 88th edn, 2007, p. 154.
86. M. Dubinin, *Carbon*, 1989, **27**, 457–467.
87. S. J. Gregg, K. S. W. Sing and H. Salzberg, *Journal of The electrochemical society*, 1967, **114**, 279Ca.
88. R. T. Yang, *Gas separation by adsorption processes*, World Scientific, 1997, vol. 1.
89. A. Abell, K. Willis and D. Lange, *Journal of colloid and interface science*, 1999, **211**, 39–44.
90. J. M. Haynes, *Matériaux et Construction*, 1973, **6**, 209–213.
91. P. A. Monson, *Microporous and Mesoporous Materials*, 2012, **160**, 47–66.
92. J. Rouquerol, D. Avnir, C. Fairbridge, D. Everett, J. Haynes, N. Pernicone, J. Ramsay, K. Sing and K. Unger, *Pure and applied chemistry*, 1994, **66**, 1739–1758.
93. K. Kaneko, *Journal of membrane science*, 1994, **96**, 59–89.
94. B. Zdravkov, J. Čermák, M. Šefara and J. Janků, *Open Chemistry*, 2007, **5**, 385–395.
95. J. Jagiello and J. P. Olivier, *Carbon*, 2013, **55**, 70–80.
96. C. Lastoskie, K. E. Gubbins and N. Quirke, *The journal of physical chemistry*, 1993, **97**, 4786–4796.
97. H. Kurig, M. Russina, I. Tallo, M. Siebenbürger, T. Romann and E. Lust, *Carbon*, 2016, **100**, 617–624.
98. S.-J. Park and W.-Y. Jung, *Journal of Colloid and Interface Science*, 2002, **250**, 93–98.

99. J. Weitkamp, M. Fritz and S. Ernst, 9th International Zeolite Conference, pp. 11–19.

100. R. V. Siriwardane, M.-S. Shen, E. P. Fisher and J. Losch, *Energy & Fuels*, 2005, **19**, 1153–1159.

101. M. Ding, R. W. Flaig, H.-L. Jiang and O. M. Yaghi, *Chemical Society Reviews*, 2019, **48**, 2783–2828.

102. X. Lin, N. R. Champness and M. Schröder, *Functional Metal-Organic Frameworks: Gas Storage, Separation and Catalysis*, 2009, 35–76.

103. Y. Li, X. Niu, J. Chen and Y. Feng, *Ferroelectrics*, 2020, **562**, 17–27.

104. K. Xia, Q. Gao, J. Jiang and J. Hu, *Carbon*, 2008, **46**, 1718–1726.

105. N. Balahmar, A. S. Al-Jumialy and R. Mokaya, *Journal of Materials Chemistry A*, 2017, **5**, 12330–12339.

106. Q. Qian, P. A. Asinger, M. J. Lee, G. Han, K. Mizrahi Rodriguez, S. Lin, F. M. Benedetti, A. X. Wu, W. S. Chi and Z. P. Smith, *Chemical reviews*, 2020, **120**, 8161–8266.

107. C. Reid and K. M. Thomas, *The Journal of Physical Chemistry B*, 2001, **105**, 10619–10629.

108. B. Adeniran, E. Masika and R. Mokaya, *Journal of Materials Chemistry A*, 2014, **2**, 14696–14710.

109. K. S. W. Sing, D. H. Everett, R. A. W. Haul, L. Moscou, R. A. Pierotti, J. Rouquerol and T. Siemieniewska, *Pure and Applied Chemistry*, 1985, **57**, 603–619.

110. M. Thommes and K. A. Cychosz, *Adsorption*, 2014, **20**, 233–250.

111. J. Landers, G. Y. Gor and A. V. Neimark, *Colloids and Surfaces A: Physicochemical and Engineering Aspects*, 2013, **437**, 3–32.

112. W. Henry, *Philosophical Transactions of the Royal Society of London*, 1803, 29–274.

113. P. B. Whittaker, X. Wang, K. Regenauer-Lieb and H. T. Chua, *Physical Chemistry Chemical Physics*, 2013, **15**, 473–482.

114. S. Brunauer, P. H. Emmett and E. Teller, *Journal of the American Chemical Society*, 1938, **60**, 309–319.

115. J. Rouquerol, P. Llewellyn and F. Rouquerol, *Studies in Surface Science and Catalysis*, 2007, **160**, 49–56.

116. E. A. Guggenheim, *Applications of Statistical Mechanics*, Oxford Clarendon Press, 1966.

117. S. Brunauer, L. S. Deming, W. E. Deming and E. Teller, *Journal of the American Chemical Society*, 1940, **62**, 1723–1732.

118. S. Zhou, D. Zhang, H. Wang and X. Li, *Marine and Petroleum Geology*, 2019, **105**, 284–292.

119. I. Langmuir, *Journal of the American Chemical Society*, 1918, **40**, 1361–1403.

120. M. Dubinin and V. Astakhov, in *Description of adsorption equilibria of vapors on zeolites over wide ranges of temperature and pressure*, ACS Publications, 1971, pp. 69–85.

121. A. Marczewski, *Adsorption Glossary*, 2002.

122. J. Jagiello, J. Kenvin, A. Celzard and V. Fierro, *Carbon*, 2019, **144**, 206–215.

123. M. Sevilla, J. B. Parra and A. B. Fuertes, *ACS Applied Materials & Interfaces*, 2013, **5**, 6360–6368.

124. C. Shull, P. Elkin and L. Roess, *Journal of the American Chemical Society*, 1948, **70**, 1410–1414.

125. E. P. Barrett, L. G. Joyner and P. P. Halenda, *Journal of the American Chemical society*, 1951, **73**, 373–380.

126. G. Horváth and K. Kawazoe, *Journal of Chemical Engineering of Japan*, 1983, **16**, 470–475.

127. Z. Tan and K. E. Gubbins, *Journal of Physical Chemistry*, 1990, **94**, 6061–6069.

128. K. Sosin and D. Quinn, *Journal of Porous Materials*, 1995, **1**, 111–

119.

129. P. Tarazona, U. M. B. Marconi and R. Evans, *Molecular Physics*, 1987, **60**, 573–595.

130. C. Lastoskie, K. E. Gubbins and N. Quirke, *Langmuir*, 1993, **9**, 2693–2702.

131. N. Seaton, J. P. R. B. Walton and N. Quirke, *Carbon*, 1989, **27**, 853–861.

132. P. Tarazona, *Physical Review A*, 1985, **31**, 2672.

133. J. P. Olivier, *Carbon*, 1998, **36**, 1469–1472.

134. A. D. Lueking, H.-Y. Kim, J. Jagiello, K. Bancroft, J. K. Johnson and M. W. Cole, *Journal of Low Temperature Physics*, 2009, **157**, 410–428.

135. T. X. Nguyen and S. K. Bhatia, *The Journal of Physical Chemistry B*, 2004, **108**, 14032–14042.

136. A. Puziy, O. Poddubnaya, B. Gawdzik and M. Sobiesiak, *Adsorption*, 2016, **22**, 459–464.

137. K. Shi, E. E. Santiso and K. E. Gubbins, *Porous Materials*, 2021, 315–340.

138. J. Jagiello and J. P. Olivier, *Adsorption*, 2013, **19**, 777–783.

139. J. Jagiello and J. Kenvin, *Journal of Colloid and Interface Science*, 2019, **542**, 151–158.

140. J. Jagiello, J. Kenvin, C. O. Ania, J. B. Parra, A. Celzard and V. Fierro, *Carbon*, 2020, **160**, 164–175.

141. J. Jagiello, *Langmuir*, 1994, **10**, 2778–2785.

142. P. Hansen, *Computational Inverse Problems in Electrocardiology*, 2001, **5**, 119–142.

143. P. C. Hansen and D. P. O'Leary, *SIAM journal on scientific computing*, 1993, **14**, 1487–1503.

144. P. Hansen, in *The L-curve and its use in the numerical treatment of*

inverse problems, ed. P. Johnston, WIT Press, Southampton, 2001, pp. 119–142.

145. G. D. Knott, *Interpolating cubic splines*, Springer Science & Business Media, 2000, vol. 18.
146. H. Prautzsch, W. Boehm and M. Paluszny, *Bézier and B-spline techniques*, Springer, 2002, vol. 6.
147. C. De Boor, *A practical guide to splines*, Springer, 1978, vol. 27.
148. J. N. Caguiat, D. W. Kirk and C. Q. Jia, *Carbon*, 2014, **72**, 47–56.
149. J. Jagiello, C. Ania, J. B. Parra and C. Cook, *Carbon*, 2015, **91**, 330–337.
150. J. Jagiello and W. Betz, *Microporous and Mesoporous Materials*, 2008, **108**, 117–122.
151. J. Jagiello, C. Ania, J. Parra, L. Jagiello and J. Pis, *Carbon*, 2007, **45**, 1066–1071.
152. M. Kanniche, R. Gros-Bonnivard, P. Jaud, J. Valle-Marcos, J.-M. Amann and C. Bouallou, *Applied Thermal Engineering*, 2010, **30**, 53–62.
153. R. Stanger, T. Wall, R. Spörl, M. Paneru, S. Grathwohl, M. Weidmann, G. Scheffknecht, D. McDonald, K. Myöhänen, J. Ritvanen *et al.*, *International journal of greenhouse gas control*, 2015, **40**, 55–125.
154. T. Wall, Y. Liu, C. Spero, L. Elliott, S. Khare, R. Rathnam, F. Zeenathal, B. Moghtaderi, B. Buhre, C. Sheng *et al.*, *Chemical engineering research and design*, 2009, **87**, 1003–1016.
155. D. Jansen, M. Gazzani, G. Manzolini, E. van Dijk and M. Carbo, *International Journal of Greenhouse Gas Control*, 2015, **40**, 167–187.
156. Y. Wang, L. Zhao, A. Otto, M. Robinius and D. Stolten, *Energy Procedia*, 2017, **114**, 650–665.
157. A. Samanta, A. Zhao, G. K. Shimizu, P. Sarkar and R. Gupta, *In-*

dustrial & Engineering Chemistry Research, 2012, **51**, 1438–1463.

158. U. E. Aronu, H. F. Svendsen, K. A. Hoff and O. Juliussen, *Energy Procedia*, 2009, **1**, 1051–1057.

159. B. Dutcher, M. Fan and A. G. Russell, *ACS applied materials & interfaces*, 2015, **7**, 2137–2148.

160. S. Delgado, B. Valentin, D. Bontemps and O. Authier, *Industrial & Engineering Chemistry Research*, 2018, **57**, 6057–6067.

161. J. Adewole, A. Ahmad, S. Ismail and C. Leo, *International Journal of Greenhouse Gas Control*, 2013, **17**, 46–65.

162. K. Ramasubramanian and W. W. Ho, *Current Opinion in Chemical Engineering*, 2011, **1**, 47–54.

163. C. E. Powell and G. G. Qiao, *Journal of Membrane Science*, 2006, **279**, 1–49.

164. R. Krishna and J. M. van Baten, *Journal of Membrane Science*, 2010, **360**, 323–333.

165. B. Zhu, K. Qiu, C. Shang and Z. Guo, *JOURNAL OF MATERIALS CHEMISTRY A*, 2015, **3**, 5212–5222.

166. W. Chen, X. Wang, Z. Hashisho, M. Feizbakhshan, P. Shariaty, S. Niknaddaf and X. Zhou, *Microporous and Mesoporous Materials*, 2019, **280**, 57–65.

167. Y. Xia, R. Mokaya, G. S. Walker and Y. Zhu, *Advanced Energy Materials*, 2011, **1**, 678–683.

168. D. Bahamon, A. Díaz-Márquez, P. Gamallo and L. F. Vega, *Chemical Engineering Journal*, 2018, **342**, 458–473.

169. N. Hedin, L. Andersson, L. Bergström and J. Yan, *Applied Energy*, 2013, **104**, 418–433.

170. Q. Zhao, F. Wu, K. Xie, R. Singh, J. Zhao, P. Xiao and P. A. Webley, *Chemical Engineering Journal*, 2018, **336**, 659–668.

171. M. T. Ho, G. W. Allinson and D. E. Wiley, *Industrial & Engineering*

Chemistry Research, 2008, **47**, 4883–4890.

172. G. D. Pirngruber, F. Guillou, A. Gomez and M. Clausse, *International Journal of Greenhouse Gas Control*, 2013, **14**, 74–83.

173. C.-T. Chou and C.-Y. Chen, *Separation and Purification Technology*, 2004, **39**, 51–65.

174. V. Presser, J. McDonough, S.-H. Yeon and Y. Gogotsi, *Energy & Environmental Science*, 2011, **4**, 3059–3066.

175. A. Kumar, D. G. Madden, M. Lusi, K.-J. Chen, E. A. Daniels, T. Curtin, J. J. Perry IV and M. J. Zaworotko, *Angewandte Chemie International Edition*, 2015, **54**, 14372–14377.

176. N. McQueen, K. V. Gomes, C. McCormick, K. Blumanthal, M. Pisciotta and J. Wilcox, *Progress in Energy*, 2021, **3**, 032001.

177. S. Deutz and A. Bardow, *Nature Energy*, 2021, **6**, 203–213.

178. L. A. Darunte, A. D. Oetomo, K. S. Walton, D. S. Sholl and C. W. Jones, *ACS Sustainable Chemistry & Engineering*, 2016, **4**, 5761–5768.

179. Y. Deng, J. Li, Y. Miao and D. Izikowitz, *Energy Reports*, 2021, **7**, 3506–3516.

180. A. Lueking, *Applied Catalysis A: General*, 2004, **265**, 259–268.

181. Q. Li and A. D. Lueking, *The Journal of Physical Chemistry C*, 2011, **115**, 4273–4282.

182. Y. Li, S. Wang, B. Wang, Y. Wang and J. Wei, *Nanomaterials*, 2020, **10**, year.

183. L. Wang and R. T. Yang, *The Journal of Physical Chemistry C*, 2012, **116**, 1099–1106.

184. Z. Liang, J. Du, L. Sun, J. Xu, Y. Mu, Y. Li, J. Yu and R. Xu, *Inorganic chemistry*, 2013, **52**, 10720–10722.

185. S. Kayal and A. Chakraborty, *Chemical Engineering Journal*, 2018, **334**, 780–788.

186. B. Adeniran and R. Mokaya, *Chemistry of Materials*, 2016, **28**, 994–1001.

187. S. Choi, M. A. Alkhabbaz, Y. G. Wang, R. M. Othman and M. Choi, *Carbon*, 2019, **141**, 143–153.

188. S.-Y. Lee and S.-J. Park, *Journal of Colloid and Interface science*, 2013, **389**, 230–235.

189. N. P. Wickramaratne and M. Jaroniec, *Journal of Materials Chemistry A*, 2013, **1**, 112–116.

190. M. Cox and R. Mokaya, *Sustainable Energy & Fuels*, 2017, **1**, 1414–1424.

191. J. Li, B. Michalkiewicz, J. Min, C. Ma, X. Chen, J. Gong, E. Mijowska and T. Tang, *Chemical Engineering Journal*, 2019, **360**, 250–259.

192. I. Cabria, M. J. López and J. A. Alonso, *Carbon*, 2007, **45**, 2649–2658.

193. Y. Gogotsi, C. Portet, S. Osswald, J. M. Simmons, T. Yildirim, G. Laudisio and J. E. Fischer, *International Journal of Hydrogen Energy*, 2009, **34**, 6314–6319.

194. E. Masika and R. Mokaya, *The Journal of Physical Chemistry C*, 2012, **116**, 25734–25740.

195. M. Rzepka, P. Lamp and M. De la Casa-Lillo, *The Journal of Physical Chemistry B*, 1998, **102**, 10894–10898.

196. L. Zhou, Y. Zhou and Y. Sun, *International Journal of Hydrogen Energy*, 2004, **29**, 475–479.

197. S. Hlushak, *Physical Chemistry Chemical Physics*, 2018, **20**, 872–888.

198. M. De la Casa-Lillo, F. Lamari-Darkrim, D. Cazorla-Amoros and A. Linares-Solano, *The Journal of Physical Chemistry B*, 2002, **106**, 10930–10934.

199. S. Biloé, V. Goetz and A. Guillot, *Carbon*, 2002, **40**, 1295–1308.

200. M. E. Casco, M. Martínez-Escandell, J. Silvestre-Albero and F. Rodríguez-Reinoso, *Carbon*, 2014, **67**, 230–235.

201. M. Sevilla, A. S. M. Al-Jumialy, A. B. Fuertes and R. Mokaya, *ACS Applied Materials & Interfaces*, 2018, **10**, 1623–1633.

202. L. S. Blankenship and R. Mokaya, *Materials Advances*, 2022, **3**, 1905–1930.

Chapter 2

Motivations & Objectives

As discussed in chapter 1, turbostratic carbons can be useful for storing or capturing small molecules in their pores. In particular, these materials have been extensively explored for their potential for use in CO_2 capture at pressures typically ranging from 0 bar to 40 bar, with the view to apply them to different CO_2 capture regimes. It is apparent that the carbons' porosity and in particular the width of their pores plays a large role in the ability of a material to capture ambient temperature CO_2; that is at low pressures smaller pores are more useful but larger pores appear to be more beneficial at higher pressures. Furthermore, there is evidence to suggest that at lower pressures the precise value of the pore width becomes more important whereas at high pressures there is less precision needed. However the understanding of these phenomena is incomplete for a number of reasons. Firstly precisely creating turbostratic carbons with very narrow pores, whose widths also lie in a very narrow range is difficult, not least because the mechanisms of pore formation are a subject of debate. Secondly measurement of the widths and volumes of narrow, poorly ordered pores using current methods is complicated and furthermore appears to be quite

inaccurate by current methods. Finally, the relationship between the width of the pores and the pressure-dependent CO_2 uptake has only been tested at a handful of pore widths and pressures.

To this end, this thesis investigates two relationships (i) that between synthesis conditions and porosity (especially pore size), and (ii) that between pore size and pressure-dependent, ambient temperature CO_2 uptake. In addition, improvements to current methods of determining pore width are evaluated, as precise measurement of pore width underpins relationships (i) and (ii). This investigation is to be performed *via* the three routes described below.

Firstly this work exploits synthesis routes with the aim of creating carbons whose pore sizes are easily controllable in chapters 4 and 5. Specifically, chapter 4 aims to further the work of the author reported in **Publication VI** and **Publication V** to ascertain if contaminants found in UCBs can be useful in creating porosity in carbons made from UCBs as well trying to simplify the synthesis from **Publication VI**. On the other hand the work reported in chapter 5 attempts gain a more precise understanding of the relationship between these conditions and the porosity of the products by utilising some novel synthesis methods to strictly control activation conditions.

Secondly the objective of chapter 6 is to verify the utility of some recently developed techniques for determining porosity of carbons. Namely comparisons are made of PSDs derived from fitting of the 2D-NLDFT (heterogeneous surface) kernel to N_2, O_2, and H_2 isotherms as well as combinations of these isotherms. Any improvement in the accuracy of calculated PSDs can then be utilised to better understand the pore formation mechanisms which take place in the novel synthesis routes discussed in chapter 5.

Finally in chapter 7 a more thorough investigation of the relationship between pressure-dependent CO_2 uptake and pore width will be introduced *via* the creation of a piece of software to test the correlation between pore width and CO_2 uptake at a given pressure, for every pressure in a given range. The novelty of the approach will not only be in its thoroughness, but also its use of a experimental PSDs and CO_2 uptake isotherms porous carbons with a high variation in their porosities. Furthermore, following on from chapter 6 more recently developed methods of determining PSDs and thus pore widths will be used in order to evaluate their utility for defining the relationship between pore width and ambient temperature, pressure-dependent CO_2 uptake.

More broadly this work aims to evaluate, develop, and improve tools for determining porosity in porous materials of all types, as well as for rigorous understanding of the relationship between porosity and uptake of a given adsorbent. It is hoped that the tools developed herein will help to advance the science of adsorption in general.

Chapter 3

Methodology

3.1 Synthetic Techniques

In the context of porous carbon materials, activation is the process of porosity development in carbonaceous material.[1] In this work, activation is principally conducted *via* chemical oxidation,[1] that is by the oxidative action of a caustic agent - either KOH (chapter 4 and 5) or the self-activation of a polymer containing Na^+ ions (chapter 5) - on the carbon framework of the precursor. The oxidation of C to CO_2 and/or CO_3^{2-} results in voids forming in the semi-graphitic structure.[2–4] Further pore-forming processes may include intercalation of free porogen ions between graphitic layers,[5] as well as the formation of cross-links between polymeric chains prior to carbonisation.[6–8]

Hydrothermal carbonisation is often used in the synthesis of turbostratic carbons to make the precursor easier to activate. The process consists of simply placing a mixture of the precursor (typically biomass) and water into a sealed vessel and heating to temperatures between 180 and 300 °C. The ease of activation is attributed to the solid product, known as hydrochar, having a high O content and low aromaticity.[9–11] Indeed, the interaction with water molecules results in the formation of microspheres with a hydrophobic core and hydrophilic shell; this means that any porogen used in a subsequent activation step has much greater contact with these O-rich moieties.

In chapter 4 activated carbons were produced from Used Cigarette Butts (UCBs) collected from two different sources. Sets C and D came from a public ash tray and were used without removing the wrapping paper. Sets E came from a single brand from a single smoker and the wrapping paper was removed before further treatment. Full details of the sample sets can be found in table 3.1. In all cases, 2.5 g UCBs were ground in a spice grinder

Table 3.1: Synthetic details of samples derived from cigarette butts.

Prefix	**Preparation**	**# Samples**
hC	From public ash tray; Ash, excess tobacco removed before grinding. Hydrochar washed with 500 cm^3 water.	9
hD	From public ash tray; Ash, excess tobacco removed before grinding.	9
hE	Single brand from single smoker. Paper, ash, excess tobacco removed before grinding.	3

before being hydrothermally carbonised with 25 cm^3 water in a teflon-lined stainless steel autoclave by heating at 5 °C min^{-1} to 250 °C. Temperature was held for 2 h before the reaction mixture was allowed to cool to ambient temperature. Samples in set C were washed with 500 cm^3 water under suction to attempt remove any contaminants, while others (sets D and E) were derived without this treatment. In either case, the resultant hydrochars was dried for at 100 °C for 24 h. Hydrochar was then activated, either with KOH or alone in a tube furnace under N_2 at a flow rate of 60 cm^3 min^{-1} by heating at a rate of 3 °C min^{-1} to the target temperature (600, 700 or 800 °C and holding for 1 h. After being allowed to cool, all samples activated with KOH were washed in 600 cm^3 of 10 vol.% HCl solution for at least 24 h, then filtered and washed with water to give neutral washings. A portion of the samples activated without KOH were not washed in order to examine the effect of the washing step on the composition, morphology and porosity of the resultant samples. Sample designation is hA-$xTTT$, where h indicates the hydrothermal carbonisation step, A is the sample prefix (see table 3.1), x is KOH:UCB ratio (wt./wt.), and TTT is activation temperature in °C. For the self activated samples i.e. those that did not use KOH in the activation step, $'$ is appended to the end to indicate those which were not washed. For example hC-0800$'$ indicates a sample activated at 800 °C in the absence of activating agent, and that was not washed. To refer to the

hydrochar itself, the designation is h*A*-hydrochar, e.g. hydrochar derived from UCB-hydrochar set hD (see table 3.1) is hD-hydrochar.

Sawdust-derived carbons were made in chapter 5 by incorporating KOH at the hydrothermal carbonisation step. An aqueous solution of KOH was made where the mass of the KOH was defined as a ratio (between 0.00 to 2.00) of the mass of the sawdust used. The solution was then mixed with the sawdust and placed in an autoclave. The autoclave and contents were heated at a ramp rate of 5 °C to the target temperature (200, 250 or 300 °C), held for 2 h and then allowed to cool. The procedure was completed by drying the resultant slurry overnight at 100 °C and then activating in a tube furnace under N_2 (60 $cm^3\,min^{-1}$) at 800 °C for 1 h following a ramp rate of 3 °C min^{-1}. These sawdust-derived carbons are designated SA*x.xx-HHH* where the prefix SA indicates activated sawdust, *x.xx* is the KOH:sawdust ratio and *HHH* is the hydrothermal carbonisation temperature. All samples were washed with600 cm^3 of 10 vol.% HCl solution for a minimum of 24 h before being filtered under suction and washed with water until the pH of the washings was neutral. Finally the samples were dried at 100 °C overnight. The hydrothermally carbonised intermediates were also isolated and washed with water (500 cm^3) under suction before drying overnight at 100 °C. The hydrochars are designated SH*x.xx-HHH* to differentiate them from the activated samples.

Additionally, in chapter 5 sodium carboxymethyl cellulose (NC) was used as a precursor for direct (without hydrothermal carbonisation) activation. The structure of NC is shown in figure 3.1. Carbons were obtained from NC with different degree of substitutions (DSs) (0.0, 0.7, 0.9 or 1.2), obtained from Sigma-Aldrich. For all samples, NC was heated under a flow of N_2 (60 $cm^3\,min^{-1}$) at a rate of 3 °C min^{-1} and held for 1 h at the target temperature of 600, 700 or 800 °C. Samples were washed in 600 cm^3 of

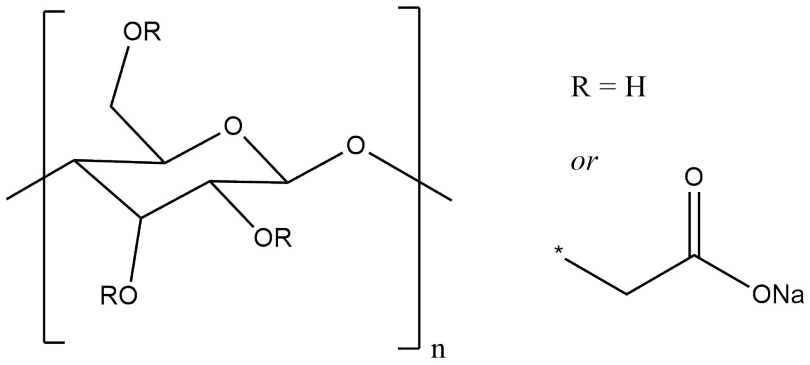

Figure 3.1: Structure of sodium carboxymethyl cellulose. Degree of substitution (DS) is taken as the average number of sodium carboxymethyl groups ($-CH_2COONa$) per monomer.

10 vol.% HCl solution, before being filtered and washed with deionised water to give neutral washings, and finally dried at 100 °C for 24 h. Samples are designated as NC$x.x$-TTT where NC indicates sodium carboxymethyl cellulose, $x.x$ is the DS, and TTT is the activation temperature.

3.2 Composition and morphology

Techniques in this section were employed to understand the composition, structure, and porosity of samples synthesised in this work, and their results are presented in chapters 4 and 5. The more precise compositional analysis techniques - X-ray Photoelectron Spectroscopy (XPS) and Inductively Coupled Plasma-Optical Emission Spectrometry (ICP-OES) - as well as electron microscopy were only used for samples produced from Used Cigarette Butts (UCBs) in chapter 4.

Thermogravimetric Analysis (TGA) measures the mass of a sample undergoing heating as a function of temperature or time.[12] TGA was used in this study primarily to determine the ash content of samples, thus giving a measure of sample purity,[13] i.e. whether the material contains any non-combustible matter, typically residual metals. For this work, TGA was

performed using a TA Q500 Thermogravimetric Analyser. All samples were analysed using a platinum pan under a flow of air at 100 cm^3/min. All experiments took place as follows; temperature was increased at 10 °C min^{-1} from ambient to 1000 °C before dwelling for 10 min.

CHN elemental microanalysis precisely determines the concentration (by weight) of carbon, nitrogen and hydrogen that make up a sample. This is achieved by total combustion of the sample at 975 °C under pure oxygen. At this stage impurities such as sulfur, phosphorous, and halogen compounds are also removed *via* various reactions. This results in a pure mixture of H_2O, CO_2 and oxides of nitrogen, which is transferred by means of a flow of He to a reduction chamber where the nitrogen oxides are reduced to N_2. This mixture of three sample gases plus the He carrier gas is then equilibrated to precise and constant temperature, volume and pressure. H_2O and CO_2 are then sequentially separated according to their thermal conductivity, leaving a flow of N_2 and He. The volumes of H_2O and CO_2 can then directly be used to calculate the sample H and C concentrations. The mixture of N_2 and He is compared with a reference flow of pure He to determine N content. For this study, CHN analysis was performed using an Exeter Analytical CE-440 Elemental Analyzer.

In general Powder X-ray Diffraction (P-XRD) is principally used to identify elements and determine inter-layer spacing within crystalline powder samples. In the case of the partially-ordered turbostratic carbons and hydrochars reported in this thesis P-XRD was used to determine the extent of graphiticity (i.e. how ordered the turbostratic domains are). In addition sharp peaks indicate the presence of crystalline material, which can be attributed to contaminants - typically residual porogen. In this study, P-XRD measurements were made using a PANalytical X'Pet Pro diffractometer, with CuKα X-rays of wavelength 1.54 Å. Data collection occurred

at 2ϑ from 2 to 80°.

X-ray photoelectron spectra are produced *via* the irradiation of a sample with an X-ray beam, resulting in the ejection of electrons from low energy atomic orbitals according to the photoelectric effect[14]. The electrons are collected and detected by the apparatus, facilitating the elucidation of the identity and quantity of elements present on the surface of the material from the kinetic energy of ejected electrons and the number of electrons ejected at each binding energy, respectively. The binding energy, E_B is calculated according to the below equation;

$$E_B = h\nu - \Phi - E_K \tag{3.1}$$

where $h\nu$ is the photon energy, Φ is the sample's work function, and E_K is the kinetic energy of the photoelectron. So-called 'shifting' of elemental characteristic E_B from those expected according equation 3.1 can be used to determine chemical and electronic states of detected species.[15] For the purpose of XPS analysis in this work, samples were prepared from selected hydrochars and turbostratic carbons by performing a TGA in air to burn off all carbonaceous material. The remaining inorganic matter was then analysed using the Kratos AXIS ULTRA with a mono-chromated Alkα X-ray source (1486.6 eV) operated at 10 mA emission current and 12 kV anode potential (120 W). Spectra were acquired with the Kratos VISION II software. A charge neutralizer filament was used to prevent surface charging. Hybrid–slot mode was used measuring a sample area of approximately 300 µm × 700 µm. The analysis chamber pressure was better than 5×10^{-9} mbar. Three areas per sample were analysed. A wide scan at low resolution (Binding energy range 1400 eV to −5 eV, with pass energy 80 eV, step 0.5 eV, sweep time 20 min) was used to estimate the total atomic % of

the detected elements. High resolution spectra at pass energy 20 eV, step of 0.1 eV, and sweep times of 10 min each were also acquired for photoelectron peaks from the detected elements and these were used to model the chemical composition. The spectra were charge corrected to the C 1s peak set to 285 eV. Casaxps (version 2.3.19 PR1.0) software[16] was used for quantification and spectral modelling.

Optical Emission Spectrometry (OES), also known as Atomic Emission Spectrometry (AES) is a technique used to quantify concentration of elements in solution by exciting them and measuring intensity of emissions at some characteristic wavelength associated with the return of the species to the ground state. These intensities are then converted to concentrations using a calibration curve. While there are multiple methods to excite the atoms, a common method is using Inductively Coupled Plasma (ICP) which also acts to separate elements in the solution. This technique is thus abbreviated to ICP-OES or ICP-AES.[17] In this work, samples were prepared for ICP-OES by dry-ashing in an alumina crucible at 600 °C for at least 16 h, the ash was then digested in an aqueous solution of 10 vol.% each of high purity HNO_3 and HCl (Aristar grade). The mixture was then sonicated for several hours, and digestion was completed via microwave, before being centrifuged at 4000 rpm for 99 min. Finally the digestate was filtered through syringe filters to remove any remaining sediment. References and blanks were prepared from the same stock digestion solution to ensure consistency. Standards were made from a 28-element standard (100 mg dm^{-3}, 2 vol.% HNO_3 matrix from Fisher) at concentrations of 0.1, 1, 10, 50 and 100 mg dm^{-3}. Measurements were made using a Perkin-Elmer Optima 2000 Spectrometer, using argon plasma.

3.2.1 Electron microscopy

Various forms of electron microscopy were used on the samples in chapter 4 in order to determine sample morphology as well as composition and dispersion of inorganic heteroatoms. The principal types are detailed here.

Scanning Electron Microscopy (SEM) uses a beam of focused electrons in order to image solid materials. As the electrons interact with the material, electrons and electromagnetic radiation are emitted via various mechanisms. Secondary electrons (SE) are a result of the ejection of electrons from atoms near the sample surface, and secondary electron images (SEI) provide high resolution images of surface morphology and texture.[18]

backscatter electrons (BSE) are electrons deflected by nuclear electrostatic charge – degree of deflection increases with nuclear charge. Though this results in much lower resolution images, backscatter electron detection (BED) images the material according to atomic weight, with heavier elements showing up as bright spots. This technique does not identify elements, but can be used to map heavier elements interspersed within a low atomic mass material.[18]

Tunneling Electron Microscopy (TEM) differs from SEM in that the electrons are transmitted through the sample as opposed to reflecting off of it. Imaging with TEM allows for much more detailed imaging, down to the atomic scale.[19]

Electron-Dispersive X-ray Analysis (EDX) relies on the excitation by X-rays of electrons within a sample to identify and quantify its elemental

components. It can be coupled with TEM in order to image the dispersion of elements within a sample, this technique is known as EDX-TEM.[18]

In this work, SEM images were taken on a JEOL 7100F FEG-SEM with detector set at a working distance of 10.00 mm. SE images were captured with an electron accelerating voltage of 1.00 or 2.00 kV, but this was increased to 15.00 kV for BSE. TEM images were taken on a JEOL 2100F FEG-TEM, with elemental dispersion determined using the EDX attachment.

3.3 Isotherms

In this work isotherms were measured in order to determine the porosity of the carbon samples as well as to find ambient temperature gravimetric CO_2 uptake capacity as a function of pressure. The techniques used for these measurements are discussed below.

All N_2 isotherms used for porosimetry were measured at $-196\,^{\circ}C$ on a 3flex analyser from Micromeritics. Prior to isotherm measurement, all samples were degassed at 300 °C for 16 h under high vacuum. Adsorption were then measured in the relative pressure range $\sim 1 \times 10^{-8}$ to ~ 1, after which the desorption isotherm was measured down to ~ 0.1. Thereafter free space was measured using He at both ambient and analysis temperature and used to adjust the previously measured isotherm. From the isotherms, A_{BET} values were determined using the Rouquerol method in the case of type-I isotherms,[20] otherwise this value was calculated using the linear portion of the BET transform within relative pressures between 0.05 and 0.30. Total pore volume (V_t) was determined from the volume adsorbed by the sample at a single point at relative pressure ~ 0.9 on the plateau

of the isotherm. Classical determination of micropore volume and surface area were determined using t-plot, with a carbon black STSA thickness curve. All PSDs are derived using the 2D-NLDFT heterogeneous surface kernel in the SAIEUS software,[21] with the regularization parameter, λ[22,23] kept constant for samples derived from the same precursor and chosen to optimise fit across all isotherms.

While the porosimetric analyses in chapters 4 and 5 use only N_2 isotherms, in chapters 6 and 7 O_2 and H_2 isotherms measured at $-196\,^{\circ}C$ were used to improve porosimetric analysis. O_2 isotherms were measured in the same manner as for N_2, however H_2 isotherms were measured up to the arbitrary pressure of 1013 mbar as H_2 is supercritical at $-196\,^{\circ}C$ and thus relative pressure is not physically meaningful. In chapter 6, the same classical measures of porosity were calculated from O_2 isotherms as previously performed using N_2 isotherms. Comparisons were made of the PSDs derived from fitting 2D-NLDFT heterogeneous surface kernels to O_2, N_2, and H_2 isotherms. In addition, Jagiello's multiple isotherm fitting procedure[24] was employed with combinations of N_2, O_2 and H_2 isotherms to yield a single PSD for a single sample. These porosities derived from these alternative techniques were compared in 6, and further used to assess the relationship between porosity and low-pressure CO_2 uptake in chapter 7.

Excess CO_2 uptake isotherms of turbostratic carbon samples reported in chapters 4 and 7 was determined *via* gravimetric analysis. This begins with the degassing of the samples under vacuum followed by precise measurement of the weight of the sample with increasing CO_2 pressure. The procedure results in an excess CO_2 uptake isotherm, from which molar gravimetric uptake can be read as a function of pressure. Measurements were taken at either 25 or 18 °C and up to 40 or 20 bar, on XEMIS or IGA analysers respectively from Hiden Isochema.

3.4 Software development

Chapter 7 describes the use of several python libraries in order to calculate linear regressions between porosity within some range of pore sizes to uptake of CO_2 at some pressure. The main libraries used in this project, known as the python Porosity Uptake Correlator (pyPUC) are `scipy`,[25] `numpy`,[26] `pandas`,[27] and `pygaps`.[28]

pyPUC is a fairly simple package whose structure is shown in figure 3.2. It is written almost exclusively in python,[29] apart from one small bash script.[30] The main functions of pyPUC can be found in `pyPUC/pyPUC/core`, while outside of this is the module `pyPUC/interface.py` which constructs a simple command line interface to run the program, and the bash script `pyPUC-cli` which executes `pyPUC/interface.py`. Finally there is a directory for the `source_data` which should be populated by the user with PSDs and experimental uptake isotherms for the project in question.

The code is well documented, however a brief discussion of the purpose of each of the modules in `pyPUC/pyPUC/core` follows here. Firstly `utils.py` defines utility methods for the other three modules. Most important are the methods `read_data()` and `define_array()`. The former simply reads the data from the `source_data` directory according to input arguments using the `pandas` library,[27] while the latter is a simple method for defining an array of pressures or pore widths for the modules `uptake_processing` or `psd_processing` using the `numpy` library.[26]

The `uptake_processing.py` and `psd_processing.py` modules are fairly self-explanatory, in each case simply processing the uptake or PSD data for all samples in `source_data/project`. The outputs from these modules can be seen in figure 3.2. The former attempts to fit each uptake isotherm

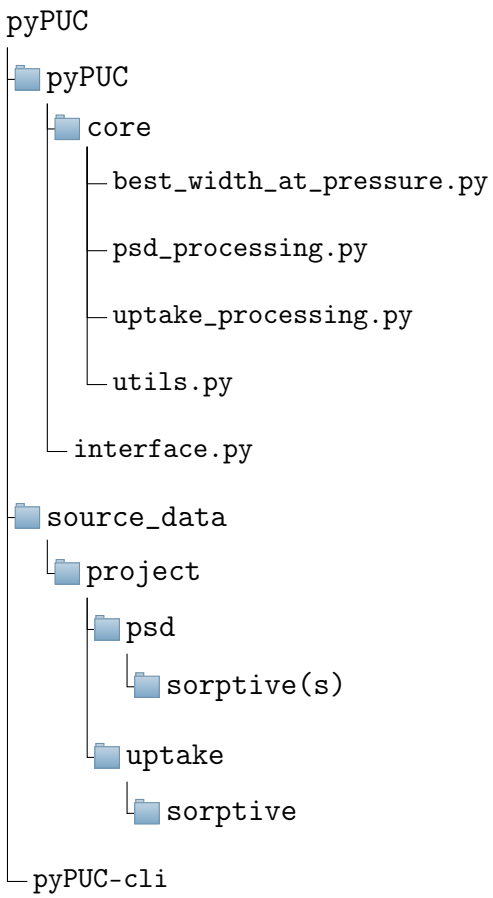

Figure 3.2: Structure of key modules and directories in the pyPUC package. There are other components in the github repository but they are not essential to the function of the package.

in the appropriate project in `source_data` to a range of model isotherms and selects the best fit, by using the `modelling` module from the library `pygaps`.[28] These model isotherms are then converted to point isotherms at pressures defined by the user. The pressures and loadings are then stored in a two-dimensional DataFrame, D_v (see table 3.2a). The latter reads in the cumulative PSDs for each sample, and determines the pore volume or surface area within each user-defined pore size range. A demonstration of how this works is shown in figure 3.3. This is done for each sample and stored in the DataFrame D_π (see table 3.2b). In either case, the data produced can be stored in memory or output as a `.csv`, alongside a simple report of the data processing (see appendix figures D.1 and D.2).

Table 3.2: An example output of processed data from the `uptake_processing.py` (a) and `psd_processing.py` modules (b). *A*, *B*, *C*, and *D* are the four samples used in this analysis. In the case of (a), the numbers are the loadings of CO_2 on the samples at each of the pressures in column *p*, and for (b) they are the surface areas of the samples within the pore size range defined by w_{min} and w_{max}.

(a)

p	A	B	C	D
1	4.27	4.01	4.27	4.35
2	5.93	5.25	5.93	5.95
3	6.94	5.96	6.94	6.91

(b)

w_{min}	w_{max}	A	B	C	D
5	4	59	282	238	260
6	4	401	514	442	465
6	5	142	232	204	204

```
import pandas as pd
import numpy as np

sample_df = pd.read_csv('psd.csv')  # PSD stored in
                                    DataFrame
w_array = [4, 5, 6]  # array of pore widths
i=0
for wmax in w_array[1:]:
    for wmin in w_array[w_array<wmax]:  # every possible
                                        combination of two w
                                        values
        rows_max = np.max(list(np.where(w < wmax)))
        rows_min = np.min(list(np.where(w > wmin)))
        max_value = sample_df.loc[rows_max, 'Vcum']
        min_value = sample_df.loc[rows_min, 'Vcum']
        param = max_value - min_value
        i+=1 # Go through all possible values of wmin for
                                            wmax
```

Figure 3.3: How the porosity within some pore width range is determined in pyPUC. Note that this is pseudo-code[31] as opposed to the actual source code.

Finally `best_width_at_pressure.py` takes the two DataFrames generated by `uptake_processing.py` and `psd_processing.py` and uses the `stats.linregress()` method from the `scipy` library[25] to perform linear regressions between each row of D_v and each row of D_π. That is, if each of D_v and D_π have three rows (1, 2, 3) then a linear regression of row 1 in D_v will be performed against each row 1, 2 and 3 of D_π. Then the same is performed for row 2 of D_v, etc.. `scipy.stats.linregress()` then returns the r^2 value, slope, and intercept of the regression which is stored

w_{min}	w_{max}	p	r^2	m	c	x	y
4	5	1	0.503	-0.005	5.77	[259 282 ...]	[4.27 4.01 ...]
4	5	2	0.667	-0.0157	9.85	[259 282 ...]	[5.93 5.25 ...]
4	5	3	0.691	-0.0225	12.5	[259 282 ...]	[6.94 5.96 ...]
4	6	1	0.457	-0.00213	5.20	[401 514 ...]	[4.27 4.01 ...]
4	6	2	0.662	-0.00591	8.46	[401 514 ...]	[5.93 5.25 ...]
4	6	3	0.696	-0.00854	10.5	[401 514 ...]	[6.94 5.96 ...]
5	6	1	0.254	-0.00196	4.61	[142 232 ...]	[4.27 4.01 ...]
5	6	2	0.390	-0.00561	6.86	[142 232 ...]	[5.93 5.25 ...]
5	6	3	0.413	-0.00814	8.28	[142 232 ...]	[6.94 5.96 ...]

Table 3.3: Example output of a D_c DataFrame from CO_2 uptake and PSD data in table 3.2. Highlighted rows indicate the regression that yields the optimum pore size range (Ω) for each of the pressures (1, 2, and 3 bar). Columns x and y indicate the surface area and loadings used for the regression, respectively. Values are truncated to save space.

in the correlation DataFrame, D_c alongside the values for w_{min}, w_{max} and P - an example of this can be seen in table 3.3. D_c can be reduced in size using the method `correlation_requirements()` which allows rows in the DataFrame to be eliminated according to various arguments. The best pair of w_{min} and w_{max}, according to the highest r^2 value for each pressure can be selected using the method `make_correlation_df()`, i.e. yielding the optimum pore size region for uptake of the sorptive, Ω.

References

1. M. Sevilla and R. Mokaya, *Energy & Environmental Science*, 2014, **7**, 1250–1280.
2. H. Wang, Q. Gao and J. Hu, *Journal of the American Chemical Society*, 2009, **131**, 7016–7022.
3. J. Wang and S. Kaskel, *Journal of Materials Chemistry*, 2012, **22**, 23710.
4. T. Otowa, R. Tanibata and M. Itoh, *Gas Separation & Purification*,

1993, **7**, 241–245.

5. D. Lozano-Castello, J. Calo, D. Cazorla-Amoros and A. Linares-Solano, *Carbon*, 2007, **45**, 2529–2536.
6. R. Lin, A. Li, L. Lu and Y. Cao, *Carbohydrate Polymers*, 2015, **118**, 126–132.
7. M. Yu, J. Li and L. Wang, *Chemical Engineering Journal*, 2017, **310**, 300–306.
8. M. Yu, Y. Han, J. Li and L. Wang, *Chemical Engineering Journal*, 2017, **324**, 287–295.
9. M. Sevilla, J. A. Maciá-Agulló and A. B. Fuertes, *Biomass and Bioenergy*, 2011, **35**, 3152–3159.
10. M. Sevilla and A. B. Fuertes, *Chemistry–A European Journal*, 2009, **15**, 4195–4203.
11. M. Sevilla and A. B. Fuertes, *Carbon*, 2009, **47**, 2281–2289.
12. A. Coats and J. Redfern, *Analyst*, 1963, **88**, 906–924.
13. IUPAC, *Compendium of Chemical Terminology*, Blackwell Scientific Publications, 2nd edn, 1997.
14. O. W. Richardson and K. T. Compton, *The London, Edinburgh, and Dublin Philosophical Magazine and Journal of Science*, 1912, **24**, 575–594.
15. J. F. Moulder, W. F. Stickle, P. E. Sobol and K. D. Bomben, *Handbook of X-ray Photoelectron Spectroscopy*, Physical Electronics, Inc., 1995.
16. N. Fairley, V. Fernandez, M. Richard-Plouet, C. Guillot-Deudon, J. Walton, E. Smith, D. Flahaut, M. Greiner, M. Biesinger, S. Tougaard, D. Morgan and J. Baltrusaitis, *Applied Surface Science Advances*, 2021, **5**, 100112.
17. T. A. Hinners, C. L. Jones, J. Biesiada, D. M. Schoengold, T. H. Starks and J. E. Campana, *Interlaboratory Evaluation of ICP-AES Method 6010*, ASTM International, 1988.

18. J. I. Goldstein, D. E. Newbury, J. R. Michael, N. W. M. Ritchie, J. H. J. Scott and D. C. Joy, *Scanning Electron Microscopy and X-ray Microanalysis*, Springer, 2017.

19. M. Knoll and E. Ruska, *Zeitschrift für Physik*, 1932, **78**, 318–339.

20. J. Rouquerol, P. Llewellyn and F. Rouquerol, *Studies in Surface Science and Catalysis*, 2007, **160**, 49–56.

21. J. Jagiello and J. P. Olivier, *Carbon*, 2013, **55**, 70–80.

22. P. C. Hansen, *SIAM review*, 1992, **34**, 561–580.

23. P. Hansen, in *The L-curve and its use in the numerical treatment of inverse problems*, ed. P. Johnston, WIT Press, Southampton, 2001, pp. 119–142.

24. J. Jagiello, C. Ania, J. B. Parra and C. Cook, *Carbon*, 2015, **91**, 330–337.

25. P. Virtanen, R. Gommers, T. E. Oliphant, M. Haberland, T. Reddy, D. Cournapeau, E. Burovski, P. Peterson, W. Weckesser, J. Bright, S. J. van der Walt, M. Brett, J. Wilson, K. J. Millman, N. Mayorov, A. R. J. Nelson, E. Jones, R. Kern, E. Larson, C. J. Carey, İ. Polat, Y. Feng, E. W. Moore, J. VanderPlas, D. Laxalde, J. Perktold, R. Cimrman, I. Henriksen, E. A. Quintero, C. R. Harris, A. M. Archibald, A. H. Ribeiro, F. Pedregosa, P. van Mulbregt and SciPy 1.0 Contributors, *Nature Methods*, 2020, **17**, 261–272.

26. C. R. Harris, K. J. Millman, S. J. van der Walt, R. Gommers, P. Virtanen, D. Cournapeau, E. Wieser, J. Taylor, S. Berg, N. J. Smith, R. Kern, M. Picus, S. Hoyer, M. H. van Kerkwijk, M. Brett, A. Haldane, J. Fernández del Río, M. Wiebe, P. Peterson, P. Gérard-Marchant, K. Sheppard, T. Reddy, W. Weckesser, H. Abbasi, C. Gohlke and T. E. Oliphant, *Nature*, 2020, **585**, 357–362.

27. W. McKinney *et al.*, Proceedings of the 9th Python in Science Conference, 2010, pp. 51–56.

28. P. Iacomi and P. L. Llewellyn, *Adsorption*, 2019, **25**, 1533–1542.

29. G. Van Rossum and F. L. Drake Jr, *Python reference manual*, Centrum voor Wiskunde en Informatica Amsterdam, 1995.

30. P. GNU, *Free Software Foundation. Bash (3.2. 48)[Unix shell program]*, 2007.

31. W. S. Davis, *The Information System Consultant's Handbook*, CRC Press, 2019, pp. 465–472.

Chapter 4

Turbostratic carbons I: from cigarette butts

What follows is the results of the synthesis of turbostratic carbons of Used Cigarette Butts (UCBs). The synthesis is described in section 3.1, and the rationale for the choice of UCBs as a carbon precursor, is described in subsection 1.1.1. Details of analytical techniques used herein can be found in sections 3.2-3.3.

Abstract

Sequential hydrothermal carbonisation and KOH-mediated activation of Used Cigarette Filters (UCFs) has previously been shown by the author to provide a solution to the problem of Cigarette Butt (CB) waste, in the form of an extremely promising H_2 storage medium (see **Publication VI**). The following study serves to expand the previous work *via* carbonisation of hydrochar derived from whole Used Cigarette Butts (UCBs) i.e. including the wrapping paper. KOH activation of UCB-hydrochar yields carbons with much lower porosity than in **Publication VI**, achieving micro-mesoporous carbons with A_{BET} of up to $1875\,m^2\,g^{-1}$ and pore volume of $0.89\,cm^3\,g^{-1}$ at an activation temperature of 700 °C. Thus, these materials are best applied to room temperature CO_2 capture, with reasonable uptakes of 2.7 and $14.1\,mmol\,g^{-1}$ achieved at 1 and 20 bar, respectively.

UCBs are an unusual carbon precursor in that they contain a relatively high quantity, and diverse range of metals. As a result the composition and elemental distribution in UCBs, as well as in derived hydrochars and turbostratic carbons is investigated, as well as the efficacy of post-synthetic washing steps. UCBs and derived, unwashed hydrochar were found to contain Al, Fe, K, Mg, Na, Ti, and Ca in concentrations above $0.10\,mg\,g^{-1}$. Many of these elements were also identified in derived turbostratic carbons. While it was hypothesised in **Publication VI** that such contaminants may have an activating effect, there is no evidence of this in this work. Indeed, the stubbornness of these elements to removal *via* HCl washing results in porosity that is lower than expected indicating that these contaminants are limiting pore accessibility.

4.1 Properties of carbons

Yields of hydrochars and derived turbostratic carbons can be found in table 4.1 (refer to table 3.1 for syntheses of the three sets of carbons). The fact that the yield of hC-hydrochar is significantly less than that of hD-hydrochar indicates that washing the hydrochar does remove some labile matter. Although hE-hydrochar was also not washed, it has a similar yield to hC-hydrochar perhaps indicating that there was a lower amount of non-carbonisable material in set E of cigarette butts. These differences in yield are also transferred to the overall yield (bracketed numbers) of derived turbostratic carbons, but not to the yield of the activation step considered on its own - indicating that whatever is removed by washing of the hydrochar does not have a significant affect on the product of the pyrolysis step. It is noteworthy that the yields of washed and unwashed carbons ($0TTT$ and $0TTT'$, respectively) are very similar, indicating that the ex-

Table 4.1: Average yields (wt.%) of carbons derived from the three sets of used cigarette butt samples. The yield is taken as that of the single step in the synthesis; numbers in brackets are overall yield. Where cell is blank, this sample does not exist.

xTTT	**Prefix**					
	hC		**hD**		**hE**	
hydrochar	35		50		39	
0600′	38	(13)	39	(19)		
0700′	35	(12)	33	(17)		
0800′	33	(12)	37	(19)		
0600	34	(12)	36	(18)	6	(14)
0700	30	(11)	31	(16)	30	(11)
0800	31	(11)	33	(17)	24	(9)
4600	8	(3)	13	(7)		
4700	10	(4)	11	(6)		
4800	9	(3)	10	(5)		

tensive post-pyrolysis washing step does not remove significant amounts of material. Yields of KOH-activated samples are of course significantly lower than samples pyrolysed in the absence of external activating agent, due to removal of C *via* the dissolution of K_2CO_3 from the carbon framework during washing.

4.1.1 Composition & Morphology

A primary goal of synthesising the carbons from cigarette butts was quantification and identification of so-called contaminant-porogens in UCBs, and monitoring their presence upon conversion of CBs to hydrochar then to turbostratic carbon. Initial identification and rough quantification of the contaminants was performed using P-XRD and TGA respectively, with reference to CHN elemental microanalysis. Attempts were made to identify and more precisely quantify components using XPS and ICP-OES. Finally, imaging of the dispersion of contaminant-metals within unwashed turbostratic carbons was performed using BSE-SEM and EDX-TEM.

Relative proportions (by weight) of C, H, and N for all UCB-derived samples, as well as their ash content can be found in table 4.2. The composition of hydrochars and carbons activated without KOH is essentially the same for samples in sets hC and hD. Furthermore the discrepancy in the ash content of hC-hydrochar and hD-hydrochar is within margin for error. As such, it can be confirmed that the post-hydrothermal carbonisation washing step only serves to remove combustible matter, i.e. non-metals. The slightly larger discrepancies in ash content between samples hC-0TTT and hD-0TTT (or hC-0TTT' and hD-0TTT') must therefore be ascribed to heterogeneous distribution of contaminants in the precursor, as opposed to removal of non-combustible contaminants prior to pyrolysis. Furthermore,

Table 4.2: C, H, and N content of hydrochars and carbons derived from cigarette butts, determined using elemental microanalysis as well as ash content according to residual mass following TGA in air.

	Concentration / wt.%				
Sample	**C**	**H**	**N**	**other**	**Ash**
hC-hydrochar	56	5	0	44	8
hD-hydrochar	53	5	0	42	7
hE-hydrochar	61	4	2	32	
hC-0600′	69	2	0	29	16
hD-0600′	67	2	0	30	20
hC-0700′	71	1	1	27	19
hD-0700′	72	0	0	27	13
hC-0800′	77	0	0	22	18
hD-0800′	77	0	0	21	12
hC-0600	68	2	0	30	20
hD-0600	67	2	1	30	17
hE-0600	77	2	2	19	2
hC-0700	71	1	1	27	14
hD-0700	72	0	0	24	16
hE-0700	81	2	2	16	
hC-0800	75	1	1	22	13
hD-0800	77	0	0	22	20
hE-0800	83	1	3	14	2
hC-4600	73	0	0	25	6
hD-4600	58	0	0	41	31
hC-4700	78	0	0	22	5
hD-4700	53	0	0	46	5
hC-4800	90	0	0	10	6
hD-4800	50	0	0	50	37

washing of the turbostratic carbons does not seem to serve any consistent, significant role in removing these contaminants. On the other hand, KOH-activated samples (i.e. hC-4TTT and hD-4TTT) show more significant compositional differences, particularly in terms of C content. This

further confirms that the reduction in yield of hD-hydrochar relative to hC-hydrochar (see table 4.1) is a result of removal of water-soluble organic material not incorporated into the hydrochar macrostructure; it appears that the KOH destroys such material in hD-4TTT, thus reducing C content. The higher C and lower ash content of hE-hydrochar and hE-0TTT samples is an indication that the majority of the non-combustible contaminants seen in the ash of hC and hD samples come from the UCB wrapping paper as opposed to the UCB itself. In fact, the ash content is zero (within margins for error) for the hE samples, and as a result the composition of these samples is much easier to discern; the 'other' column simply represents the O content. Unsurprisingly C content increases, and O content decreases with increasing activation temperature as consistently reported elsewhere.[1,2]

The presence of sharp peaks in the P-XRD patterns confirms the presence of crystalline material in most of the hydrochar and turbostratic carbon samples (see appendix, figures B.1-B.4). Due to the complexity of the patterns it is difficult to assign peaks to any particular phase. Therefore, XPS was used and identified Ti, Na, K, and Ca in dry-ashed UCBs (see appendix, figure B.5). although absolute concentrations are not determinable by this technique as (i) there are likely adventitious C and O atoms on the surface of the ash, and (ii) it is unlikely that all atomic species are accounted for. ICP-OES allowed more precise determinations of metals in UCBs, their wrapping paper, and a derived hydrochar - results are shown in table 4.3. These results confirm the presence of metals identified in XPS, as well as identifying Al, Fe, and Mg in all samples. Zn was only found in quantifiable amounts for the UCB wrapping paper. These metals have previously been identified in UCBs by Iskander and others.[3–6] All trace elements were found to have a higher occurence in the paper as opposed

Table 4.3: Gravimetric concentrations of metals in UCB (including paper), wrapping paper and its derived, unwashed hydrochar according to ICP-OES. Samples derived from same batch of UCB as used to make hC and hD samples - see table 3.1

Analyte (λ / nm)		**Concentration / mg g^{-1}**		
		UCB	**UCB paper**	**hydrochar**
Al	(396.153)	1.58	46.0	4.81
Fe	(283.204)	2.81	38.6	3.66
K	(766.490)	2.91	17.9	4.60
Mg	(285.210)	0.71	11.0	1.13
Na	(589.590)	0.27	6.25	0.73
Ti	(334.940)	1.07	8.75	0.87
Ca	(317.933)	13.1	283	17.2
Zn	(213.857)	-	0.50	-

to the whole UCB. This may explain the much higher ash content of hydrochars and turbostratic carbon derived from whole UCBs as compared to unwrapped UCFs, i.e. hC/hD samples versus those derived from hE and those reported in **Publication VI** respectively.

4.1.1.1 Electron Microscopy

Electron microscopy was used to determine the distribution of heavy elements within hydrochars and turbostratic carbons. Initially, comparison of BSE to SE was used to gain a rough measure of elemental distribution, and an example thereof is shown in figure 4.1. In the case of hydrochar samples (figure 4.1(a, b)), there appears to be a random, continuous distribution of heavy elements throughout the sample. On the other hand, unwashed turbostratic carbons derived without the use of KOH as porogen (exemplified in figure 4.1(c, d) by hD-0600′) show more distinct clusters of heavy elements, though the distribution is no less random. The lack of uniformity of heavy element distribution is unsurprising as these elements are unlikely to be distributed regularly in the UCB precursor, and the hydrothermal

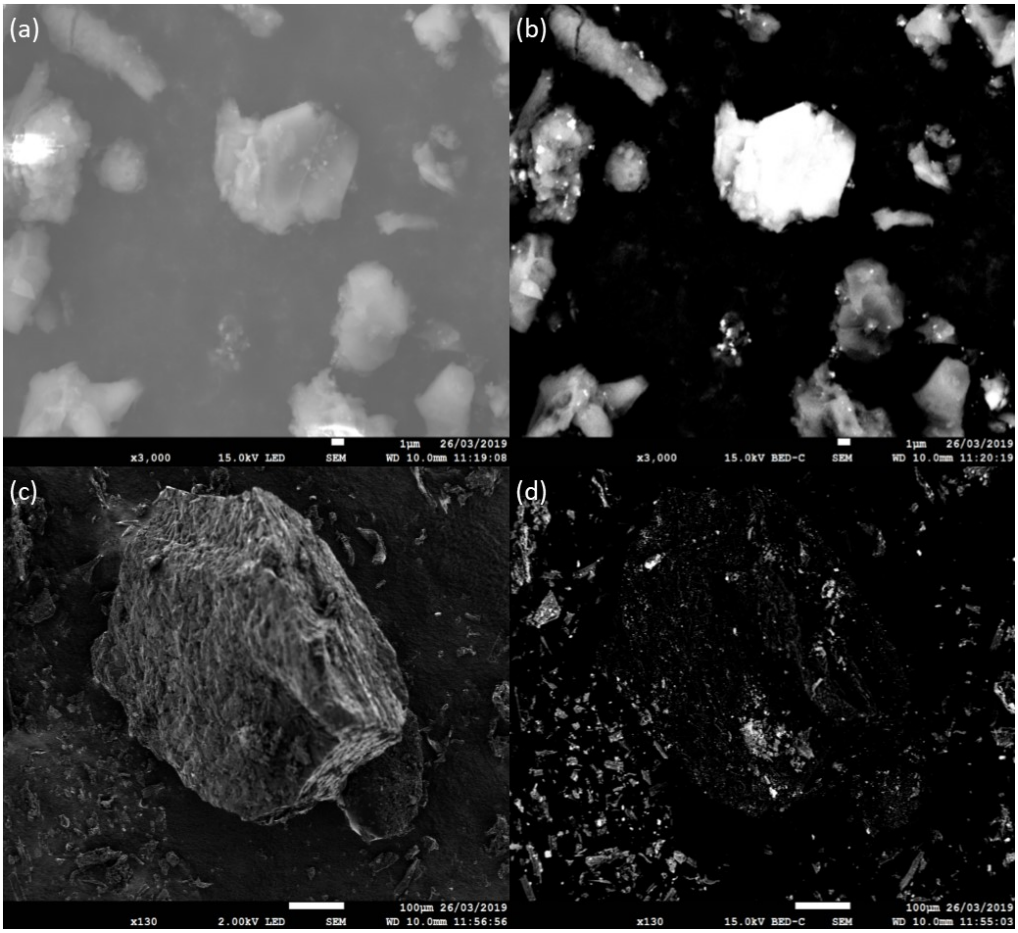

Figure 4.1: SE (a, c) and BSE (b, d) images of samples hD-hydrochar (a, b) and hD-0600′ (c, d).

and pyrolytic processes are unlikely to produce any more compositional homogeneity.

For more detailed analysis of the distribution of elements in turbostratic carbons, EDX-TEM was used. Representative images derived using this technique are shown in figure 4.2, and quantification at three different sites in table 4.4. Most of the elements quantified by ICP-OES; Al, Ca, Cu, K, and Ti are also identifiable by EDX-TEM, the Fe and Na are notably absent. In addition, Au and Cr are also present, though not in quantifiable amounts. The images in figure 4.2 show that heavy elements in the turbostratic carbons form clusters over the surface of the carbon structure. Ti and Al are the only metals whose concentrations were quantifiable at any

site examined, with site 2 having Ti as the majority component. Al could only be quantified at site 3, wherein Ti was notably absent in measurable quantities. Thus, it appears that at Ti and Al form discrete clusters within

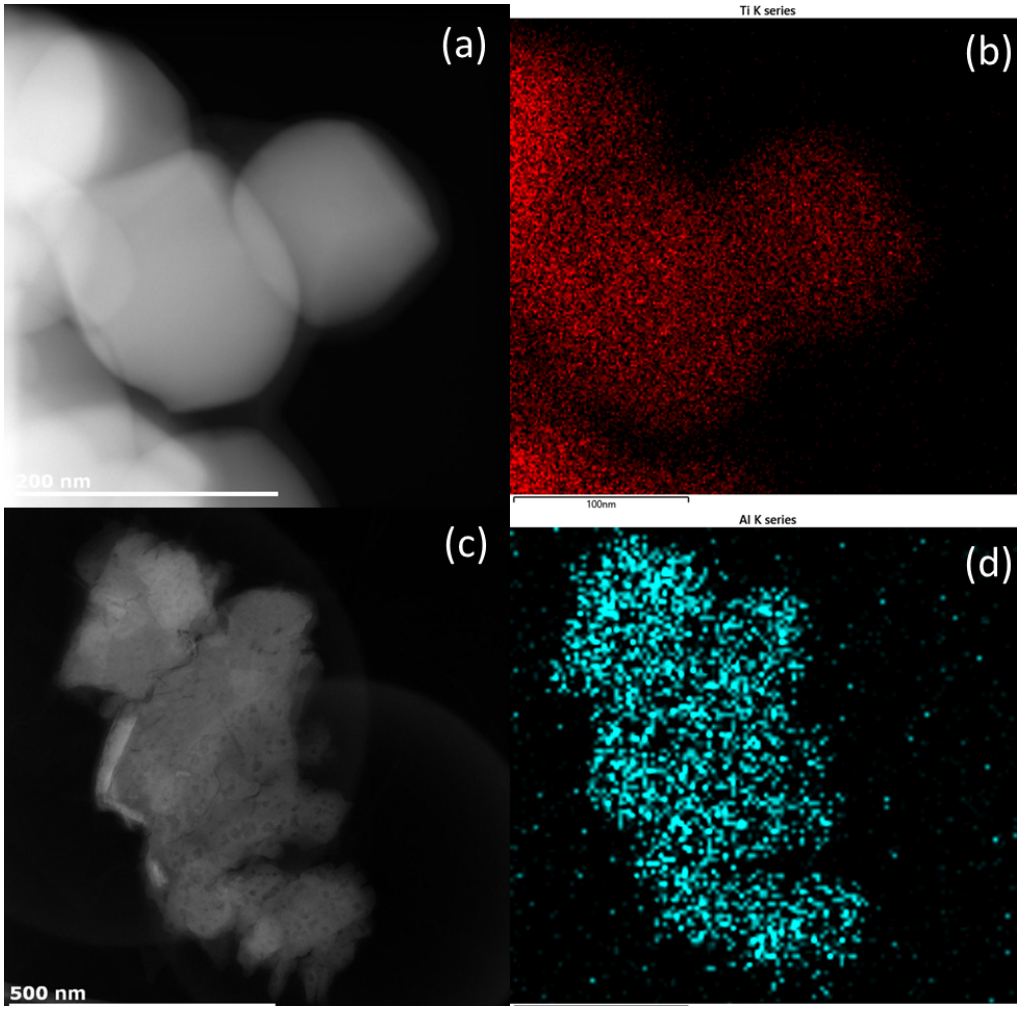

Figure 4.2: TEM (a, c) and EDX-TEM (b, d) images of hD-0700′ at sites 1 (a, b) and 3 (c, d). (b) and (d) show distribution of Ti and Al particles respectively.

Table 4.4: Concentrations of C, O, Al and Ti at three different sites in hD-4700 according to EDX-TEM

Analyte	**Concentration / wt.% (Atomic %)**					
	Site 1		**Site 2**		**Site 3**	
C	80	(90)	33	(36)	73	(82)
O	8	(7)	4	(5)	14	(12)
Al	-	(-)	-	(-)	3	(2)
Ti	10	(3)	60	(29)	-	(-)

this turbostratic carbon. On the other hand, the other metals identified by ICP-OES (see table 4.3) must be distributed more evenly meaning that they can not be as readily quantified in the small (roughly 100 µm^2) sites examined.

4.1.2 Porosity

As a result of the discovery of high quantities of non-combustible matter in turbostratic carbons which both were and were not washed, the effect of the washing step on porosity was examined. The results, i.e. porosity of samples hD-0TTT and hD-0TTT' are shown in table 4.5 alongside that for sets hC-4TTT and hD-4TTT. Isotherms and resultant PSDs for

Table 4.5: Porosity of UCB-derived carbons from N_2 isotherms. A_{BET} determined using the Rouquerol method where applicable. Total pore volume, V_t determined using the single point method. Numbers in brackets indicate micropore surface area and pore volume. Peak pore width, w_{peak} (for samples hC-4TTT and hD-4TTT) taken as peak of the PSDs in figure 4.3.

Sample	$\mathbf{A_{BET}}$ / $\mathbf{m^2\,g^{-1}}$		$\mathbf{V_t}$ / $\mathbf{cm^3\,g^{-1}}$		$\mathbf{w_{peak}}$ / **Å**
hD-0600′	10	(-)	-	(-)	
hD-0700′	170	(150, 89%)	0.07	(0.06, 86%)	
hD-0800′	226	(198, 88%)	0.09	(0.08, 89%)	
hD-0600	120	(104, 87%)	0.05	(0.04, 80%)	
hD-0700	122	(101, 83%)	0.05	(0.04, 80%)	
hD-0800	146	(125, 86%)	0.06	(0.05, 83%)	
hC-4600	1428	(1054, 73%)	0.63	(0.43, 68%)	7
hD-4600	1487	(1036, 69%)	0.64	(0.41, 64%)	7
hC-4700	1875	(917, 49%)	0.89	(0.37, 42%)	8
hD-4700	1807	(611, 33%)	0.88	(0.25, 28%)	9
hC-4800	1958	(626, 32%)	1.00	(0.26, 26%)	8
hD-4800	979	(206, 21%)	0.52	(0.09, 17%)	8

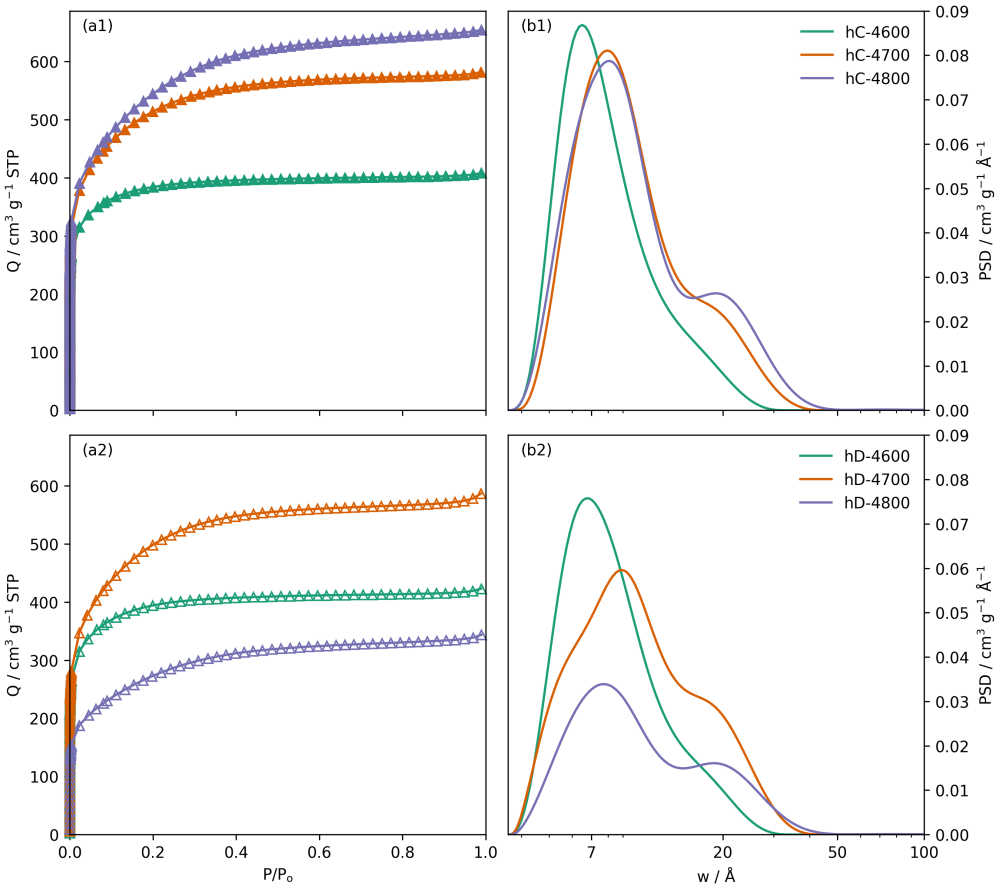

Figure 4.3: Isotherms and resultant PSDs for samples hC-4TTT and hD-4TTT.

samples hC-4TTT and hD-4TTT are displayed in figure 4.3.*. It is unclear whether washing in HCl had any effect at all on porosity - indeed, for activation at 700 and 800 °C there are significant reductions in A_{BET} after washing. Perhaps this is simply a marker of physical agglomeration of particles during the washing process, and has little to do with internal porosity. Additionally, the porosity of these samples is not higher than would be expected for pyrolysed biomass; self-activation of a pure cellulose acetate-derived hydrochar yielded a carbon with A_{BET} >500 $m^2\,g^{-1}$,† indeed UCB-derived self-activated carbons have previously been shown to

*Isotherms and PSDs for hD-0TTT and hD-0TTT' can be found in the appendix, figure C.3, as well as full plots of isotherms and fits for all samples for which porosity is reported herein in figures C.1 and C.2. Due to poor equilibration, the PSDs cannot be considered to be accurate. This issue is discussed in more depth in chapter 6 and **Publication I**.

†Full porosimetric details of this sample are in appendix, figure C.4 and table C.1.

exhibit far higher surface areas.[7–11] As such there is no proof that the non-combustible contaminants can act as porogens. Of course this is not definitive as removal of contaminants proved impossible in these samples. The porosity that hD-0TTT carbons *do* possess is principally (over 80 %, by surface area) in the micropore region, though again this is to be expected for biochars/self-activated carbons.[12–14]

Carbons activated using KOH have moderate surface areas, and a much lower relative microporosity than samples hD-0TTT, ranging from 71 % to as low as 21 % when activated at 600 and 800 °C respectively. That is, these carbons are much more mesoporous, and mesoporosity increases with activation temperature. Indeed, the mesoporosity is reflected in the broad curvature of the N_2 isotherms used to determine these textural characteristics as show in figure 4.3(a1, a2). This is in contrast to the carbons reported in **Publication VI**, where the author reported A_{BET} of more than double that shown in this work, and all carbons were mostly microporous. This is likely a result of the relatively high (estimated) oxygen content, and thus low activation resistance (see **Publication III**, **section 4.1.2.**) of the hydrochars formed in this work (see table 4.2) as opposed to any limitations on porosity development resulting from the non-combustible contaminants. The lowest possible estimates of O-content for hC-hydrochar and hD-hydrochar are 37 and 35 wt.% respectively,[‡] compared to 25 wt.% for UCB-derived hydrochar in **Publication VI**.

Washing of the hydrochar does not appear to have a consistent effect on porosity of derived KOH-activated carbons. That is, A_{BET} and pore volume are the essentially the same for both sets of carbons activated with

[‡]Minimum O-content taken as the difference between 'other' and ash content of the hydrochars (table 4.2). The true value is likely much higher as the ash contains the oxides of non-combustible contaminants, thus weight reported is greater than in the carbon itself.

KOH at 600 and 700 °C, while porosity of hD-4800 is approximately half that of hC-4800. On the other hand, activation at 700 and 800 °C of unwashed hydrochar results in much lower absolute microporosity relative to washed hydrochar. This may be a result of combustion of volatile compounds dried into the unwashed hydrochar, which produces oxidising gases such as CO and CO_2 leading to uncontrolled degradation of the carbon framework, and thus pore broadening.[1,2] This pore width broadening with increasing activation temperature is also evidenced by the PSDs of the carbons (see figure 4.3(b1, b2)), with significantly more of the porosity above 20 Å for samples activated at 700 and 800 °C relative to 600 °C. The pores also become centered around higher values of w (see table 4.5) with increasing activation temperature, though this trend is somewhat obscured for samples hD-4TTT - but this may simply be an effect of reduction in overall porosity resulting from combustion of volatiles in the activation process. Pore size hierarchy does not appear to be significantly affected by the presence (or lack of) a hydrochar washing step.

4.2 CO_2 uptake

While the ultra-high surface areas of carbons reported in **Publication VI** made them excellent candidates for H_2 storage, this is not the case for UCB-derived KOH-activated carbons prepared in this work. The lower surface area and more hierarchical pore structure of these carbons (table 4.5) make them much better candidates for CO_2 capture. As such, room temperature molar CO_2 uptake was measured up to 40 bar, and results thereof are tabulated in table 4.6 and shown in full in figure 4.4.

At 20 bar, the highest surface area samples - hD-4700, hC-4700 and hC-

Table 4.6: CO_2 uptakes (measured at 25 °C) at 1 and 20 bar for samples hC-4*TTT* and hD-4*TTT*.

Sample	**CO_2 uptake / mmol g^{-1}**	
	1 bar	**20 bar**
hC-4600	2.6	9.8
hD-4600	1.5	6.1
hC-4700	2.3	12.1
hD-4700	2.3	14.1
hC-4800	2.7	12.6
hD-4800	1.5	9.7

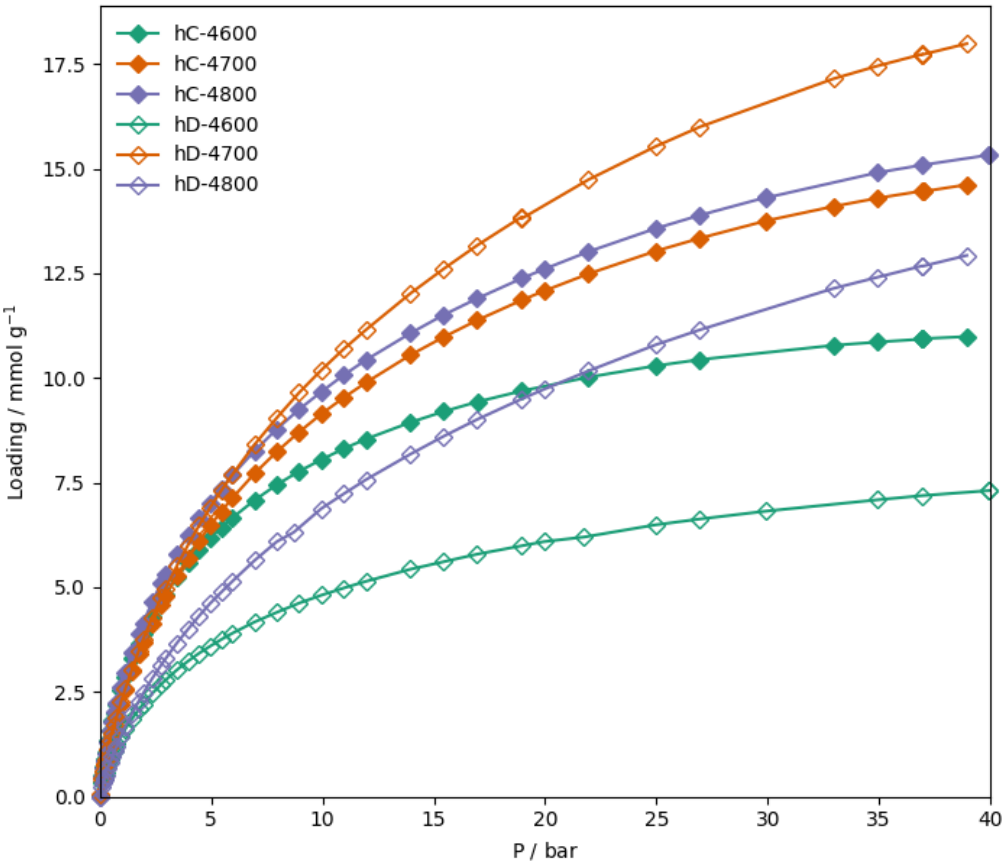

Figure 4.4: CO_2 uptake isotherms measured at 25 °C for samples hC-4*TTT* and hD-4*TTT*.

4800 - perform the best as a result of maximisation of available adsorption sites for attractive London forces between CO_2 and the material surface. The more mesoporous hD-4700 (see table 4.5) has a 17 % greater CO_2 uptake than the more microporous hC-4700 at 20 bar. This is likely be-

cause mesopores fill at higher pressure than micropores. Conversely, if we compare hC-4600 and hD-4600 the origin of the discrepancy in their CO_2 uptake is unclear at both 1 and 20 bar, as their porosity is essentially identical. The only major distinction is compositional; hD-4600 has a far higher ash content (see table 4.2). Perhaps some contaminant prevents ingress of CO_2 into hD-4600's pores. Optimum low pressure CO_2 uptake is achieved by two samples with quite different porosity; hC-4600 and hC-4800. The high degree of microporosity ($A_{BET} = 1023\,m^2\,g^{-1}$, $V_t = 0.64\,cm^3\,g^{-1}$) in hC-4600 counteracts the greater overall porosity of hC-4800, whose pore volume is 56 % greater than hC-4600.

The CO_2 uptakes of the two samples synthesised at 600 °C approach a plateau at pressures in excess of 10 bar. This behaviour is likely a result of the fairly narrow PSDs of these carbons. On the other hand, the slope of isotherms for the other four samples does not decrease to the same extent as they have a greater degree of hierarchy in their PSDs. Thus the samples synthesised at 700 and 800 °C are more suitable for applications such as PSA.[2] The activation temperature-porosity-gas uptake capacity relationship is similar to that for carbons synthesised in **Publication V** and **Publication VI**, in that optimum porosity for CO_2 uptake is achieved at a lower than expected activation temperature of 700 °C. In general in a series of turbostratic carbons derived through the activation of biomass, the optimum gas uptake is achieved for samples activated at ∼800 °C.[15]

4.3 Conclusion

The KOH-mediated pyrolysis of whole UCBs does not yield carbons with ultrahigh porosity as shown in **Publication VI**. This appears to be due

to compositional differences, i.e. that the wrapping paper is not as readily activated as the CA present in the filters themselves. As a result, KOH-activated materials do not show promise as H_2 storage media, but instead their medium A_{BET} (approaching $2000\,m^2\,g^{-1}$) and hierarchical PSDs make them useful for ambient temperature CO_2 capture; CO_2 uptakes of 2.7 and $14.1\,mmol\,g^{-1}$ were achieved at 1 and 20 bar respectively.

Of further interest is the function of the two washing steps, i.e. after hydrothermal carbonisation and after pyrolysis. It appears that removal of non-combustible contaminants is inconsistent, although washing the hydrochar *does* remove volatile organic matter, which may slightly increase the concentration of C in derived turbostratic carbons. On the other hand, washing of the carbons pyrolysed in the absence of KOH has inconsistent effects on porosity, and indeed on the concentration of non-combustible matter in the samples with ash contents of up to 20 wt.% even in washed carbons. In addition the porosity of these samples is lower than is found for carbon derived from the sequential hydrothermal carbonisation and pyrolysis of pure CA, suggesting some interference of the stubborn metal contaminants with pore accessibility.

The difficulty in the removal of non-combustible contaminants led the author to investigate their nature. It was found through a combination of ICP-OES, XPS, and electron microscopy that Al, Fe, K, Mg, Na, Ti, and Ca are present in whole UCBs and unwashed hydrochar. In addition, nanoclusters of Au and Cr were also identified in an unwashed turbostratic carbon.

References

1. L. S. Blankenship and R. Mokaya, *Materials Advances*, 2022, **3**, 1905–1930.
2. M. Sevilla and R. Mokaya, *Energy & Environmental Science*, 2014, **7**, 1250–1280.
3. Q. Chevalier, H. El Hadri, P. Petitjean, M. Bouhnik-Le Coz, S. Reynaud, B. Grassl and J. Gigault, *Chemosphere*, 2018, **194**, 125–130.
4. L. S. Cardoso, F. N. Estrela, T. Q. Chagas, W. A. M. da Silva, D. R. de Oliveira Costa, I. Pereira, B. G. Vaz, A. S. de Lima Rodrigues and G. Malafaia, *Environmental Science and Pollution Research*, 2018, **25**, 8592–8607.
5. F. Y. Iskander, *Journal of Radioanalytical and Nuclear Chemistry*, 1992, **159**, 105–110.
6. R. Jenkins, C. Goldey and T. Williamson, *Beiträge zur Tabakforschung International/Contributions to Tobacco Research*, 1985, **13**, 59–65.
7. S. M. Soltani, S. K. Yazdi and S. Hosseini, *Applied Nanoscience*, 2013, **4**, 551–569.
8. S. K. Yazdi, S. M. Soltani and S. Hosseini, *Advanced Materials Research*, 2012, **587**, 88–92.
9. M. Lee, G. P. Kim, H. Don Song, S. Park and J. Yi, *Nanotechnology*, 2014, **25**, 345601.
10. C. Yu, H. Hou, X. Liu, L. Han, Y. Yao, Z. Dai and D. Li, *Frontiers in Materials*, 2018, **5**, 63.
11. C. B. Koochaki, R. Khajavi, A. Rashidi, N. Mansouri and M. E. Yazdanshenas, *Biomass Conversion and Biorefinery*, 2019.
12. K. Weber and P. Quicker, *Fuel*, 2018, **217**, 240–261.
13. J. Jagiello, J. Kenvin, A. Celzard and V. Fierro, *Carbon*, 2019, **144**,

206–215.

14. W. Suliman, J. B. Harsh, N. I. Abu-Lail, A.-M. Fortuna, I. Dallmeyer and M. Garcia-Pérez, *Science of the Total Environment*, 2017, **574**, 139–147.

15. A. Ariharan and V. Balasubramanian, *Indian Journal of Chemical Technology*, 2018, **25**, 140–149.

Chapter 5

Turbostratic carbons II: Impregnation methods

What follows is the results of the synthesis of turbostratic carbons *via* impregnation techniques. The synthesis is described in section 3.1, and the rationale for the impregnation techniques is described in subsection 1.1.2. Details of analytical techniques used herein can be found in sections 3.2-3.3.

Abstract

In recent years, various researchers have investigated alternative methods of introduction of oxidative chemical porogen to precursor in the synthesis of activated carbons. These differ from the standard physical mixing method in that they attempt to increase the homogeneity of the precursor-porogen mixture while simultaneously decreasing distances between porogen and precursor atoms. These techniques include solution impregnation and the carbonisation of organic salts. Such techniques are collectively termed as impregnation techniques for the purposes of this chapter, and have been shown to yield more precise control over pore size, geometry, and pore network connectivity as well as showing promise in facilitation development of improved microporosity.

What is lacking in these studies is insight into the effect of the relative quantity of impregnated porogen as well as activation temperature on the pore structure and elemental composition of the derived porous carbons. Thus, this chapter reports the investigation of these variables by two means, (i) hydrothermal impregnation of KOH into sawdust (SD) followed by pyrolysis, and (ii) carbonisation of sodium carboxymethyl cellulose (NC) at varying degrees of substitution. It was found that in the case of the SD-derived materials, C content is drastically improved by this technique relative to more 'traditional' methods. In addition at a KOH:SD ratio of 2.00, a carbon with unusually low bulk density ($\sim$0.031 g cm^{-3}), and high mesoporosity (73 % by surface area) is produced. As for NC-derived carbons, in many cases a two-phase highly oxygen-rich product was produced. These properties appear to be a function of both the amount of Na in the precursor, as well as activation temperature. Network connectivity and/or pore geometry in the carbons also appears to be a result of these two vari-

ables. This work provides scope for investigation of the pore formation mechanisms of these highly unusual carbons.

5.1 Hydrothermal Sawdust KOH-impregnation

Eleven SH*x.xx-HHH* samples were produced from the sawdust precursor. In the case of *x.xx* >0.00, removal of K salts *via* washing resulted in the sole product being small amounts of flakey carbonaceous matter that was difficult to isolate as an intermediate. As a result, compositional and porosimetric analysis was difficult to achieve. Furthermore, extensive washing appears to remove extremely fine particles which may have some function in the subsequent pyrolysis step. The three hydrochars, SH0.00-*HHH* were much easier to isolate and analyse. The eleven turbostratic carbons (SA*x.xx-HHH*) were the typical black powders, however SA2.00-250 was very diffuse and clearly has a much lower density relative to the other samples and indeed to that of typical activated/turbostratic carbons.

5.1.1 Composition

CHN elemental microanalysis was used to determine the composition of sawdust precursor and derived carbons; results are show in table 5.1. TGA shows that all samples are fully carbonaceous, i.e. there are no residual K compounds present after washing - see appendix, figure B.6. Thus, in the CHN analysis, the remainder of the sum of C, H and N gravimetric concentrations is assumed to be made up by O in table 5.1. In addition, for all carbons there is a single burn-off event at 600 °C, as reported previously both for carbons prepared directly from sawdust or from sawdust-derived hydrochar.[1] Therefore, the thermal stability of carbons derived from sawdust does not seem to be significantly affected by the quantity (or even presence) of KOH as a porogen, the method of preparing the precursor, or the method of introducing KOH to the precursor.

Table 5.1: Composition of SA*x.xx-TTT* carbons according to elemental microanalysis. O content is the remaining wt.% after consideration of the C, H, and N.

Sample	**Concentration / wt.%**				**Atomic ratio**	
	C	**H**	**N**	**O**	**O/C**	**H/C**
SD	45	6	1	48	0.80	1.62
SA0.00-200	87	1.4	1.7	11	0.09	0.19
SA0.50-200	88	0.44	0.03	12	0.10	0.06
SA1.00-200	90	0.15	0.94	8.8	0.07	0.02
SA0.00-250	85	0.94	0.33	14	0.12	0.13
SA0.25-250	87	0.04	0.05	13	0.12	0.13
SA0.50-250	93	0.00	0.52	6.2	0.05	-
SA1.00-250	90	0.00	0.00	9.6	0.08	-
SA2.00-250	93	0.00	0.00	7.5	0.06	-
SA0.00-300	86	0.89	0.55	12	0.11	0.12
SA0.50-300	91	0.09	0.15	8.6	0.07	0.01
SA1.00-300	92	0.14	0.00	7.4	0.06	0.02

The elemental composition of the sawdust is similar to that previously reported by the Mokaya group.[1,2] Carbons derived from the slurries formed *via* hydrothermal carbonisation at 250 and 300 °C without the use of KOH have slightly lower C contents than their KOH-activated counterparts, and retained some H and N. On the other hand, KOH-activated samples with KOH:SD mass ratio >0.25 are at least 90 % carbon with the heteroatoms - excluding O - almost completely removed. On the other hand, SA0.00-200 has a very similar O/C atomic ratio to SA0.50-200. This indicates that at some hydrothermal carbonisation temperature between 200 and 250 °C, KOH facilitates the breakdown of O-rich moieties in the sawdust, resulting in their removal during the activation step. Further, the addition of KOH only significantly facilitates this degradation once KOH:C mass ratio is greater than 0.25. The O/C atomic ratios of the SA*x.xx*-250 ($x.xx > 0.00$) carbons are lower than those of previously reported carbons derived by the sequential hydrothermal carbonisation at 250 °C and activation with

KOH at 800 °C. In their report, Balahmar and Mokaya find that the the lowest O/C (0.12) was achieved at a KOH:hydrochar mass ratio of 4.[1] Thus, the inclusion of KOH in the hydrothermal carbonisation step provides for a route to a more carbon-rich material, without necessitating the use of higher quantities of KOH.

5.1.2 Porosity

It was initially attempted to produce porous carbons *via* hydrothermal carbonisation with a KOH solution, i.e. without pyrolysis. Unsurprisingly this proved ineffective as activation typically requires temperatures in excess of 400 °C.[3,4] A_{BET} of these samples (i.e. SH*x.xx-HHH*) was not in excess of $10\,m^2\,g^{-1}$. As for the pyrolised samples, porosity was reasonable, with A_{BET} of least $300\,m^2\,g^{-1}$ for samples synthesised without KOH, and above $990\,m^2\,g^{-1}$ for the KOH-activated samples. Full textural characteristics are shown in table 5.2, as well as the isotherms from which they are derived and PSDs in figure 5.1.*

In the case of SA0.00-*HHH* samples, overall surface area and pore volume ($456\,m^2\,g^{-1}$ and $0.18\,cm^3\,g^{-1}$) was maximised where the hydrothermal carbonisation temperature was 250 °C. Increasing hydrothermal carbonisation temperature generally reduces C content in the resultant hydrochar,[5–7] however temperatures above 250 °C have also been shown to result in the break down of the poylmerised product into volatile organic moieties.[8–10] As such, the apparent optimisation of porosity found by preparation with hydrothermal carbonisation at 250 °C is likely a result of both of these factors affecting the activation resistance[4,11] and thus ultimately the porosity of the resultant activated carbon.

*Individual PSDs and the kernel fits they are derived from can be found in the appendix, figures C.5-C.7.

Table 5.2: Porosity of SA*x.xx-TTT* carbons. A_{BET} derived using the Rouquerol method, the total pore volume, V_t is taken using the single point method. Values in brackets indicate the microporous portion of A_{BET} and V_t, calculated using t-plot. Peak pore width, w_{peak} is the maximum of the PSD determined using NLDFT, as shown in figure 5.1.

Sample	$\mathbf{A_{BET}}$ / $\mathbf{m^2\,g^{-1}}$		$\mathbf{V_t}$ / $\mathbf{cm^3\,g^{-1}}$		$\mathbf{w_{peak}}$ / **Å**
SA0.00-200	339	(311, 92%)	0.14	(0.12, 85%)	8
SA0.50-200	1174	(1092, 93%)	0.47	(0.42, 89%)	7
SA1.00-200	1524	(1398, 92%)	0.61	(0.54, 89%)	7
SA0.00-250	452	(418, 92%)	0.18	(0.16, 89%)	6
SA0.25-250	994	(922, 93%)	0.39	(0.35, 90%)	6
SA0.50-250	1319	(1242, 94%)	0.51	(0.47, 92%)	6
SA1.00-250	1341	(1238, 92%)	0.53	(0.48, 91%)	6
SA2.00-250	2396	(644, 27%)	0.84	(0.27, 32%)	8
SA0.00-300	323	(294, 91%)	0.13	(0.11, 85%)	9
SA0.50-300	1084	(989, 91%)	0.44	(0.38, 86%)	6
SA1.00-300	1295	(1140, 88%)	0.54	(0.44, 82%)	6

As for the KOH-activated samples, in general increasing KOH:SD ratio is associated with increases in overall porosity, with SA2.00-250 achieving the highest surface area and pore volume of 2396 $m^2\,g^{-1}$ and 0.84 $cm^3\,g^{-1}$ respectively. In general this improvement does not appear to significantly affect microporosity which remains in the range 88-94 and 81-92 % in terms of surface area and pore volume respectively. This is, until KOH:SD ratio is increased to 2.00, wherein development of mesoporosity reduces percent micropore surface area to 27 %. This is reflected in the N_2 isotherm for this sample (see figure 5.1(a2)) which displays a large adsorption knee, unlike the very pure type I isotherms[12] of the remaining samples.

The additional KOH:SD ratio of 0.25 and 2.00 were included at hydrothermal carbonisation temperature of 250 °C due to the relative similarity of isotherms and resultant porosities where KOH:SD ratio is 0.50 or 1.00. In all cases, percent microporosity remains approximately the same, and the pore size is identical at these two ratios (see table 5.2). There are of course

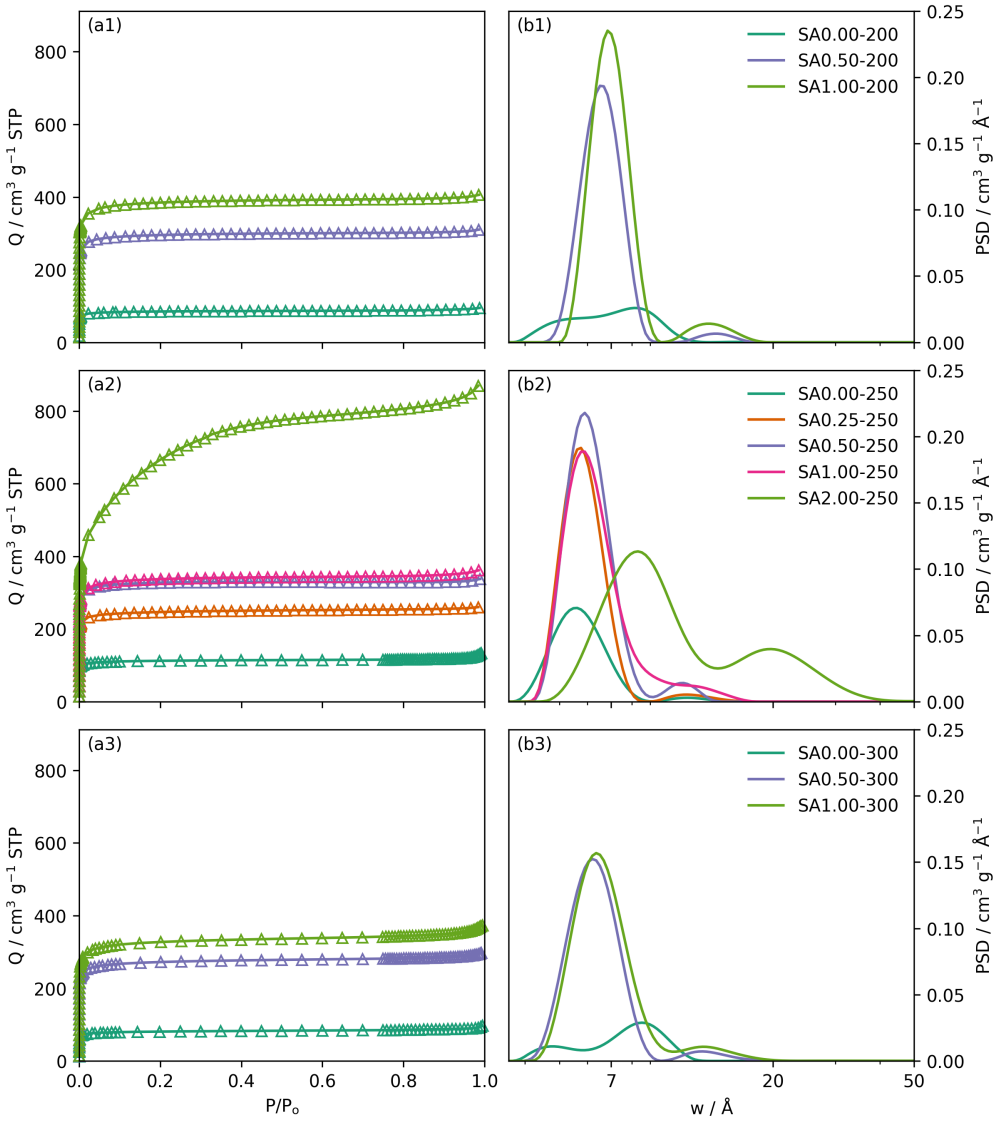

Figure 5.1: Isotherms (column a) and resultant PSDs (column b) for SA samples hydrothermally carbonised at 200, 250 and 300 °C (rows 1, 2 and 3 respectively).

small improvements in overall porosity (most pronounced according to pore volume), when the ratio is increased from 0.50 to 1.00, but not to the extent that might be expected for a doubling of the amount of porogen in the reaction mixture. This is most evident when examining differential PSDs (see figure 5.1(b1-3)) where for all SA*x.xx-HHH* samples with *x.xx* between 0.25 and 1.00 the profile is essentially the same, with porosity centered at 6-8 Å, and having minor shifts in position and/or size of the maximum which may simply be attributable to fitting of the kernel to the at times

poorly equilibrated isotherm (see appendix, figures C.5-C.7). Similarly, for samples wherein *x.xx* is 0.00, the PSD is much broader with low porosity at any given value of w, but all porosity remains in the micropore region. Conversely, SA2.00-250 displays a clear hierarchical PSD with significant porosity in both the micropore and small mesopore range.

In their 2017 work Balahmar *et al.* report carbons which were synthesised by activation with KOH at 800 °C either of untreated sawdust or sawdust-derived hydrochar synthesised at 250 °C.[1] Figure 5.2 compares these results. A_{BET} is compared in terms of both KOH:precursor mass ratio, and atomic K:C ratio; the latter according to the elemental composition of the precursor (sawdust or hydrochar). The three methods, i.e. direct activation of sawdust, activation of hydrochar, and hydrothermal impregnation of KOH into sawdust do not seem to show any significant difference in terms of the overall A_{BET} of the final product. Indeed, there is a clear strong linear correlation between amount of KOH used and A_{BET}; $r^2 = 0.90$, regardless of whether mass of KOH or amount of K is considered. The slopes of the linear regressions on figure 5.2(a1, a2) are 523 and 386 $m^2\,g^{-1}$, respectively. Thus, increases in A_{BET} with increasing amount of KOH can be precisely predicted. Furthermore, the temperature used in the hydrothermal impregnation step (this work) does not significantly effect A_{BET} of the final product. However, the microporosity of the product is significantly effected by synthetic method. At a KOH:precursor mass ratio of 2.00, microporosity is maximised by direct activation of sawdust at 84 %, which decreases to 63 % for activation of sawdust-derived hydrochar, and finally to 27 % for the hydrothermal impregnation method. These results are also reflected by the very broad, principally mesoporous PSD of SA2.00-250 relative to the comparable samples reported in the paper by Balahmar and co-workers.[1]

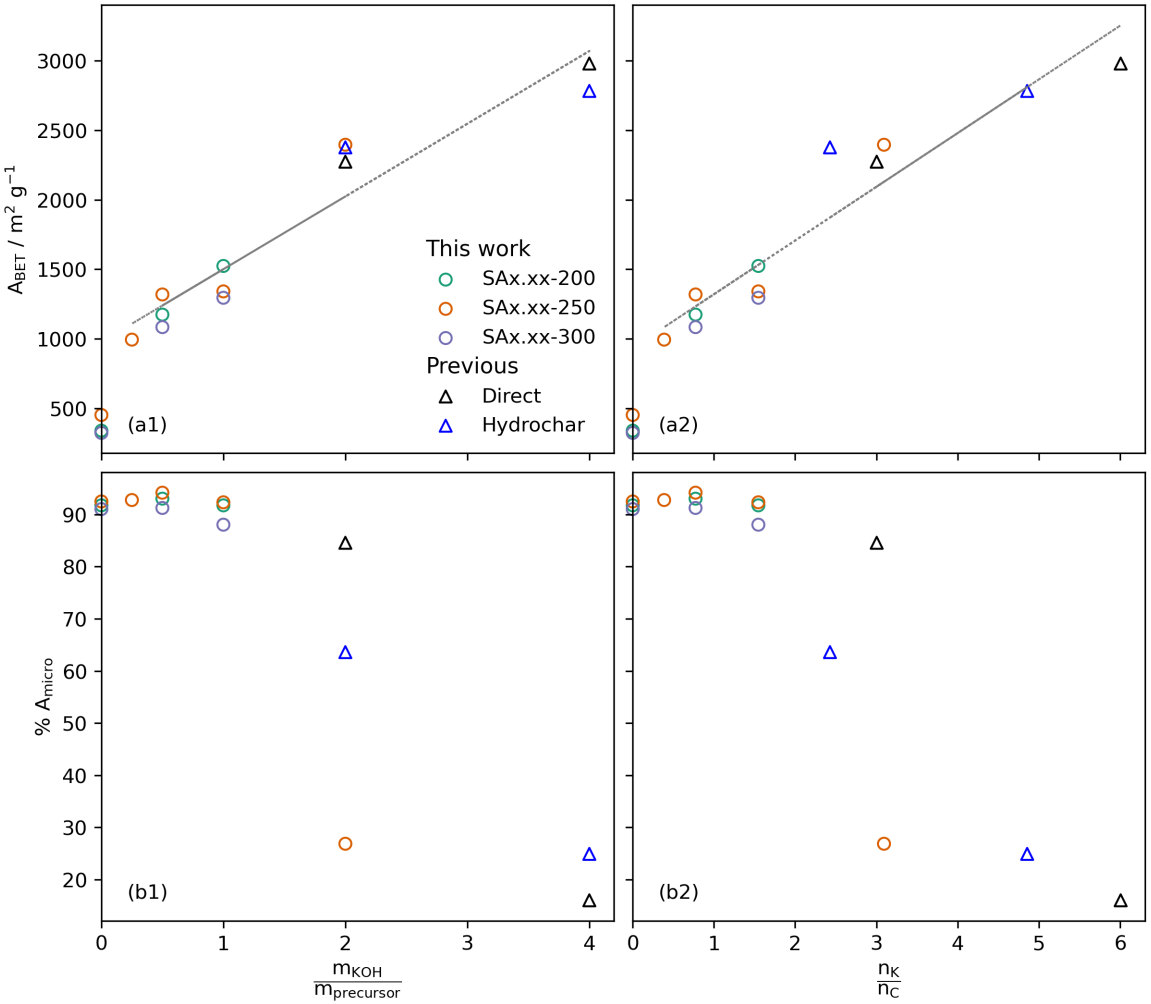

Figure 5.2: Relationship between amount of KOH used in activation of sawdust and porosity. Samples reported by Balahmar *et al.* included to show effect of different methods of preparation.[1] Amount of KOH shown as KOH:precursor mass ratio (column 1), and as K:C atomic ratio (column 2). Porosity shown in terms of total A_{BET} (row a) and micropore surface area calculated using t-plot (row b).

Density As mentioned in section 5.1, sample SA2.00-250 was noticeably more diffuse than the other samples. In lieu of access to appropriate pycnometric equipment, bulk density (ρ_b) of samples found here was estimated by using ambient temperature He freespace measurements used to calibrate the measurement of N_2 isotherms. The sample volume was taken as the difference between this freespace and the ambient freespace of the empty tube, thus calculation of the ρ_b was trivial as sample mass is already known. These estimated bulk densities are shown in figure 5.3. Densities of these carbons are at the low end of that reported for KOH-activated carbons,[11,13,14] however similar values have been reported by some groups.[15–17] Additionally, for KOH activated samples, ρ_b is negatively correlated with amount of KOH used during activation, similarly to reports by Tseng *et al.*.[15] The extremely low bulk density ($0.031\,\mathrm{g\,cm^{-3}}$) of SA2.00-250 may be

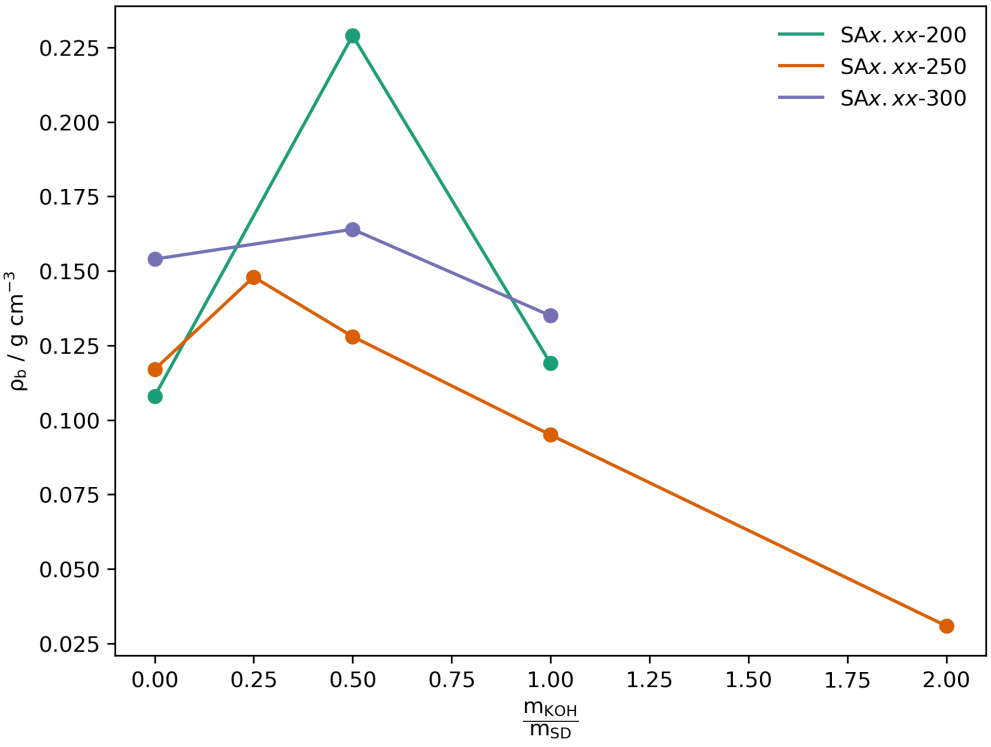

Figure 5.3: Effect of KOH:SD ratio on bulk density, ρ_b of carbons synthesised using the three htc temperatures. ρ_b estimated from freespace measurements.

ascribed to an effect described by Deng and co-workers in 2015, i.e. that high production of gases by the activating agent results in bulk densities as low as $0.043\,\mathrm{g\,cm^{-3}}$ and hierarchical PSDs.[18] While the gas production in the work by Deng *et al.* is thought to be a result of decomposition of the $KHCO_3$ porogen, in this study reactions of excess aqueous KOH with the precursor during the hydrothermal impregnation step may form porogens that have a similar capacity to release gases such as CO_2. This does not however serve to explain the low densities of the remaining samples which are almost exclusively microporous.

5.2 Sodium Carboxymethyl Cellulose

Twelve carbon samples were produced from sodium carboxymethyl cellulose with varying DS. On removal from the furnace, samples derived from precursors containing Na glowed red due to exposure of small amounts of elemental Na to air, thus indicating this species is a product of the activation process. While there is some debate as to whether elemental metals form during activation with KOH or NaOH,[3,4,19–21] it is clear that it occurs here. In addition, these samples took the form of a single, hard mass whereas activated carbons are typically powders. On washing with HCl, the samples broke up into a fine powder. This indicates that residual Na compounds or other by-products of activation may be holding particles together in some way.

5.2.1 Composition

TGA (shown in figure 5.4) of the twelve samples confirms that the washing process removed any residual Na compounds, i.e. the samples are all fully carbonaceous. In order to simplify direct comparisons between the combustion behaviour of the samples, the initial mass loss (moisture loss) at 100 °C is ignored, and initial mass is taken to be that of the dry sample. In addition, the residual mass has been adjusted to 0 wt.% for all samples to improve plot readability.[†] For some of the turbostratic carbons there is a large loss of mass at between 400 and 500 °C, before the remainder of the sample is burned off. This is followed by a second burn-off event between 800 and 900 °C. In the case of samples with only a single burn-off temperature, this occurs at between 500 and 650 °C. The dual burn-offs appear to be associated with the presence of Na in the precursor, as all

[†]Unadjusted TGA curves can be found in the appendix, figure C.8.

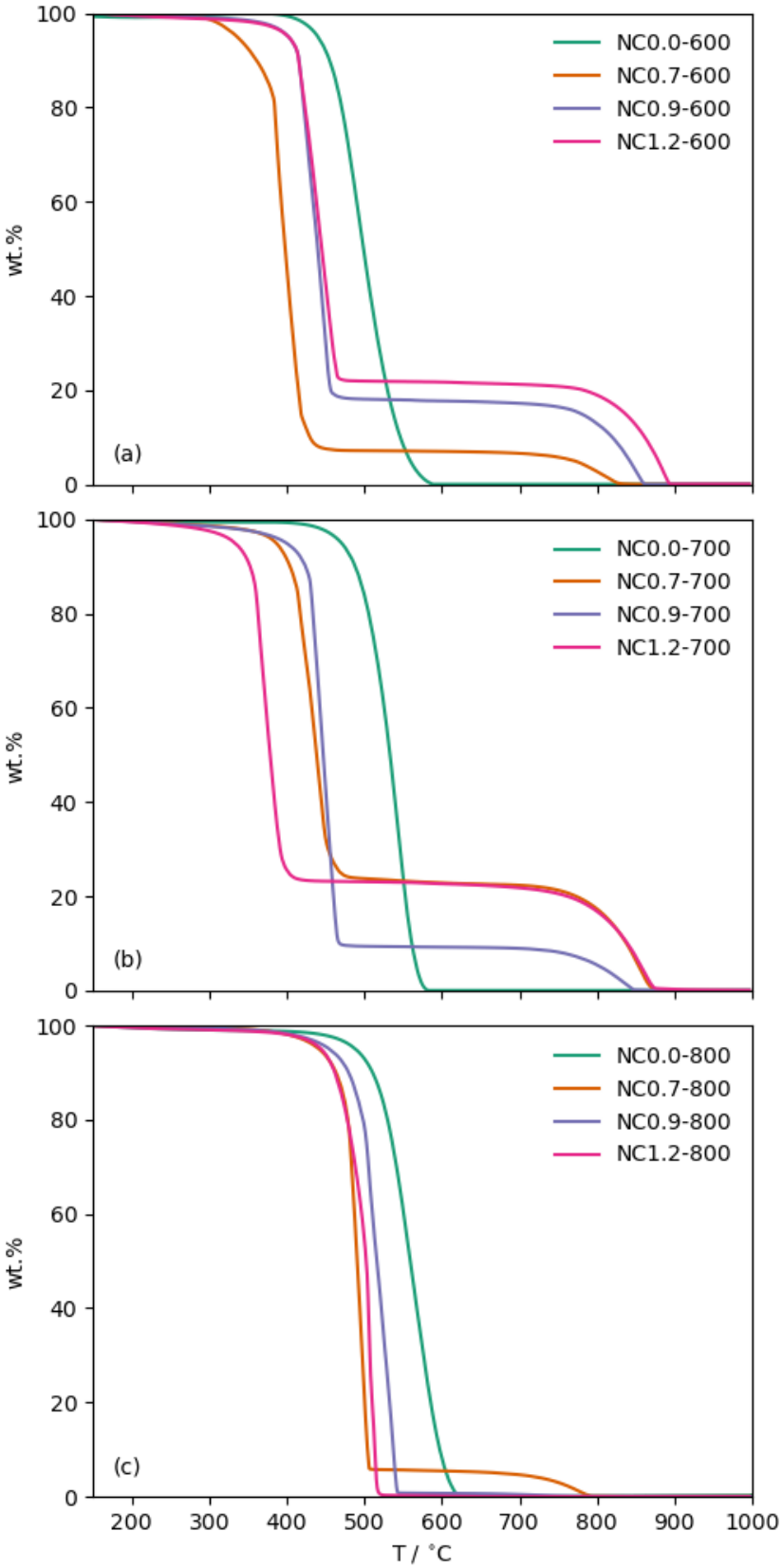

Figure 5.4: TGA curves for all NC$x.x$-TTT samples, adjusted for water evaporation, and residual masses set to 0, where within 1 wt.%. Original (unadjusted) thermograms are provided in figure C.8.

NC0.0-*TTT* samples only display a single-burn off. Furthermore, both the amount of Na in the precursor and the activation temperature influence the temperature and mass decrease in the first mass loss (when it is present). For example, for NC*x.x*-600 samples, the mass loss associated with the initial burn-off decreases with increasing DS, while the temperature of this process increases. The trend for NC*x.x*-700 is more convoluted, and for NC*x.x*-800 samples only NC0.7-800 displays the dual burn-off behaviour. Nonetheless, it appears that the oxidative porogen (here in the form of Na and/or CH_2COONa and/or other various derivatives) produces two phases in the resultant carbons to varying extents depending on the activation temperature and Na:C ratio.

Results of CHN elemental microanalysis are shown in table 5.3, alongside calculated concentrations of C, H, O, and Na in each of the four precursors. While there are variations in C, H and O content between the four precursors, the most significant change is with respect to the Na:C ratio. The effect of precursor Na:C ratio on product O:C ratio is shown in figure 5.5. Typically, increased oxidative porogen concentration results in higher relative O contents in the derived porous carbon, commonly believed to be due to increased destruction of the C framework.[22–24] What is interesting in the case of these sodium carboxymethyl cellulose-derived carbons is that there is a consistent minimum in atomic O:C ratio for carbons derived from precursors with a Na:C of 0.12, i.e. a DS of 0.9, regardless of activation temperature. The effect of quantity of porogen on the mechanism of oxidative chemical activation is not typically investigated for such low porogen:C ratios, so there is little to base a mechanistic hypothesis on for this case. However, it is possible that there is a balance being struck between formation of cross-links and activation with the Na^+ cation (or its derivatives). Cross-link formation, if it occurs ought to result in the loss of

Table 5.3: Composition of sodium carboxymethyl cellulose at all values of DS, and of NC*x.x-TTT* carbons according to CHN elemental microanalysis. For NC*x.x-TTT* carbons, O content is taken as remainder of the sum of C and H contents as samples are clean according to TGA. N content not shown as it is zero for all samples.

Sample	**Concentration / wt.%**				**Atomic ratio**		
	C	**H**	**O**	**Na**	**O/C**	**H/C**	**Na/C**
NC0.0	44	6.2	49	0	0.83	0.14	-
NC0.0-600	87	1.9	11	0	0.10	0.26	-
NC0.0-700	91	0.97	8.5	0	0.07	0.13	-
NC0.0-800	92	0.46	7.4	0	0.06	0.06	-
NC0.7	41	5.2	47	7.4	0.87	0.13	0.09
NC0.7-600	76	2.8	21	0	0.21	0.43	-
NC0.7-700	65	0.38	35	0	0.40	0.07	-
NC0.7-800	85	0.37	15	0	0.13	0.05	-
NC0.9	40	5.1	46	8.8	0.88	0.13	0.12
NC0.9-600	83	0.26	17	0	0.16	0.04	-
NC0.9-700	75	0.36	25	0	0.25	0.06	-
NC0.9-800	90	0.3	9.5	0	0.08	0.03	-
NC1.2	39	4.8	46	11	0.89	0.12	0.14
NC1.2-600	66	0.89	33	0	0.38	0.16	-
NC1.2-700	64	0.61	36	0	0.42	0.11	-
NC1.2-800	76	0.06	24	0	0.24	0.01	-

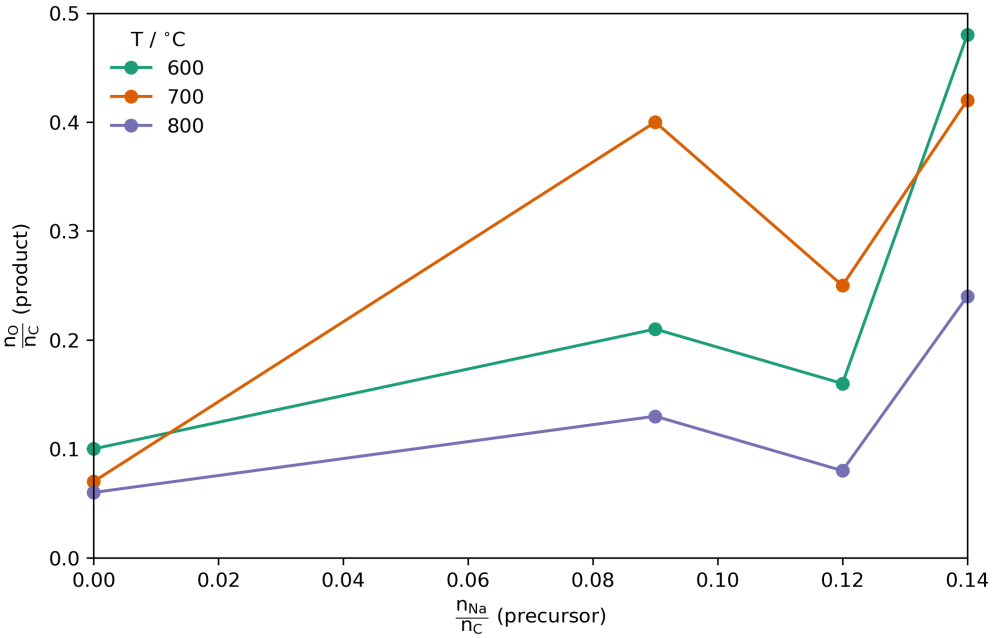

Figure 5.5: The effect of precursor Na:C ratio on the O:C ratio in the product at each of the three pyrolysis temperatures, T.

O due to the condensation of the two carboxylate groups to form the anyhdride linkage. Thus the drop in the O concentration at a DS of 0.9 may indicate the dominance of the (O-removing) cross-linking process over the (O-increasing) oxidative action of the porogen. Similarly, the high O content of samples synthesised at 700 °C relative to the other two temperatures may be a function of the two competitive mechanisms. That is, pyrolysis at 700 °C is optimal for cross-link formation. It should be noted however, that cross-linkages between sodium carboxymethyl cellulose chains have thus far only been shown to form as a result of low temperature, solution phase reactions with the use of reagents to promote their formation.[25–27]

5.2.2 Porosity

The samples in this work were not expected to have a high degree of porosity, and thus not expected to be particularly suitable candidates for gas sorption applications. Classical measures of porosity of the twelve carbons are displayed in table 5.4, and the N_2 isotherms from which these quantities are derived as well as the resultant PSDs are shown in figure 5.6. Full details of PSDs and fitting to NLDFT kernels are shown in the appendix, figures C.9-C.11.[‡] Most samples are highly microporous according to t-plot calculations, having 87-91 % and 75-90 % micropore surface area and pore volume respectively. The notable exceptions to this are NC0.7-600 wherein A_{BET} and V_t are so low that t-plot calculations are rendered extremely imprecise, as well as NC1.2-600 and NC1.2-800. The slightly lower microporosity of the latter two samples may be attributed to increased mesopore development due to higher quantities of porogen.

There are some clear trends with respect to overall porosity and both

[‡]Due to poor equilibration, these PSDs cannot be considered to be accurate, this is discussed in more depth in chapter 6 and **Publication I**.

Table 5.4: Porosity of NC*x.x-TTT* carbons. A_{BET} derived using the Rouquerol method. The total pore volume, V_t is taken using the single point method. Values in brackets indicate the microporous portion of A_{BET} and V_t, calculated using t-plot. Peak pore width w_{peak} is the maximum of the PSD determined using NLDFT, as shown in figure 5.6.

Sample	$\mathbf{A_{BET}}$ / $\mathbf{m^2\,g^{-1}}$		$\mathbf{V_t}$ / $\mathbf{cm^3\,g^{-1}}$		$\mathbf{w_{peak}}$ / **Å**
NC0.0-600	587	(530, 90%)	0.24	(0.21, 88%)	6
NC0.7-600	21	(13, 62%)	0.01	(-)	7
NC0.9-600	577	(505, 88%)	0.25	(0.19, 76%)	6
NC1.2-600	238	(213, 89%)	0.10	(0.08, 80%)	6
NC0.0-700	531	(485, 91%)	0.21	(0.19, 90%)	6
NC0.7-700	162	(151, 93%)	0.07	(0.06, 85%)	7
NC0.9-700	364	(325, 89%)	0.16	(0.13, 81%)	7
NC1.2-700	190	(169, 89%)	0.08	(0.06, 75%)	5
NC0.0-800	403	(356, 88%)	0.17	(0.13, 76%)	6
NC0.7-800	491	(427, 87%)	0.21	(0.16, 76%)	6
NC0.9-800	650	(570, 87%)	0.28	(0.22, 79%)	6
NC1.2-800	476	(382, 80%)	0.21	(0.15, 71%)	5

quantities of activating agent and activation temperature. The porosity of NC0.0-*TTT* samples decreases with increasing activation temperature, while maintaining fairly constant microporosity ($(90 \pm 2)\,\%$, by surface area), and average pore size of 6 Å. This indicates that for biochars, increasing activation temperature only serves to destroy porosity created at lower temperatures, while not broadening the PSD significantly. It has been previously observed that biochar porosity is optimised with pyrolysis temperature of around 600 °C,[28–30] although values for A_{BET} and V_t in these reports are around an order of magnitude less than shown by carbons reported herein from cellulose. Indeed, Zhang *et al.* reported A_{BET} and V_t of only $4.1\,m^2\,g^{-1}$ and $0.02\,cm^3\,g^{-1}$ respectively for a carbon derived from the pyrolysis of cellulose at 800 °C,[31] compared to the A_{BET} of $403\,m^2\,g^{-1}$ for NC0.0-800. The samples reported here are more comparable in terms of porosity to that of the biochar reported in chapter 4 derived from pure cellulose acetate (see table C.1). This much higher surface area may simply

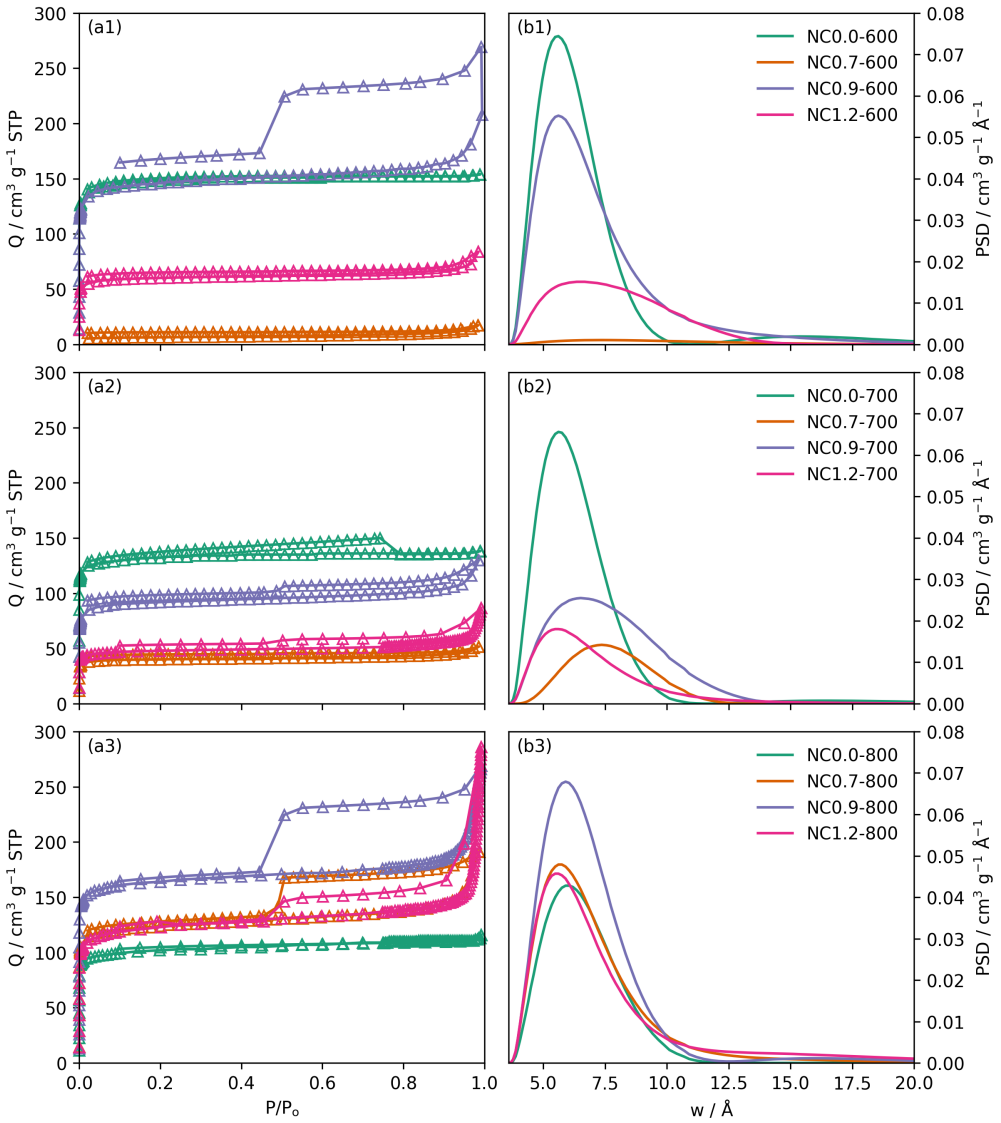

Figure 5.6: Isotherms (column a) and resultant PSDs (column b) for NC samples activated at 600 (row 1), 700 (row 2), and 800 (row 3) °C.

be a result of washing of the biochars, which removes some soluble matter that contributed to pore blocking but may also be indicative of the low activation resistance of purely cellulosic materials relative to the traditionally carbonised ligno-cellulosic biomass.[2,32–34]

Carbons derived from sodium carboxymethyl cellulose with a DS between 0.7 and 1.2 consistently showed highest porosity at DS of 0.9. While there is typically some optimum porogen:C ratio for activation with NaOH or KOH, it is usually much higher than the extremely low value reported

here.[1,3,35–37] A DS of 0.9 corresponds to an atomic Na:C ratio of just 0.12, while Balahmar *et al.* reported that directly activated carbons from sawdust showed much higher A_{BET} ($1202\,m^2\,g^{-1}$) at a K:C atomic ratio of 0.19, which more than doubled when the amount of porogen was doubled.[1] Similarly, Tseng found that A_{BET} of corn cob char-derived carbons was maximised at $2500\,m^2\,g^{-1}$ using a Na:C atomic ratio of 0.83. Indeed V_t continued to increase as Na:C was increased to 1.3.[35§] On the other hand, Roberts *et al.* reported surface areas up to $1051\,m^2\,g^{-1}$, for carbons derived from the pyrolysis of freeze-dried sodium poly(4-styrenesulfonate), which has an Na:C ratio of 0.13, similar to the sodium carboxymethyl cellulose reported here.[38] Indeed, others have corrobrated that polymeric salts with a similar amount of metal cation can produce carbons with similar surface areas.[39–41] These relatively high values for A_{BET} at relatively low porogen:C ratios can be attributed to the development of porosity prior to oxidative chemical activation by the formation of cross-linkages between polymer chains.

Hysteresis Similarly to reported N_2 isotherms on carbons derived from other polymeric salts,[38–41] carbons produced in this work from sodium carboxymethyl cellulose show type I(a) character, with some degree of type II character and hysteresis (see figure 5.6 (a1, a2, a3)). These hystereses appear to be permanent, as they are reproduced when the equilibration time is increased up to 45 s for the desorption branch, as shown in the appendix, figure C.12. According to the IUPAC technical report on phyisorption and porosimetry, this hysteresis character is a result of network effects wherein wider pores only have access to the surface *via* a much smaller pore entrance. During desorption this results in the larger pores remaining full until the narrow pore entrances are emptied at a much lower pressure.[12]

§Atomic ratios not provided by original reports, determined by the author.

In their reports on polymeric salt-derived carbons, Hines *et al.* and Yadav *et al.* ascribe this behaviour to a mixed micro-/mesoporous structure.[39,41] The mesoporosity of the samples reported here is generally lower than those from polymeric sodium salts,[38,39] perhaps on account of the lower activation temperatures used in this work. Indeed, hysteresis is most prominent for samples activated at 800 °C, and with the largest hyseresis occurring for samples derived from sodium carboxymethyl cellulose at a DS of 0.9. This indicates that these network effects are dependent upon the harshness of the activation conditions. In particular, the reduction in the size of the hysteresis loop between samples NC0.9-800 and NC1.2-800 (figure 5.6 (a3)) indicates that at a certain Na:C ratio, pore entrances are broadened by the action of the excess porogen. The nature of the pore geometry and network connectivity may be investigated further by the use of a larger sorptive such as SF_6, as previously reported by Jagiello and others.[42–44] The anomalously smaller hysteresis of all samples activated at 700 °C requires further investigation, but may be connected to the high O content of these samples as discussed in section 5.2.1.

5.3 Conclusion

This chapter has explored two alternative novel routes to the synthesis of turbostratic carbons, wherein it was attempted to increase porogen-precursor contact, and improve the homogeneity of the distribution of the porogen. In addition, the effect of small changes to the porogen:precursor ratio was also studied, as well as activation or hydrothermal carbonisation temperature. It was found that these techniques yield carbons which show unusual trends in porosity and elemental composition with respect to turbostratic carbons derived through more traditional techniques.

In the case of carbons derived *via* the hydrothermal impregnation of KOH into sawdust, the extremely carbon-rich products were almost exclusively microporous. However, at a sufficiently high KOH:SD mass ratio (2.00), a carbon with extremely low density and unusually high mesoporosity (27 %) is produced. This is in contrast to sawudst-derived carbons derived through conventional activation methods. Such a product may be useful for electrochemical applications such as ion-transport.

On the other hand, the samples derived from the activation of sodium carboxymethyl cellulose give insight not only into the competitive pore-formation effects of polymeric cross-linking and oxidative chemical activation, but also show the fine control over porosity that is possible with the use of small, accurately quantified amounts of porogen. The overall porosity of carbons in this set peaks at extremely low porogen:C atomic ratios (1.2), however what is more interesting is the indication of variations in pore network connectivity and/or pore geometry as shown by the synthetic condition-dependent appearance of hysteresis shown by N_2 isothermal porosimetry. This apparent trend in porosity is mirrored by apparent changes in the composition of the carbons, indicating that it may be a function of the two competitive phenomena facilitating porogenesis from this precursor.

While the findings in this chapter give scope for a multitude of routes of further investigation, it is clear that as for the carbons in chapter 4, N_2 is insufficient as a probe molecule for accurately and thoroughly determining the porosity of these samples. In particular it appears that carbons in this work possess a high degree of ultramicroporosity, however the poor equilibration of the isotherms at low relative pressures means that precise PSDs are impossible to determine. This has lead to the author exploring alternative techniques to attempt to understand the complex relationship

between activation conditions and porosity in these unusual turbostratic carbons in chapter 6.

References

1. N. Balahmar, A. S. Al-Jumialy and R. Mokaya, *Journal of Materials Chemistry A*, 2017, **5**, 12330–12339.
2. N. Balahmar and R. Mokaya, *Journal of Materials Chemistry A*, 2019, **7**, 17466–17479.
3. M. Sevilla and R. Mokaya, *Energy & Environmental Science*, 2014, **7**, 1250–1280.
4. L. S. Blankenship and R. Mokaya, *Materials Advances*, 2022, **3**, 1905–1930.
5. M. Sevilla and A. B. Fuertes, *Carbon*, 2009, **47**, 2281–2289.
6. G. K. Parshetti, S. K. Hoekman and R. Balasubramanian, *Bioresource Technology*, 2013, **135**, 683–689.
7. D. Kim, K. Lee and K. Y. Park, *Fuel*, 2014, **130**, 120–125.
8. Y. Gao, X.-H. Wang, H.-P. Yang and H.-P. Chen, *Energy*, 2012, **42**, 457–465.
9. L.-P. Xiao, Z.-J. Shi, F. Xu and R.-C. Sun, *Bioresource technology*, 2012, **118**, 619–623.
10. T. Wang, Y. Zhai, Y. Zhu, C. Li and G. Zeng, *Renewable and Sustainable Energy Reviews*, 2018, **90**, 223–247.
11. A. Altwala and R. Mokaya, *Energy & Environmental Science*, 2020, **13**, 2967–2978.
12. M. Thommes, K. Kaneko, A. V. Neimark, J. P. Olivier, F. Rodriguez-Reinoso, J. Rouquerol and K. S. Sing, *Pure and Applied Chemistry*, 2015, **87**, 1051–1069.

13. M. E. Casco, M. Martínez-Escandell, K. Kaneko, J. Silvestre-Albero and F. Rodríguez-Reinoso, *Carbon*, 2015, **93**, 11–21.

14. J. Machnikowski, K. Kierzek and K. Torchała, *Energy & fuels*, 2012, **26**, 3697–3702.

15. R.-L. Tseng, S.-K. Tseng, F.-C. Wu, C.-C. Hu and C.-C. Wang, *Journal of the Chinese Institute of Chemical Engineers*, 2008, **39**, 37–47.

16. R. A. Rashid, A. H. Jawad, M. A. M. Ishak and N. N. Kasim, *Desalination and Water Treatment*, 2016, **57**, 27226–27236.

17. C. Guan, L. S. Loo, K. Wang and C. Yang, *Energy conversion and management*, 2011, **52**, 1258–1262.

18. J. Deng, T. Xiong, F. Xu, M. Li, C. Han, Y. Gong, H. Wang and Y. Wang, *Green Chemistry*, 2015, **17**, 4053–4060.

19. D. Lozano-Castello, J. Calo, D. Cazorla-Amoros and A. Linares-Solano, *Carbon*, 2007, **45**, 2529–2536.

20. S. Kelemen and C. Mims, *Surface Science*, 1983, **133**, 71–88.

21. R. Xue and Z. Shen, *Carbon*, 2003, **41**, 1862–1864.

22. S.-J. Park and W.-Y. Jung, *Journal of Colloid and Interface Science*, 2002, **250**, 93–98.

23. W. Chen, M. Gong, K. Li, M. Xia, Z. Chen, H. Xiao, Y. Fang, Y. Chen, H. Yang and H. Chen, *Applied Energy*, 2020, **278**, 115730.

24. R.-L. Tseng, *Journal of Hazardous Materials*, 2007, **147**, 1020–1027.

25. R. Lin, A. Li, L. Lu and Y. Cao, *Carbohydrate Polymers*, 2015, **118**, 126–132.

26. M. Yu, J. Li and L. Wang, *Chemical Engineering Journal*, 2017, **310**, 300–306.

27. M. Yu, Y. Han, J. Li and L. Wang, *Chemical Engineering Journal*, 2017, **324**, 287–295.

28. E. F. Zama, Y.-G. Zhu, B. J. Reid and G.-X. Sun, *Journal of Cleaner Production*, 2017, **148**, 127–136.

29. F. Ronsse, S. Van Hecke, D. Dickinson and W. Prins, *Global Change Biology Bioenergy*, 2013, **5**, 104–115.

30. L. Leng, Q. Xiong, L. Yang, H. Li, Y. Zhou, W. Zhang, S. Jiang, H. Li and H. Huang, *Science of the Total Environment*, 2021, **763**, 144204.

31. C. Zhang, L. Chao, Z. Zhang, L. Zhang, Q. Li, H. Fan, S. Zhang, Q. Liu, Y. Qiao, Y. Tian, Y. Wang and X. Hu, *Renewable and Sustainable Energy Reviews*, 2021, **135**, 110416.

32. E. A. Hirst, A. Taylor and R. Mokaya, *Journal of Materials Chemistry A*, 2018, **6**, 12393–12403.

33. Z. Zhang, D. Luo, G. Lui, G. Li, G. Jiang, Z. P. Cano, Y.-P. Deng, X. Du, S. Yin, Y. Chen, M. Zhang, Z. Yan and Z. Chen, *Carbon*, 2019, **143**, 531–541.

34. J. Deng, T. Xiong, H. Wang, A. Zheng and Y. Wang, *ACS Sustainable Chemistry & Engineering*, 2016, **4**, 3750–3756.

35. R.-L. Tseng, *Journal of Colloid and Interface Science*, 2006, **303**, 494–502.

36. J. Singh, S. Basu and H. Bhunia, *Journal of the Taiwan Institute of Chemical Engineers*, 2019, **102**, 438–447.

37. O. Boujibar, A. Souikny, F. Ghamouss, O. Achak, M. Dahbi and T. Chafik, *Journal of Environmental Chemical Engineering*, 2018, **6**, 1995–2002.

38. A. D. Roberts, X. Li and H. Zhang, *Carbon*, 2015, **95**, 268–278.

39. P. Yadav, A. Banerjee, S. Unni, J. Jog, S. Kurungot and S. Ogale, *ChemSusChem*, 2012, **5**, 2159–2164.

40. D. Puthusseri, V. Aravindan, S. Madhavi and S. Ogale, *Energy & Environmental Science*, 2014, **7**, 728–735.

41. D. Hines, A. Bagreev and T. J. Bandosz, *Langmuir*, 2004, **20**, 3388–3397.

42. M. Lopez-Ramon, J. Jagiełło, T. Bandosz and N. Seaton, *Langmuir*,

1997, **13**, 4435–4445.

43. J. Jagiello, T. J. Bandosz, K. Putyera and J. A. Schwarz, *Journal of Chemical and Engineering Data*, 1995, **40**, 1288–1292.

44. M. Navarro, N. Seaton, A. Mastral and R. Murillo, *Carbon*, 2006, **44**, 2281–2288.

Chapter 6

Improved porosimetric techniques for highly ultramicroporous carbons

Abstract

It has been shown both in recent literature, and according to the work in chapters 4 and 5 that porosimetry based on N_2 isotherms at $-196\,^{\circ}C$ is insufficient for the precise analysis of porosity in ultramicroporous carbons. This is a result of both N_2's high quadrupole moment as well as its poor diffusion into ultramicropores. The investigation of alternative adsorbates for these materials, in particular H_2 and O_2 has shown some promise in this regard, and the development of the dual isotherm fitting method allows for a unified PSD to be determined with this method. As such this chapter investigates the relative utility of the simultaneous fitting of O_2/H_2 isotherms to Non-Local Density Functional Theory (NLDFT) kernels in determining porosity of carbons found in this work, as compared to dual isotherm N_2/H_2 as well as to single isotherm NLDFT porosimetry and classical methods such as BET.

It was found that the O_2/H_2 method provides an extremely high level of detail in the differences in porosity of carbons activated with differing amounts of porogen. That is, not only can overall changes in porosity be observed, but more significantly very small changes in pore width are observable with this technique. The latter cannot be achieved using dual isotherm N_2/H_2 fitting, or indeed by any other means investigated in this work. As a result, O_2/H_2 analysis provides hints at pore formation mechanisms in these types of porous carbons that are not evident according to N_2/H_2 analysis. Furthermore, it is apparent that the use of the H_2 isotherm provides knowledge of porosity in the small ultramicropore region which is inaccessible to either of the larger probes, O_2 or N_2. Finally, the NLDFT methodology used in this work provides quite different understanding of the variation of apparent surface area with synthetic conditions as compared to the tra-

ditional BET method, which is likely a result of the greater suitability of the NLDFT kernel to the analysis of ultramicroporous turbostratic carbons examined herein.

6.1 Experimental background

In chapters 4 and 5, it became clear that derivation of PSDs and related porosimetric values from the typical N_2 ($-196\,^{\circ}C$) isotherm was not sufficiently accurate. In particular, for carbons with a low degree of activation isotherm measurement became impractical due to extremely long equilibration times - see figure 6.1. In many cases this resulted in limited isotherms that do not include points at ultra-low pressures ($P/P_0 < 10^{-4}$) (examples of such isotherms are shown in figures C.2, C.9-C.11). PSDs from these incomplete and/or poorly equilibrated isotherms indicate a high degree of porosity in the ultramicropore region, however ultramicropores fill at ultra-low pressures. Thus, as noted in previous chapters there can be very minimal confidence in the results derived from this technique. This

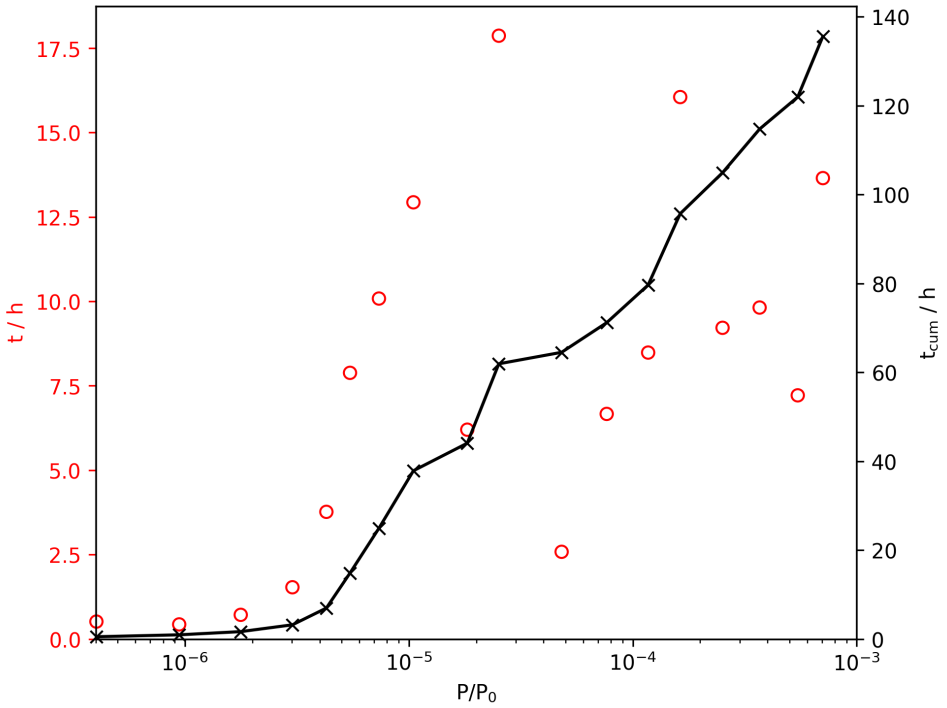

Figure 6.1: An example of the egregiously long equilibration times for individual points, t and cumulative analysis time, t_{cum} in the measurement of an N_2 isotherm at $-196\,^{\circ}C$ on sample hD-0700. The isotherm only reached a P/P_0 of 10^{-3} before being cancelled by the instrument.

issue has been reported as early as 1982.[1] A solution in the literature to this problem has been to employ CO_2 isotherms at 0 °C in order to probe ultramicropores and small supermicropores.[2–5] The porosity up to some upper-limit (usually taken as somewhere around 10 Å) can then be calculated.[6,7] PSDs have also been calculated from these isotherms,[2] and indeed Jagiello and co-workers have developed techniques to fit NLDFT kernels simultaneously to CO_2 and N_2 isotherms.[3,8] However, in the case of turbostratic carbons, the effect of the quadrupole moment of both CO_2 and N_2 on the accuracy of the resultant PSD means that the much less polar H_2 and O_2 are now becoming common replacements to elucidate the full porosity of such materials.[9–11] Furthermore, O_2 and H_2 isotherms can be measured at −196 °C, unlike CO_2 which is solid at this temperature - thus eliminating the need to change temperature control apparatus. Therefore, this chapter investigates the relative utility of both N_2/H_2 and O_2/H_2 pairs in determining PSDs of the ultramicroporous carbons produced in chapters 4 and 5.

6.2 Exploring alternative porosimetric adsorbates

Section 6.1 laid out the need to explore alternative porosimetric techniques for analysis of the ultramicroporous carbons produced in previous chapters. While a comprehensive comparison of dual fitting to N_2/H_2 and O_2/H_2 isotherm pairs is detailed in **Publication I** (contained in this chapter), what follows here are the results of some initial analytical experiments using N_2 and O_2, and combined O_2/H_2 isotherms.

While the purpose of this chapter is to use more advanced, NLDFT tech-

niques in the determination of porosity from physisorption isotherms, comparing the classical measures of surface area and pore volume yielded by N_2 and O_2 isotherms at $-196\,^{\circ}C$ also gives some interesting insights. Results of these analyses are displayed in table 6.1. The important distinctions between these adsorbates are their molecular cross-sectional areas (σ), kinetic diameters (d_k) and quadrupole moments (μ). As stated before, O_2 is significantly less polar than N_2, these adsorbates having μ of 0.155 and 0.697 respectively.[12–14] In terms of d_k they are similar, and σ_{O_2} is only slightly smaller than σ_{N_2} at 0.143 and 0.162 nm^2 respectively. However, it should be noted that there is no definitive, exact value for these σ values as they vary according to the surface the molecule is being adsorbed onto.[15–17] This variability is much more significant in the case of N_2 due to its greater polarity - indeed σ_{N_2} can vary for individual molecules of N_2 on a single adsorbent at different adsorption sites.[9]

Table 6.1: Comparison of classical measures of porosity derived using N_2 and O_2 porosimetry. A_{BET} calculated using the Rouquerol method,[18] and V_t using the single-point approach. Values in brackets indicate the microporous portion of surface area and pore volume as determined by t-plot using a Carbon Black STSA thickness curve. The two hD-0700 samples in table are repeat syntheses of the same sample.

Sample	**A_{BET} / $m^2\,g^{-1}$**				**V_t / $cm^3\,g^{-1}$**			
	N_2		**O_2**		**N_2**		**O_2**	
NC0.0-800	449	(408)	595	(532)	0.17	(0.13)	0.24	(0.20)
NC0.7-800	580	(495)	645	(563)	0.21	(0.16)	0.25	(0.18)
NC0.9-800	669	(578)	876	(749)	0.28	(0.22)	0.37	(0.29)
SA1.00-200	1410	(1306)	1513	(1333)	0.61	(0.54)	0.62	(0.51)
SA0.00-250	949	(838)	596	(514)	0.18	(0.16)	0.25	(0.20)
SA0.50-250	906	(826)	1161	(1066)	0.51	(0.47)	0.40	(0.34)
SA1.00-250	1081	(971)	1266	(1138)	0.54	(0.48)	0.45	(0.37)
hD-0700*(1)*	278	(242)	428	(355)	0.18	(0.11)	0.16	(0.12)
hD-0700*(2)*	317	(265)	411	(346)	0.19	(0.12)	0.15	(0.11)

These issues with these classical analyses notwithstanding, the values for A_{BET} derived from O_2 porosimetry are generally higher than that from N_2. The relative percentage of surface area taken up by micropores is however consistent from both techniques, being between 83 and 92 % for all samples. On the other hand, V_t does not show any consistency in the way it varies between the two techniques. It is likely that simply due to the large uncertainties in determination of pore volume *via* the single-point method, any pattern is obscured. The increases in A_{BET} found when using O_2 at −196 °C as a molecular probe may indicate the ability of O_2 to diffuse into pores inaccessible to N_2. It is also interesting to note that A_{BET} is far more consistent for the two repeats of hD-0700 when determined using O_2 rather than N_2, perhaps giving further indication of the improvements in reliability of results attained using this alternative adsorbate. It is however difficult to categorically assert O_2's superiority over N_2 for this application from this evidence, due to the aforementioned problems with these classical techniques.

Initial investigations into dual isotherm analysis were for the purpose of comparing porosity as given by fitting of the 2D-NLDFT-HS kernel to N_2 isotherms to that determined by the dual fitting of the appropriate 2D-NLDFT-HS kernels to O_2 and H_2 isotherms on carbon samples that appear to have a high proportion of ultramicropores. An example of this comparison is shown in figure 6.2. In general, it was found that the dual O_2/H_2 fit yields greater overall porosity than the single isotherm fit. Furthermore, the PSDs are consistently bimodal for the dual isotherm fit. While micropores are typically subdivided at 7.0 Å into ultramicropores and supermicropores (as indicated by the dotted line in figure 6.2), the minimum between the two regions is at a consistently lower pore width than this. For this purpose, the pore volume (V_{NLDFT}) and surface area (A_{NLDFT})

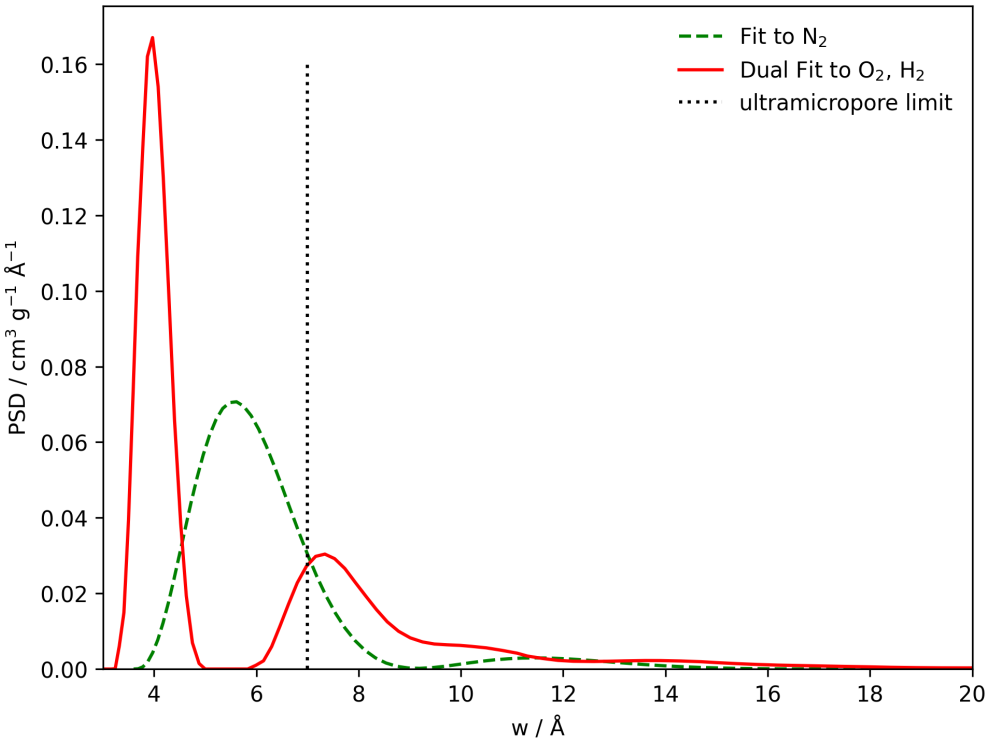

Figure 6.2: An example of the different PSDs from single fit to N_2 and dual fit to O_2 and H_2 isotherms on sample SA0.00-250. The ultramicropore limit is also shown; clearly the dual fit shows a separation in pore regions that is different to the ultramicropore limit of 7.0 Å.

Table 6.2: Pore volume (V_{NLDFT}) and surface area (A_{NLDFT}) of selected samples from chapters 4 and 5 in the micropore region, divided into two regions according to the local minimum (w_{locmin}). Porosities calculated with simultaneous fit of 2D-NLDFT-HS kernels to O_2 and H_2 isotherms.

Sample	**w_{locmin} / Å**	**V_{NLDFT} / cm^3 g^{-1}**		**A_{NLDFT} / m^2 g^{-1}**	
		1	**2**	**1**	**2**
NC0.0-800	5.5	0.14	0.09	715	184
NC0.7-800	5.3	0.12	0.15	620	366
NC0.9-800	5.4	0.13	0.20	669	507
SA1.00-200	6.1	0.20	0.38	868	824
SA0.00-250	5.4	0.12	0.33	627	811
SA0.50-250	6.1	0.17	0.35	812	820
SA1.00-250	6.1	0.19	0.37	841	195
hD-0700*(1)*	5.7	0.10	0.10	464	217
hD-0700*(2)*	5.5	0.09	0.09	444	217

are given in table 6.2 as subdivided into these two regions according to the variable local minimum (w_{locmin}). The separate regions appear to be a result of different probeable pore sizes of the two adsorptives; an issue which is discussed in more depth in **Publication I**, **section 3.3.1.**.

The proportion of micropores taken up by these lower width peaks (peak 1) varies, with V_{NLDFT} ranging from 27 % to 61 % and A_{NLDFT} from 44 % to 81 % (see table 6.2). This variation appears to be inversely related to degree of activation and indeed is the topic of **Publication I**. In the case of the NC*x.x-TTT* and SA*x.xx*-250 samples it is clear that the proportion of microporosity taken up by the initial peak falls precipitously with porogen:precursor ratio. The consistency found between the two repeats of hD-0700 (see table 6.1) when using O_2 to determine classical measures of porosity is also present with these dual isotherm 2D-NLDFT-HS analyses. This lends further credence to the notion that the dual isotherm porosimetric method explored here may be superior to current, single isotherm methods.

The finer detail attained in the derived PSDs from the dual O_2/H_2 fits is of great interest as ultramicropores have been attributed to the low pressure uptake of adsorbates such as CO_2 and H_2.[19–23] What has not yet been investigated is the comparison of dual N_2/H_2 fits with O_2/H_2. This, therefore is investigated in **Publication I**. Furthermore, the work in chapter 7 shows that the porosity as shown by these dual isotherm techniques does have physical significance at least in terms of CO_2 uptake capacity.

6.3 Publication I: Confirmation of pore formation mechanisms in biochars and activated carbons by dual isotherm analysis

Contribution of the author: The author performed all synthesis and instrumental analysis of samples in the work, analysed the results and wrote the manuscript.

Note: For this publication, the sample names are slightly different. The variable *x.xx* in SA*x.xx-HHH* samples is truncated to *x.x*, i.e. SA0.5-250 in the publication is equivalent to SA0.50-250 in chapter 5. As for NC*x.x-TTT* samples only samples with *TTT* of 800 °C are examined, thus NC0.9 is identical to NC0.9-800 in chapter 5.

Materials Advances

ROYAL SOCIETY OF CHEMISTRY

PAPER

View Article Online
View Journal | View Issue

Check for updates

Cite this: *Mater. Adv.*, 2022, 3, 3961

Confirmation of pore formation mechanisms in biochars and activated carbons by dual isotherm analysis†

L. Scott Blankenship, *[a] Jacek Jagiello [b] and Robert Mokaya [a]

In this study biochars and activated carbons were synthesized either directly *via* the pyrolysis of sodium carboxymethyl cellulose (NC) or *via* hydrothermal carbonization of sawdust (SD) in an aqueous solution of KOH. The amount of porogen was varied by modulating the degree of sodium carboxymethyl substitution on NC or the amount of KOH mixed in solution with SD. Pore size distributions (PSDs) of these carbons were determined from the dual fit of kernels based on the two-dimensional version of the nonlocal density functional theory (2D-NLDFT) heterogeneous surface models to either N_2 and H_2 or O_2 and H_2 isotherms measured at −196 °C. By comparing PSDs of carbons from the same starting material at increasing degrees of activation, we show that those derived using O_2 and H_2 isotherms not only give more detail of variations in pore size but that the results also fit better with current understandings of porosity development in carbons derived through oxidative activation. This is likely a result of superior diffusion of O_2 into ultramicropores at low pressure relative to N_2.

Received 9th February 2022,
Accepted 29th March 2022

DOI: 10.1039/d2ma00141a

rsc.li/materials-advances

Open Access Article. Published on 30 March 2022. Downloaded on 11/1/2022 11:56:41 AM.
This article is licensed under a Creative Commons Attribution 3.0 Unported Licence.

1. Introduction

Porosimetry *via* the measurement of gas adsorption isotherms has provided a great depth of insight into the nature of pore channels in solids, particularly on disordered-like materials for which other techniques are not suitable for pore sizing. While N_2 at −196 °C remains the dominant adsorptive used in such experiments due to its availability, studies have concluded that it is lacking in some properties required for good isotherm measurement and thus accurate determination of textural parameters.[1–5] In the case of porous carbons as well as other porous materials such as conjugated microporous polymers (CMPs), it is well established that pores of width similar to the size of the N_2 molecule are common. This can lead to inadequate diffusion of N_2 into such pores when it is used as an adsorptive.[5–7] Further, polar groups on the surface of many carbons may interact with the N_2 molecule's large quadrupole moment, which obfuscates the molecular cross-sectional area used in the calculation of various measures of porosity.[2,8,9] As such, alternative adsorptives have enjoyed some use in recent years, including Ar, O_2, H_2, CO_2, CH_4, CF_4, and SF_6 as they are either smaller in size or have a lower quadrupole moment than N_2 – or both (see Table 1).[10–15] Simultaneously the development of advanced DFT kernels for an array of adsorptives on carbons, in particular the 2D-NLDFT heterogeneous surface model mean that quantities such as pore size, volume, and surface area can now be more accurately determined than in the past. This model accounts for surface roughness present in the graphene sheets which make up turbostratic porous carbons by assuming a corrugated slit pore model.[15,16] The nanoporous carbon structure based on curved graphene building blocks was demonstrated by using atomic resolution images taken within nanoporous carbon samples.[17]

Nonetheless, a single isotherm cannot typically be used to accurately determine pore sizes across the entire micropore

Table 1 Physical properties of relevant molecules for porosimetry measurements[20–23]

Species	d_k/Å	T_b/°C	μ
H_2	2.89	−252	0.260
CO_2	3.30	−78[a]	2.139
CH_4	3.80	−161	0.000
N_2	3.64	−196	0.697
O_2	3.46	−183	0.155
Ar	3.40	−186	—
CF_4	4.70	−128	—
SF_6	5.50	−51	—

[a] Sublimes. k_d = kinetic diameter, T_b = boiling point, μ = quadrupole moment

[a] *School of Chemistry, University of Nottingham, University Park, Nottingham, NG7 2RD, UK. E-mail: leo.blankenship@nottingham.ac.uk*
[b] *Micromeritics Instrument Corporation 4356 Communications Drive, Norcross, GA, 30093, USA*

† Electronic supplementary information (ESI) available: One table, five figures, all isotherms in human- and machine-readable.aif files. See DOI: 10.1039/d2ma00141a

© 2022 The Author(s). Published by the Royal Society of Chemistry

Open Access Article. Published on 30 March 2022. Downloaded on 11/1/2022 11:56:41 AM.
This article is licensed under a Creative Commons Attribution 3.0 Unported Licence.

region. For example, while H_2 sorption at −196 °C can probe pores as small as 3 Å its upper limit is ∼10 Å. Conversely, O_2 adsorption at −196 °C is best utilized for probing pores larger than 7 Å, although it has been shown to also penetrate pores smaller than this limit to some degree.[18] In order to take advantage of the information gained from measuring two isotherms, Jagiello *et al.* developed a method whereby appropriate kernels could be simultaneously fit to two isotherms to yield a single pore size distribution (PSD).[2,5] This method was tested by using a variety of combinations of isotherms, including N_2/CO_2, O_2/H_2, and N_2/H_2. Generally speaking, the results derived from each of these combinations yields similar PSDs.[2,4,5] However, as reported by Beda *et al.*, N_2's poor diffusion into ultramicropores means that N_2 and O_2 isotherms on so-called hard carbons can be quite different, and as a result PSDs may differ significantly with O_2 showing much more porosity in the ultramicropore region.[18] In addition, the high quadrupole moment of CO_2 can lead to incorrect results due to its interaction with polar moieties which are common on activated carbons.[19] The combination of O_2 and H_2 may provide more accurate information than the N_2 and CO_2 isotherms due to the former pair's lower quadrupolarity.[2,4] Despite being fairly reactive gases at room temperature, under cryogenic conditions the reactivity is extremely low, so is unlikely to affect carbon surface chemistry.

Within the group of turbostratic porous carbons, there are two closely related subtypes. The first is biochar, which is produced upon the pyrolysis of biomass or other carbon-rich material.[24,25] So-called activated carbon, on the other hand, differs from biochar due to the addition of an activating agent/porogen to aid in the development of porosity.[25–27] This activating agent can produce porosity either through physical or chemical means. The former proceeds *via* gasification using an oxidizing gas such as CO_2, which burns away volatile matter.[26,28,29] Gasification also occurs during biomass pyrolysis as CO_2 is produced from volatile carbon moieties, as such biochar can be thought of as a form of physically activated carbon.[24–26] At sufficiently low temperatures (<900 °C), gasification produces very narrow pores of width <7 Å, referred to as ultramicropores.[5]

For chemical activation, while there is a large variety of porogens, amongst the most popular are the alkali metal hydroxides KOH and NaOH due to the fact that they facilitate a high degree of control over porosity, this being especially the case for KOH.[26] Additionally, the majority of pores generated by alkali metal hydroxides have widths typically <20 Å, *i.e.* micropores. Such pore structures are desirable for their utility in applications such as small molecule capture and storage as well as in supercapacitors.[26,30–32] In alkali metal hydroxide (MOH) activation, pores are developed *via* the oxidation of C to CO_2, which in turn leads to further gasification. Finally, residual alkali metal atoms (M) intercalate into voids between graphitic layers resulting in further micropore development.[27,33–36]

$$6MOH + 2C \rightleftharpoons 2M + 3H_2 + 2M_2CO_3$$

$$2M_2CO_3 \rightarrow M_2O + CO_2\uparrow$$

$$M_2O + C \rightarrow 4M + CO_2\uparrow$$

The use of MOH increases the overall pore volume and broadens the PSD relative to that for carbons derived in the absence of a porogen.[5,25,26] Thus so-called biochars are highly ultramicroporous, while MOH-activated carbons possess a higher degree of supermicroporosity (micropores of width >7 Å). As mentioned above, there are a variety of reasons that N_2 may be unsuitable as a probe for these smaller pores present in biochars. Therefore, given the critical importance of being able to accurately determine textural properties with respect to any targeted applications, herein we investigate the use of combinations of N_2, O_2, and H_2 isotherms and their effectiveness in assessing the porosity of biochars and activated carbons.

2. Experimental

2.1. Carbon synthesis

Carbons were synthesized with and without the use of a porogen, but keeping all other variables constant. In the case of carbons derived from sawdust, this was done by addition of KOH at the hydrothermal carbonization step. For carbons from sodium carboxymethyl cellulose the degree of substitution, *i.e.* the average number of carboxymethyl sodium groups per monomer was varied from 0.0 to 0.9.

2.1.1. *Via* hydrothermal carbonisation of sawdust. Sawdust was treated by hydrothermal carbonization at 250 and 300 °C for 2 h at a ramp rate of 5 °C min^{-1} in an aqueous solution of KOH. The concentration of sawdust was 0.32 g cm^{-3} in each experiment, whereas KOH:sawdust (w/w) was varied from 0.0, 0.5 to 1.0 at each hydrothermal carbonization temperature. This produced a total of six black slurries which were dried overnight at 100 °C in an alumina boat, and then activated by heating under nitrogen at 800 °C for 1 h (ramp rate 3 °C min^{-1}) and allowed to cool. In all cases the resultant carbons were stirred in HCl (10% v/v, 600 cm^3) thoroughly prior to filtration and washing in water (∼5 L) to remove any chloride salts, until washings were neutral (pH 7). Finally, samples were dried at 100 °C, yielding six carbons designated SA*x*-*T*, where *x* indicates KOH : sawdust ratio and *T* is the hydrothermal carbonization temperature.

2.1.2. From Sodium carboxymethyl cellulose. Sodium carboxymethyl cellulose (Sigma) with a degree of substitution of 0.0, 0.7, and 0.9 (the first being pure cellulose) was heated under nitrogen to 800 °C for 1 h (ramp rate 3 °C min^{-1}) then cooled, washed, and dried in the same manner as the SA*x*-*T* samples. This yielded three samples designated NC*x* where *x* indicates the degree of substitution.

2.2. Characterisation

CHN Elemental analysis of the raw sawdust precursor was performed using an Exeter Analytical CE-440 Elemental Analyser. O content is assumed to be the remaining percentage when

© 2022 The Author(s). Published by the Royal Society of Chemistry

Open Access Article. Published on 30 March 2022. Downloaded on 11/1/2022 11:56:41 AM.
This article is licensed under a Creative Commons Attribution 3.0 Unported Licence.

C, H, and N are accounted for, as other elements do not occur in significant quantities.

Thermogravimetric analysis was performed using a TA Q500 Thermogravimetric Analyser, in order to determine if any residual metals remained in the carbon samples (see Table S1, ESI†). All samples were analysed using a platinum pan and in the presence of air/argon. The parameters for all experiments were: Ramp 10 °C minute^{-1} from 20–1000 °C with an isotherm for 10 minutes at 1000 °C, gas flow: 60 mL minute^{-1}.

H_2, O_2 and N_2 isotherms were measured at −196 °C using a Micromeritics 3flex sorptometer. In the case of O_2 and N_2 isotherms were measured up to P_o (~220 and 1013 mbar, respectively), which is measured as each equilibrated point in the isotherm is recorded to account for small variations in temperature. However for H_2 the isotherm P_o is taken as a constant of 1013 mbar for convenience because H_2 is supercritical at −196 °C. All samples were degassed at 300 °C for 16 h prior to isotherm measurement. Porosity calculations were performed *via* the dual-fitting of 2D-NLDFT heterogeneous surface kernels on either O_2 and H_2 or N_2 and H_2 isotherms using SAIEUS software.[16,37] While 2D-NLDFT kernels account for surface roughness *via* the use of a corrugated slit-pore model,[16] network connectivity is accounted for by the use of two differently sized probe molecules.[15] All dual-fit calculations were performed using an overall pore width minimum of 3.00 Å, a minimum for the O_2 or N_2 kernel of 3.60 Å and the pore width maximum was set at 500.00 Å. For consistency the fitting parameter, λ[38–40] is fixed at 4. For comparison, conventional determinations of pore volume (*via t*-plot) were obtained from N_2 isotherms alone. Raw isotherms are available as human- and machine-readable AIF files in the SI.[41]

2.2.1. Equilibration interval and rate of change. The instrument operation software allows for designation of a so-called equilibration interval, t_E, as a parameter for the isotherm. This is used in order to estimate when equilibration of the adsorption system has occurred. In the measurement of a single point on the isotherm, the pressure is measured at intervals of t_E and a rate of change in pressure, R, is determined over the case of ten intervals. For example, for a t_E of 10 s, pressure will be measured ten times over 100 s and R is calculated over this period. When $R < 0.010\%$, the system is considered to be at equilibrium and the isothermal point, $V(P/P_o)$ is determined. As such, t_E can be decreased in order to speed up analysis but this risks reducing precision of measurement, *i.e.* the system is less likely to actually be at equilibrium when the isothermal point is recorded.

3. Results and discussion

3.1. Diffusion of adsorptives

During the measurement of isotherms, it became obvious that the duration of measurement of N_2 isotherms on the SA0.0-*T* and NC0.0 (biochar) samples was impractical. Using the initial t_E of 45 s for P/P_o up to 10^{-3}, only one or two points were achieved after >72 h. To avoid this problem, t_E were iteratively reduced to 15 s for determination of N_2 isotherms on SA0.0-*T*. Even with this modification, overall analysis time was up to 50 h; twice the time taken for a similarly determined O_2 isotherm. This implies that the pore structure of biochars is such that N_2 has difficulty diffusing into the smallest pores, possibly indicating that the pore width is similar to the kinetic diameter of the adsorptive. Alternatively, this may be a result of the interaction between polar moieties outside of the ultramicropores and N_2's quadrupole moment. The attraction between N_2 and such moieties may be competitive with N_2's diffusion into ultramicropores. The less activated materials are also likely to have a higher oxygen content and thus more polar functional groups, meaning it is difficult to distinguish which of these phenomena is creating this effect. However, similarly slow diffusion of N_2 has been observed for ultramicroporous CMPs with no polar groups.[7] Regardless, the poor diffusion onto the biochar/less activated samples calls into question the accuracy of textural parameters derived from N_2 isotherms.

This discrepancy is most evident when comparing the time taken between isothermal points, t, as shown in Fig. 1a. While t is broadly similar for O_2 and N_2 isotherms of SA1.0-250 as well the O_2 isotherm of SA0.0-250, t is much higher in the low relative pressure region for the N_2 isotherm of SA0.0-250, with a

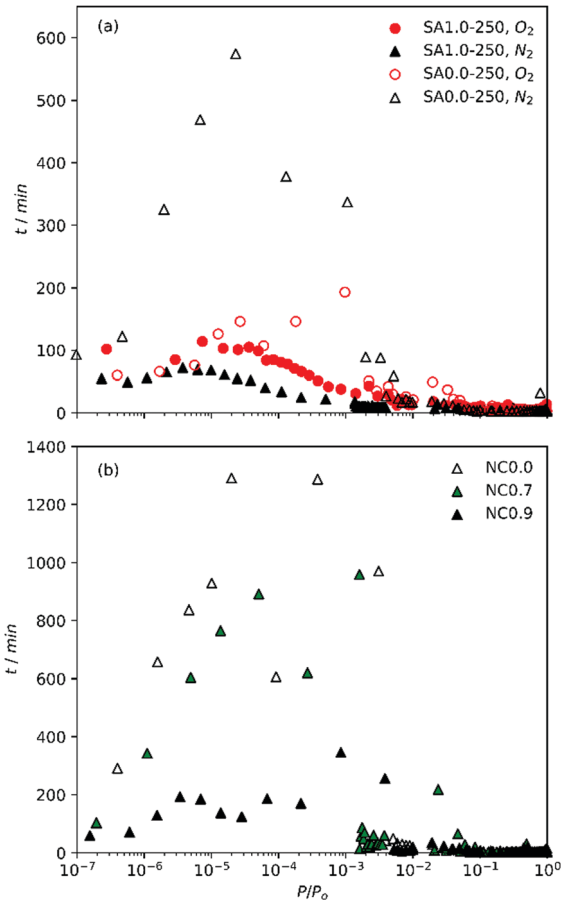

Fig. 1 Time between points with increasing relative pressure of (a) O_2 and N_2 isotherms on SA1.0-250 and SA0.0-250 and (b) N_2 isotherms of NCx carbons.

Open Access Article. Published on 30 March 2022. Downloaded on 11/1/2022 11:56:41 AM.
This article is licensed under a Creative Commons Attribution 3.0 Unported Licence.

single point taking up to 10 h to measure. This suggests that the slow diffusion may be related to compatibility of N_2 with some feature of the biochar's porosity. Similarly, when comparing the time taken between points for the NC*x* samples synthesized with increasing amounts of Na within the cellulosic structure (Fig. 1b) it is apparent that expansion of the porosity by use of a porogen improves the ability of N_2 to diffuse into the pores, and that this improvement is accelerated at some point between a degree of substitution of 0.7 and 0.9. That is, while NC0.7 allows faster diffusion than NC0.0, the improvement is only small but there is a far more marked change in *t* when *x* rises to 0.9. Indeed, while *t* can be extremely large (approaching 24 h) for NC0.0 and NC0.7, the maximum *t* for NC0.9 is closer ($\sim$6 h) to that for the activated carbons derived from sawdust. Our observations of the lengthy measurement of N_2 isotherms relative to O_2 are counter to work recently published by Beda *et al.*, wherein measurement of N_2 isotherms on so-called hard-carbons was fast relative to O_2.[18]

This may be an indication of relative pore sizes *i.e.* that ultramicropores in biochars reported in this work are partially penetrable by N_2, unlike those in hard carbons reported by Beda *et al.*

Table 2 shows the atomic ratios of porogen to carbon. As the principle pore development process in activated carbons begins with oxidation of carbon by the porogen, pore broadening therefore increases with increased porogen/C ratio. These ratios are much lower in the NC*x* samples than for SA*x*-*T*. While variables such as precursor structure and composition as well as differences in reaction kinetics of Na *vs.* K also play a factor,[33–35] it is also clear that the higher amounts of K used in the synthesis of SA*x*-*T* samples results in porosity that is much more amenable to N_2 diffusion into the pores.

Gravimetric yields of samples described in this work can be found in Table S1 (ESI†). In general, yield decreases with increasing amount of activating agent. The yield of SA0.0-300 is much higher (26%) than that of SA0.0-250 (15%). This is likely a result of greater stability of hydrochar synthesised at 300 °C on account of the lower amounts of oxygen rich-moieties.[42]

3.2. The isotherms

Inspection of isotherms further reveals some uncertainty in the accuracy of N_2 measurements on SA0.0-*T* carbons (see Fig. S1, ESI†). While a characteristic plateau exists for N_2 isotherms of SA0.5-*T* (Fig. S1(2a, b), ESI†) and SA1.0-*T* (Fig. S1(3a, b), ESI†) samples, indicating micropore filling, this is not the case for SA0.0-*T* samples (Fig. S1(1a, b), ESI†), where there is a linear increase in adsorption in the mesopore region. This is not observed in O_2 isotherms, wherein monolayer completion is much more obvious. All samples also have a high H_2 uptake indicating the presence of pores in the so-called ultramicropore region, which may hinder adsorption of N_2.

Furthermore, isotherms for NC*x* carbons (Fig. S2, ESI†) lend further credence to the notion that significant pore broadening does not occur until a critical ratio of porogen/C (in the range 0.09–0.12) is achieved. For both NC0.0 (Fig. S2(a), ESI†) and NC0.7 (Fig. S2(b), ESI†), the maximum H_2 adsorption is similar to or greater than that of N_2, indicating the presence of a high proportion of ultramicropores. For NC*x* samples where porogen/C ratio is increased to 0.12 (NC0.9), H_2 adsorption falls significantly below the maximum for N_2, indicating that porosity has broadened into the supermicropore region. Samples NC0.7 and NC0.9 also exhibit a rapid increase in adsorption for O_2 and N_2 as P/P_o approaches 1 such that the resulting isotherms exhibit some type II character. Such shape is likely a morphological effect, either due to condensation of sorptive in macropores or large interparticle voids.[1] As the materials contain no non-carbonaceous matter (within experimental error, see Table S1, ESI†) this cannot be ascribed to some chemical effect. Type II character is not observed for NC0.0, thus it can be assumed that the morphological phenomenon is a result of some action of Na^+.

In the case of both NC0.0 and SA0.0-300 (Fig. S1(1b), ESI†), the H_2 isotherm actually crosses the N_2 isotherm which is anomalous since under the conditions used H_2 is supercritical, meaning that multilayer adsorption cannot occur. As such this high level of adsorption must be due to monolayer adsorption of H_2 in pores impenetrable to N_2. Such pores however do appear to be penetrable by O_2, which is interesting as while O_2 is slightly smaller than N_2 the kinetic diameters of the two molecules are quite similar – 3.46 and 3.64 Å for O_2 and N_2 respectively.[20,21]

3.3. Dual-fit analysis

Dual fits to O_2/H_2 and N_2/H_2 isotherms for SA*x*-*T* and NC*x* carbons are shown in Fig. S3 and S4 (ESI†), respectively. As indicated from the isotherms themselves, PSDs for SA*x*-*T* carbons (Fig. 2(1P, 2P), S5(1P, 2P), ESI†) derived using O_2/H_2 isotherms indicate greater porosity than when using N_2/H_2, and the same is true for PSDs of NC*x* carbons (Fig. 3(1P, 2P)). The position of the first maximum ($\sim$4 Å) is consistent across all derived PSDs regardless of the subset of isotherms is used as this is mainly derived from the H_2 isotherm. However, with regards to the second maximum, the two sets of PSDs for both SA*x*-*T* and NC*x* offer slightly different pictures. While N_2/H_2 derived PSDs show either only small differences or indeed a small decrease in pore size for the activated carbons, O_2/H_2 PSDs show that porosity expands out of the ultramicropore and into the supermicropore region when KOH is used as porogen. Furthermore, there is some indication of PSD broadening in the second maximum. The latter narrative fits much better with

Table 2 Atomic ratios of components in precursors, determined from molecular compositions for NCx samples and from weight ratios and elemental (CHN) analysis in the case of SA*x* samples

Sample	Porogen/C	Porogen/O	O/C
NC0.0	0.00	0.00	0.83
NC0.7	0.09	0.11	0.86
NC0.9	0.12	0.13	0.87
SA0.0	0.00	0.00	0.72
SA0.5	0.21	0.72	0.72
SA1.0	0.43	1.45	0.72

© 2022 The Author(s). Published by the Royal Society of Chemistry

Open Access Article. Published on 30 March 2022. Downloaded on 11/1/2022 11:56:41 AM.
This article is licensed under a Creative Commons Attribution 3.0 Unported Licence.

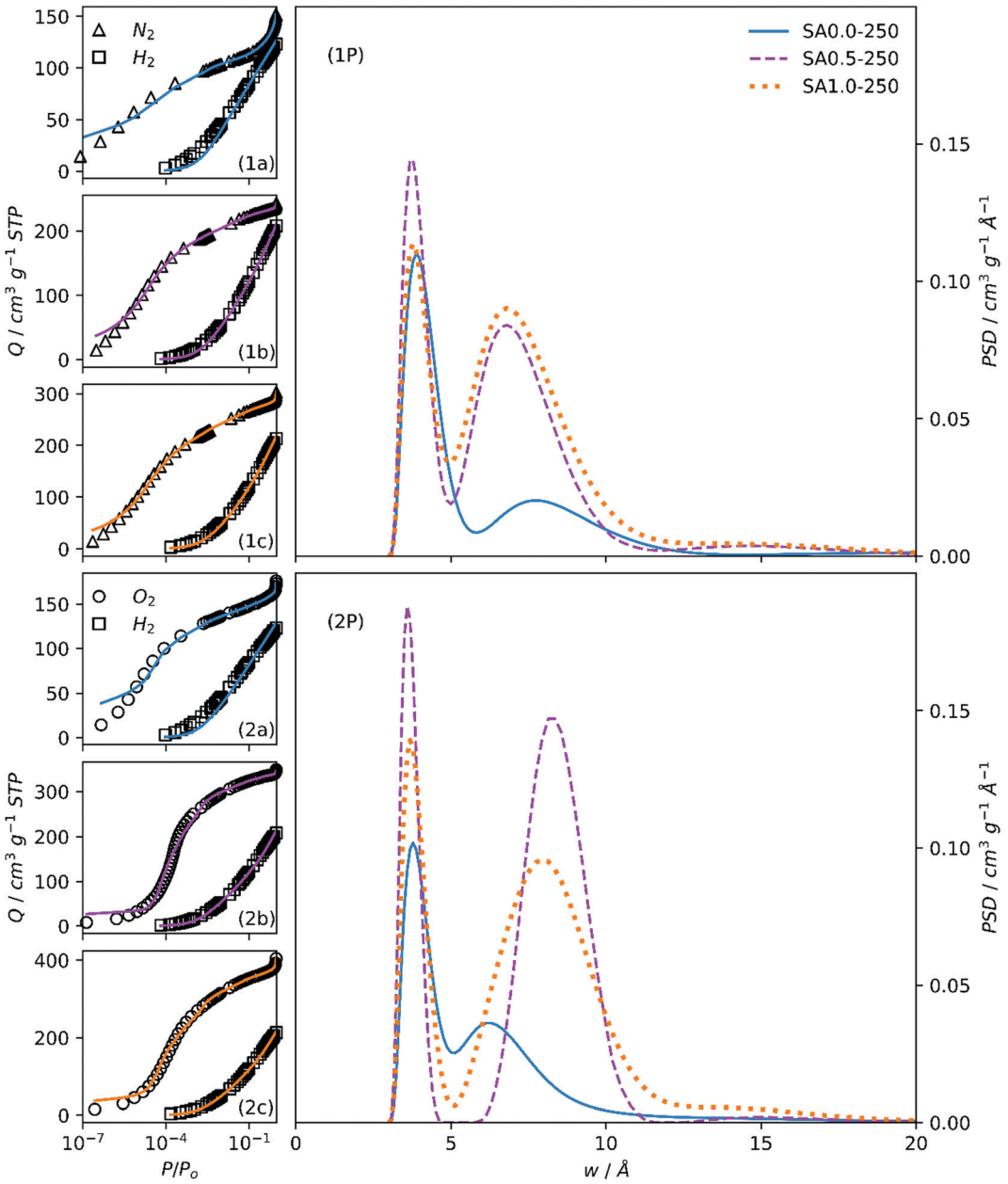

Fig. 2 Fits to N_2/H_2 (1a, 1b, 1c) and O_2/H_2 (2a, 2b, 2c) isotherms of samples SAx-250 and resultant PSDs (1P, 2P).

current understanding of pore formation in carbons, in that the use of alkali metal hydroxide porogens during pyrolysis leads to increases in pore size relative to those formed *via* gasification of biomass (*i.e.*, pyrolysis with no added porogen). Again, this discrepancy in trends in pore size with amount of porogen according to simultaneous fitting of kernels the two isotherm pairs is likely a failing of the N_2 isotherm in that ultramicropores are not adequately probed during analysis.

While results from dual O_2/H_2 fitting to their respective 2D-NLDFT kernels indicate greater compliance with current understanding of porosity development in carbons, this does not alone confirm its superiority over N_2/H_2 for this application. On examining the fits, it is obvious that the respective 2D-NLDFT kernels struggle to account for the isotherm shape at low pressures in the case of both O_2 and N_2. This is particularly evident for the SA0.0-*T* samples, suggesting either incomplete equilibration of the system at such low pressures or inability of the O_2 and N_2 kernels to account for ultramicropore geometry and internal texture of in biochars, or a combination of both limitations.

O_2/H_2 analysis also gives far more information on differences in porosity between SA0.5-*T* and SA1.0-*T* samples. While the PSD calculated *via* N_2/H_2 indicates that the porosity of these two activated carbons is practically identical except for a slight increase in overall pore volume, O_2/H_2 analysis, on the other hand, shows a broadening in the second maxima, which results

Open Access Article. Published on 30 March 2022. Downloaded on 11/1/2022 11:56:41 AM.
This article is licensed under a Creative Commons Attribution 3.0 Unported Licence.

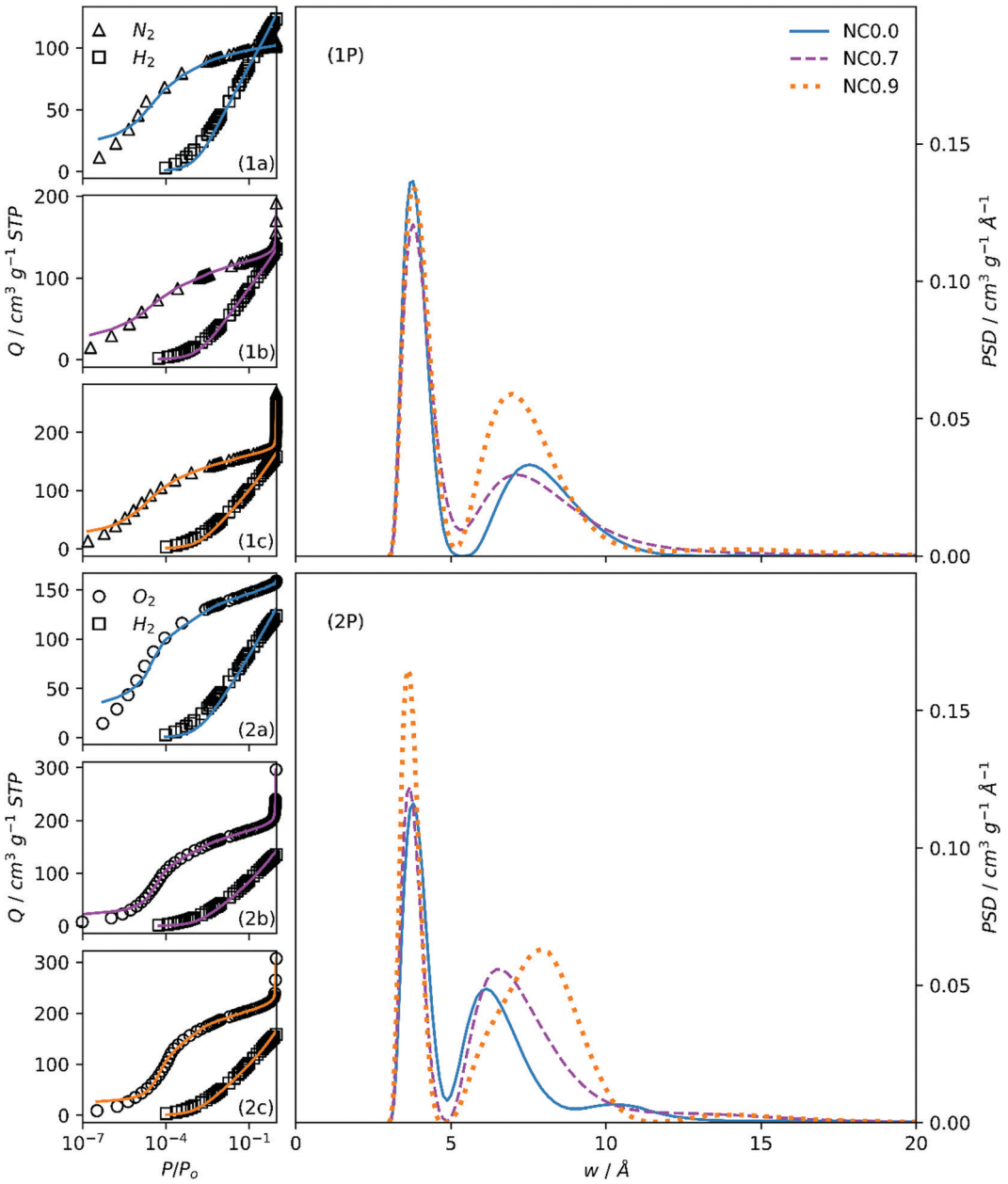

Fig. 3 Fits to N_2/H_2 (1a, 1b, 1c) and O_2/H_2 (2a, 2b, 2c) isotherms of samples NCx and resultant PSDs (1P, 2P).

in the obfuscation of the two, initially distinct pore regions. A mechanistic explanation for this is that in the case of SA0.5-*T*, the principal route of porosity expansion comes *via* the formation of new pores by simple oxidation of as yet non-porous carbon, resulting in pores centred at *ca.* 8 Å but without significantly disturbing the ultramicropores previously formed by carbon gasification. Due to the relative increase in the quantity of K in the synthesis of SA1.0-*T*, the cation is able to infiltrate ultramicropores and *via* this intercalation expands them, resulting in the merging of the two previously distinct pore size regions.

The variation in porogen/C ratio for SA*x*-*T* carbons with increasing *x* is relatively large. Comparing PSDs of NC*x* carbons (Fig. 3(1P, 2P)) facilitates the observation of changes in porosity when the changes in porogen/C ratio are relatively small (see Table 2). Unsurprisingly, the N_2/H_2 calculations again show little difference between each of the three samples apart from an indication of higher overall pore volume for NC0.9.

On the other hand, there is a gradual migration of the second PSD maxima into the supermicropore region as porogen/C is increased, accompanied by a broadening of this peak. This again is a result of the oxidative effect of the (Na^+) cation leading to PSD broadening. While the maximum O_2 adsorption for NC0.9 and NC0.7 carbons is almost twice that of NC0.0, this is not indicated in the PSDs in the range displayed. This is because the increased porosity that causes this feature is in the macropore region.[1]

© 2022 The Author(s). Published by the Royal Society of Chemistry

Open Access Article. Published on 30 March 2022. Downloaded on 11/1/2022 11:56:41 AM.
This article is licensed under a Creative Commons Attribution 3.0 Unported Licence.

Table 3 Total (V_t), micropore (V_{mic}), and ultramicropore (V_{umic}) pore volumes of SAx-T and NCx carbons determined using classical and dual-isotherm NLDFT calculations. Classical volumes determined using the single-point and t-plot methods for V_t and V_{mic}, respectively. NLDFT calculations employed dual-fitting of isotherms to respective 2D-NLDFT, heterogeneous surface kernels. Numbers in brackets indicate percentage of pore volume made up by pores in the given pore width subregion

	Pore volume/cm^3 g^{-1}							
	N_2 classical		Dual N_2/H_2 NLDFT			Dual O_2/H_2 NLDFT		
Sample	V_t	V_{mic}	V_t	V_{mic}	V_{umic}	V_t	V_{mic}	V_{umic}
SA0.0-250	0.25	0.13 (50%)	0.29	0.22 (78%)	0.16 (54%)	0.26	0.23 (90%)	0.18 (68%)
SA0.0-300	0.17	0.10 (57%)	0.25	0.20 (79%)	0.14 (56%)	0.24	0.22 (90%)	0.17 (67%)
SA0.5-250	0.37	0.32 (87%)	0.44	0.42 (97%)	0.26 (60%)	0.50	0.49 (98%)	0.15 (30%)
SA0.5-300	0.44	0.38 (85%)	0.50	0.47 (95%)	0.29 (58%)	0.53	0.48 (91%)	0.21 (39%)
SA1.0-250	0.45	0.37 (83%)	0.51	0.47 (92%)	0.26 (52%)	0.54	0.50 (92%)	0.20 (37%)
SA1.0-300	0.54	0.44 (81%)	0.63	0.58 (92%)	0.32 (50%)	0.70	0.63 (89%)	0.29 (41%)
NC0.0	0.16	0.14 (90%)	0.23	0.22 (99%)	0.15 (65%)	0.22	0.21 (95%)	0.16 (76%)
NC0.7	0.21	0.16 (77%)	0.35	0.25 (70%)	0.16 (47%)	0.38	0.24 (65%)	0.14 (58%)
NC0.9	0.28	0.22 (80%)	0.45	0.31 (69%)	0.20 (44%)	0.40	0.28 (71%)	0.13 (44%)

These inconsistencies in porosity development according to the two dual isotherm methods are further illustrated by the calculated total pore volumes, as well as the pore volume arising from micropores and ultramicropores (Table 3). Classical calculations from N_2 isotherms alone reveal much smaller overall pore volumes for all samples as well as lower proportions of micropores compared to their dual-fit 2D-NLDFT counterparts for NCx and SAx-T carbons. This is because, firstly N_2 alone cannot probe the smallest of ultramicropores,[4,5] thus up to 32% of total pore volume (relative to N_2/H_2 analysis) is unaccounted for. Secondly, single point and t-plot calculations do not account for chemical and energetic heterogeneity of the internal pore surface unlike the 2D-NLDFT models.[16] Additionally, determination of total- and micropore volume by classical methods is notoriously unreliable. For example, the single-point pore volume determination relies on the isotherm possessing an obvious plateau.[1] As discussed above, these plateaus do not strictly exist for the N_2 isotherms of the SA0.0-T samples. As such, significant errors may arise using single-point methods.

On the other hand, the dual O_2/H_2 fit predicts a much higher proportion of both micropores and ultramicropores than N_2/H_2 for SA0.0-T carbons. Again, this is likely a result of poor diffusion of N_2 into ultramicropores, which limits their detection. For the so-called activated carbon samples, N_2/H_2 shows roughly similar proportions of ultramicroporosity compared to the aforementioned biochars, while O_2/H_2 shows drastic decreases. The latter picture from O_2/H_2 seems more likely due to known mechanisms of porosity development by KOH. Interestingly, estimates of percent microporosity are fairly consistent for calculations of both sets of isotherms for SA0.5-T and SA1.0-T samples indicating that N_2 diffusion limitations are not so prevalent in supermicropores.

For NCx carbons, both overall pore volumes and absolute and percentage micropore volumes are relatively consistent across the two dual isotherm techniques. The most significant difference is in the absolute and percentage micropore volume, especially for samples NC0.0 and NC0.7. This again is an indication of the diffusion limitations encountered during measurement of N_2 isotherms on these samples. While this difference in percent ultramicropore volume is 11% for these two samples, NC0.9 shows identical proportions of ultramicropores for both methods. In fact, the percentage of *micropores*, is the most similar here too – within 2%. While the broadening of the PSD with increasing porogen/C ratio from principally ultramicroporous into the supermicropore and larger regions is evident when using both techniques, this is far more obvious according to analysis of O_2/H_2 isotherms.

Interestingly, all three measures of porosity agree on one matter – that is, when comparing the relative contribution of the different pore width regions between SAx-T samples with the same KOH : SD ratio (x), but varying hydrothermal carbonization temperature (T). The hydrothermal carbonization temperature does not seem to affect what percentage of pores are made up by micropores and ultramicropores. However, *total* pore volumes do vary with T; in the case of the activated carbons SA0.5-T and SA1.0-T, hydrothermal carbonization at 300 °C can increase V_t by up to 30% at KOH:SD ratio 1.0 according to O_2/H_2 NLDFT calculations. The apparent difference decreases when classical techniques are used, and in the case of SA0.5-T, dual O_2/H_2 analysis shows an increase in V_t of only 6% as T increases from 250 to 300 °C. The two dual isotherm 2D-NLDFT analyses nonetheless tend to show similar differences in V_t, so perhaps this discrepancy is a result of the relative robustness of DFT methods. On the other hand, the biochars show the opposite trend, with V_t decreasing when T is raised to 300 °C. This is only by a small amount (7–14%) compared to the value derived from dual isotherm calculations, but it is evident nevertheless. This decrease in porosity of biochars with hydrothermal carbonization temperature is likely a result of a correlated decreased O/C content in the hydrochar, as well as an increase in the diameter of the characteristic microspheres.[42] The latter phenomenon means that there is an increase in the proportion of stable hydrophobic aromatic moieties (in the core) relative to the more easily activated hydrophilic groups in the shell of the hydrochar microspheres. This compositional change is known to increase so-called activation resistance and therefore can result in a less porous

Open Access Article. Published on 30 March 2022. Downloaded on 11/1/2022 11:56:41 AM.
This article is licensed under a Creative Commons Attribution 3.0 Unported Licence.

carbon upon pyrolysis.[43–45] Additionally, when KOH is included during hydrothermal carbonization it catalyses the breakdown of the activation-resistant lignin[45–47] which may further explain the improvements in porosity for T = 300 °C.

3.3.1. Comparison to single fit. When PSDs are derived from two isotherms simultaneously, the SAIEUS software accounts for pore regions that are apparent in both isotherms. As an example, consider an adsorptive A which probes pores between 3 and 7 Å while adsorptive B can probe pores larger than 5 Å. For a sample which has some pores of width ~5–7 Å, SAIEUS will not simply add the PSDs from A and B within the full range of widths, but instead takes into account this overlap.

It is interesting therefore to compare PSDs derived through single and dual fits to isotherms as in Fig. 4. Further, the agreement between single and dual fits is interesting in terms of the degree to which a sample is activated, as such a low activation sample (SA0.0-250, Fig. 4(1a–c)) and highly activated sample (SA1.0-250, Fig. 4(2a–c)) were investigated. Single fit PSDs were calculated using identical parameters to those used in dual fitting, except that the maximum pore width for H_2 was limited to 10 Å. Of the three individually fit adsorptives, only H_2 produces a bimodal PSD similar to that found in dual fits, while N_2 and O_2 both show a single maximum at or above 7 Å. It appears that the position of the first maximum for H_2 (~4 Å) corresponds almost exactly in all cases to that found in dual isotherm PSDs. On the other hand, the shape and position of the second maximum (>5 Å) appears to be some combination of the two single-isotherm PSDs. This is most apparent in the case of SA0.0-250 (Fig. 4(1b, 1c)). Conversely in the case of SA1.0-250 (Fig. 4(2b, 2c)) the position and shape of the second maximum in the dual fit is approximately the same that of the sole N_2 or O_2 peak. These observations suggest that as PSD broadens with increasing degree of activation the fitting algorithm is able to rely more on individual isotherms for different sections of the PSD, *i.e.* H_2 for pores 3–7 Å, N_2 or O_2 for pores >7Å. Whereas for so-called biochar samples, as the second maximum is lower than 7 Å

3.4. Three-way fit analysis

In order to further understand discrepancies between O_2/H_2 and N_2/H_2 analyses, the 2D-NLDFT heterogeneous surface kernels were simultaneously fit to all three (O_2, N_2, H_2) isotherms for some samples. In particular, the aim here is to compare the quality of fit according to the degree of activation in each sample. The fits and PSDs achieved by this method are compared for SA0.0-300 and SA1.0-300 in Fig. 5. When the fits are examined using a logarithmic relative pressure axis (Fig. 5(1b, 2b)), it is very apparent that the fit is extremely poor for SA0.0-300, particularly in the low pressure region. While individual O_2/H_2 and N_2/H_2 analyses for SA0.0-300 had trouble with isothermal points below $P/P_o = 10^{-4}$ (see Fig. S3(1b, 2b), ESI†) this low quality of fit is very pronounced for the three-way fit in the entire low pressure, (*i.e.* micropore) region of the isotherm.

On the other hand, the three-way fit for SA1.0-300 is much more satisfactory. It is also of note that for both of these samples the fit to the H_2 isotherm is always good, indicating that the uncertainties are a result of disagreements between the N_2 and O_2 isotherms rather than H_2. As for the PSDs, while peak positions for SA1.0-300 are essentially the same as those seen in

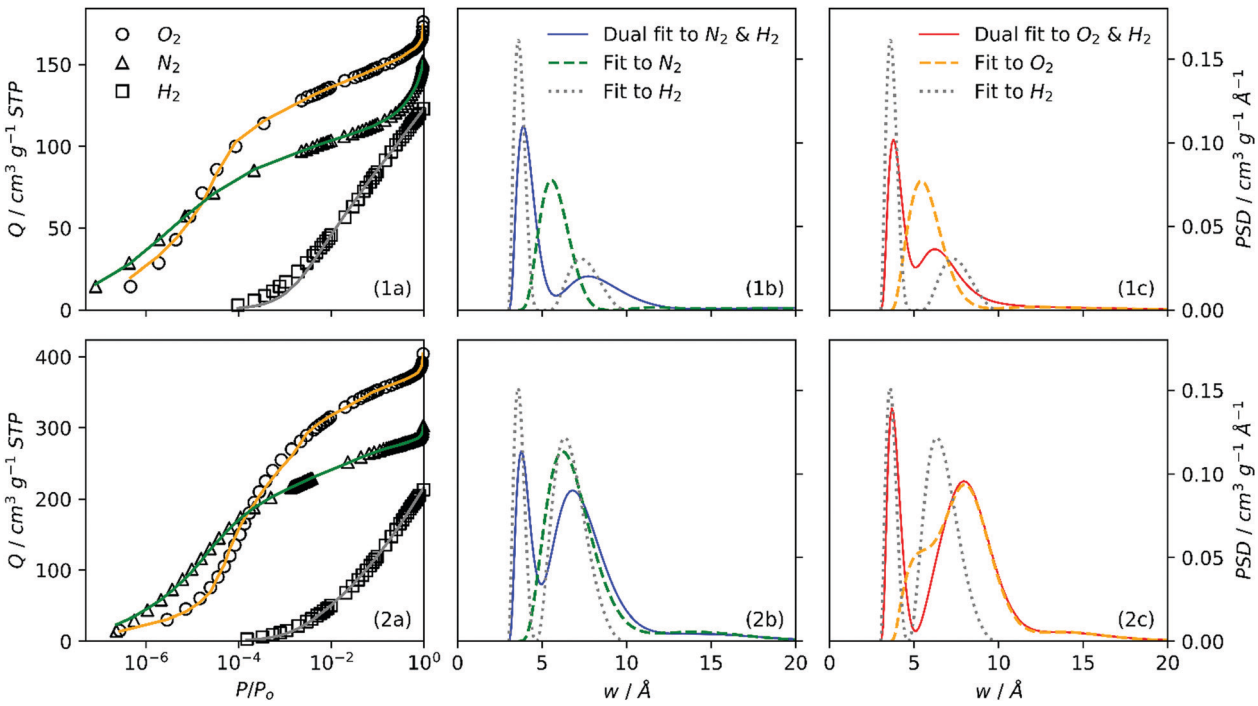

Fig. 4 Individual fits to O_2, N_2 and H_2 isotherms for SA0.0-250 (1a) and SA1.0-250 (1b) and resultant PSDs from individual N_2 and H_2 (1b, 2b), and O_2 and H_2 (1c, 2c) isotherms. Corresponding dual fits overlaid for comparison (1b, 1c, 2b, 2c).

© 2022 The Author(s). Published by the Royal Society of Chemistry

Open Access Article. Published on 30 March 2022. Downloaded on 11/1/2022 11:56:41 AM.
This article is licensed under a Creative Commons Attribution 3.0 Unported Licence.

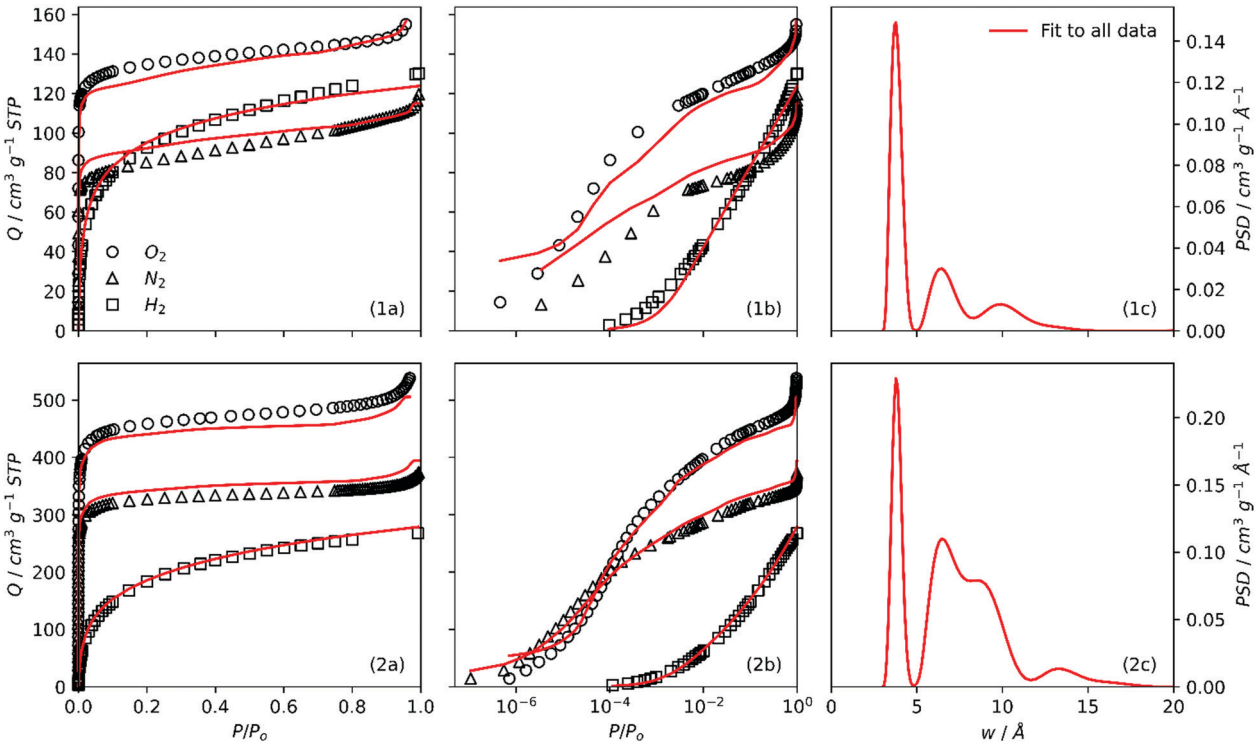

Fig. 5 Simultaneous fit of O_2, N_2, and H_2 isotherms of SA0.0-300 (1a, 1b) and SA1.0-300 (2a, 2b) using *x*-axis in linear (1a, 2a) and logarithmic (1b, 2b) scales, as well as PSDs determined from the three-way fit (1c, 2c). Fits determined using same same parameters as in dual fits, *i.e.* identical upper and lower pore limits, and $\lambda = 4$.

either of the dual isotherm analyses (Fig. S3(1f, 2f), ESI†) the same is not apparent for SA0.0-300.

To summarise, while there is consistency between O_2 and N_2 fits for more highly activated samples, this is not true for less-activated, so-called biochar samples. In other words when probing ultramicropores, O_2 and N_2 produce different PSD results, which can be attributed to the poor diffusion of N_2 into smaller pores. As porosity broadens into the supermicropore region, pores can accurately be measured by either adsorptive.

4. Conclusions

This study compares porosity in biochars and carbons activated using alkali metals as determined by two methods of dual isotherm analysis, namely using the adsorptive pairs N_2/H_2 and O_2/H_2. In particular, the reliability of using N_2 in such analyses is called into question due to evident diffusion limitations in carbon samples with a low degree of activation (biochars) or where the smallest pores (ultramicropores) are prevalent. As these diffusion limitations are not present for carbons activated to a higher degree using Na^+ or KOH, we conclude that the problems are associated with the size of pores found in biochars. Indeed, when using O_2 (which penetrates these pores with much less difficulty) PSDs derived using the dual isotherm 2D-NLDFT method are centred at widths below 7 Å, *i.e.* in the ultramicropore region. Theoretically, improved ultramicropore penetration by N_2 could be achieved either by allowing the system to equilibrate for longer times at low pressure, or by measuring the isotherm at a higher temperature. These modifications would however be impractical as in the first case the duration of isotherm measurements would be excessive. As for increasing temperature, this would require use of a different cryogen and/or higher pressures for 'total' isotherm measurement. This proves impractical on current, standard porosimetric sorptometers while the use of O_2 and H_2 requires the trivial task of attaching an additional cylinder to the sorptometer.

Furthermore, using O_2 and H_2 gives a more realistic picture of porosity development with increasing degree of oxidative chemical activation as carbons are activated with an increasing amount of porogen. That is, as the ratio of porogen/C is increased we consistently observe a broadening in the PSD for samples derived both from sodium carboxymethyl cellulose and sawdust. This is in contrast to results derived using N_2 and H_2 wherein despite increases in overall porosity with increasing porogen/C ratio, there is little change in the widths of pores at higher levels of activation. Indeed, for some sample sets a contraction in pore width is observed as the amount of activating agent is increased. The narrative given by PSDs derived using N_2 and H_2 cannot be accounted for by current understanding of mechanisms of porosity development during oxidative chemical activation. The subtle effects of increasing

© 2022 The Author(s). Published by the Royal Society of Chemistry

Open Access Article. Published on 30 March 2022. Downloaded on 11/1/2022 11:56:41 AM.
This article is licensed under a Creative Commons Attribution 3.0 Unported Licence.

amounts of porogen on the fine pore structure of these carbons is only detectable by the highly sensitive methods used in this work. Such sensitivity means that it is paramount to select the appropriate adsorptives for the material.

Finally, attempts at fitting the 2D-NLDFT heterogeneous surface kernels simultaneously to all three isotherms gives very poor fits to the O_2 and N_2 isotherms for biochars. In theory, due to the similar size of these adsorptives, fitting these two isotherms together should be facile. This lends further credence to the notion that there is in fact an inconsistency in the porosity which is probed by these two adsorptives. As these problems are not present for more highly activated samples, it is clear that above a certain pore width, O_2 and N_2 are equally able to probe the porosity of such carbons. In other words O_2 penetrates pores in the ultramicropore region to a much greater extent.

Thus, we suggest that for carbons with a low degree of activation, N_2 is an inadequate probing gas for determination of porosity as it does not adequately probe ultramicropores. When determining PSDs and other textural quantities for such carbons it is therefore advisable to look to non-traditional adsorptives such as O_2. This logic should also be extended to the use of adsorptives when attempting to understand the development of porosity in carbons as the amount of activating agent is increased. Further, the understanding of porosity in non-carbonaceous ultramicroporous materials (such as CMPs) or carbonaceous materials with richer surface functionality may benefit from a similar analysis.

Author contributions

L. Scott Blankenship: conceptualisation, methodology, formal analysis, investigation, writing – original draft, visualization. Jacek Jagiello: methodology, software, validation, formal analysis, writing – review & editing. Robert Mokaya: resources, writing – review & editing, supervision, funding acquisition.

Conflicts of interest

The authors declare that they have no known competing financial interests or personal relationships that could have appeared to influence the work reported in this paper.

Acknowledgements

We are thankful to the EPSRC (Low-Dimensional Materials & Interfaces DTP) for a studentship for LSB. RM thanks the Royal Society for a Royal Society Wolfson Research Merit Award.

Notes and references

1 M. Thommes, K. Kaneko, A. V. Neimark, J. P. Olivier, F. Rodriguez-Reinoso, J. Rouquerol and K. S. Sing, *Pure Appl. Chem.*, 2015, **87**, 1051–1069.
2 J. Jagiello, J. Kenvin, C. O. Ania, J. B. Parra, A. Celzard and V. Fierro, *Carbon*, 2020, **160**, 164–175.
3 J. Jagiello and M. Thommes, *Carbon*, 2004, **42**, 1227–1232.
4 J. Jagiello, C. Ania, J. B. Parra and C. Cook, *Carbon*, 2015, **91**, 330–337.
5 J. Jagiello, J. Kenvin, A. Celzard and V. Fierro, *Carbon*, 2019, **144**, 206–215.
6 F. Rodriguez-Reinoso, J. de, D. Lopez-Gonzalez and C. Berenguer, *Carbon*, 1982, **20**, 513–518.
7 L. Qin, G.-j. Xu, C. Yao and Y.-h. Xu, *Chem. Commun.*, 2016, **52**, 12602–12605.
8 J. Garrido, A. Linares-Solano, J. Martin-Martinez, M. Molina-Sabio, F. Rodriguez-Reinoso and R. Torregrosa, *Langmuir*, 1987, **3**, 76–81.
9 A. L. McClellan and H. F. Harnsberger, *J. Colloid Interface Sci.*, 1967, **23**, 577–599.
10 A. D. Lueking, H.-Y. Kim, J. Jagiello, K. Bancroft, J. K. Johnson and M. W. Cole, *J. Low Temp. Phys.*, 2009, **157**, 410–428.
11 J. Jagiello and W. Betz, *Microporous Mesoporous Mater.*, 2008, **108**, 117–122.
12 M. Konstantakou, A. Gotzias, M. Kainourgiakis, A. K. Stubos and T. A. Steriotis, in *Applications of Monte Carlo Method in Science and Engineering*, ed. S. Mordechai, IntechOpen, 2011.
13 A. D. Buckingham, R. L. Disch and D. A. Dunmur, *J. Am. Chem. Soc.*, 1968, **90**, 3104–3107.
14 C. Nguyen and D. D. Do, *J. Phys. Chem. B*, 1999, **103**, 6900–6908.
15 M. Lopez-Ramon, J. Jagiełło, T. Bandosz and N. Seaton, *Langmuir*, 1997, **13**, 4435–4445.
16 J. Jagiello and J. P. Olivier, *Carbon*, 2013, **55**, 70–80.
17 J. Guo, J. R. Morris, Y. Ihm, C. I. Contescu, N. C. Gallego, G. Duscher, S. J. Pennycook and M. F. Chisholm, *Small*, 2012, **8**, 3283–3288.
18 A. Beda, C. Vaulot and C. M. Ghimbeu, *J. Mater. Chem. A*, 2021, **9**, 937–943.
19 M. Seredych, J. Jagiello and T. J. Bandosz, *Carbon*, 2014, **74**, 207–217.
20 D. Lide, *Handbook of Chemistry and Physics*, CRC Press, 88th edn, 2017.
21 D. W. Breck, *Zeolite molecular sieves*, Wiley, New York, 1974.
22 B. E. Poling, J. M. Prausnitz and J. P. O'connell, *Properties of gases and liquids*, McGraw-Hill Education, 2001.
23 C. Graham, D. A. Imrie and R. E. Raab, *Mol. Phys.*, 1998, **93**, 49–56.
24 K. Weber and P. Quicker, *Fuel*, 2018, **217**, 240–261.
25 A. Downie, A. Crosky and P. Munroe, in *Biochar for Environmental Management: Science and Technology*, ed. J. Lehman and S. Joseph, 2009, ch. 2, p. 14.
26 M. Sevilla and R. Mokaya, *Energy Environ. Sci.*, 2014, **7**, 1250–1280.
27 Y. Yamashita and K. Ouchi, *Carbon*, 1982, **20**, 41–45.
28 J. F. González, J. M. Encinar, C. M. González-García, E. Sabio, A. Ramiro, J. L. Canito and J. Gañán, *Appl. Surf. Sci.*, 2006, **252**, 5999–6004.

© 2022 The Author(s). Published by the Royal Society of Chemistry

Open Access Article. Published on 30 March 2022. Downloaded on 11/1/2022 11:56:41 AM.
This article is licensed under a Creative Commons Attribution 3.0 Unported Licence.

29 J. Ganan, J. Gonzalez, C. Gonzalez-Garcia, A. Ramiro, E. Sabio and S. Roman, *Appl. Surf. Sci.*, 2006, **252**, 5988–5992.
30 I. Susanti and N. Widiastuti, *Mal. J. Fundam. Appl. Sci.*, 2019, **15**, 249–253.
31 X. Fang, G. Li, J. Li, H. Jin, J. Li, V. Jegatheesan, S. Li, H. Wang and M. Yang, *Desalin. Water Treat.*, 2017, **96**, 120–127.
32 J. E. Park, G. B. Lee, S. Y. Hwang, J. H. Kim, B. U. Hong, H. Kim and S. Kim, *Appl. Sci.*, 2018, **8**, 1596.
33 M. Lillo-Ródenas, J. Juan-Juan, D. Cazorla-Amorós and A. Linares-Solano, *Carbon*, 2004, **42**, 1371–1375.
34 M. Lillo-Ródenas, D. Cazorla-Amorós and A. Linares-Solano, *Carbon*, 2003, **41**, 267–275.
35 E. Raymundo-Pinero, P. Azaïs, T. Cacciaguerra, D. Cazorla-Amorós, A. Linares-Solano and F. Béguin, *Carbon*, 2005, **43**, 786–795.
36 R. Xue and Z. Shen, *Carbon*, 2003, **41**, 1862–1864.
37 J. Jagiello, *Langmuir*, 1994, **10**, 2778–2785.
38 P. Hansen, in *Computational Inverse Problems in Electrocardiology*, ed. P. Johnston, WIT Press, Southampton, 2001, pp. 119–142.
39 P. C. Hansen and D. P. O'Leary, *SIAM J. Sci. Comput.*, 1993, **14**, 1487–1503.
40 P. C. Hansen, *SIAM Rev.*, 1992, **34**, 561–580.
41 J. D. Evans, V. Bon, I. Senkovska and S. Kaskel, *Langmuir*, 2021, **37**, 4222–4226.
42 M. Sevilla and A. B. Fuertes, *Chem. – Eur. J.*, 2009, **15**, 4195–4203.
43 A. E. Ogungbenro, D. V. Quang, K. A. Al-Ali, L. F. Vega and M. R. M. Abu-Zahra, *J. Environ. Chem. Eng.*, 2018, **6**, 4245–4252.
44 A. M. Aljumialy and R. Mokaya, *Mater. Adv.*, 2020, **1**, 3267–3280.
45 N. Balahmar and R. Mokaya, *J. Mater. Chem. A*, 2019, **7**, 17466–17479.
46 E. Evstigneev, *Russ. J. Appl. Chem.*, 2011, **84**, 1040–1045.
47 K. Latham, G. Jambu, S. Joseph and S. Donne, *ACS Sustainable Chem. Eng.*, 2014, **2**, 755–764.

© 2022 The Author(s). Published by the Royal Society of Chemistry

6.4 Further analysis

Publication I contains only the PSDs from the analysis of the SA*x.xx*-250 and SA*x.xx*-300 series as well as NC*x.x*-800 series for *x.x* in the range 0.0 to 0.9. Since publication, dual isotherm analyses of SA0.50-200, SA1.00-200 and NC1.2-800 has been completed. A discussion of the results follows here, particularly in relation to the utility of dual isotherm analyses on monitoring PSD development with changes in sample preparation conditions.

As discussed in section 5.1, the classically derived porosities of samples synthesised from sawdust (SD) with identical KOH:SD ratios, do not vary significantly with temperature. Nonetheless, it is interesting to compare such results using different porosimetric techniques. The PSDs and associated fits are displayed in the appendix, figures C.13, C.14. While the dual O_2/H_2 fits do appear to show small shifts in the position of the second maximum in the PSD for SA0.50-*HHH* samples with hydrothermal impregnation temperature (see figure C.13(2P)), this is not evident for SA1.00-*HHH* samples (figure C.14(2P)). Indeed it could be concluded that the dual N_2/H_2 fits show just as much variation in the position of the second maximum. Thus, the PSD broadening observed in **Publication I** according to dual isotherm O_2/H_2 analysis is apparently only associated with KOH:SD ratio, as opposed to hydrothermal impregnation temperature.

A comparison of the trends in apparent surface area with hydrothermal carbonisation temperature (T_{htc}) as determined by the BET method on an N_2 isotherm,[24] as well as *via* fitting of 2D-NLDFT-HS kernels to N_2, O_2, H_2 isotherms and dual fitting to N_2/H_2, O_2/H_2 pairs is shown in figure 6.3. For samples derived with both KOH:SD ratios of 0.50 and 1.00, the 2D-NLDFT method consistently shows a minimum in apparent surface area

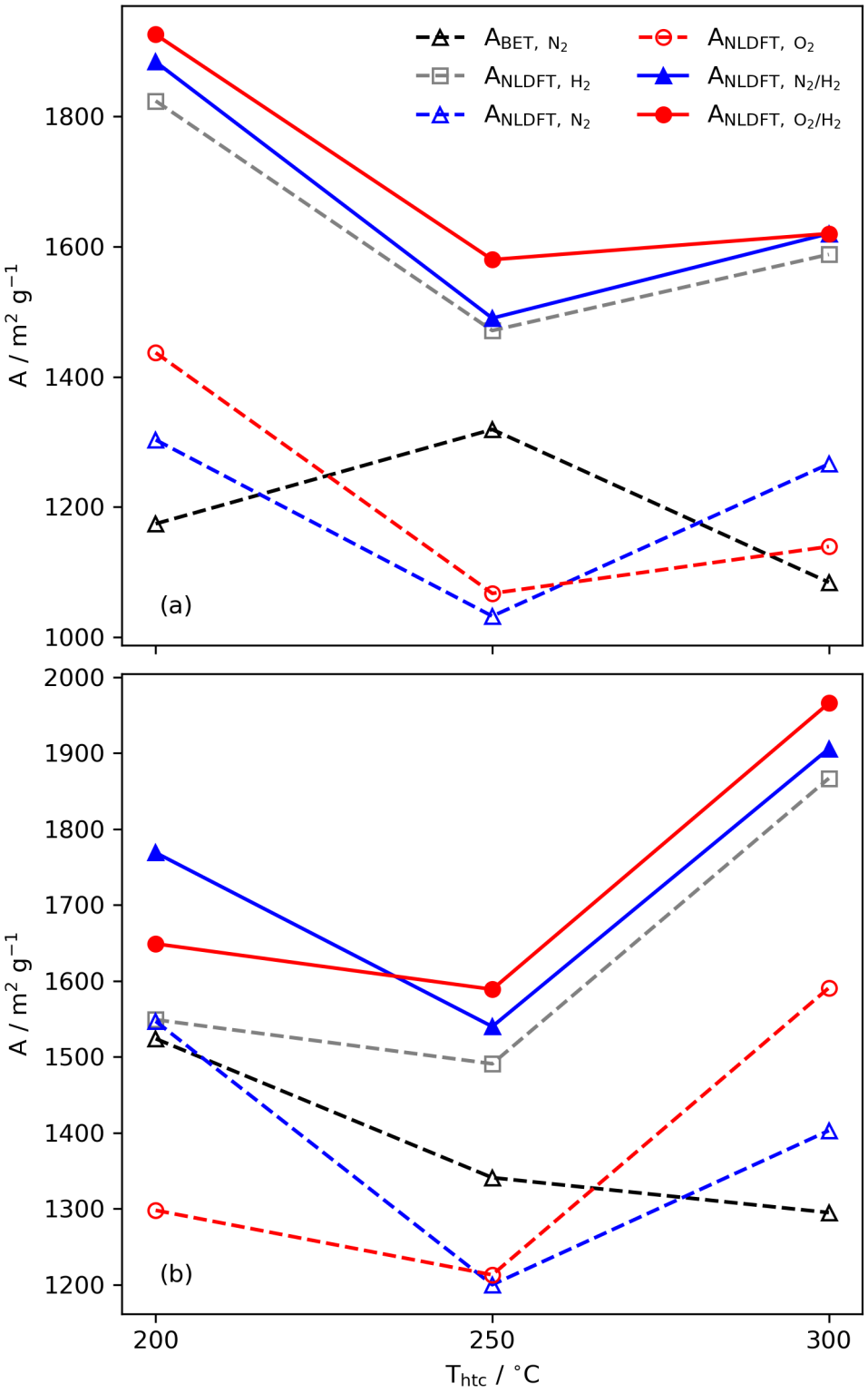

Figure 6.3: Trends in surface area with hydrothermal impregnation temperature T_{htc} of SD-derived carbons, as determined *via* the BET method as well as from fitting of 2D-NLDFT-HS kernel to H_2, N_2, O_2 isotherms as well as dual-fitting to N_2/H_2 and O_2/H_2 pairs. Subfigures (a) and (b) are for KOH:SD ratios of 0.50 and 1.00 respectively.

at T_{htc} of 250 °C. This is in contrast to A_{BET,N_2} which shows a *maximum* at this temperature for KOH:SD of 0.50, and a consistent decrease with temperature when the ratio is 1.00. Thus this discrepancy in the trend is likely a result of the inadequacy of the BET method for determining surface area in microporous materials, rather than an artefact of the nature of N_2 adsorption. Namely, the BET method relies on the formation of a monolayer in order to accurately quantify surface area, which is not possible in micropores as the probe molecule kinetic diameter is of the same order as the distance between pore walls (i.e. the pore width, w).[18,25–27] Furthermore, the nature of the adsorption is uncertain, as it is unknown to what degree the probe molecule is adsorbed on each of the pore walls in the (apparently) slit-shaped pores.[18,24] NLDFT-derived porosity, and in particular surface area determination does not have these assumptions that are unsuitable for highly microporous materials. Indeed, the kernel of model isotherms used in the 2D-NLDFT-HS method[28] is specifically designed for and suited to this kind of material.

Of further interest are the relative apparent surface areas determined by each probe molecule using the 2D-NLDFT-HS method. O_2 and N_2 single fits give approximately similar values and are in a similar range as those derived using A_{BET}. Simultaneously dual isotherm O_2/H_2 and N_2/H_2, as well as single isotherm H_2 derived areas match well with one another, but give significantly higher values than the previously mentioned methods. This further confirms that the use of H_2 as a probe molecule allows for the penetration of pores inaccessible to the larger O_2 and H_2 as was mentioned in **Publication I**. The similarity in apparent surface areas derived using H_2 alone, with the dual fit methods for a KOH:SD ratio of 0.50 is striking, indicating that all relevant porosity is accessible by H_2 for these materials. There is greater discrepancy when KOH:SD is increased to 1.00, probably

a result of PSD broadening through more aggressive action of the porogen, and thus creating porosity accessible to N_2 or O_2 but which will not be filled by H_2 at pressures up to 1 bar.

In section 5.2, a surprising reduction in total porosity for *x.x* of 1.2 was discussed. That is, while increasing the degree of substitution (DS) of Na from 0.7, to 0.9 porosity increases (A_{BET} and V_t), but these metrics reduce again when DS is increased further to 1.2 (see table 5.4). This drop in overall porosity is also accompanied by small reductions in % microporosity, and the trend occurs regardless of activation temperature. The more advanced techniques detailed in this chapter should give more detail as to the changes in porosity, and as such the PSDs and associated isotherms and fits are shown in figure 6.4. This is of course a reproduction of **figure 3** in **Publication I**, but with the inclusion of NC1.2-800 (referred to as NC1.2 in the publication).

The analysis performed using dual N_2/H_2 porosimetry (see figure 6.4(1P)) indicates that the reduction in porosity for NC1.2-800 is associated with a decrease in the size of the peaks in the PSD relative to NC0.9-800. That is, there is no significant shift in in the position of the maxima but simply a reduction in overall porosity associated with both of these maxima. This is consistent with the overall conclusion in **Publication I**, in that N_2/H_2 analysis doesn't show variation in pore widths with degree of activation. On the other hand, O_2/H_2 analysis (see figure 6.4(2P)) shows a contraction in the breadth of the PSD for *x.x* of 1.2. Indeed, the position of the second maximum is the same as that for NC0.0-800.

In section 5.2 it was suggested that the trends in porosity were a result of competitive pore forming processes; while pore formation was dominated by formation of cross-links at DS of 0.7 and 0.9, oxidative chemical activation

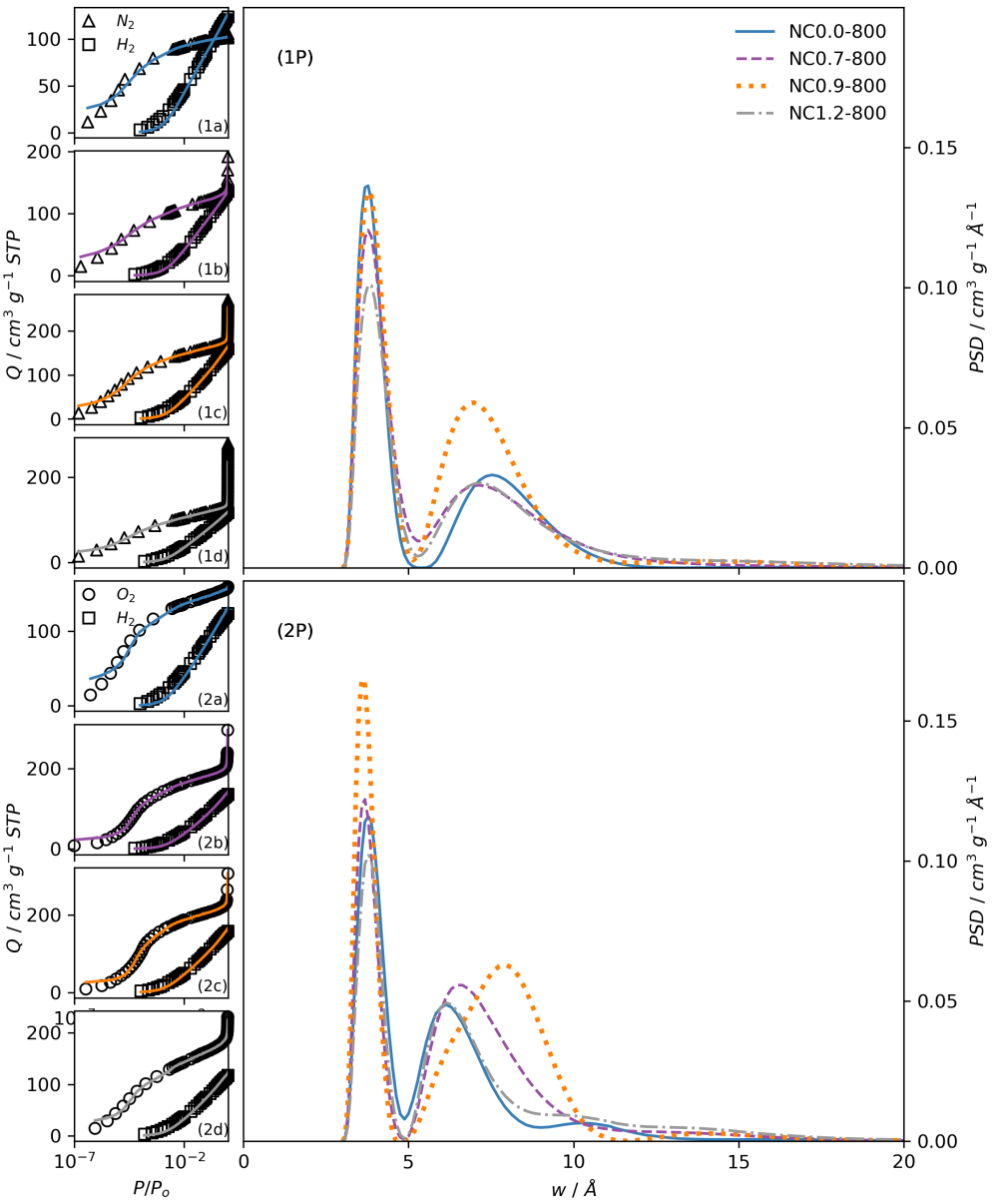

Figure 6.4: Fits to N_2/H_2 (1a, 1b, 1c) and O_2/H_2 (2a, 2b, 2c) isotherms of samples NC$x.x$-800 (for all values of $x.x$ from 0.0 to 1.2), and resultant PSDs (1P, 2P).

began to take on a larger role at DS of 1.2. In the case of NC0.0-800, no cross-link formation can occur thus porosity is formed *via* gasification. The contraction in PSD for NC1.2-800 shown by O_2/H_2 analysis indicates that this higher quantity of Na present during pyrolysis results in the destruction of cross-links and thus of the broader pores that are associated with their formation. The porosity that remains is that formed solely *via* gasification

as present in the Na-free samples. On the other hand, the information given by N_2/H_2 analysis indicates that there is a loss in porosity that is much more mechanistically difficult to explain. Perhaps the reduction in size of the second maximum could simply be put down to of pore collapse *via* overactivation, but this ought to be associated with much more significant increase in mesoporosity which is not present here. It is much more difficult to derive nuanced, logical hypotheses on these pore formation mechanisms from the N_2/H_2 analysis.

6.5 Summary & future work

Porosimetry performed using O_2 shows promise in more accurate determination of PSD, and porosity in general in ultramicroporous carbons. In particular, simultaneous fitting of the respective 2D-NLDFT-HS kernel to O_2 and H_2 isotherms consistently reveals a bimodal PSD. While this is also present for dual fits to N_2 and H_2, the O_2/H_2 method seems to show broadening in the PSD with increasing degree of activation which is not present in analysis performed using the former pair. These results ought to inform the selection of porosimetric adsorbates for highly ultramicroporous carbons. Furthermore, the results from dual isotherm analyses give further insights into potential mechanistic details of the somewhat unusual pore formation mechanisms in the turbostratic carbons reported in chapter 5.

There was an attempt to fit three isotherms (N_2, O_2, and H_2) to their respective 2D-NLDFT-HS kernels simultaneously which proved fruitless. This gave poor fits to the experimental data, especially for carbons with a low degree of activation. This may indicate the difficulty N_2 has in penetrating the smallest of ultramicropores and thus its limited utility in measuring

porosity at these pore widths. However, three-way fits may indeed prove to be useful in the future in particular for materials with greater PSD hierarchy. For example, a simultaneous fit to SF_6, O_2 and H_2 isotherms (at -50, -196 and $-196\,^{\circ}C$ respectively) would minimise the overlap of accessible pores for each of the three adsorbates, as the d_k is 5.50 Å, so excludes the smallest of ultramicropores. This analysis may however not be necessary and the same information could be gleaned by using SF_6 and H_2, which would minimise the overlap of pore sizes accessible to both adsorbates In addition, SF_6 has a zero quadrupole moment compared to O_2's of 0.155 which ought to reduce errors produced by carbon surface heterogeneity.

6.6 Publication I Supporting Information: Confirmation of pore formation mechanisms in biochars and activated carbons by dual isotherm analysis

Contribution of the author: The author performed all synthesis and instrumental analysis of samples in the work, analysed the results and wrote the manuscript.

Note: For this publication, the sample names are slightly different. The variable *x.xx* in SA*x.xx-HHH* samples is truncated to *x.x*, i.e. SA0.5-250 in the publication is equivalent to SA0.50-250 in chapter 5. As for NC*x.x-TTT* samples only samples with *TTT* of 800 °C are examined, thus NC0.9 is identical to NC0.9-800 in chapter 5.

Supplemental information

Confirmation of pore formation mechanisms in biochars and activated carbons by dual isotherm analysis

L. Scott Blankenship,[a] Jacek Jagiello,[b] and Robert Mokaya[a]

[a] School of Chemistry, University of Nottingham, University Park, Nottingham, NG7 2RD, UK
[b] Micromeritics Instrument Corporation 4356 Communications Drive, Norcross GA, 30093, USA

Table S1: Gravimetric yields and residual mass after TGA of samples described in this work

Sample	Yield / wt.%	TGA residual / wt.%
NC0.0	20	0.3
NC0.7	16	0.3
NC0.9	16	0.8
SA0.0-250	15	0.0
SA0.5-250	11	0.0
SA1.0-250	10	0.1
SA0.0-300	26	0.0
SA0.5-300	10	0.3
SA1.0-300	9	0.2

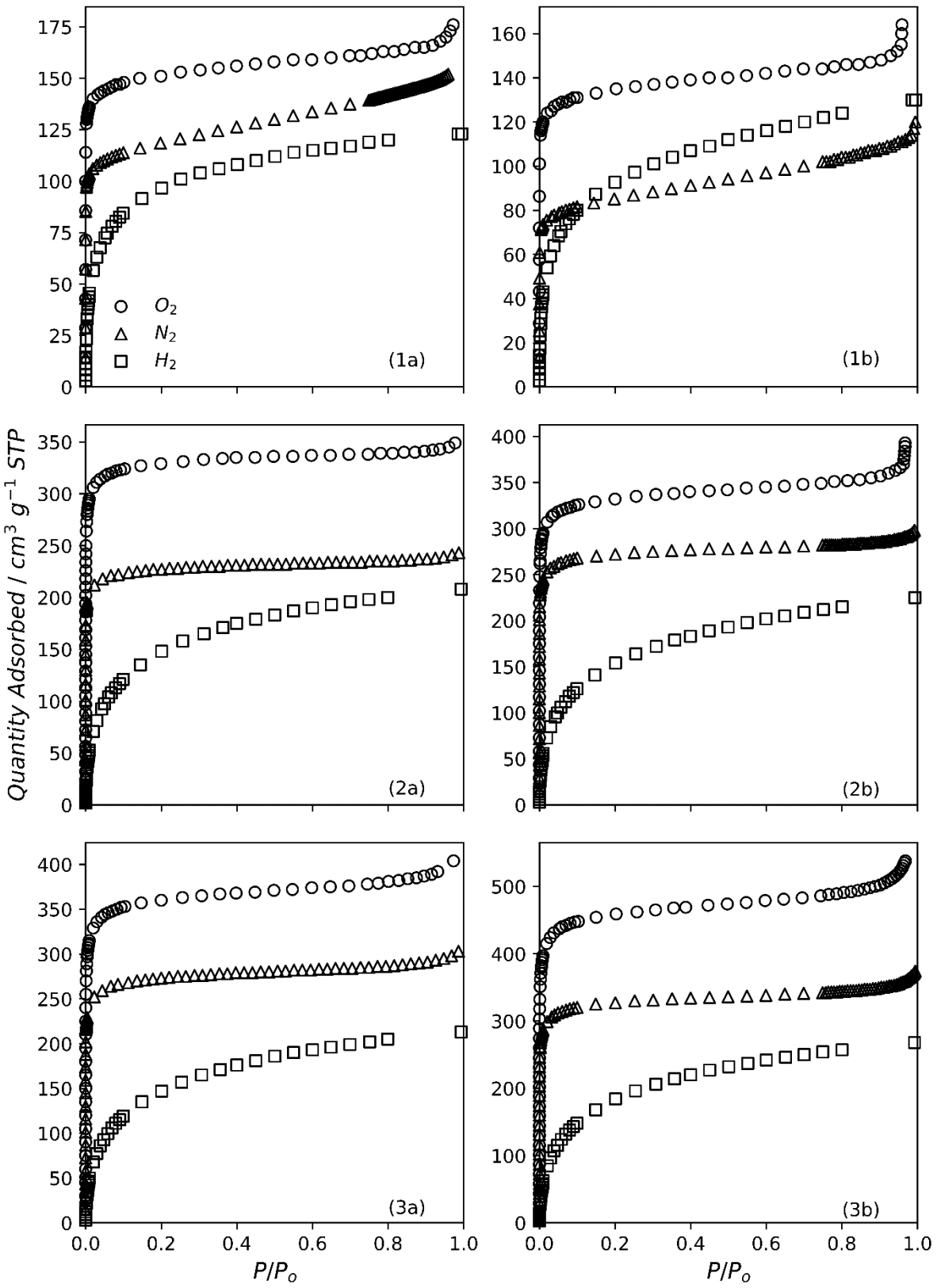

Figure S1: O_2, N_2, and H_2 isotherms at 77 K on SAx-250 (column a) and SAx-300 (column b) for KOH:SD ratios of 0.0, 0.5, and 1.0 – rows 1, 2, 3 respectively.

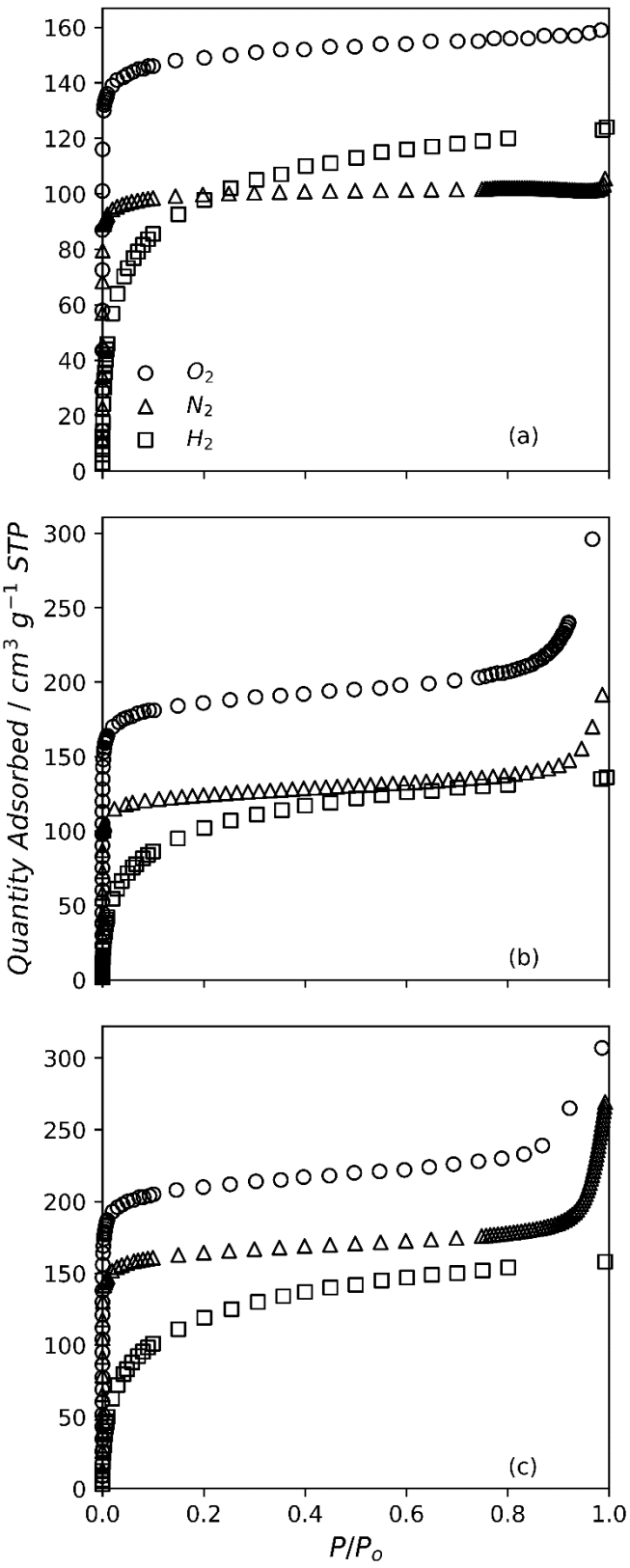

Figure S2: O_2, N_2, and H_2 isotherms at 77 K on NC0.0 (a), NC0.7 (b), and NC0.9 (c).

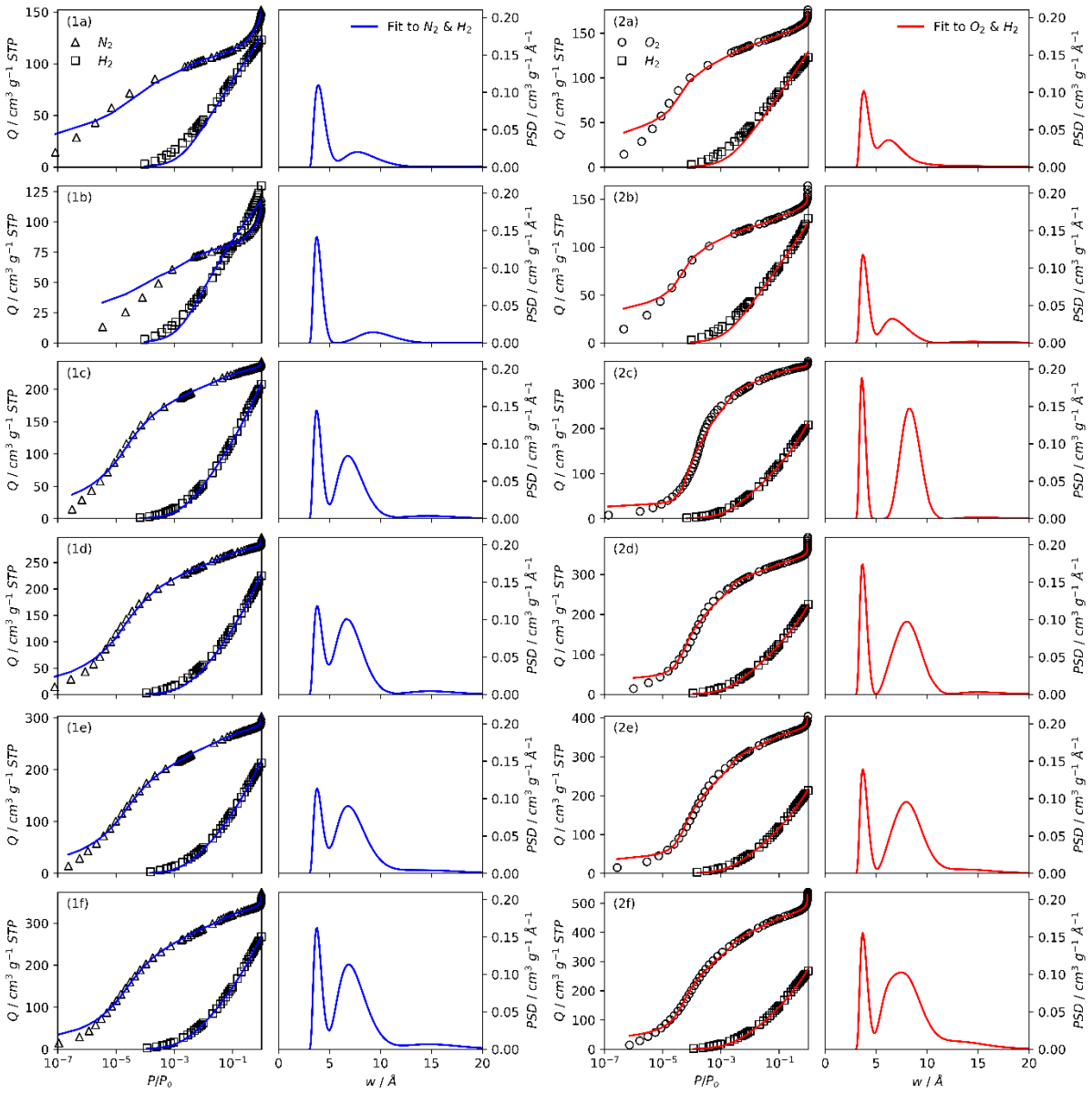

Figure S3: Dual fits of N2/H2 (column 1) and O2/H2 (column 2) isotherms for carbons SA0.0-250 (a), SA0.0-300 (b), SA0.5-250 (c), SA0.5-300 (d), SA1.0-250 (e), and SA1.0-300 (f).

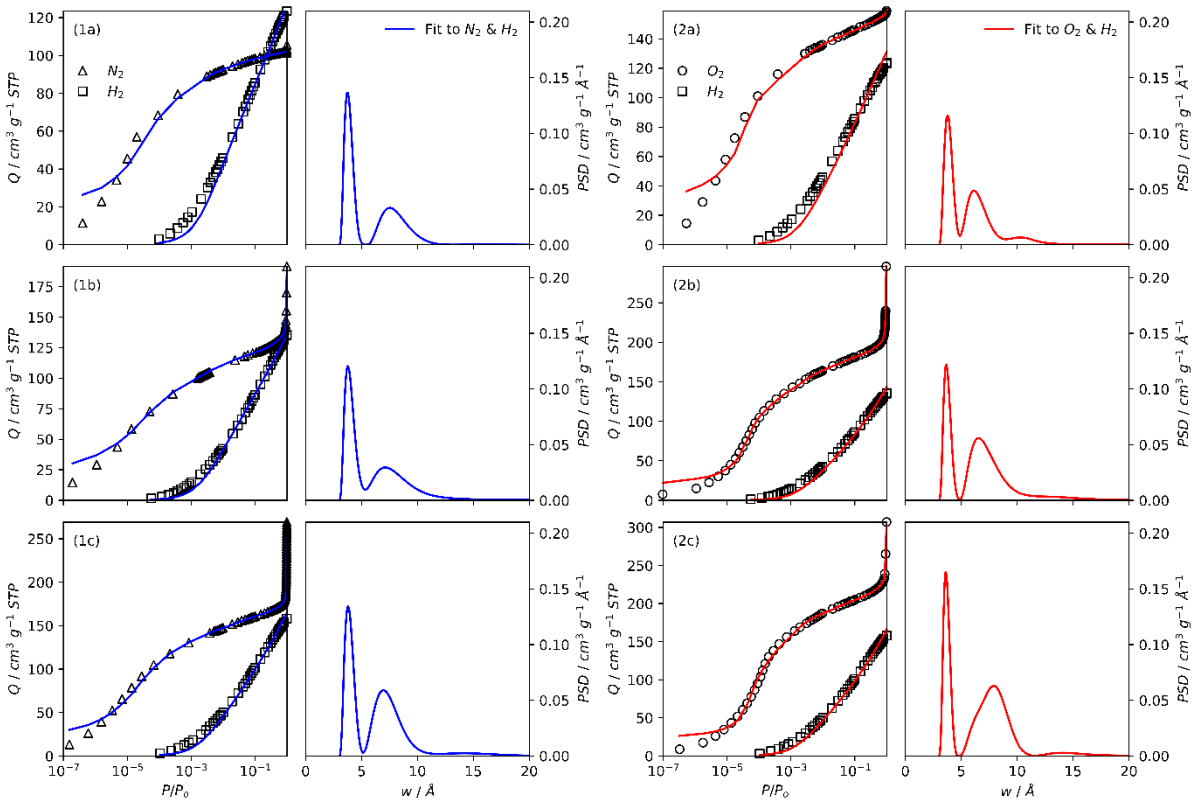

Figure S4: Dual fits of N_2/H_2 (column 1) and O_2/H_2 (column 2) isotherms for carbons NC0.0 (a), NC0.7 (b), and NC0.9 (c).

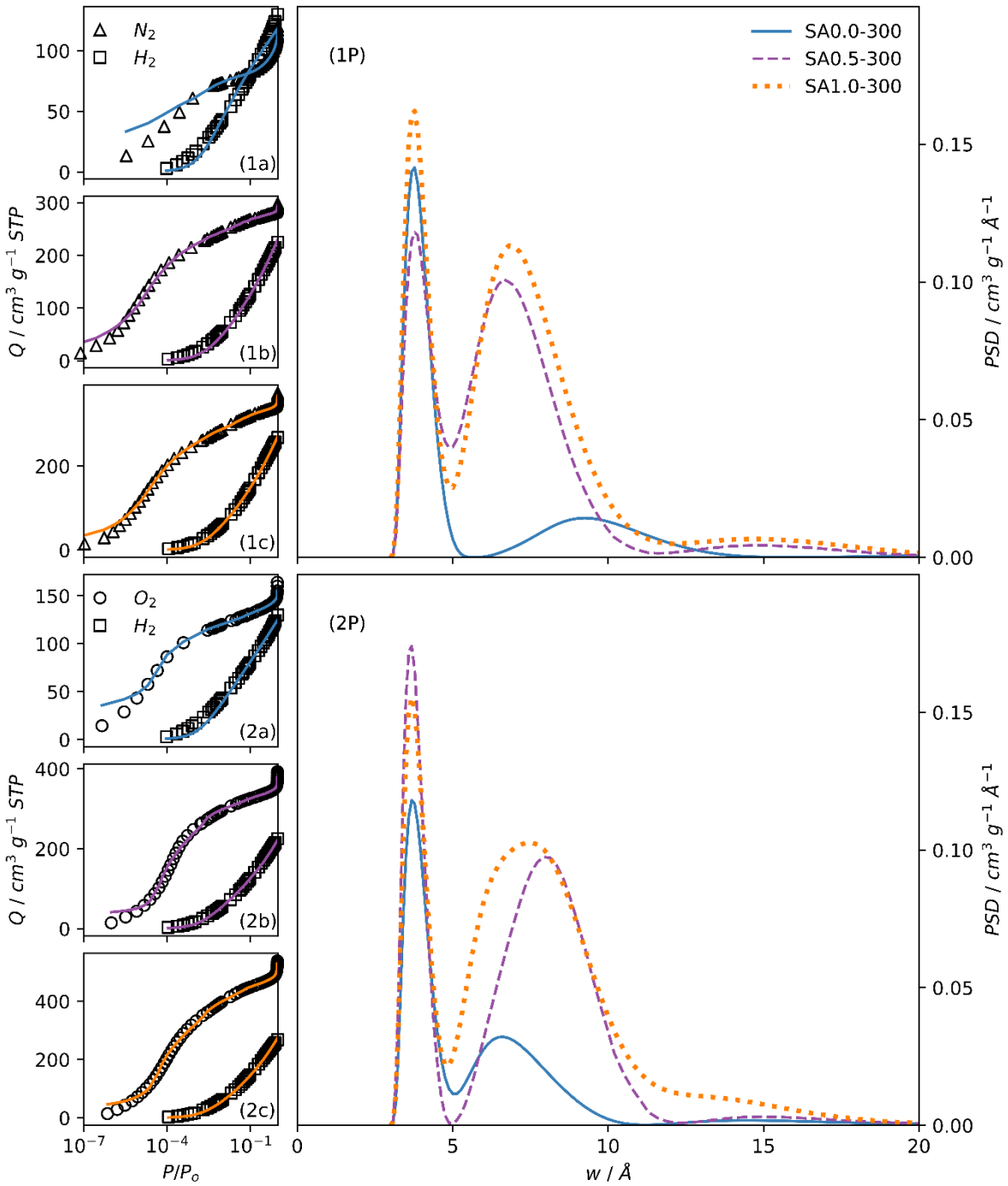

Figure S5: Fits to N_2/H_2 (1a, 1b, 1c) and O_2/H_2 (2a, 2b, 2c) isotherms of samples SAx-300 and resultant PSDs (1P, 2P)

References

1. F. Rodriguez-Reinoso, J. de D. Lopez-Gonzalez and C. Berenguer, *Carbon*, 1982, **20**, 513–518.
2. J. Jagiello and M. Thommes, *Carbon*, 2004, **42**, 1227–1232.
3. J. Jagiello, C. Ania, J. B. Parra and C. Cook, *Carbon*, 2015, **91**, 330–337.
4. J. Garrido, A. Linares-Solano, J. Martin-Martinez, M. Molina-Sabio, F. Rodriguez-Reinoso and R. Torregrosa, *Langmuir*, 1987, **3**, 76–81.
5. D. Lozano-Castelló, D. Cazorla-Amorós and A. Linares-Solano, *Carbon*, 2004, **42**, 1233–1242.
6. E. Furimsky, *Fuel Processing Technology*, 2000, **67**, 205–230.
7. K. S. Sing, *Carbon*, 1989, **27**, 5–11.
8. J. Jagiello, J. Kenvin, A. Celzard and V. Fierro, *Carbon*, 2019, **144**, 206–215.
9. J. Jagiello, J. Kenvin, C. O. Ania, J. B. Parra, A. Celzard and V. Fierro, *Carbon*, 2020, **160**, 164–175.
10. L. S. Blankenship, J. Jagiello and R. Mokaya, *Materials Advances*, 2022.
11. D. Grau-Marin, J. Silvestre-Albero, E. O. Jardim, J. Jagiello, W. R. Betz and L. E. Peña, *Carbon*, 2020, **157**, 495–505.
12. D. Lide, *Handbook of Chemistry and Physics, volume 88th edition*, CRC Press, 88th edn, 2007, p. 154.
13. B. E. Poling, J. M. Prausnitz and J. P. O'connell, *Properties of Gases and Liquids*, McGraw-Hill Education, 2001.
14. C. Graham, D. A. Imrie and R. Raab, *Molecular Physics*, 1998, **93**, 49–56.
15. K. Kodera and Y. Onishi, *Bulletin of the Chemical Society of Japan*, 1959, **32**, 356–361.

16. K. Kodera and Y. Onishi, *Bulletin of the Chemical Society of Japan*, 1960, **33**, 338–343.

17. H. K. Livingston, *Journal of Colloid Science*, 1949, **4**, 447–458.

18. J. Rouquerol, P. Llewellyn and F. Rouquerol, *Studies in Surface Science and Catalysis*, 2007, **160**, 49–56.

19. V. Presser, J. McDonough, S.-H. Yeon and Y. Gogotsi, *Energy & Environmental Science*, 2011, **4**, 3059–3066.

20. M. Sevilla and R. Mokaya, *Energy & Environmental Science*, 2014, **7**, 1250–1280.

21. I. Cabria, M. J. López and J. A. Alonso, *Carbon*, 2007, **45**, 2649–2658.

22. M. De la Casa-Lillo, F. Lamari-Darkrim, D. Cazorla-Amoros and A. Linares-Solano, *The Journal of Physical Chemistry B*, 2002, **106**, 10930–10934.

23. E. Masika and R. Mokaya, *The Journal of Physical Chemistry C*, 2012, **116**, 25734–25740.

24. S. Brunauer, P. H. Emmett and E. Teller, *Journal of the American Chemical Society*, 1938, **60**, 309–319.

25. B. Coasne and R.-M. Pellenq, *The Journal of Chemical Physics*, 2004, **120**, 2913–2922.

26. F. Ambroz, T. J. Macdonald, V. Martis and I. P. Parkin, *Small Methods*, 2018, **2**, 1800173.

27. K. S. Walton and R. Q. Snurr, *Journal of the American Chemical Society*, 2007, **129**, 8552–8556.

28. J. Jagiello and J. P. Olivier, *Carbon*, 2013, **55**, 70–80.

Chapter 7

python Porosity Uptake Correlator (pyPUC)

Abstract

For the optimal exploitation of porous materials in environmentally relevant physisorption applications, the relationship between widths of pores within the adsorbent and uptake capacity for the adsorbate in question must be well understood. As these applications typically utilise the pressure-dependency of adsorption, an understanding of the optimal pore size for uptake of the adsorbate as a function of pressure is required. Current methods for investigating this relationship are currently limited by (i) reliance on computational modelling to approximate the result, (ii) only investigating this problem at a few discrete pressures, and often (iii) using the unsuitable measure of the 'average' pore width. This work seeks to address all three of these inadequacies with the python Porosity Uptake Correlator; a software that uses experimental DataSets composed of gravimetric uptake isotherms and Pore Size Distributions (PSDs) of a group of samples that are compositionally similar, yet with diversity in terms of their porosity. Porosity (of all samples) within some pore size range is correlated to uptake of the adsorbate at a given pressure *via* linear regression. This process is then repeated for all defined pore size ranges and pressures, yielding a relationship between porosity within pores within some width range and association with improved uptake of the adsorbent (defined by the Pearson coefficient, r^2).

In **Publication II**, pyPUC was applied to the uptake of CO_2 on turbostratic carbons, which gave some novel insights into this adsorption process. Firstly, while ultramicropores are very important for low pressure CO_2 uptake, at pressures above 1.0 bar, their influence diminishes significantly. However there is an indication that the traditional division of micropores into ultramicropores and supermicropores at 7.0 Å may not truly

have physical significance to CO_2 uptake. Finally, the comparative investigation of the utility of N_2, O_2, and H_2 as well as the pairs N_2/H_2, and O_2/H_2 as porosimetric probes for the exploration of the porosity- and pressure-dependent CO_2 uptake relationship shows that traditional N_2 porosimetry can be improved on as a predictor for low-pressure CO_2 uptake in these materials. pyPUC shows promise in providing similarly nuanced conclusions in future applications with other adsorbate-adsorbent pairs.

7.1 Rationale for pyPUC

It is more reasonable to target a range of pore sizes as the optimum for uptake of an adsorbent at a given pressure, than to use a singular pore size. As mentioned in the previous section, values for this optimum pore size range are determined *via* modelling, and then confirmed experimentally.[1–5] This means that the question "What is the optimum pore size range for uptake of this adsorbate by my material, at this pressure?" is never really asked by experimentalists. Furthermore, the lower limit of the range of optimum pore sizes is never considered. It is reasonable to expect, for example that at very high pressures ultramicropores have minimal contribution to the uptake capacity of CO_2 by carbons. The python Porosity Uptake Correlator (pyPUC) developed in this work aims to provide a simple way for researchers to determine the relationship between porosity of a material within some range of pore sizes to uptake of an adsorbate, as a function of pressure. pyPUC does not claim to give a definitive answer to this question, but provides a thorough analysis of this relationship, in terms of a linear regressions between experimentally derived porosity within some range of pore widths, and uptake at some pressure. As the author hopes this project to be critiqued, developed, and built on by the general community of adsorption researchers all code is open source.*

It has been widely reported that low-pressure (<1.0 bar) CO_2 uptake in turbostratic carbons is strongly related to ultramicroporosity.[5–8] However, generally in these reports assessment of ultramicroporosity is performed *via* N_2 porosimetry, and as mentioned in chapter 6 and further explored in **Publication I** this technique is insufficient for elucidating PSDs in the ultramicropore region.[9–11] Presser added to this technique by using Ar and

*Source code available on github.

CO_2 (−196 and 0 °C respectively) isotherms to measure pores smaller than 10 Å and found that pores smaller than 8 Å were most significant for CO_2 uptake at 1.0 bar, but this decreased with decreasing pressure.[5]

While results from dual fitting of 2D-NLDFT kernels to O_2 and H_2 isotherms in **Publication I** show finer detail in the porosity development in carbons with increasing degree of activation as compared to conventional N_2 porosimetry, there is as yet no information on whether this has any significance on CO_2 uptake. As such, comparisons of the relationship between porosity (as derived classically from N_2 isotherms and from dual fits to O_2 and H_2 in different pore width regions) and CO_2 uptake are shown in figure 7.1. While microporosity from dual O_2/H_2 measurements shows an advantage over the classical measurements in terms of surface area, this is not reflected when pore volume is examined (see figure 7.1(a1, a2)). However if microporosity determined using dual O_2/H_2 porosimetry is subdivided at the traditional point of 7.0 Å (figure 7.1(b1, b2)), ultramicropore surface area becomes significant at pressures <0.2 bar. On the other hand, ultramicropore *volume* does not influence CO_2 uptake any more than micropore volume even at very low pressure.

The inconsistent results in terms of surface area and pore volume mentioned above may simply indicate the relative magnitude of the effects which surface area and pore volume of a material have on adsorption capacity. Indeed, previous reports have only considered the relationship of pore volume below some pore width with CO_2 uptake.[5–8] This may be because surface area appears to have a relatively small influence on low pressure CO_2 uptake[12–15]. However, when the PSDs are subdivided using the variable local minimum technique (see section 6.2), the results for both surface area and pore volume are far more consistent as shown in figure 7.1(c1, c2). In other words, both surface area and pore volume in region 1 - that is the pores

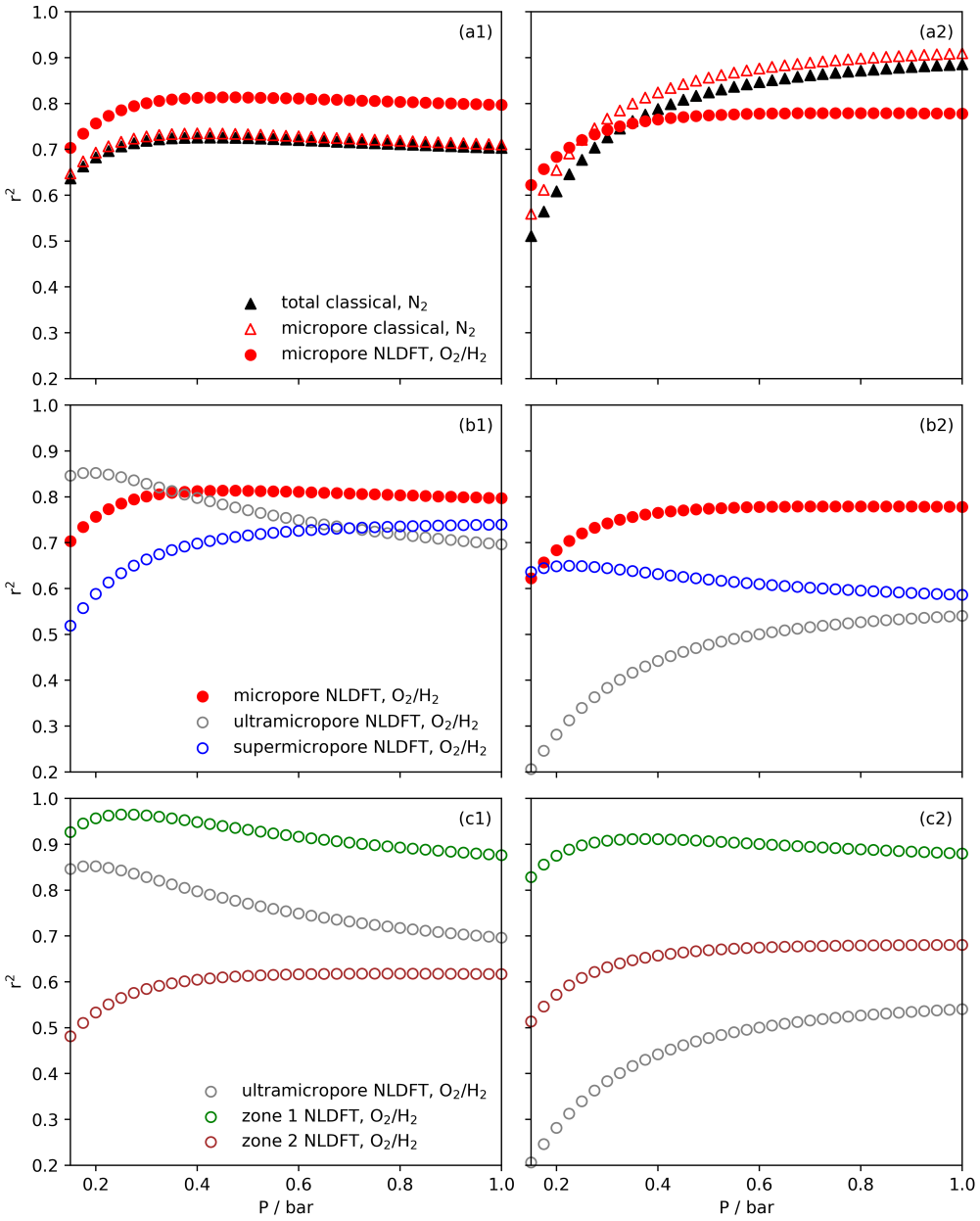

Figure 7.1: Comparison of r^2 values derived from the linear regression of porosity as determined by different techniques and within differing pore width ranges against the gravimetric uptake (loading) of CO_2 as a function of pressure. Linear regressions performed with using cumulative PSDs and CO_2 uptake isotherms of samples from section 6.2. Column (1) shows porosity in terms of surface area, and (2) in terms of pore volume. The classical microporosity values in (a1) and (a2) are derived using t-plot, whereas the total porosity is derived using the BET and single point methods for surface area and pore volume respectively.

of widths smaller than the local minimum - are strongly associated with CO_2 uptake at all pressures below 1 bar. In fact r^2 values are highest at all pressures using this variable local minimum technique than for any of the other techniques shown in this figure. This indicates that these bimodal PSDs may have some physical significance to the low-pressure uptake of CO_2.

In summary, these results indicate that the use of different sorptives can give radically different relationships between PSD and CO_2 uptake as a function of pressure. This shows further applications of the pyPUC project, as the validity and utility of different porosimetric probes can be thoroughly investigated in their utility for determining optimum pore size range for CO_2 uptake. While initial results are not conclusive, it appears that dual isotherm porosimetry may be important for understanding the relationship between pore size and CO_2 uptake. While the variable local minimum method is impractical, subdividing the micropore region at 6.0 Å may be more applicable to low pressure CO_2 uptake. This is further investigated in **Publication II**, **section 3.2**.

7.2 Publication II: Brute force determination of the optimum pore sizes for CO_2 uptake

Contribution of the author: The author came up with the concept of the pyPUC software, designed and implemented it, and performed all analyses. A portion of the experimental work necessary to create DataSet 1, and all experimental work for DataSet 2 was also done by the author. The author wrote the paper in its entirety.

Journal Name

ARTICLE TYPE

Cite this: DOI: 00.0000/xxxxxxxxxx

Brute force determination of the optimum pore sizes for CO_2 uptake†

L. Scott Blankenship,[a*] Nawaf Albeladi,[ab‡] Thria Alkhaldi,[ac‡] Asma Madkhali,[ad‡] and Robert Mokaya[a]

Received Date
Accepted Date

DOI: 00.0000/xxxxxxxxxx

Porosity, and in particular pore size is the one of the most important considerations in the development of porous carbons for CO_2 capture. Current methods for determining the optimum pore size for adsorption of CO_2 either make very broad assumptions (in computational studies), or are not sufficiently thorough (in experimental studies). Herein we present a brute force, first principles method for determining the range of pore sizes, Ω, best suited to adsorption of a given sorptive at a range of pressures. This is then used to determine Ω for CO_2 in a broad pressure range according to N_2 porosimetry. The analysis is then extended to other porosimetric sorptives and combinations thereof to assess their efficacy in determining Ω for CO_2.

1 Introduction

Porous carbons have been extensively investigated for their potential use in gas storage and/or capture applications, in particular related to energy storage applications including for alternative fuels such as H_2 and CH_4 or for CO_2 capture.[1–9] A material's capacity for a particular sorptive is known to be related to the porosity of the material, and in particular the pore width plays an important role.[5,10–21] Pore entrances for sorption of some gas at a given pressure and temperature must be large enough for the molecule in question can diffuse into it. This lower limit to the so-called pore size range is not necessarily solely determined by the size of the molecule; for example while N_2 has a nominal kinetic diameter (d_k) of 3.60 Å, it has been observed that at -196 °C in biochars this molecule diffuses extremely slowly into pores of width 4 Å.[22–24] On the other hand, adsorption can be improved by optimising the interactions between parallel pore walls and adsorptive molecules. That is, when the distance between pore walls is sufficiently small adsorbed molecules are affected by physical attraction to both walls, which increases the heat of adsorption and thus the retention of molecules within the pores.[25,26] This is particularly significant at low pressures where the adsorbate-adsorbent interactions dominate.[13,15,27–34] It follows therefore, that there is a range of optimum pore sizes for adsorption of any given molecule at some pressure and temperature.

There have been several attempts to determine the optimum pore size for given sorptives under some conditions. In general, the approach to this has been to either identify the 'ideal' pore size, i.e. a single width such as 6 Å for H_2 with slight variations depending on temperature and pressure.[12,28] An alternative method is to propose larger regions, i.e. an optimum pore size range (herein referred to as Ω);[15,35,36] for H_2 it has been reported that ultramicropores, i.e. pores of width <7 Å are ideal.[20,31] These regions or single widths are determined *via* purely computational methods or from experimentally determined uptakes and pore size distributions (PSDs). Computational methods attempt to determine the uptake of the sorptive in an idealised sorbent with pores of a single width *via* DFT or GCMC methods.[5,12,37] Whereas experimental data can be used to performing linear regressions of uptake at a given pressure against pore volume in a certain range (usually all pores below some maximum).[11,13,15,17,35,38] By the latter method, Presser *et al* determined (N=24) that at 1.0 bar, pores in activated carbons of width <8 Å are most strongly associated with gravimetric CO_2 uptake, while this reduced to 5 Å for uptake at 0.1 bar. Pores larger than 10 Å, as well as the oft-used parameter of average pore size were shown to be poor predictors of uptake at these low pressures.[13] Average pore size can however be useful when compared against so-called uptake density (uptake per unit surface area). For example, Masika *et al* found that uptake density of H_2 (1 bar, -196 °C) reduced drastically as average pore width increased from 10 to 20 Å.[16]

[a] *School of Chemistry, University of Nottingham, University Park, Nottingham, NG7 2RD, UK. Email: leo.blankenship@nottingham.ac.uk*
[b] *Chemistry Department, Faculty of Sciences Yanbu, Taibah University, Yanbu Al Bahr, 46423, Saudi Arabia*
[c] *Department of Chemistry, Jeddah University, Jeddah 23442, Saudi Arabia*
[d] *Department of Chemistry, University College in Samtah, Jazan University, Samtah 86736, Saudi Arabia*

† Electronic Supplementary Information (ESI) available: [Supplementary figures and tables; raw (.aif) isotherms; PSD and modelling analysis summaries as .csv; and raw outputs of D_v, D_π, and D_c for each DataSet (.csv)]. See DOI: 00.0000/00000000.

‡ These authors contributed equally to this work.

Current experimental approaches to determining Ω are limited in that they typically only consider a small set of possible Ωs, which is informed by theoretical data, and only at one or two pressures. Furthermore, the lower limit of the Ω is not typically varied – the assumption being that pores larger than the diameter of the sorptive will always be strong contributors to sorptive uptake under all conditions. As for computational studies, not only is the use of materials having a single pore width unrealistic for amorphous porous carbon, it is difficult to account for factors such as surface chemical and energetic heterogeneity and variation in pore geometry. Thus we present the python Porosity Uptake Correlator (pyPUC); a combined, iterative experimental and computational approach to Ω determination. Regressions are performed using experimental data between all possible Ωs at a large range of pressures and used to determine the Ω at each pressure. Both the range and increment of the possible Ωs and pressures can be easily adjusted to give an extremely fine level of detail. As a demonstration, pyPUC is applied to the determination of Ω for CO_2 uptake in amorphous carbons at 25 °C where porosity is determined from N_2 sorption isotherms obtained at -196 °C. The relative efficacy of H_2, O_2, and N_2 (-196 °C) isothermal porosimetry as well as dual fit N_2/H_2 and O_2/H_2 analyses is then assessed for their ability to predict Ω for CO_2 in highly ultramicroporous carbons.

2 Methods

2.1 pyPUC

The pyPUC software requires both uptake isotherms (υ) for the adsorptive in question, and cumulative PSDs (π) for a set of porous samples. Firstly, a model isotherm is fit to each experimental isotherm in υ using the pyGAPS adsorption isotherm processing framework, *via* the modelling package initially developed in pyIAST.[39,40] These model isotherms are converted to point isotherms according to some user-defined pressure range and increment. Thus, discrete loadings are determined for all samples at identical pressures, and is stored in the so-called loading DataFrame (D_υ).

Next, from π the apparent pore volume (V) or surface area (S) of each sample between the minimum and maximum pore width (w_{min} and w_{max}, respectively) is determined *via*;

$$\begin{aligned} V &= V(w_{max}) - V(w_{min}), \\ S &= S(w_{max}) - S(w_{min}) \end{aligned} \tag{1}$$

This is repeated across all pairs of w_{max} and w_{min} prescribed by the user, thus generating a parameter DataFrame (D_π). The number of parameters calculated N_π is thus related to the number of pore widths defined in the calculation N_w by;

$$N_\pi = \frac{1}{2}\frac{N_w!}{(N_w-2)!} \tag{2}$$

Thereafter, linear regressions are determined between every row of D_υ and D_π to give the correlation DataFrame (D_c), i.e. D_c shows how well each pore width range in D_π correlates to the loading of the sorptive on the sample at each pressure in D_υ. Each row of D_c contains the Pearson coefficient (r^2), slope (m) and intercept (c) of the regression. Finally, the best correlation at each pressure is found simply through the maximum r^2 value[41] for a given pressure after the exclusion of regressions giving a negative slope. Thus, the Ω associated with uptake of the sorptive at each pressure is given.

2.2 Carbon synthesis

Carbons were synthesised by pyrolysis of various biomasses and synthetic polymers either alone or with the aid of a porogen. In all cases they were washed after synthesis to remove any non-carbonaceous matter. Synthetic summaries are provided in for DataSet 1 (33 samples) and DataSet 2 (12 samples) in tables S1.1 and S2.1 respectively.

2.3 Isotherm measurement and processing

All raw experimental isotherms measured as described below are available in the electronic supplementary information as human- and machine-readable .aif files.[42] N_2, O_2, and H_2 isotherms for determination of PSDs were measured at -196 °C on a Micromeritics 3flex porosimeter at pressures up to P_0 for N_2 and O_2 and 1013 mbar for H_2. PSDs were determined using the appropriate SAIEUS software with the 2D-NLDFT heterogeneous surface kernel(s), in order to adequately account for chemical and energetic heterogeneity. Within SAIEUS it is possible to select an appropriate fitting parameter, λ[43–45] which controls the roughness of the PSD. λ was selected to provide the most realistic differential PSD based on known properties of carbons, and in all cases was between 2.5 and 5.0 and kept constant for carbons derived from the same precursor (see tables S1.1 and S2.1). Isotherms and derived PSDs can be found in figures S1.6-S1.10 and S2.4-S2.12.

Gravimetric CO_2 uptakes were measured on gravimetric analysers provided by Hiden; either the Xemis analyser at 25 °C (0-40 bar) or the IGA at 18 °C (0-20 bar) for DataSet 1 and 2 respectively. Fits were attempted with Langmuir,[46,47] Double Site Langmuir (DSLangmuir),[47] Triple Site Langmuir (TSLangmuir),[47] Guggenheim-Anderson-de Boer (GAB),[48–50] Freundlich,[51] Dubinin-Raduschkevich (DR)[52] and Toth[53] theoretical isotherms using pyGAPS (see section 2.1). The best fit was then selected by minimum root mean square error (RMSE). CO_2 isotherms as well as their best fits and details thereof can be found in figures S1.1-S1.5 and S2.1-S2.3

3 Results and Discussion

3.1 From N_2 isotherms only

We first present the use of pyPUC to determine Ω according to porosity derived from isotherms of the "traditional" porosimetric molecule, N_2. This is to establish the validity of this brute force method and to compare results derived in this way to those reported in the literature. A set of 33 carbon samples were used in this section.

3.1.1 DataFrame preparation.

The 33 activated carbons and biochars used in the initial analysis have varied PSDs in the range 3.6-100 Å (by pore volume)

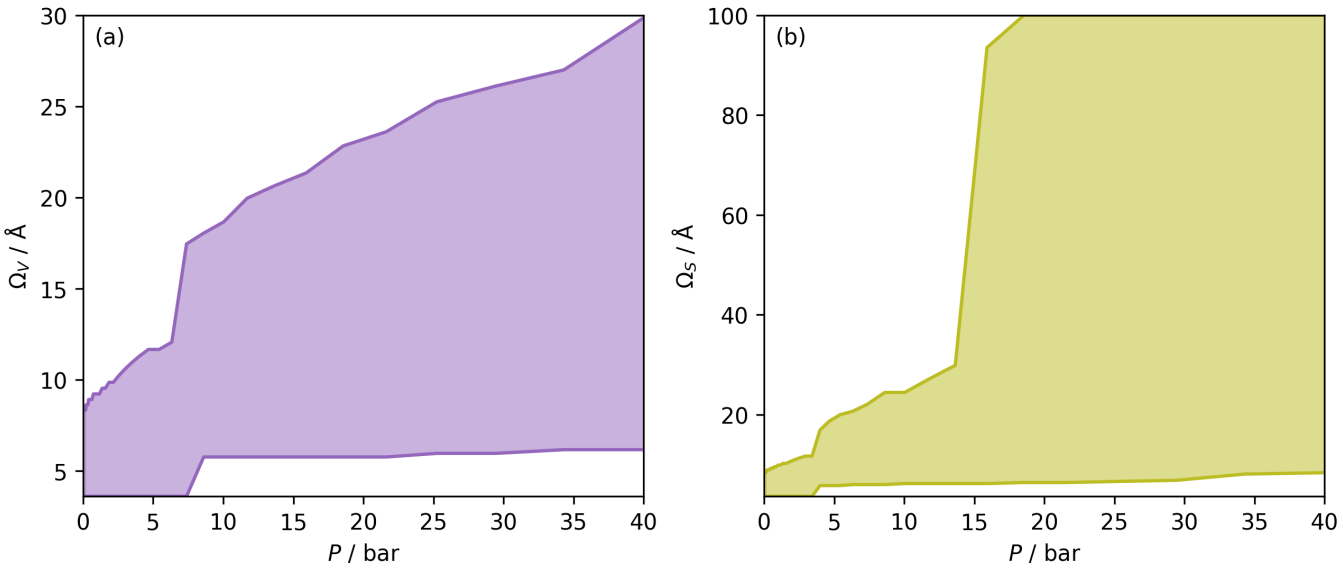

Fig. 1 : Ω_V (a) and Ω_S (b) at each pressure, i.e. optimum w_{max} and w_{min} plotted against pressure. The shaded area is thus the Ω in each case.

according to fits to N_2 isotherms with the 2D-NLDFT heterogeneous surface kernel (see figures S1.6-S1.10). It was possible to fit model isotherms to the experimental CO_2 isotherms in the full range 0.10-40 bar with a maximum root mean square error (RMSE) of 0.168 (figure S1.1-S1.5), although fits were slightly poorer for some isotherms at low pressures, notably *aP-2800*, *aP-2900* and *aP-3700* (figure S1.1(b2, b3, b5), respectively). It should be noted, that while a wide range of model fits were attempted, only DSLangmuir, TSLangmuir and Toth models provided the best fits to the experimental isotherms. DSLangmuir was by far the most common best fit, while Toth was only used for two samples. The model isotherms were output as 40 points in the range 0.1-40 bar defined using a base-10 logarithmic increment between points to give D_υ. Similarly, D_π was calculated using a base-10 logarithmic increment to give 100 w values between 3.6 and 100 Å. Determination of D_c therefore required 198 000 linear regressions, which were used to determine the Ω at each of the 40 pressures defined in D_υ in terms of V and S i.e. Ω_V and Ω_S respectively. A more detailed calculation, using a D_π of 500 values between 3.6 and 500 Å was also performed in order to ascertain the effect of increasing level of detail on the calculated Ω. This calculation took almost 7 days each for Ω_V and Ω_S compared to the original calculation which was completed within 24 h and results are not significantly different. As such this data was not used as the basis of the study. A comparison can be seen in figure S1.11.

3.1.2 The optimum pore size region, Ω.

Figure 1 shows Ω_V (a) and Ω_S (b) in the pressure range studied. As expected, in both cases the range of Ω broadens with increasing pressure. This shows the positive effect on high pressure CO_2 uptake of hierarchical PSDs. It is also notable that for both V and S while w_{max} increases almost constantly, there are basically only two values for w_{min}, starting at 3.6 Å and then increasing to around 7.0 Å at some pressure. In other words, there is a pressure range in which ultramicropores are strongly associated with CO_2 uptake. This range is up to 7.4 and 3.4 bar for V and S, respectively.§ At 0.10 bar, w_{max} is approximately 8 Å and increases to 17 and 11 Å for V and S, respectively once Ω begins to exclude the ultramicropores. That is, with increasing pressure supermicropores have an increasing influence on CO_2 uptake. The fact that the pressure range wherein w_{min} is 3.6 Å is much smaller for S relative to V may be a result of reduced influence of London interactions between the carbon surface and the sorptive as pressure increases. Increased pressure means that multilayer adsorption, and thus interactions between CO_2 molecules becomes more dominant.

Once Ω begins to exclude ultramicropores, there is a sharp increase in w_{max}. As a result, Ω_S includes both supermicropores and small mesopores after 6 bar. Conversely, Ω_V remains strictly in the supermicropore region until 13 bar. Again, this seems to be a result of an indication of the difference in the how surface area vs pore volume improve adsorption of CO_2. That is smaller pores result in improved sorptive-sorptive interactions, while larger pores provide more surface for CO_2 to interact with. This is further exhibited by the large increase in w_{max} up to 100 Å for Ω_S at 16 bar which does not exist for Ω_V. Of course, this upper limit for Ω_S is not real but represents the upper limit of w_{max} established in the determination of D_π. Nevertheless, these results may inform design of porous carbons for different applications; for example a carbon with high porosity below 8.0 Åis best suited for low pressure capture of CO_2, whereas carbons for so-called pressure-swing adsorption (PSA) should have hierarchical micro-mesoporous PSDs with minimal porosity below 8.0 Å. This confirms previous reports. [13,15,27,54,55]

§ In the more detailed calculation (see figure S1.11) this limit is found to be slightly lower.

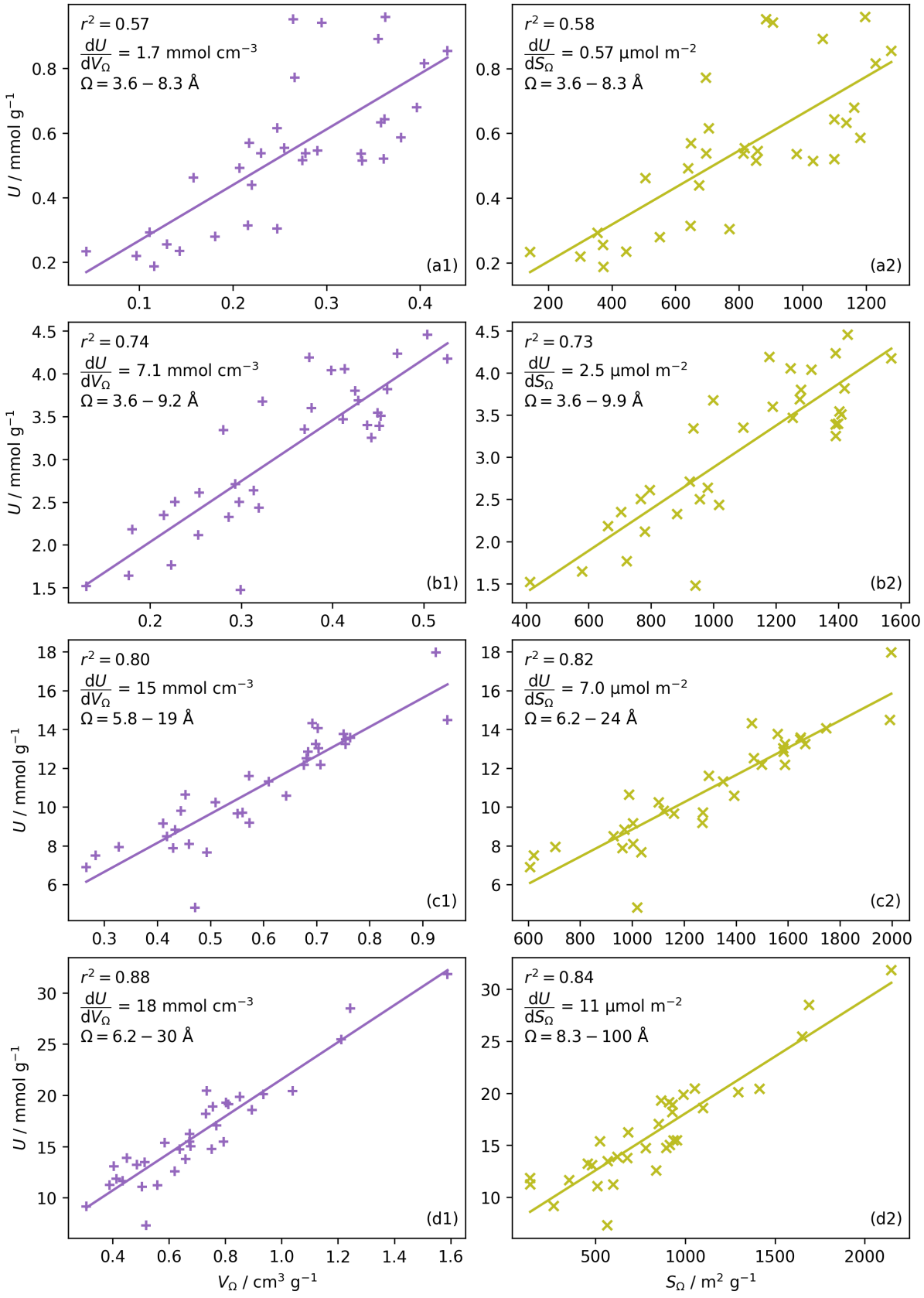

Fig. 2 : CO_2 uptake, U vs pore volume, V_Ω (column a) and surface area, S_Ω column (b) in Ω, at 0.10 (row 1), 1.0 (row 2), 10 (row 3), and 40 (row 4) bar.

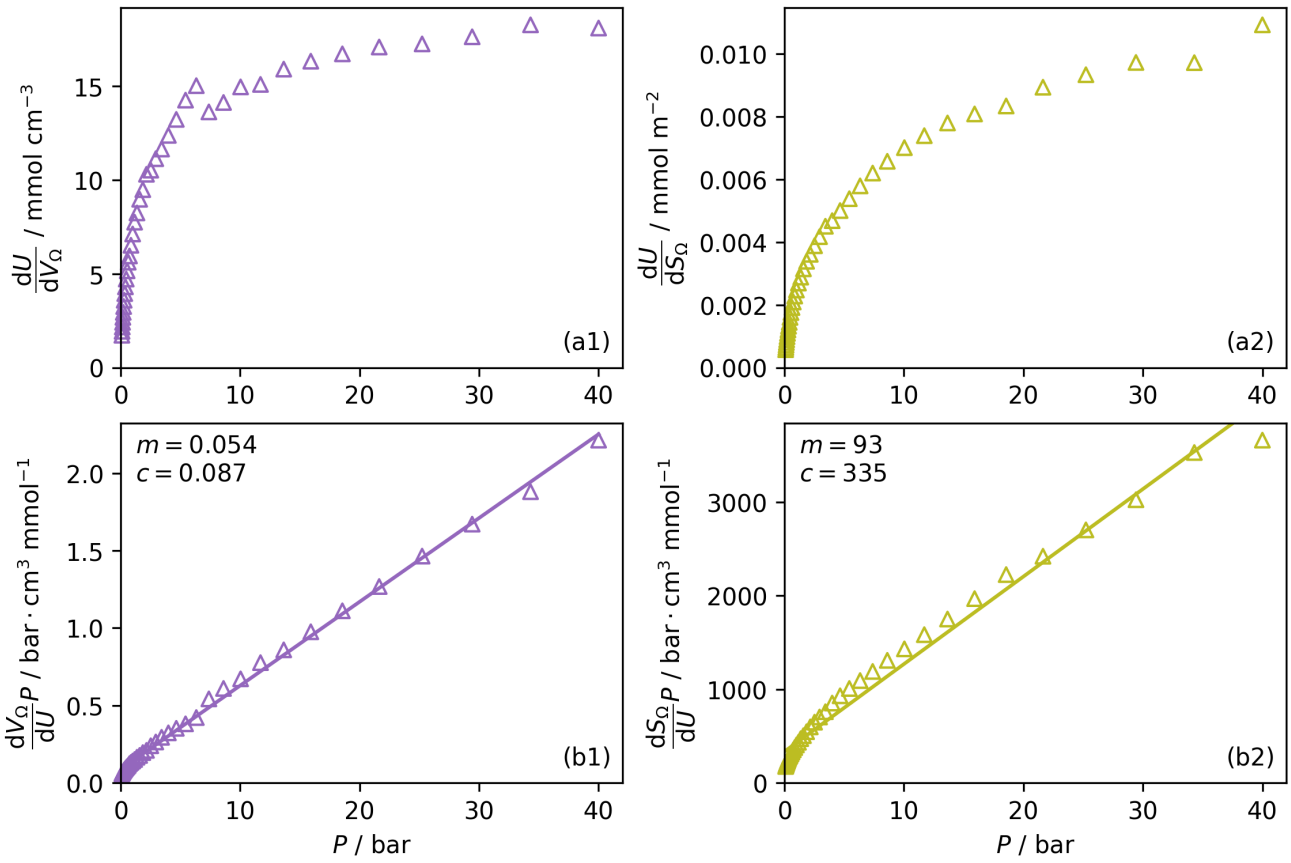

Fig. 3 : Change in $\frac{dU}{dV_\Omega}$ (a1) and $\frac{dU}{dS_\Omega}$ (a2) with P, and in a linearised form (b1) and (b2).

3.1.3 Relative strength of correlations.

Figure 1, however does not tell the full story as it presents each of the Ωs as equal. That is, there is no consideration of relative Pearson coefficients (r^2), which is presented in figure 2. While positive correlations were established for each pressure in question, r^2 ranges from 0.57 at 0.10 bar (figure 2 (a1)) to 0.88 at 40 bar (figure 2 (a4)). Indeed, r^2 steadily improves with increasing pressure and this trend is shared both for the volume and surface area of pores within Ω, i.e. V_Ω and S_Ω respectively. The relatively poor fit at low pressure may be a result of the imprecision of PSDs derived from N_2 isotherms in the ultramicropore region.[22,24,34] In addition, as mentioned before fitting of models to CO_2 isotherms to $P < 1.0$ bar was in some cases less successful than for higher pressures thus there may be inaccuracies in the determined gravimetric uptake at such pressures.

3.1.4 Effect of increasing pressure on influence of Ω on CO_2 uptake.

Figure 2 also shows the approximate relationship between uptake at the pressure (U) in question and pore volume or surface area within the Ω in the form $\frac{dU}{dV_\Omega}$ or $\frac{dU}{dS_\Omega}$, as derived from the linear regression. It is thus possible to predict the effect of increasing pore volume within the Ω on CO_2 uptake at that pressure, i.e. increasing volume of pores of width 3.6-8.3 Å by 1 $cm^3\ g^{-1}$ ought to result in an increase in uptake of 1.7 mmol g^{-1} CO_2 at 0.1 bar, whereas the same increase in pore volume in the range 6.2-30 Å (approximately the supermicropore and small mesopore region) results in an improvements in CO_2 uptake at 40 bar of 18 mmol g^{-1}. If we examine slopes of fits in figure 2, (column b), a similar pattern appears, with an increase in surface area of 1000 $m^2\ g^{-1}$ in pores between 3.6 and 8.3 Å corresponding to a meager 0.57 mmol g^{-1} improvement in CO_2 uptake compared with an increase in uptake of 11 mmol g^{-1} at 40 bar when surface area in pores of width 8.3-100 Å increases by the same amount.

Furthermore, a clear positive, semi-logarithmic trend is observed between $\frac{dU}{dV_\Omega}$ and P, i.e. it takes the form of a gas adsorption isotherm (see figure 3). A similar transform to that used in determination of a Langmuir isotherm[46] demonstrates a strong relationship of the form;

$$\frac{dU}{dV_\Omega} = \frac{P}{mP + c} \tag{3}$$

where the slope m is 0.054 cm^3 $mmol^{-1}$ with an r^2 of 0.997. The intercept, c does not have any physical significance as it ought to be a multiple of CO_2 uptake at 0 bar, and thus should be zero. Its non-zero value is likely a reflection of the relatively high uncertainty in the relationship between U and V at pressures below 1

bar. A similarly strong fit ($r^2 = 0.980$) can be observed for $\frac{dU}{dS_\Omega}$ by the same treatment as in equation 3, where $m = 93$ m^2 mmol^{-1}. However the relationship between $\frac{dU}{dS_\Omega}P$ and P is not exactly linear. Nevertheless, it is clear that with increasing pressure, improvements in Ω_V or Ω_S correspond to rapid improvements in U at low pressures, but these improvements diminish at higher pressures. This is likely a result of a reduction in enthalpy of adsorption with increasing adsorbate loading.

3.1.5 Association of arbitrary pore-size regions with uptake.

While sections 3.1.2, 3.1.3, and 3.1.4 discuss Ω, i.e. the absolute best pore size for CO_2 uptake at a given pressure (according to our methods), experimentally targeting porosity of amorphous porous carbons within such precise limits (e.g. 3.6-9.2 Å at 1 bar) is unlikely to be practicable. Besides, these limits are 'fuzzy', in that the next best pore size region to Ω typically has a similar r^2 value at the pressure in question. It is useful therefore to examine the dependence of r^2 as determined in the D_c on pressure within specific pore size regions, as shown in figure 4. For brevity, these results are discussed and displayed in terms of pore volume only. The traditional division of nanopores separates micropores into so-called ultramicropores (<7 Å) and supermicropores (7-20 Å). As shown in figure 4(a1) ultramicropores are not particularly strongly associated with CO_2 uptake at any pressure, although r^2 does improve at low pressures - in contrast to previous reports.[13,15] On the other hand, supermicroporosity does appear to correlate fairly strongly ($0.6 < r^2 < 0.8$) with uptake at pressures between 10 and 40 bar. This analysis also shows that mesoporosity does not show any particularly strong relationship with a carbon's ability to capture CO_2 at any pressure below 40 bar - the maximum r^2 is only 0.52. That is not to say that mesopores are not important for high pressure CO_2 adsorption, indeed as discussed in 3.1.2, both Ω_V and Ω_S at 40 bar include small mesopores, in addition to supermicropores, with r^2 of 0.88 and 0.84, respectively.

In section 3.1.2 and figure 1 we see that at lower pressures Ω is approximately 3.6-10 Å. Therefore, a reasonable alternative to the traditional subdivision of micropores at 7 Å could be at 10 Å. As shown in figure 4(a2), pores of width <10 Å do indeed show improved correlation with CO_2 uptake at relatively low pressures with r^2 reaching 0.79 at 2.9 bar. Conversely the larger subdivision, i.e. between 10 and 20 Å does not show improvements relative to the supermicropore designation, and has much poorer correlations at high pressures. Expanding this pore size region to include all pores above 10 Å does not significantly improve r^2 values in the pressure range used in this study. In other words it appears that pore size regions to target for high (10-40 bar) and medium (<10 bar) pressure uptake overlap, with the former being pores above 7 Å , and the latter below 10 Å. Low pressures (<1 bar) require even smaller pores of widths less than 8-9 Å (see figures 1 and 2(a1-2, b1-2)).

Figure 4(b1 and b2) show the effect of a broadening pore size region on the relationship between r^2 and P, with a fixed lower limit of 3.6 and 7.0 Å respectively. These lower limits correspond to the two values of w_{min} mentioned in 3.1.2. In both cases

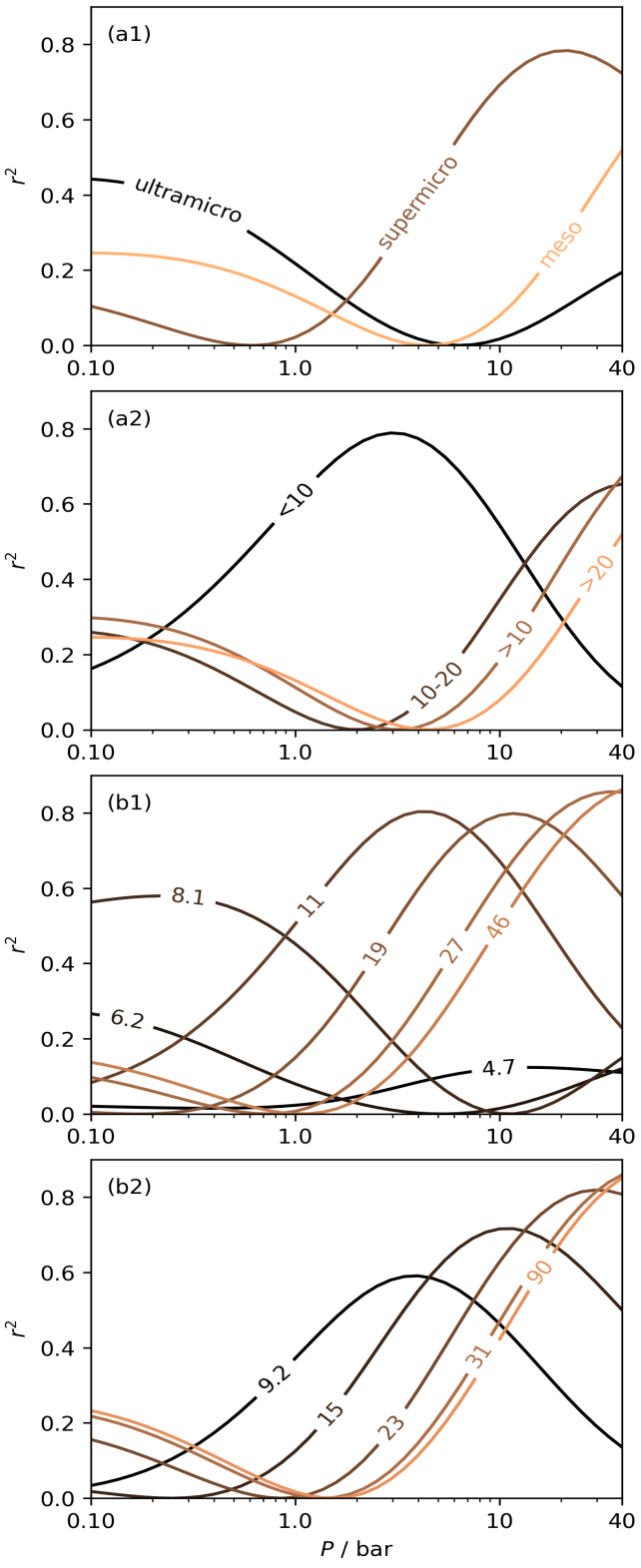

Fig. 4 : Dependence of r^2 on pressure within different pore size regions by pore volume, i.e. ultramicropores, supermicropores and mesopores (a1); pores of width <10, 10-20, >10, and >20 Å (a2); increasing w_{max} with a fixed w_{min} of 3.6 (b1) and 7.0 Å (b2).

small increases in w_{max} have a strong effect on the pressure at which correlation is strongest for the pore size region. However at higher values of w_{max}, this discrepancy is reduced. For example pores of width 7.0-31 and 7.0-90 Å have their strongest association ($r^2 \approx 0.85$) with CO_2 uptake at 40 bar. This corresponds roughly to Ω_V at 40 bar (figure 2(d1)) and shows that at high pressures larger pores may not significantly effect adsorption of CO_2. It is interesting to note that very narrow pore size ranges i.e. 3.6-4.7 and 3.6-6.2 Å (figure 4(b1)) do not show any significant relationship to CO_2 uptake, in fact r^2 never exceeds 0.27 for either of these pore size regions, so any variation in r^2 here is essentially meaningless. That is, there appears to be a lower limit to pore size that positively effects uptake at pressures of 0.10 bar and greater which is around 8.1 Å.

3.2 Highly ultramicroporous carbons

We recently reported on relative improvements in precision of PSD determination by use of dual fits to O_2 and H_2 isotherms relative to N_2 and H_2.[34] This was particularly relevant to so-called biochars and carbons activated with small amounts of porogen, both having a high proportion of ultramicropores. The rationale being that N_2's poor diffusion into ultramicropores meant that PSDs, especially at the smaller end of the micropore region, are imprecise. In addition, when NLDFT kernels were fit to N_2, O_2 and H_2 isotherms individually there were notable discrepancies in derived PSDs, which were more evident for the more ultramicroporous carbons.[34] In the previous section it was noted that the Pearson coefficient for Ω was very low at low pressures, which may be a result of imprecise PSDs for DataSet 1 in the ultramicropore region. It is useful therefore to examine the relative results of Ω determination using PSDs from single N_2, O_2 and H_2 isotherms as well as from dual kernel fitting. The following sections examine PSDs from these sorptives and combinations thereof in the determination of optimum porosity in the 12 carbons in DataSet 2. Synthetic details for these samples can be found in table S2.1.

3.2.1 Analysis using PSDs from single isotherm H_2, N_2, and O_2 fits.

CO_2 uptake isotherms, their fits, and PSDs from the three sorptives can be found in figures S2.1-S2.3 and S2.4-S2.6. A comparison of Ω_V derived using each of the three isotherms (i.e. $\Omega_V^{sorptive}$) in question in the pressure range 0.10-20 bar can be found in figure 5.¶ It is clear that no single sorptive is providing a reasonable Ω_V for DataSet 2 throughout the prescribed pressure range. In particular, Ω_V from N_2 ($\Omega_V^{N_2}$) isotherms (figure 5(a1)) gives the unreasonable conclusion that up to 2.1 bar $\Omega_V^{N_2}$ is constant at around 5.8-6.3 Å. This is both a surprisingly narrow range, and it is unlikely that there would be effectively no broadening of $\Omega_V^{N_2}$ with increasing P up to this point. Similarly, after 2.1 bar $\Omega_V^{O_2}$ (figure 5(a2) drops to a very narrow, relatively constant range (approximately 10-11 Å). This may simply be an effect of the minimal improvements in CO_2 for these carbons above 2 bar (see figures

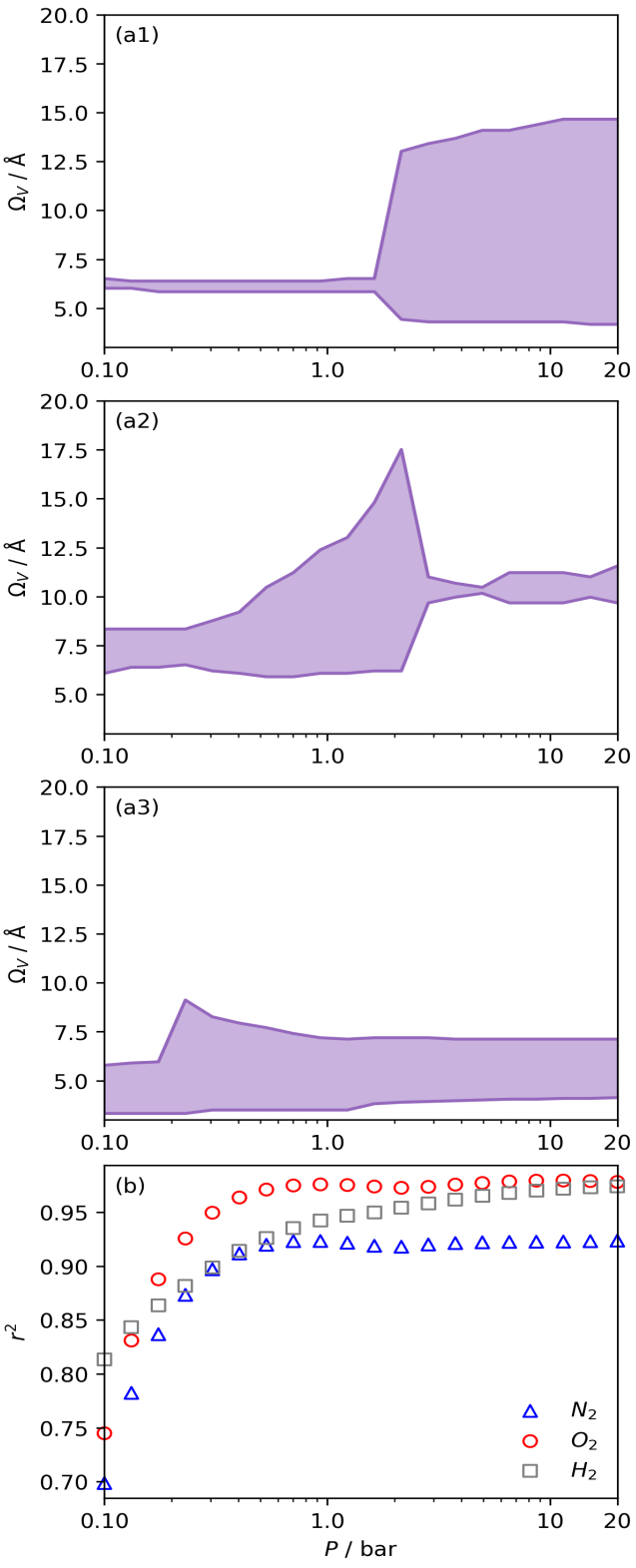

Fig. 5 : Ω_V calculated from DataSet 2 using PSDs derived from N_2 (a1), O_2 (a2), and H_2 (a3) isotherms as well as corresponding r^2 values (b).

¶ Results for $\Omega_S^{sorptive}$ are sufficiently similar to not require a separate discussion here. A comparison is displayed in figure S2.13.

S2.1-S2.3), which is attributable to the very minimal porosity of these carbons in the supermicropore and mesopore regions (see figures S2.4-S2.6).[34] As such discussions of these analyses are best limited to uptakes at $P < 2$ bar.

For analyses using both O_2 and H_2 there is a broadening in Ω_V with increasing P at relatively low pressures which is not present according to N_2 analysis. In addition, as shown in figure 5(b), r^2 is lower at all pressures for correlations derived using $\Omega_V^{N_2}$ data compared to $\Omega_V^{O_2}$ and $\Omega_V^{H_2}$. While $\Omega_V^{O_2}$ data shows the best correlations in general, r^2 from $\Omega_V^{H_2}$ data is greater at 0.10 and 0.13 bar. In other words, for this set of carbons, porosity accessible to CO_2 is best determined using H_2 isotherms up to 0.13 bar, and thereafter (up to around 2 bar) using O_2 isotherms. This follows from the standpoint of H_2 having access to - and thus predicting the presence of - pores of widths as small as 3.0 Å, while the lower limit for O_2 is 3.6 Å. Thus the contribution of pores of widths less than 3.6 Å to low pressure CO_2 uptake can only be accounted for using H_2 porosimetry, yielding $\Omega_V^{H_2} = 3.3$-5.9 Å. At 0.17 bar and above, pores above 6.0 Å appear to become more heavily utilised for CO_2 adsorption according to relative magnitudes of r^2. The upper limit of porosity measurable by H_2 at -196 °C is unknown, however it is usually said to be between 8.0-10 Å.[22,24] This explains why results for $\Omega_V^{H_2}$ become less reasonable at pressures above 0.3 bar; H_2 porosimetry is unsuitable for prediction of CO_2 uptake at these pressures. Indeed, in determination of PSDs for from H_2 isotherms, w_{max} was set to 10 Å.

Figure 6 presents further information on the relative efficacy of the three sorptives in measuring pores of widths below some limit (w_{max}), and the relationship between pores of these widths and CO_2 uptake between 0.10 and 2.0 bar. It is striking that when w_{max} is set at 5.0 or 6.0 Å, only H_2 porosimetry provides reasonable correlations ($r^2 > 0.60$) at any pressure. Indeed, in the case of O_2 (see figure 6(b)) r^2 is zero at all pressures and thus cannot be displayed within the figure. Strong correlations only begin to be shown when w_{max} is set to 10. PSDs derived from O_2 isotherms do show porosity in the ultramicropore region, thus it may be concluded that the ultramicropores accessible to O_2 are not important for CO_2 uptake, while those ultramicropores accessible to H_2 *do* contribute to CO_2 uptake. The latter statement can be accounted for by the fact H_2 has access to pores undetectable by O_2. Similar rationale can be applied to the plot for N_2 (figure 6(a)). When w_{max} is increased past 10 Å, r^2 vs P plots become very similar in the case of calculations made using both N_2 and O_2 derived PSDs. This indicates that there is little measurable improvement in CO_2 adsorption by broadening the PSD past 10 Å, however this may simply be a result of the relatively narrow PSDs present in these samples.

In summary, examination of D_c for DataSet 2 with each of the three porosimetric sorptives shows that low pressure (<2.0 bar) CO_2 uptake is improved by increasing volume in pores below 10 Å. In addition, N_2 is consistently outperformed by O_2 and/or H_2 at measuring porosity appropriate for CO_2 uptake. However, while porosity as determined by O_2 improves CO_2 uptake at pressures above 0.13 bar, H_2 is needed to determine optimum porosity for uptake at ultra-low pressures. It is therefore logical to consider

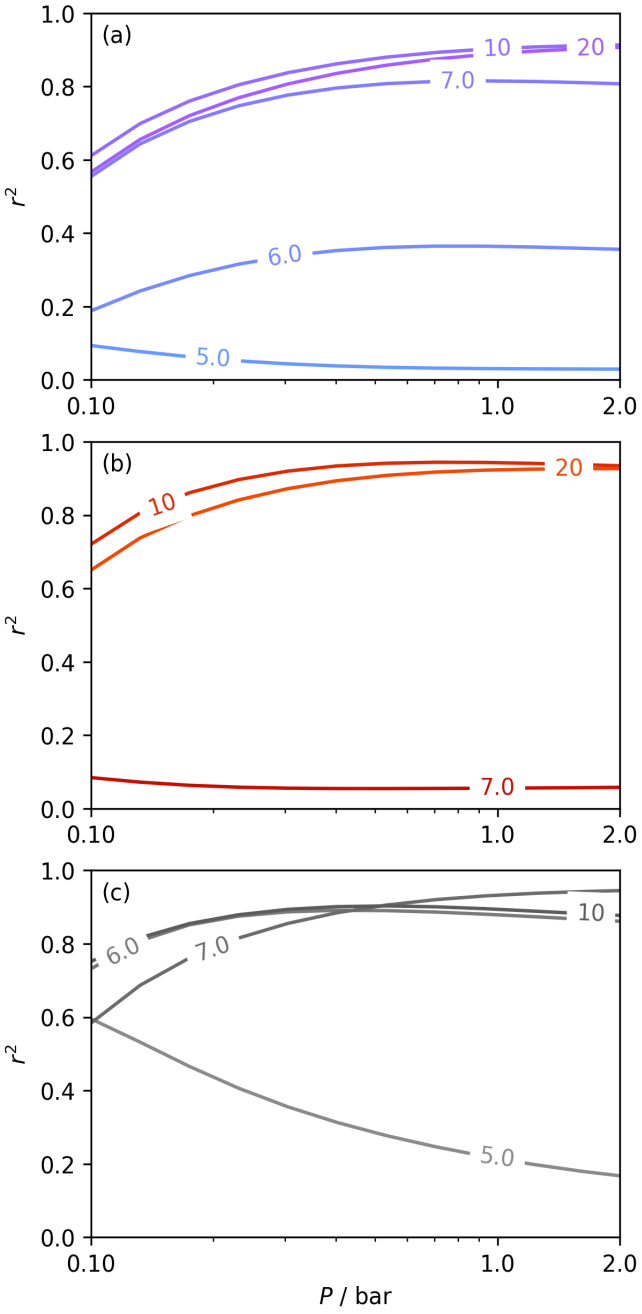

Fig. 6 : Comparison of dependence of r^2 on pressure with increasing w_{max} as determined using PSDs from N_2 (a), O_2 (b), and H_2 (c) isotherms.

PSDs as determined *via* dual isotherm analysis as a way to extend the range of pressures at which optimum pore size for CO_2 can be accurately determined.

3.2.2 Analysis using PSDs from dual isotherm N_2/H_2 and O_2/H_2 fits.

Fitting the 2D-NLDFT heterogeneous surface kernel to H_2 simultaneously with N_2 or O_2 allows the calculation of the range of the PSD in the range 3.0-500 Å. Thus, using these dual-fit PSDs in the calculation of D_c and Ω should allow for consideration of the

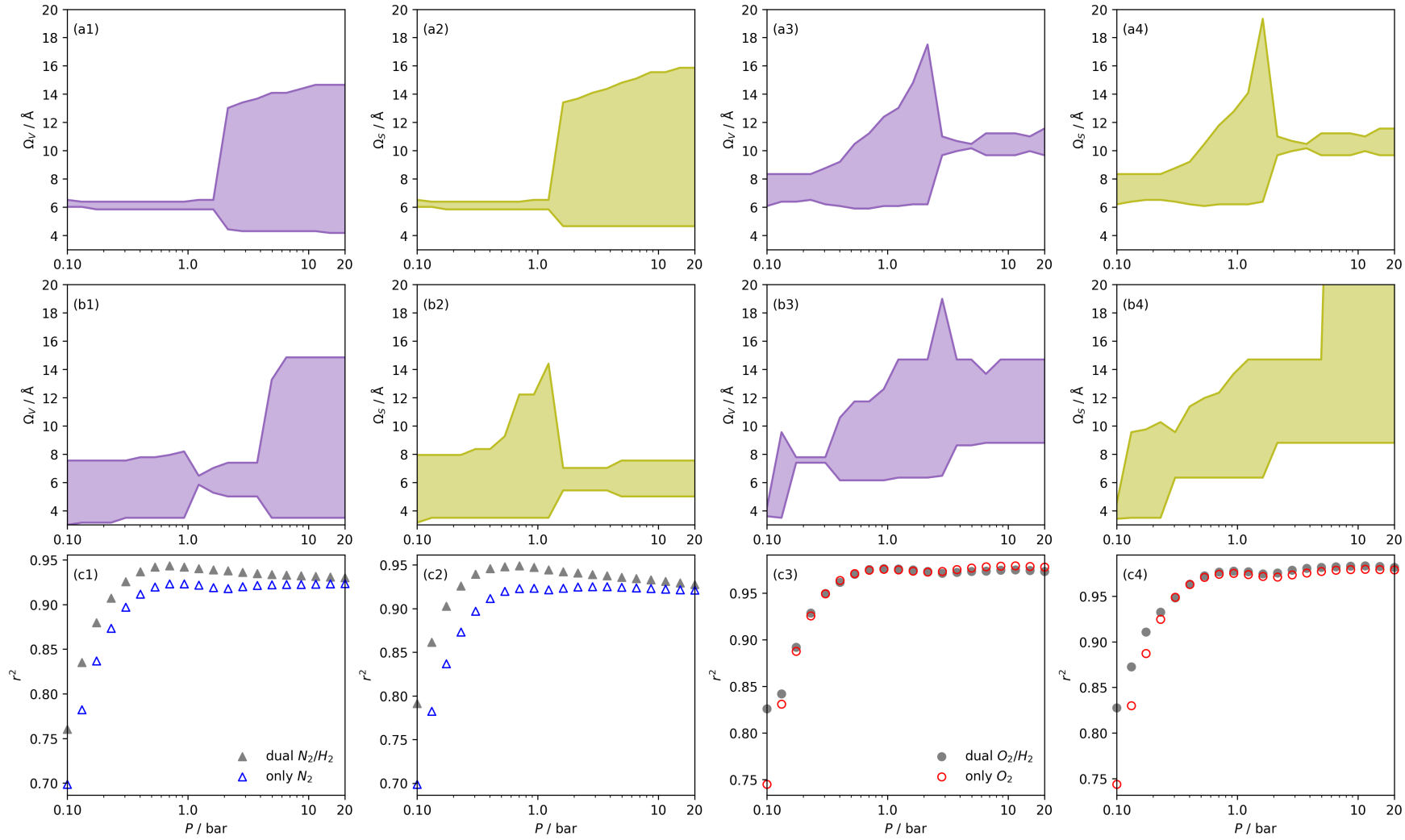

Fig. 7 : Comparison of Ω_V (a1, b1, a3, b3) and Ω_S (a2, b2, a4, b4) as determined by N_2 (a1, a2), O_2 (a3, a4) and dual N_2/H_2 (b1, b2) and O_2/H_2 (b3, b4) porosimetry. Row (c) contains comparisons of r^2 with P for the two Ω plots directly above.

affinity of all pores in this range for CO_2 in the defined pressure range. Figure 7 compares Ω_V and Ω_S from single isotherm (N_2 and O_2) fits to those obtained by dual fitting with H_2. In all cases, the Ω vs P plot for the dual fit (Figure 7(b1-4)) appears more reasonable than the corresponding plot for single fit (Figure 7(a1-4)), especially when $P < 1.0$ bar. In the case of $\Omega_V^{N_2/H_2}$ the improvement over single fit is principally in that the breadth of pore sizes (approx. 3.0-8.0 Å) in $\Omega_V^{N_2/H_2}$ below 1.0 bar is much more realistic than for $\Omega_V^{N_2}$. There is however no broadening within this region with increasing pressure, unlike for $\Omega_S^{N_2/H_2}$ which may be a result of the nature of adsorbate-adsorbent relative to adsorbate-adsorbate interactions as highlighted in section 3.1.2. In addition to the relationship between Ω and P being more realistic in terms of both surface area and pore volume, the r^2 is consistently better for both $\Omega_V^{N_2/H_2}$ (c1) and $\Omega_S^{N_2/H_2}$ (c2) than their single-isotherm PSD counterparts. That is to say, that extending the range of accurate, measurable porosity well into the ultramicropore region yields improved certainty in the determination of optimum porosity for CO_2 uptake.

r^2 values for $\Omega_V^{O_2/H_2}$ and $\Omega_S^{O_2/H_2}$ only shows noticeable improvements at pressures below 0.30 bar compared to their single isotherm counterparts (figure 7(c3-4)). This again indicates the importance of porosity penetrable by H_2 alone in the adsorption of CO_2 at low pressures. For $\Omega_V^{O_2/H_2}$ (figure 7(b3)) this corresponds to a significantly smaller range at low pressures, with pores in the range 3.6-4.2 Å being most associated with CO_2 uptake at 0.10 bar, compared to 6.1-8.3 Å for $\Omega_V^{O_2}$ (a3). Broadening in $\Omega_V^{O_2/H_2}$ is also briefly apparent as P increases to 0.13 bar, but falls to an unrealistically narrow range again quickly. On the other hand $\Omega_S^{O_2/H_2}$ (figure 7(b4)) gives the most physically reasonable result as it broadens consistently with increasing P. Furthermore, we see three distinct values of w_{min} of 3.5, 6.3, and 8.8 Å. The latter two values reflect the results shown in figure 1, indicating that the use of dual O_2/H_2 isotherms gives information on the pressures at which the influence of the smallest of ultramicropores on CO_2 uptake is greatest, that is below 0.30 bar.

The utility of dual isotherm porosimetry with H_2 as one of the probes in CO_2 porosity uptake correlations is further emphasised on examination of the dependency of r^2 on P with broadening PSDs (see figure 8). In the case of the corresponding plots for single isotherm fits (figure 6) H_2 was the only probe molecule that provided strong correlations where w_{max} is 5.0 or 6.0 Å. While dual N_2/H_2 porosimetry (figure 8(a)) provides some improvements for these narrow pore width ranges compared to single isotherm N_2 (figure 6(a)), the most significant improvements are for O_2/H_2 relative to O_2. Indeed, for all values of w_{max} between 5.0 and 7.0 Å there are reasonable r^2 values (>0.50) (figure 8(b)) at some pressure, with $w_{max} = 5.0$ Å showing the greatest improvement relative to the its single isotherm counterpart. In fact, the plot for 5.0 Å shows improvement even relative to its corresponding plot from single isotherm H_2 porosimetry (figure 6(c)), as r^2 does not fall below 0.50 at pressures below 5.0 bar. In other words, while H_2 porosimetry shows that pores of width less than 5.0 Å have a reasonable association with CO_2 uptake at 0.10 bar only, combined O_2/H_2 porosimetry shows that this continues to much higher pressures.

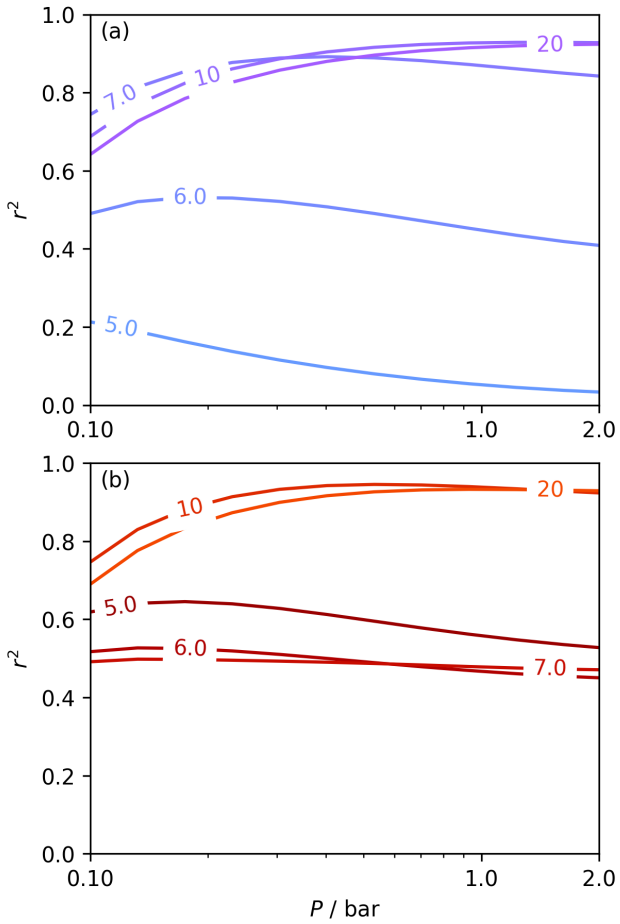

Fig. 8 : Comparison of dependence of r^2 on pressure with increasing w_{max} as determined using PSDs from dual N_2/H_2 (a) and O_2/H_2 (b) isotherms.

It appears therefore that dual O_2/H_2 porosimetry may give a more nuanced and reasonable picture of porosity relevant to CO_2 uptake within samples in DataSet 2 as compared to both dual N_2/H_2 analysis as well as PSDs from single sorptives. In particular, if we compare results from O_2/H_2 analysis to the traditional N_2 analysis it is interesting that the presence of micropores of width <5.0 Å according to the former figure 8(b)) are at least as important as micropores in general according to the latter for CO_2 uptake at very low pressures (see figures 8(b) and 6(a), respectively). While more investigation is necessary to determine the precise reasons for the differences in results given by dual isotherm O_2/H_2 and the other methods measurement of the porosity most relevant to CO_2 uptake in highly ultramicroporous carbons, it remains clear that both the certainty of these results from the former and their correspondence with accepted theory of gas adsorption in pores is better.

4 Conclusions

pyPUC shows promise in its ability to thoroughly and definitively elucidate the relationship between porosity within some pore size

range, and uptake of a gas at some pressure. We have examined its utility in determining the optimum pore size region in terms of pore volume or surface area (Ω_V or Ω_S) for CO_2 capture in carbons between 0.10 and 40 bar. More than broadly confirming reports by previous experimental and theoretical studies, this work gives a much higher level of precision concerning the relationship between Ω and P. Furthermore, it is possible to approximately predict the the increase in CO_2 uptake achieved by increasing porosity within the Ω. Apart from optimum pore sizes ranges, we also find the relationship between pores within arbitrary width ranges on CO_2 uptake.

In addition this method allows facile, comprehensive comparison of such results using different isothermal porosimetric methods for PSD determination. This is particularly relevant to highly ultramicroporous carbons, wherein the utility of N_2 has been called into question. Here, we show that dual isotherm analysis, and in particular O_2/H_2 analysis improves our predictions of CO_2 uptake especially at very low pressures.

The pyPUC method can be easily expanded to be used for calculations related to the uptake of other sorptives, under different conditions, and with other variables (e.g. surface chemistry) accounted for. Results from our methods may help improve the design of porous materials for a wide range of adsorption applications.

Acknowledgements

We are thankful to the EPSRC (Low-Dimensional Materials & Interfaces DTP) for a studentship for LSB. In addition, LSB thanks Paul Iacomi for the development of pyGAPS, and assistance with implementation of some of its features in pyPUC as well as to Hassan Akhtar who assisted and advised on some of the code. The use of the University of Nottingham's Augusta HPC service was essential to the completion of this work. We thank the government of the Kingdom of Saudi Arabia for funding PhD studentships for NA, TA and AM. RM thanks the Royal Society for a Royal Society Wolfson Research Merit Award.

Author Contributions

L. Scott Blankenship: Conceptualization, Methodology, Software, Formal Analysis, Data Curation, Investigation, Writing – Original Draft, Visualization
Nawaf Albeladi: Investigation
Thria Alkhaldi: Investigation
Asma Madkhali: Investigation
Robert Mokaya: Validation, Resources, Writing – Review & Editing, Funding acquisition

Conflicts of interest

The authors declare that they have no known competing financial interests or personal relationships that could have appeared to influence the work reported in this paper.

Notes and references

1 M. Sevilla and R. Mokaya, *Energy & Environmental Science*, 2014, **7**, 1250–1280.
2 T. C. Drage, J. M. Blackman, C. Pevida and C. E. Snape, *Energy & Fuels*, 2009, **23**, 2790–2796.
3 M. G. Plaza, S. Garcia, F. Rubiera, J. J. Pis and C. Pevida, *Chemical Engineering Journal*, 2010, **163**, 41–47.
4 A. Altwala and R. Mokaya, *Energy & Environmental Science*, 2020, **13**, 2967–2978.
5 S. Biloé, V. Goetz and A. Guillot, *Carbon*, 2002, **40**, 1295–1308.
6 M. Beckner and A. Dailly, *Applied Energy*, 2016, **162**, 506–514.
7 J. Juan-Juan, J. Marco-Lozar, F. Suárez-García, D. Cazorla-Amorós and A. Linares-Solano, *Carbon*, 2010, **48**, 2906–2909.
8 K.-S. Lin, A. K. Adhikari, K.-C. Chang, C.-L. Chiang and C.-H. Wang, *Journal of Nanoscience and Nanotechnology*, 2014, **14**, 2700–2708.
9 Q. Zhao, F. Wu, K. Xie, R. Singh, J. Zhao, P. Xiao and P. A. Webley, *Chemical Engineering Journal*, 2018, **336**, 659–668.
10 J. Alcaniz-Monge, M. A. de la Casa-Lillo, D. Cazorla-Amorós and A. Linares-Solano, *Carbon*, 1997, **35**, 291–297.
11 D. Lozano-Castello, D. Cazorla-Amoros, A. Linares-Solano and D. F. Quinn, *Carbon*, 2002, **40**, 989–1002.
12 I. Cabria, M. J. López and J. A. Alonso, *Carbon*, 2007, **45**, 2649–2658.
13 V. Presser, J. McDonough, S.-H. Yeon and Y. Gogotsi, *Energy & Environmental Science*, 2011, **4**, 3059–3066.
14 W. Zhao, V. Fierro, C. Zlotea, E. Aylon, M. Izquierdo, M. Latroche and A. Celzard, *International Journal of Hydrogen Energy*, 2011, **36**, 11746–11751.
15 M. Sevilla, J. B. Parra and A. B. Fuertes, *ACS Applied Materials & Interfaces*, 2013, **5**, 6360–6368.
16 E. Masika and R. Mokaya, *The Journal of Physical Chemistry C*, 2012, **116**, 25734–25740.
17 Z. Geng, C. Zhang, D. Wang, X. Zhou and M. Cai, *Journal of Energy Chemistry*, 2015, **24**, 1–8.
18 B. Adeniran and R. Mokaya, *Chemistry of Materials*, 2016, **28**, 994–1001.
19 Y.-K. Choi and S.-J. Park, *Bulletin of the Korean Chemical Society*, 2016, **37**, 830–834.
20 G. Sethia and A. Sayari, *Carbon*, 2016, **99**, 289–294.
21 T. K. Das, S. Banerjee, P. Sharma, V. Sudarsan and P. U. Sastry, *International Journal of Hydrogen Energy*, 2018, **43**, 8385–8394.
22 J. Jagiello, J. Kenvin, A. Celzard and V. Fierro, *Carbon*, 2019, **144**, 206–215.
23 D. Grau-Marin, J. Silvestre-Albero, E. O. Jardim, J. Jagiello, W. R. Betz and L. E. Peña, *Carbon*, 2020, **157**, 495–505.
24 J. Jagiello, J. Kenvin, C. O. Ania, J. B. Parra, A. Celzard and V. Fierro, *Carbon*, 2020, **160**, 164–175.
25 D. H. Everett and J. C. Powl, *Journal of the Chemical Society, Faraday Transactions 1: Physical Chemistry in Condensed Phases*, 1976, **72**, 619–636.
26 J. Jagiello and M. Thommes, International Conference on Carbon for Energy Storage and Environment Protection, 2005.

27 N. P. Wickramaratne and M. Jaroniec, *Journal of Materials Chemistry A*, 2013, **1**, 112–116.
28 M. De la Casa-Lillo, F. Lamari-Darkrim, D. Cazorla-Amoros and A. Linares-Solano, *The Journal of Physical Chemistry B*, 2002, **106**, 10930–10934.
29 K. R. Matranga, A. Stella, A. L. Myers and E. D. Glandt, *Separation Science and Technology*, 1992, **27**, 1825–1836.
30 S. Reljic, E. Jardim, C. Cuadrado-Collados, M. Bayona, M. Martinez-Escandell, J. Silvestre-Albero and F. Rodríguez-Reinoso, in *CO 2 Adsorption in Activated Carbon Materials*, 2021, pp. 139–152.
31 N. Texier-Mandoki, J. Dentzer, T. Piquero, S. Saadallah, P. David and C. Vix-Guterl, *Carbon*, 2004, **42**, 2744–2747.
32 Z. Tan and K. E. Gubbins, *Journal of Physical Chemistry*, 1990, **94**, 6061–6069.
33 C. M. Simon, J. Kim, D. A. Gomez-Gualdron, J. S. Camp, Y. G. Chung, R. L. Martin, R. Mercado, M. W. Deem, D. Gunter and M. Haranczyk, *Energy & Environmental Science*, 2015, **8**, 1190–1199.
34 L. S. Blankenship, J. Jagiello and R. Mokaya, *Available at SSRN 3946228*, 2022.
35 J. Li, B. Michalkiewicz, J. Min, C. Ma, X. Chen, J. Gong, E. Mijowska and T. Tang, *Chemical Engineering Journal*, 2019, **360**, 250–259.
36 S.-Y. Lee and S.-J. Park, *Journal of Colloid and Interface science*, 2013, **389**, 230–235.
37 S. Hlushak, *Physical Chemistry Chemical Physics*, 2018, **20**, 872–888.
38 G. Sethia and A. Sayari, *Carbon*, 2015, **93**, 68–80.
39 P. Iacomi and P. L. Llewellyn, *Adsorption*, 2019, **25**, 1533–1542.
40 C. M. Simon, B. Smit and M. Haranczyk, *Computer Physics Communications*, 2016, **200**, 364–380.
41 K. Pearson, *Proceedings of the Royal Society of London*, 1895, **58**, 240–242.
42 J. D. Evans, V. Bon, I. Senkovska and S. Kaskel, *Langmuir*, 2021, **37**, 4222–4226.
43 P. C. Hansen, *SIAM review*, 1992, **34**, 561–580.
44 P. C. Hansen and D. P. O'Leary, *SIAM Journal on Scientific Computing*, 1993, **14**, 1487–1503.
45 P. Hansen, in *The L-curve and its use in the numerical treatment of inverse problems*, ed. P. Johnston, WIT Press, Southampton, 2001, pp. 119–142.
46 I. Langmuir, *Journal of the American Chemical Society*, 1916, **38**, 2221–2295.
47 I. Langmuir, *Journal of the American Chemical society*, 1918, **40**, 1361–1403.
48 E. A. Guggenheim, *Applications of Statistical Mechanics*, Oxford Clarendon Press, 1966.
49 R. B. Anderson, *Journal of the American Chemical Society*, 1946, **68**, 686–691.
50 J. H. de Boer, *The Dynamical Character of Adsorption*, Oxford Clarendon Press, 1953, vol. 76.
51 H. Freundlich, *Zeitschrift für Physikalische Chemie*, 1907, **57**, 385–470.
52 B. Bering, M. Dubinin and V. Serpinsky, *Journal of Colloid and Interface Science*, 1966, **21**, 378–393.
53 J. Tóth, *Journal of Colloid and Interface Science*, 1994, **163**, 299–302.
54 M. E. Casco, M. Martínez-Escandell, J. Silvestre-Albero and F. Rodríguez-Reinoso, *Carbon*, 2014, **67**, 230–235.
55 M. Sevilla, A. S. M. Al-Jumialy, A. B. Fuertes and R. Mokaya, *ACS Applied Materials & Interfaces*, 2018, **10**, 1623–1633.

7.3 Summary & Future Work

The pyPUC method is a thorough, intuitive, and assumption-less route to understanding the relationship between adsorbent pore size and physisorptive uptake capacity of some adsorbate. It expands upon both purely computational and purely experimental methods by performing a broad analysis of the correlation (*via* the Pearson coefficient, r^2) of porosity within pores of some range of widths and adsorbate uptake at some pressure. Its utility has been demonstrated in **Publication II** with CO_2 on turbostratic carbons, with porosity derived from N_2 isotherms as well as by comparing results derived using PSDs from different porosimetric adsorbates.

The relationship between CH_4 uptake in turbostratic carbons and pore size is one of the least well understood in the field of small gas molecule capture and storage.[1,16–18] This problem should be considered a priority for the use of pyPUC - indeed as CH_4 is a non-polar molecule and larger than CO_2,[19,20] results from this analysis should be less influenced by carbon surface chemistry and very small ultramicropores and thus may provide a simpler understanding of the relationship between pore size and pressure-dependent gas uptake. Similarly pyPUC ought to be applied to H_2 storage; while the relationship between pore size and H_2 uptake capacity is perhaps one of the best understood, the analysis could provide some interesting insights. However, this could be problematic in that the general consensus is that optimum pore size for H_2 uptake is 6.0 Å[2,21] so porosity ought to be probed by a small sorptive like H_2 - it could be considered unreasonable to determine porosity with the same molecule for which the materials' uptake capacity is being assessed.

pyPUC currently only considers the uptake capacity in the derivation of the Ω. In the future, pyPUC should be expanded to include isosteric heat

of adsorption q_{st} as a variable. While q_{st} is typically determined using the Clausius-Clapeyron method,[22,23] the analysis could perhaps be made more efficient by employing the Whittaker method which has been shown to yield comparable results and only requires a single isotherm.[24,25] pyPUC could then be used to derive a relationship between porosity in some range of pore sizes and q_{st}.

7.4 Publication II Supporting Information: Brute force determination of the optimum pore sizes for CO_2 uptake

Supplementary Information

Brute force determination of the optimum pore sizes for CO_2 uptake†

L. Scott Blankenship,[a*] Nawaf Albeladi,[ab‡] Thria Alkhaldi,[ac‡] Asma Madkhali,[ad‡] and Robert Mokaya[a]

[a] *School of Chemistry, University of Nottingham, University Park, Nottingham, NG7 2RD, UK. Email: leo.blankenship@nottingham.ac.uk*

[b] *Chemistry Department, Faculty of Sciences Yanbu, Taibah University, Yanbu Al Bahr, 46423, Saudi Arabia*

[c] *Department of Chemistry, Jeddah University, Jeddah 23442, Saudi Arabia*

[d] *Department of Chemistry, University College in Samtah, Jazan University, Samtah 86736, Saudi Arabia*

† Electronic Supplementary Information (ESI) available: [Supplementary figures and tables; raw (.aif) isotherms; PSD and modelling analysis summaries as .csv; and raw outputs of D_v, D_π, and D_c for each dataset (.csv)]. See DOI: 00.0000/00000000.

‡ These authors contributed equally to this work.

S1 DataSet 1

Sample code: *PP(xxx)-yTTT*

Where *PP* denotes precursor(s); see table below. *xxx* is used in the case of mixed precursors and denotes the ratio (in %) of second precursor to first. *y* is weight ratio of KOH:precursor. *TTT* is the activation temperature in °C.

Table S1.1 Synthetic information and PSD fitting parameter, λ for samples in dataset 1

Prefix	Number of samples	Precursor	Notes	λ
aP	7	Air carbonised (400 °C) prickly pear		2.5
PUxxx	11	Potassium Hydrogen Phthalate (P), Urea (U)	1 h carbonisation at T	4.0
aT	9	Air carbonised (350 °C) hookah tobacco		3.5
hC	3	Hydrothermally carbonised (350 °C) used cigarette butts	Hydrochar not washed	4.0
hD	3	Hydrothermally carbonised (250 °C) used cigarette butts	Hydrochar washed	4.0

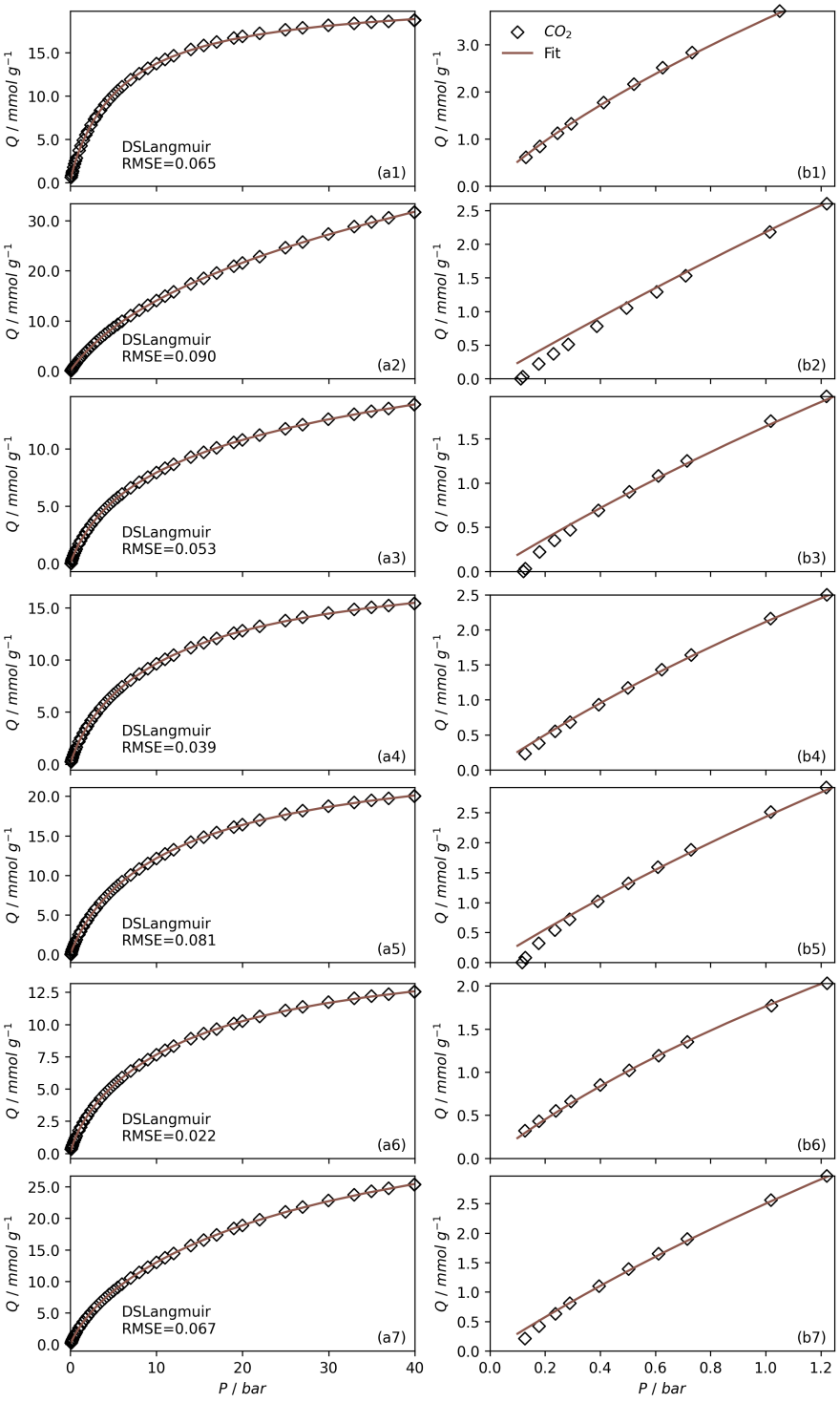

Figure S1.1 CO_2 uptake isotherms and fits in the range 0-40 and 0-1 bar, column (a) and (b) respectively for samples aP-2700, aP-2800, aP-2900, aP-3700, aP-3800, aP-4700, aP-4800 in order in rows (1-7).

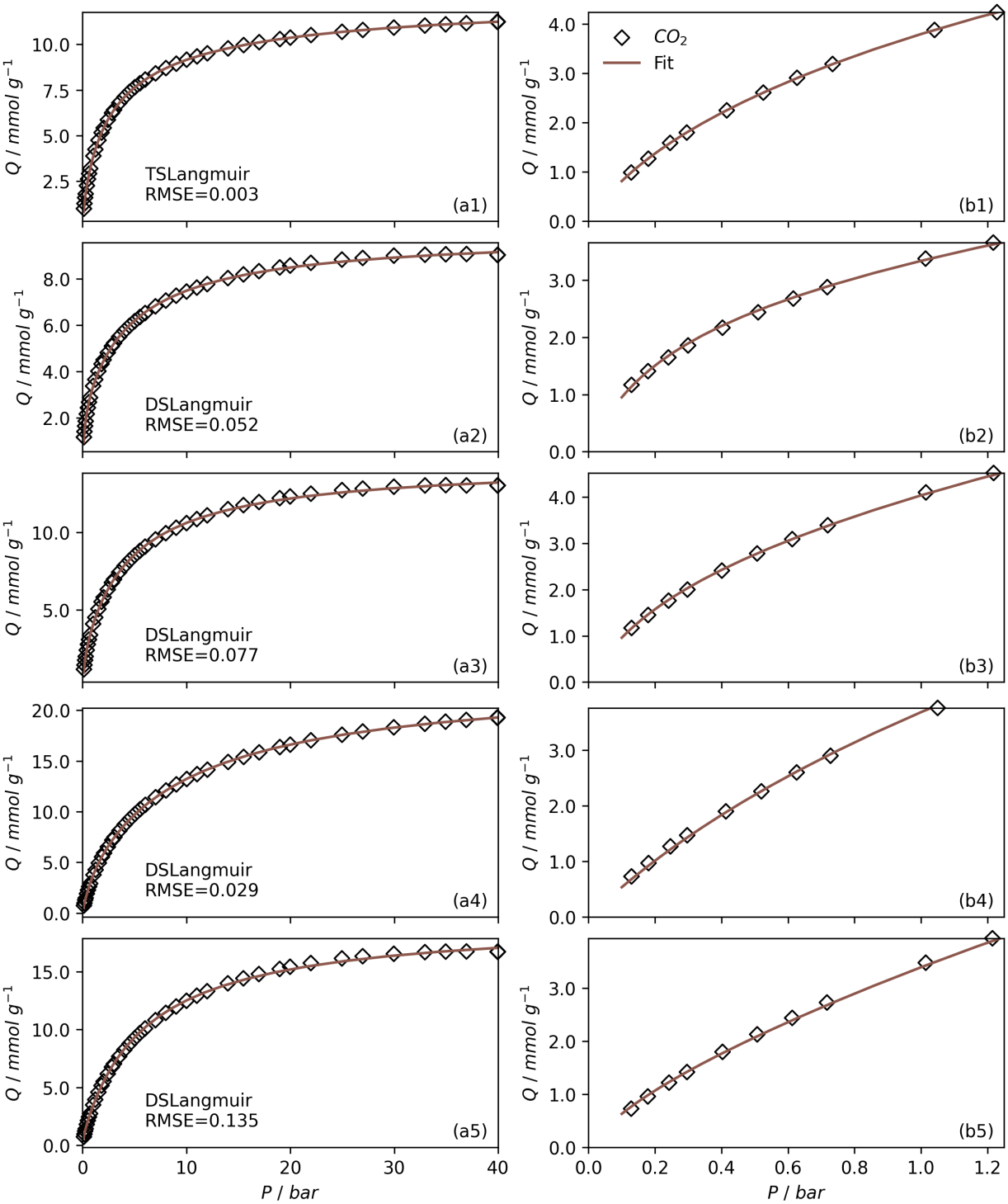

Figure S1.2 CO_2 uptake isotherms and fits in the range 0-40 and 0-1 bar, column (a) and (b) respectively for samples PU000-800, PU025-800, PU025-700, PU025-800, PU025-900 in order in rows (1-5).

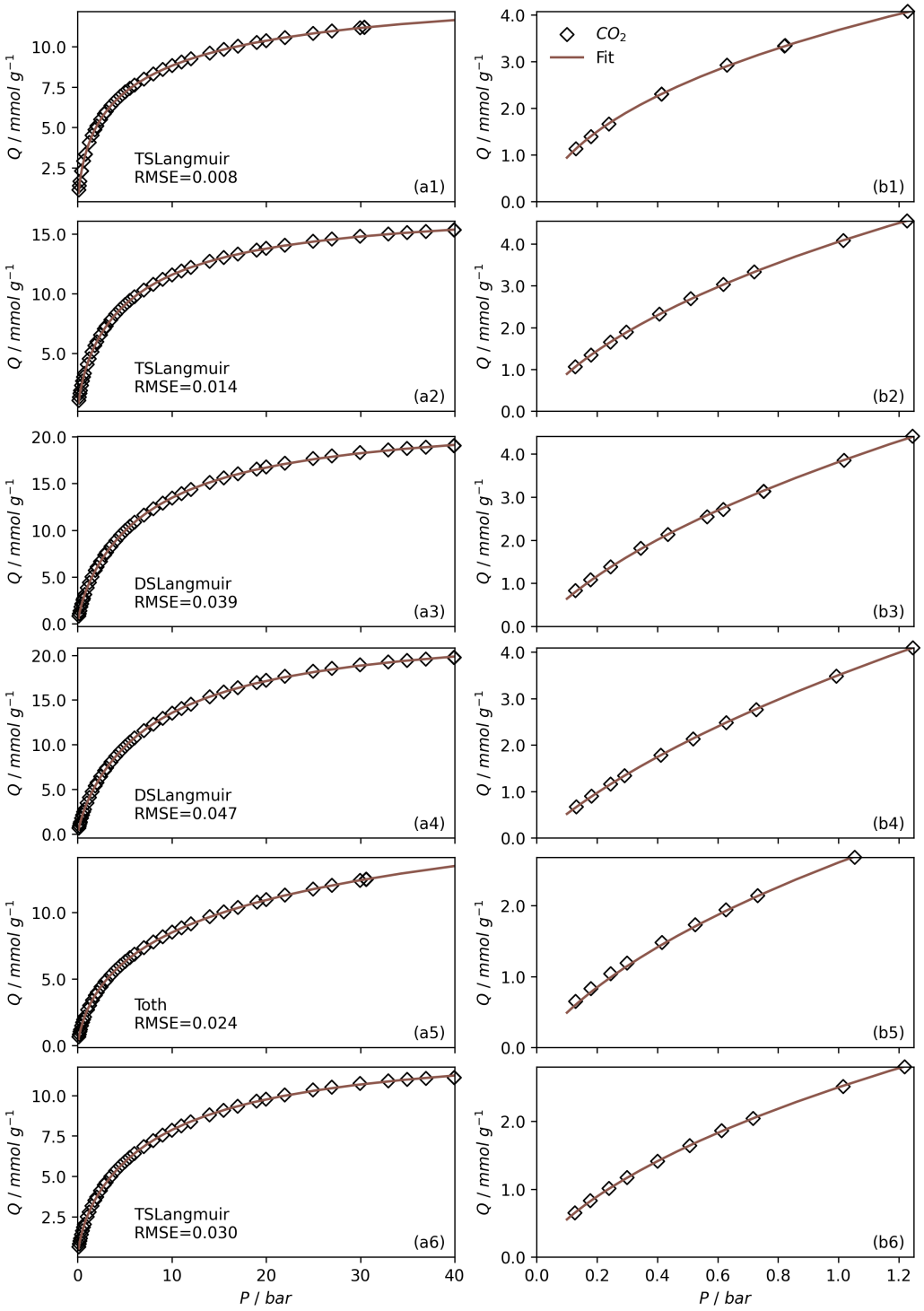

Figure S1.3 CO_2 uptake isotherms and fits in the range 0-40 and 0-1 bar, column (a) and (b) respectively for samples PU050-600, PU050-700, PU050-800, PU050-900, PU100-800, PU100-900 in order in rows (1-6).

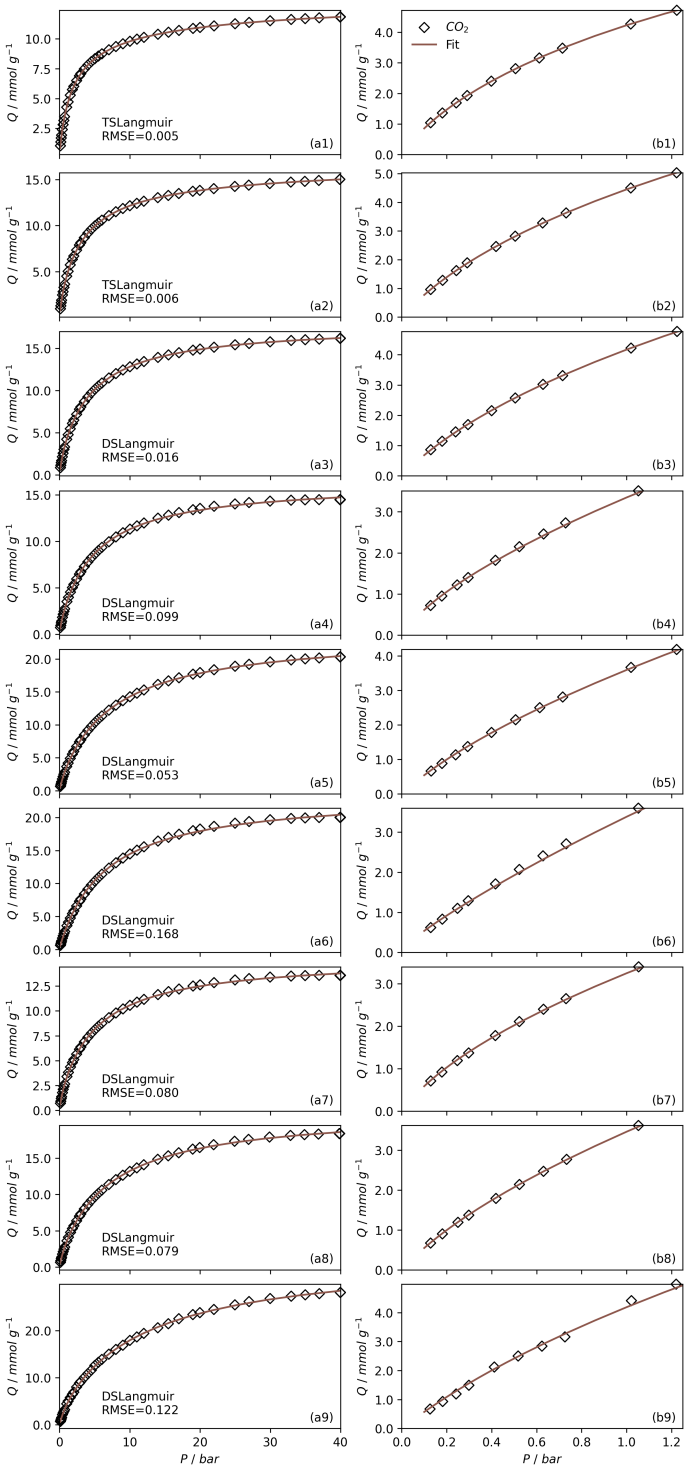

Figure S1.4 CO_2 uptake isotherms and fits in the range 0-40 and 0-1 bar, column (a) and (b) respectively for samples aT-2600, aT-2700, aT-2800, aT-2800, aT-4600, aT-4700, aT-4800, aT-6600, aT-6700, aT-6800 in order in rows (1-9).

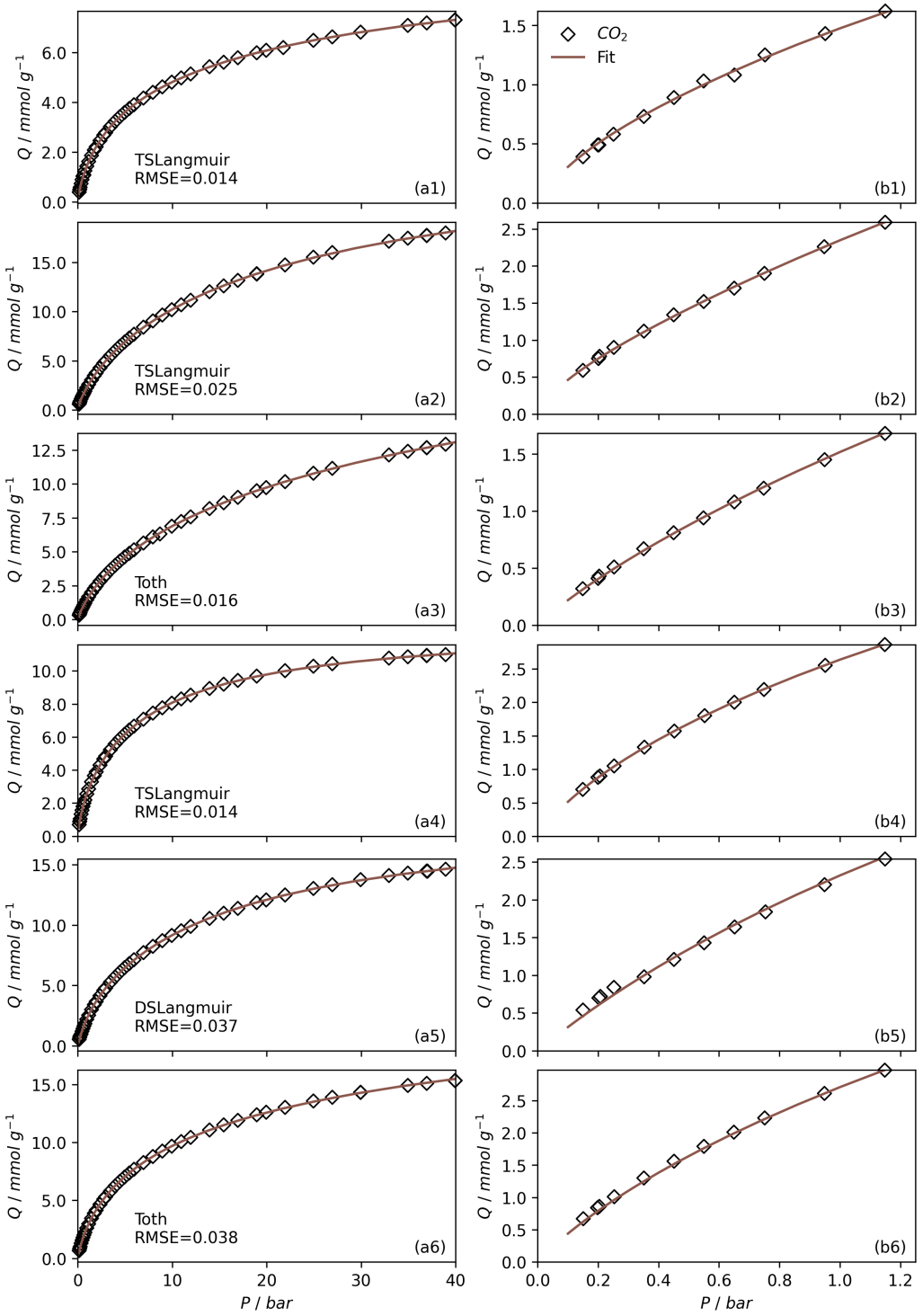

Figure S1.5 CO_2 uptake isotherms and fits in the range 0-40 and 0-1 bar, column (a) and (b) respectively for samples hD-4600, hD-4700, hD-4800, hC-4600, hC-4700, hC-4800 in order in rows (1-6).

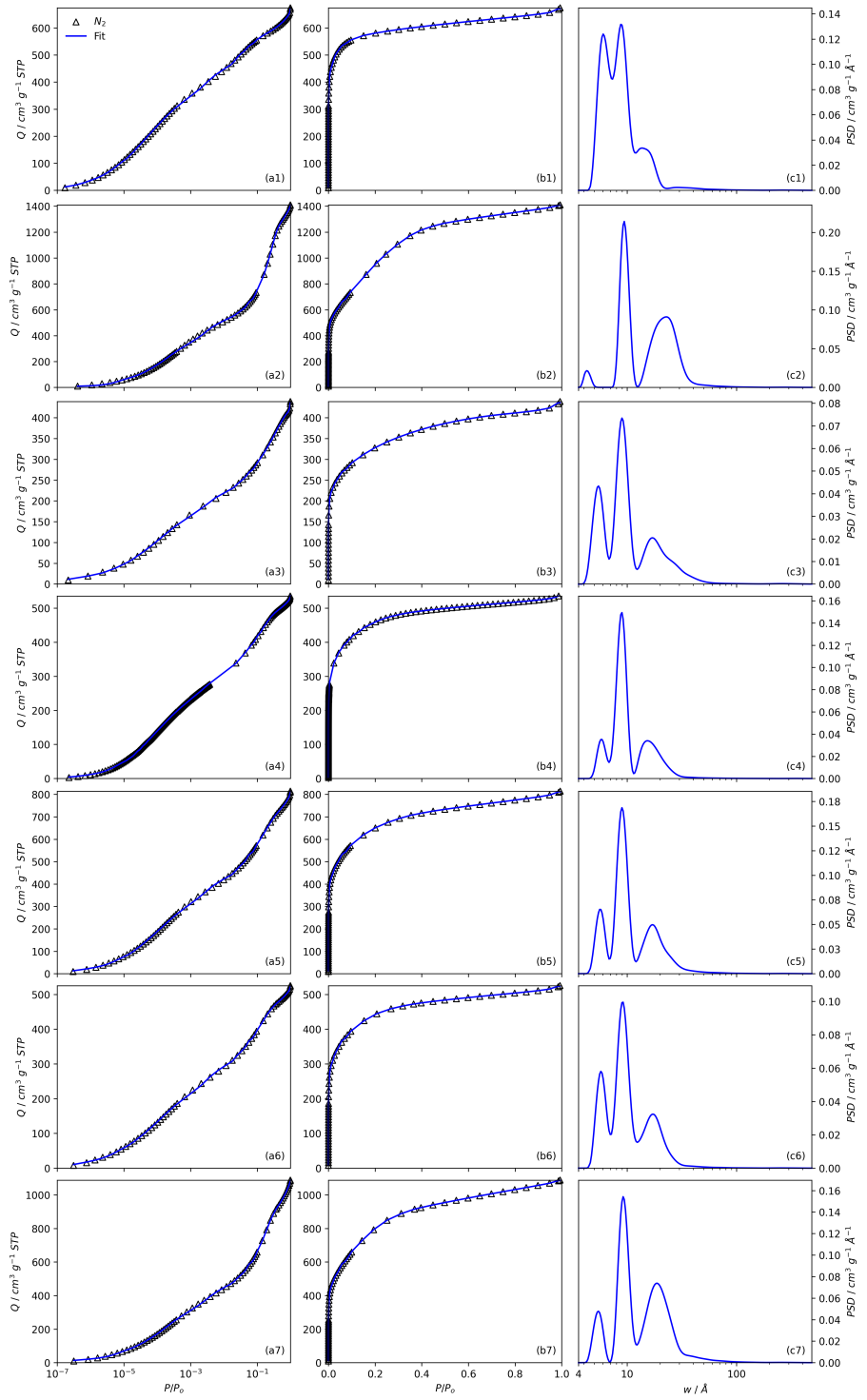

Figure S1.6 Fits to N_2 isotherms with logarithmic (column a) and linear (column b) relative pressure scale, and resultant differential PSDs (column c) for samples aP-2700, aP-2800, aP-2900, aP-3700, aP-3800, aP-4700, aP-4800 in order in rows (1-7).

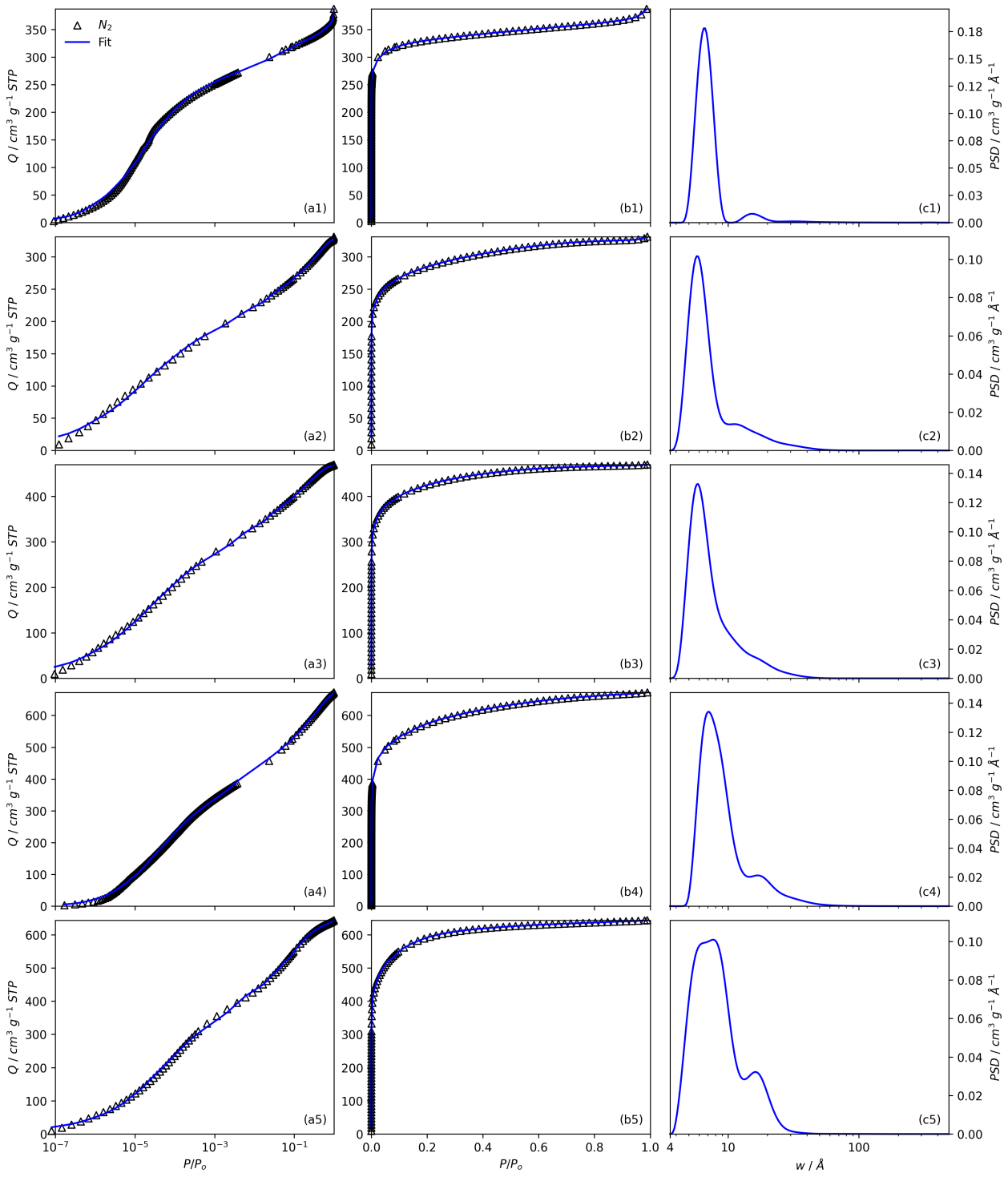

Figure S1.7 Fits to N_2 isotherms with logarithmic (column a) and linear (column b) relative pressure scale, and resultant differential PSDs (column c) for samples PU000-800, PU025-800, PU025-700, PU025-800, PU025-900 in order in rows (1-5).

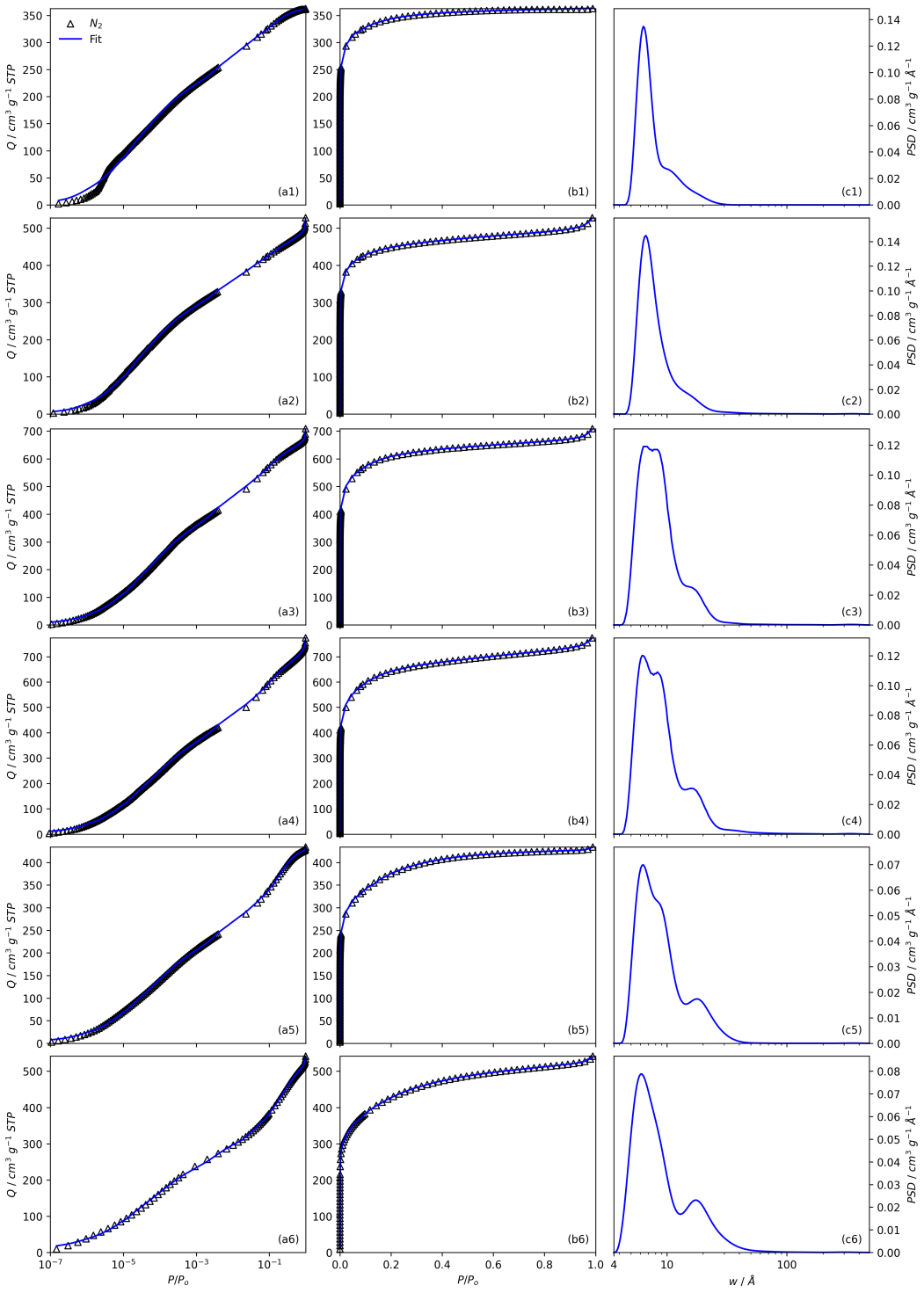

Figure S1.8 Fits to N_2 isotherms with logarithmic (column a) and linear (column b) relative pressure scale, and resultant differential PSDs (column c) for samples PU050-600, PU050-700, PU050-800, PU050-900, PU100-800, PU100-900 in order in rows (1-6).

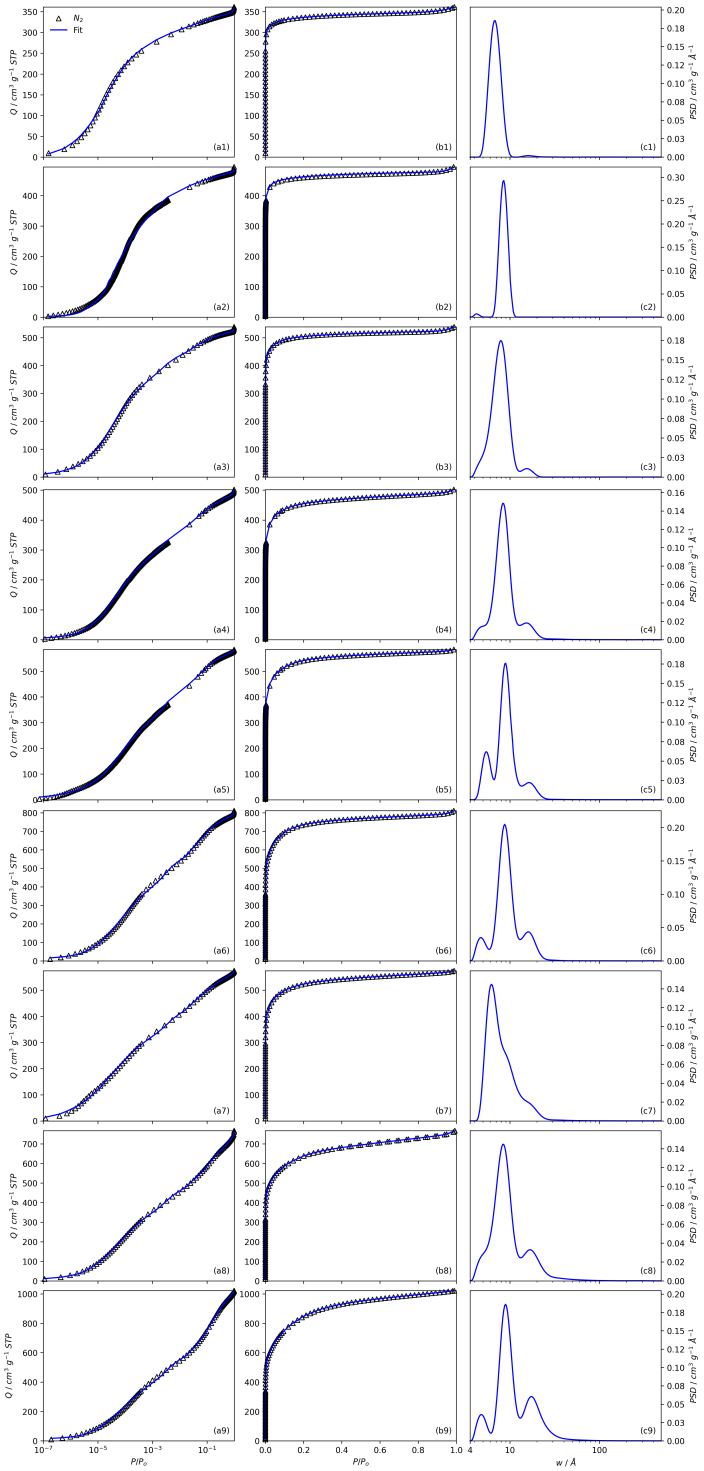

Figure S1.9 Fits to N_2 isotherms with logarithmic (column a) and linear (column b) relative pressure scale, and resultant differential PSDs (column c) for samples aT-2600, aT-2700, aT-2800, aT-2800, aT-4600, aT-4700, aT-4800, aT-6600, aT-6700, aT-6800 in order in rows (1-9).

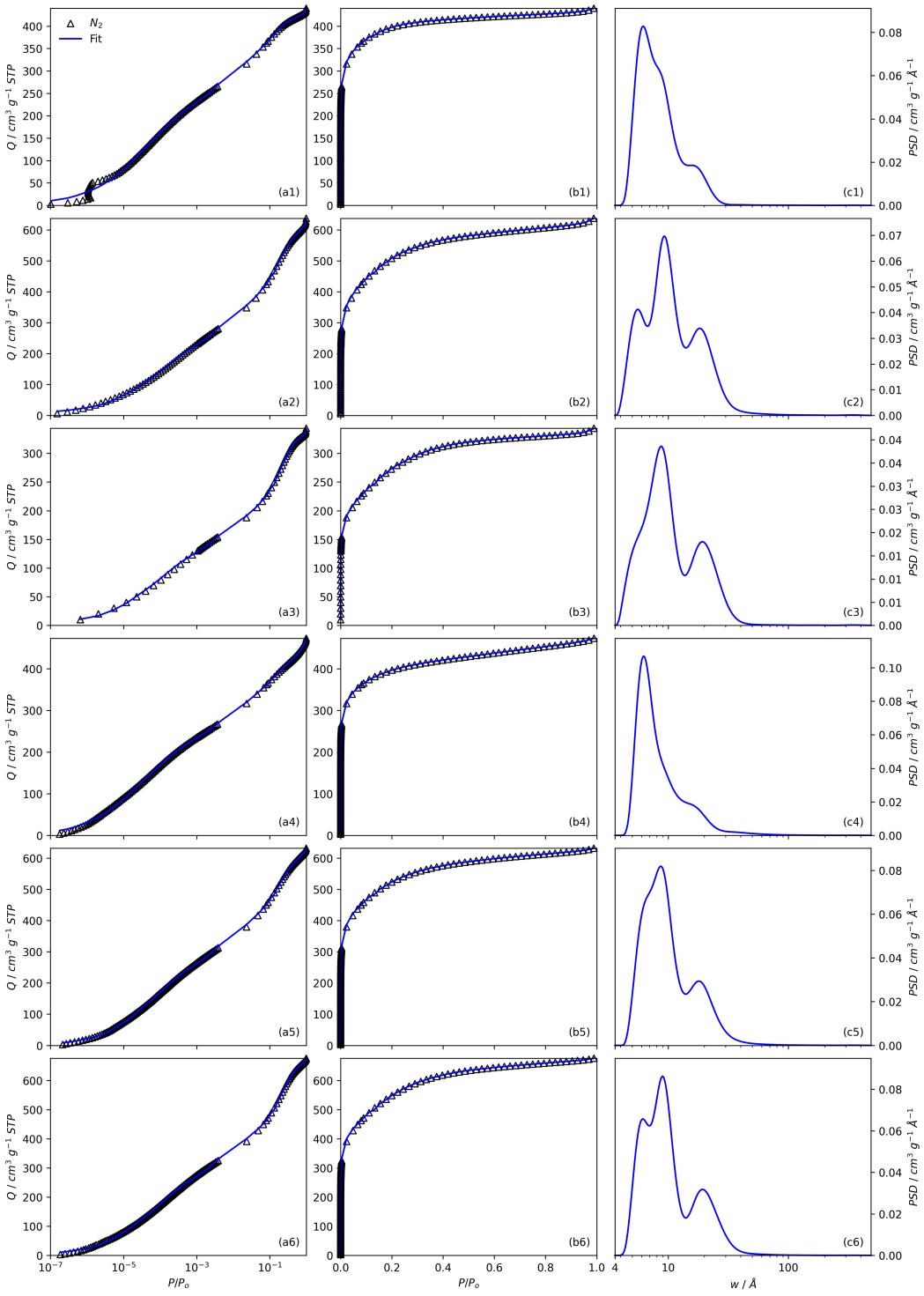

Figure S1.10 Fits to N_2 isotherms with logarithmic (column a) and linear (column b) relative pressure scale, and resultant differential PSDs (column c) for samples hD-4600, hD-4700, hD-4800, hC-4600, hC-4700, hC-4800 in order in rows (1-6).

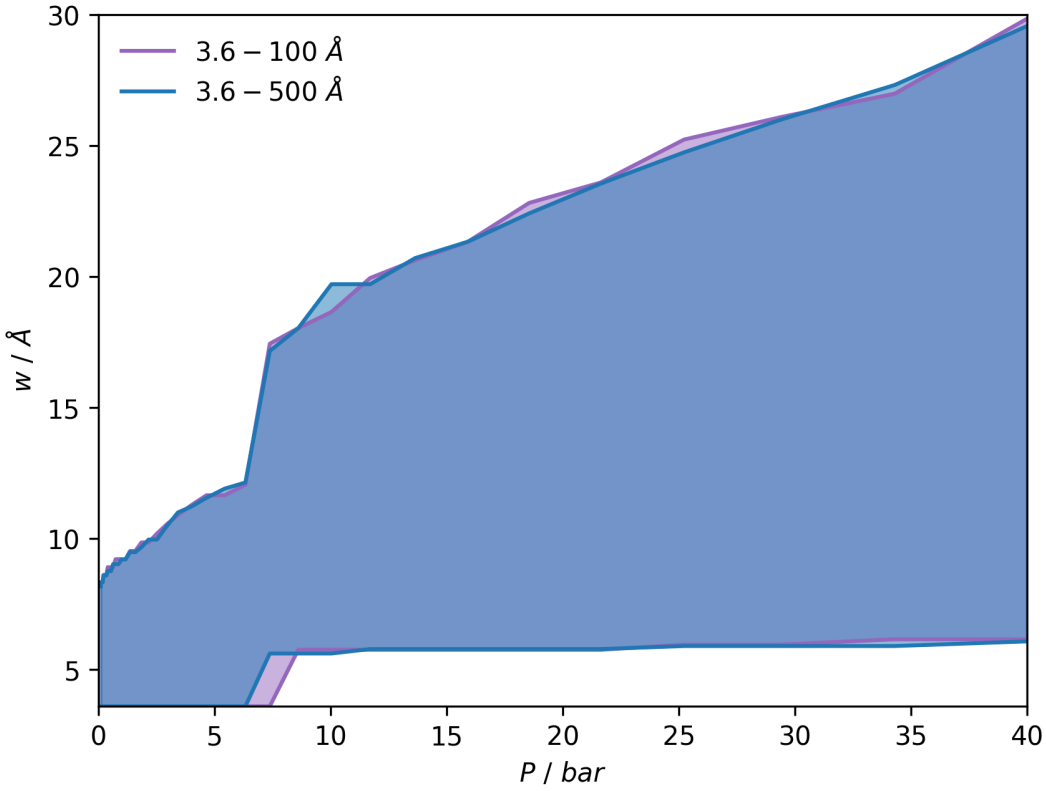

Figure S1.11 Comparison of Ω_V when D_π is calculated from 3.6-100 and 3.6-500 Å using 100 and 500 widths, respectively.

S2 Dataset 2

Sample code: *PPy.y-(HHH)*
Where *PP* denotes precursor(s); see table below. *y.y* s the ratio of porogen (KOH or $NaOOCCH_2$) to precursor. *HHH* is only used for SD samples, and signifies the hydrothermal carbonisation temperature. More detailed information found in original paper.[1]

Table S2.1 Synthetic information and PSD fitting parameter, λ for samples in dataset 2

Prefix	Number of samples	Precursor	Notes	λ
NC	4	Sodium carboxymethyl cellulose	*y.y* determined by degree of substitution	3.5
SD	8	Eucalyptus sawdust	Prepared by hydrothermal carbonisation with KOH at weight ratio defined by *y.y* prior to activation	4.0

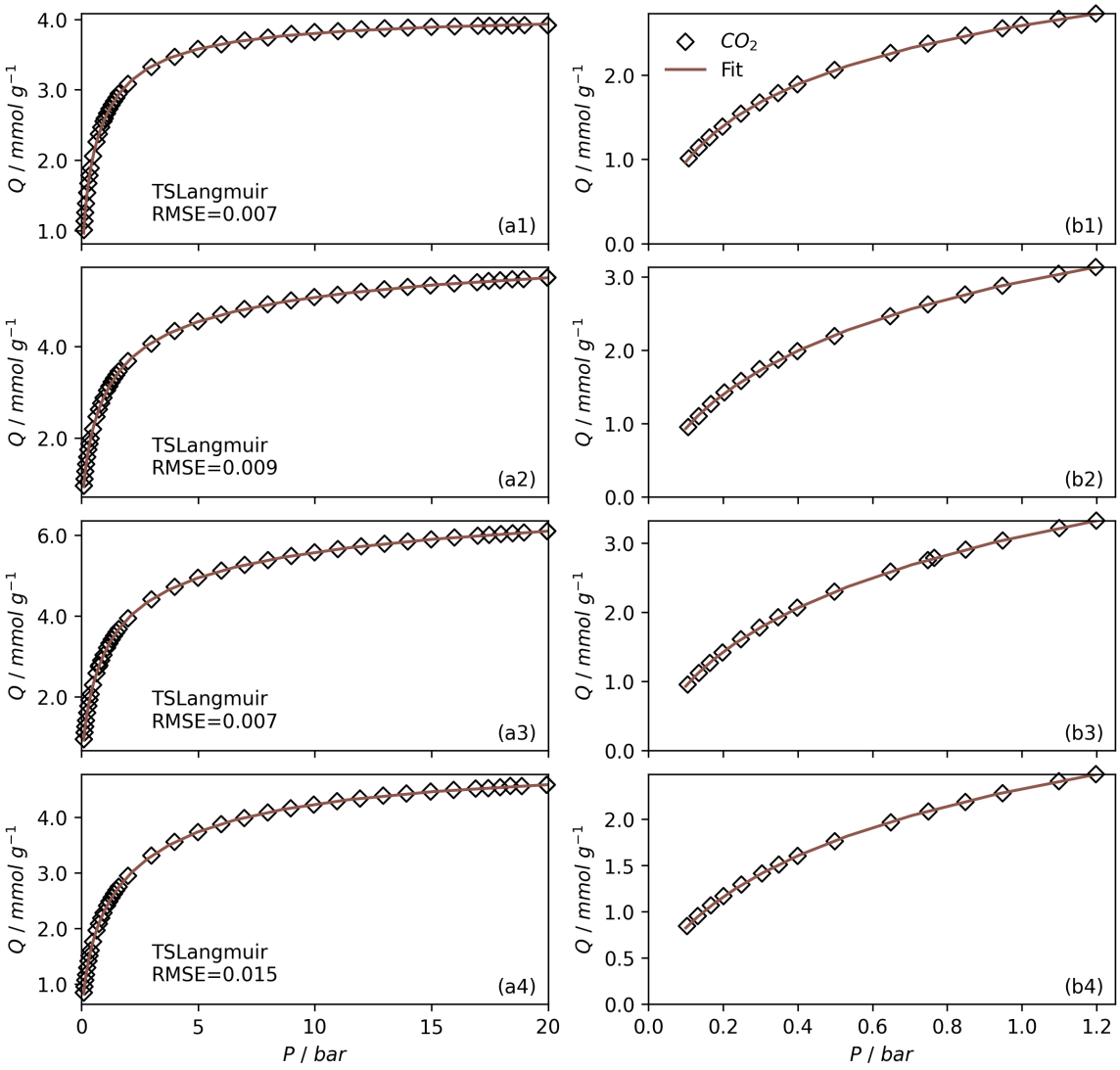

Figure S2.1 CO_2 uptake isotherms and fits in the range 0-20 and 0-1 bar, column (a) and (b) respectively for samples NC0.0, NC0.7, NC0.9, and NC1.2 in order in rows (1-4).

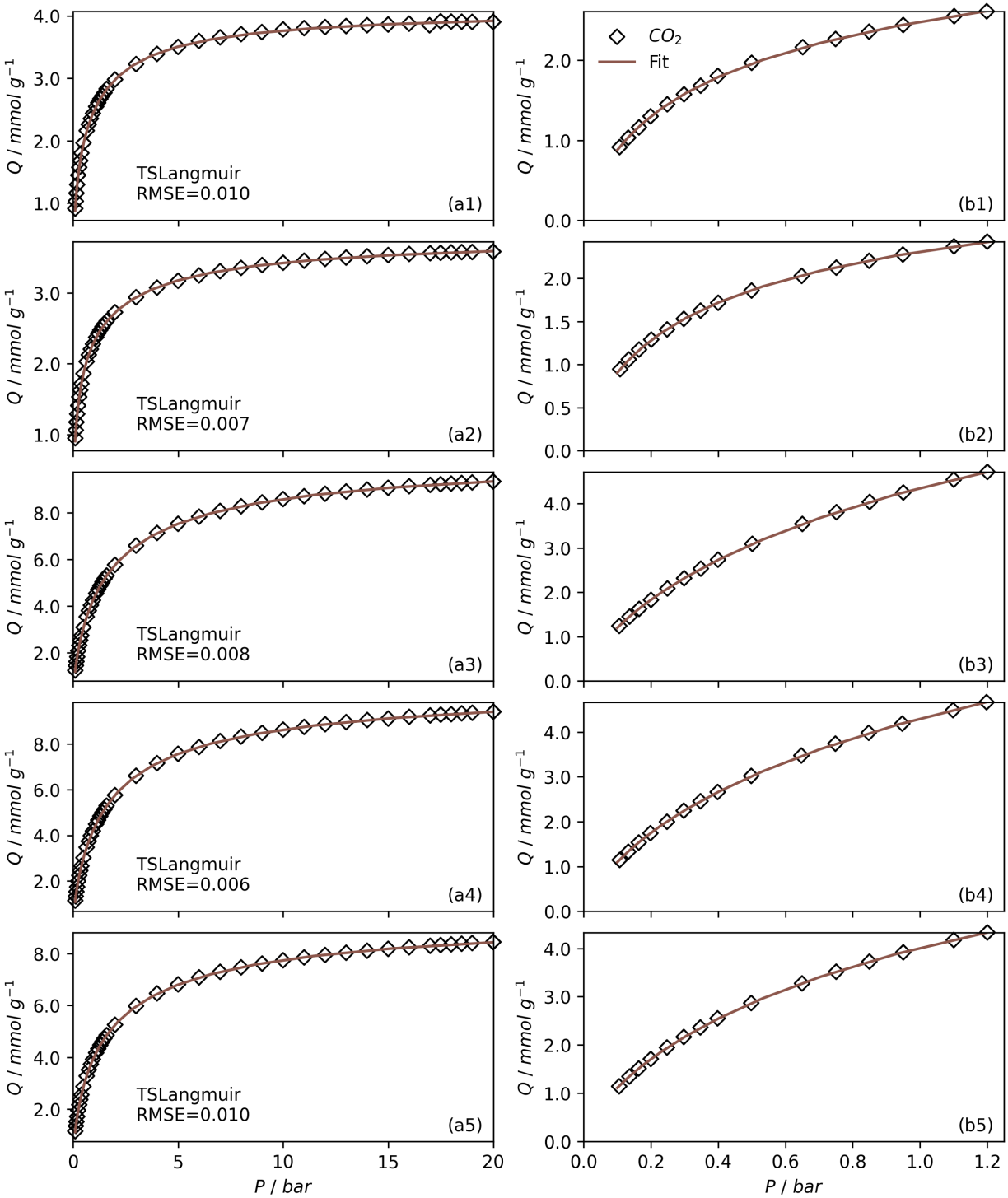

Figure S2.2 CO_2 uptake isotherms and fits in the range 0-20 and 0-1 bar, column (a) and (b) respectively for samples SA0.0-250, SA0.0-300, SA0.5-200, SA0.5-250, SA0.5-300 in order in rows (1-5).

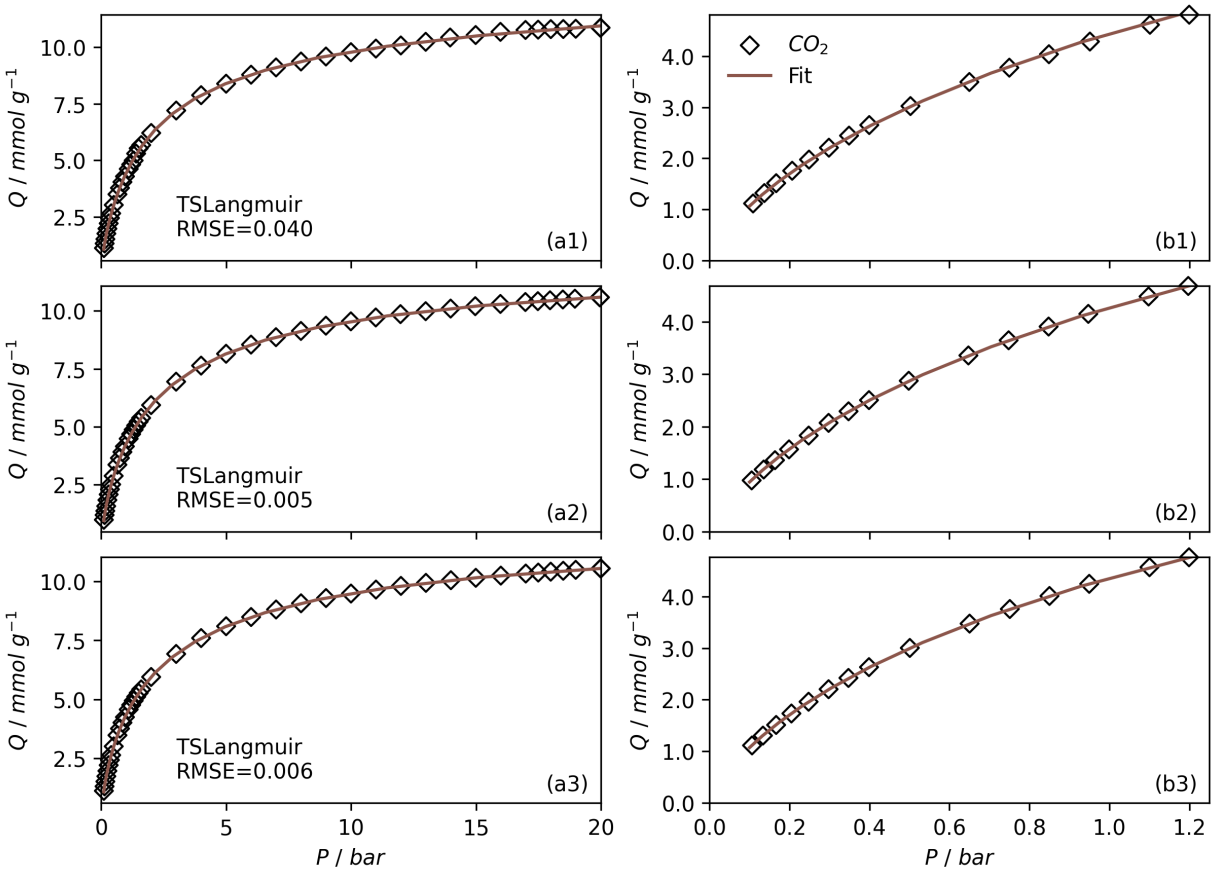

Figure S2.3 CO_2 uptake isotherms and fits in the range 0-20 and 0-1 bar, column (a) and (b) respectively for samples SA1.0-200, SA1.0-250, SA1.0-300 in order in rows (1-3).

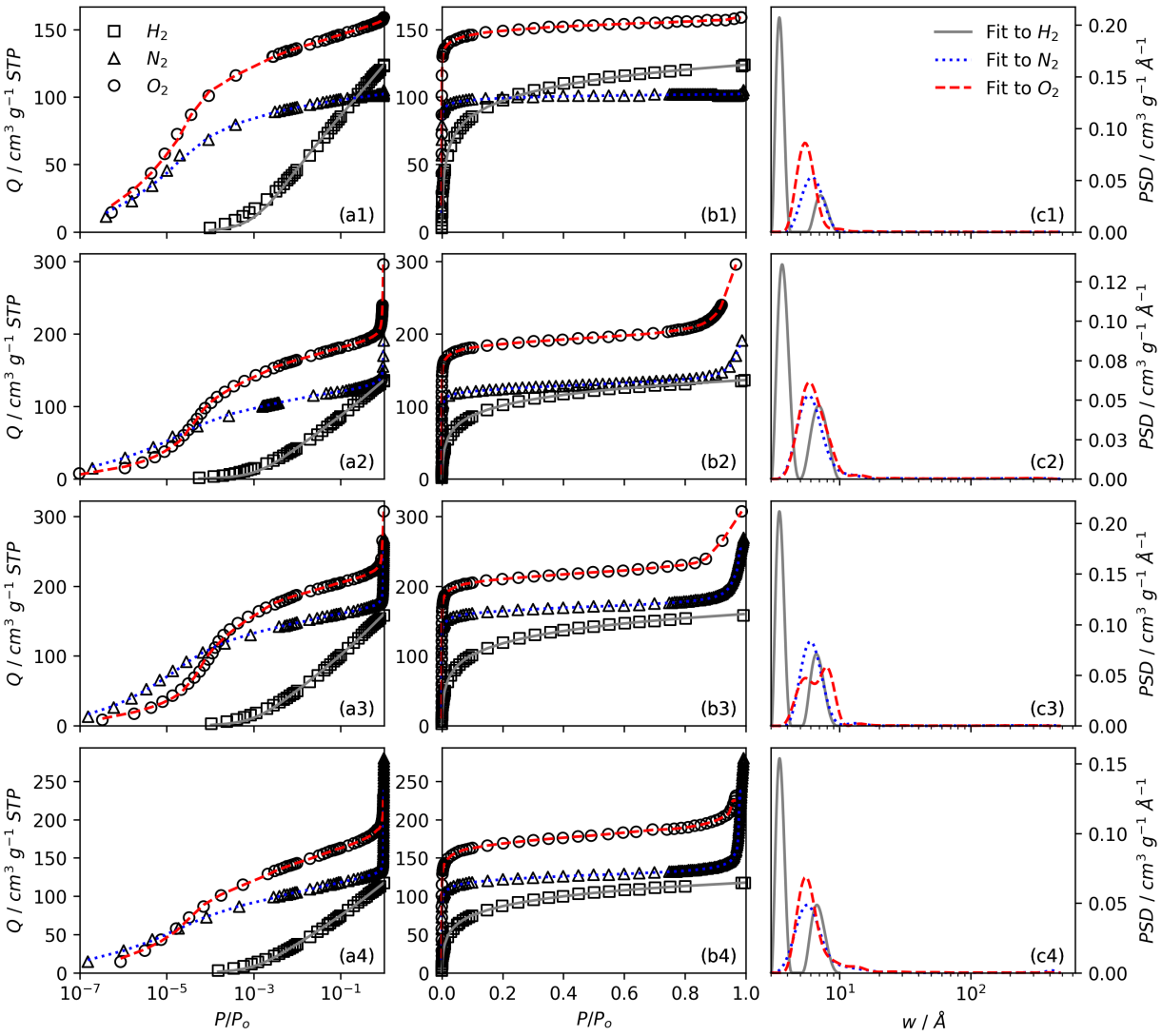

Figure S2.4 Individual fits to H_2, N_2, and O_2 isotherms with logarithmic (column a) and linear (column b) relative pressure scale, and resultant differential PSDs (column c) for samples NC0.0, NC0.7, NC0.9, and NC1.2 in order in rows (1-4).

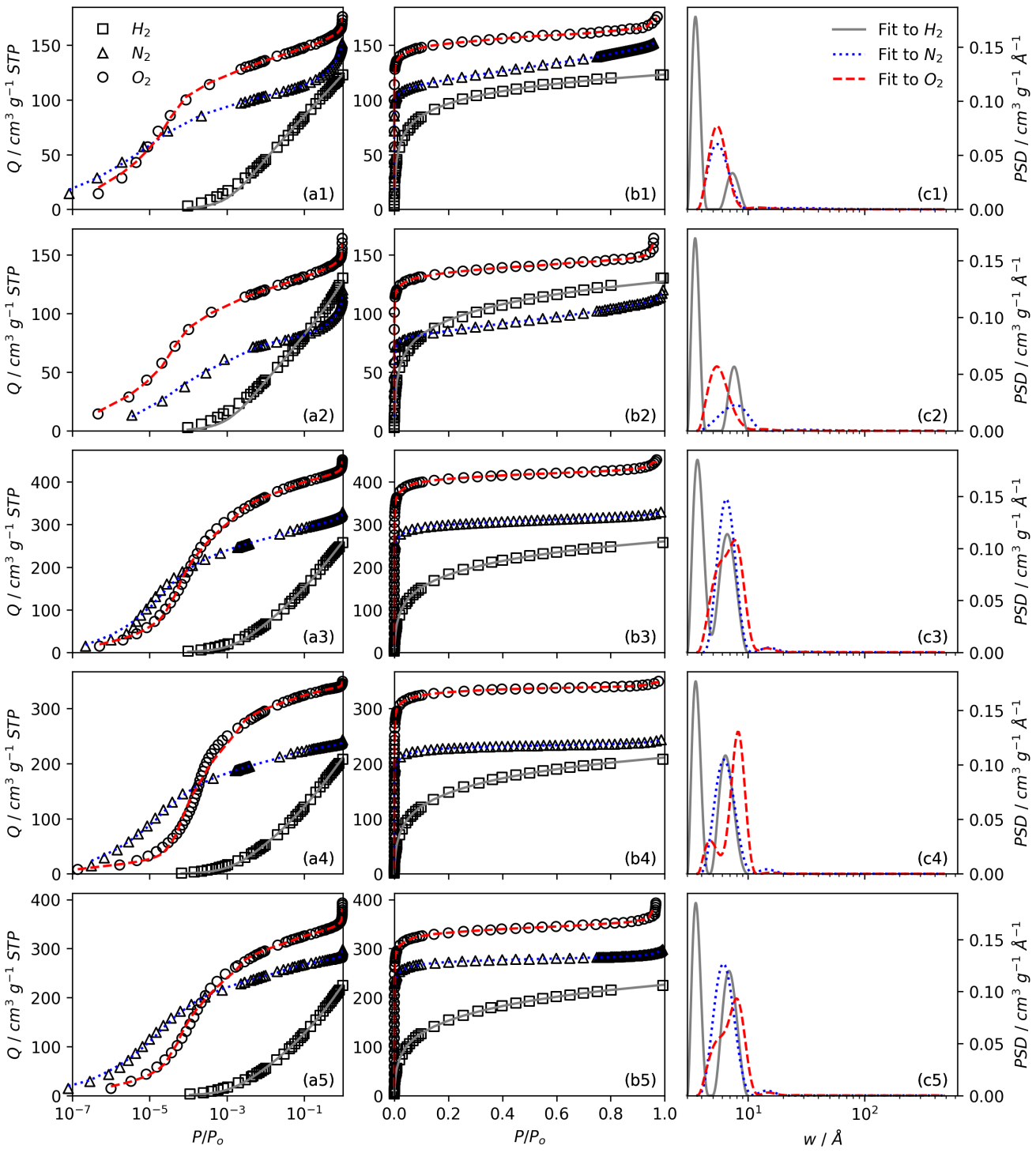

Figure S2.5 Individual fits to H_2, N_2, and O_2 isotherms with logarithmic (column a) and linear (column b) relative pressure scale, and resultant differential PSDs (column c) for samples SA0.0-250, SA0.0-300, SA0.5-200, SA0.5-250, SA0.5-300 in order in rows (1-5).

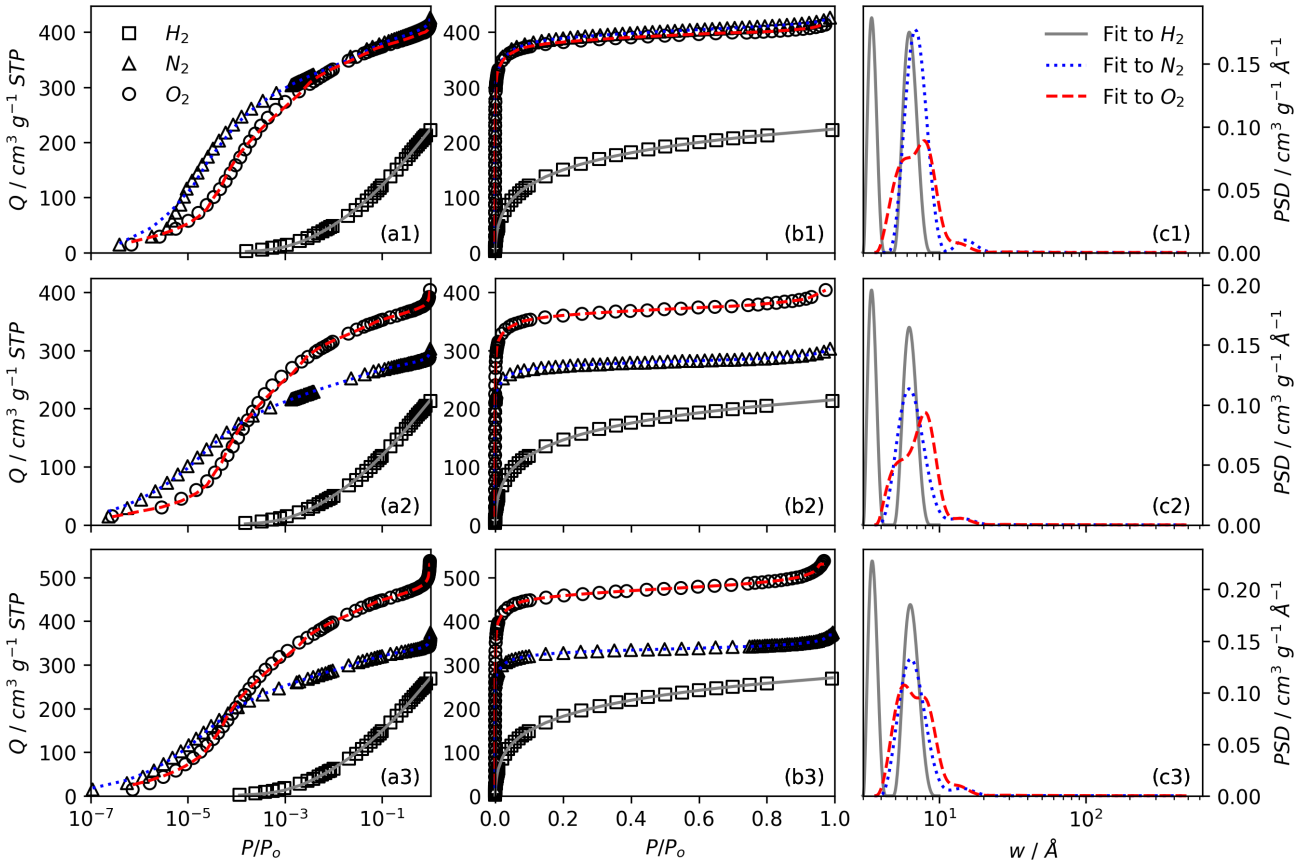

Figure S2.6 Individual fits to H_2, N_2, and O_2 isotherms with logarithmic (column a) and linear (column b) relative pressure scale, and resultant differential PSDs (column c) for samples SA1.0-200, SA1.0-250, SA1.0-300 in order in rows (1-3).

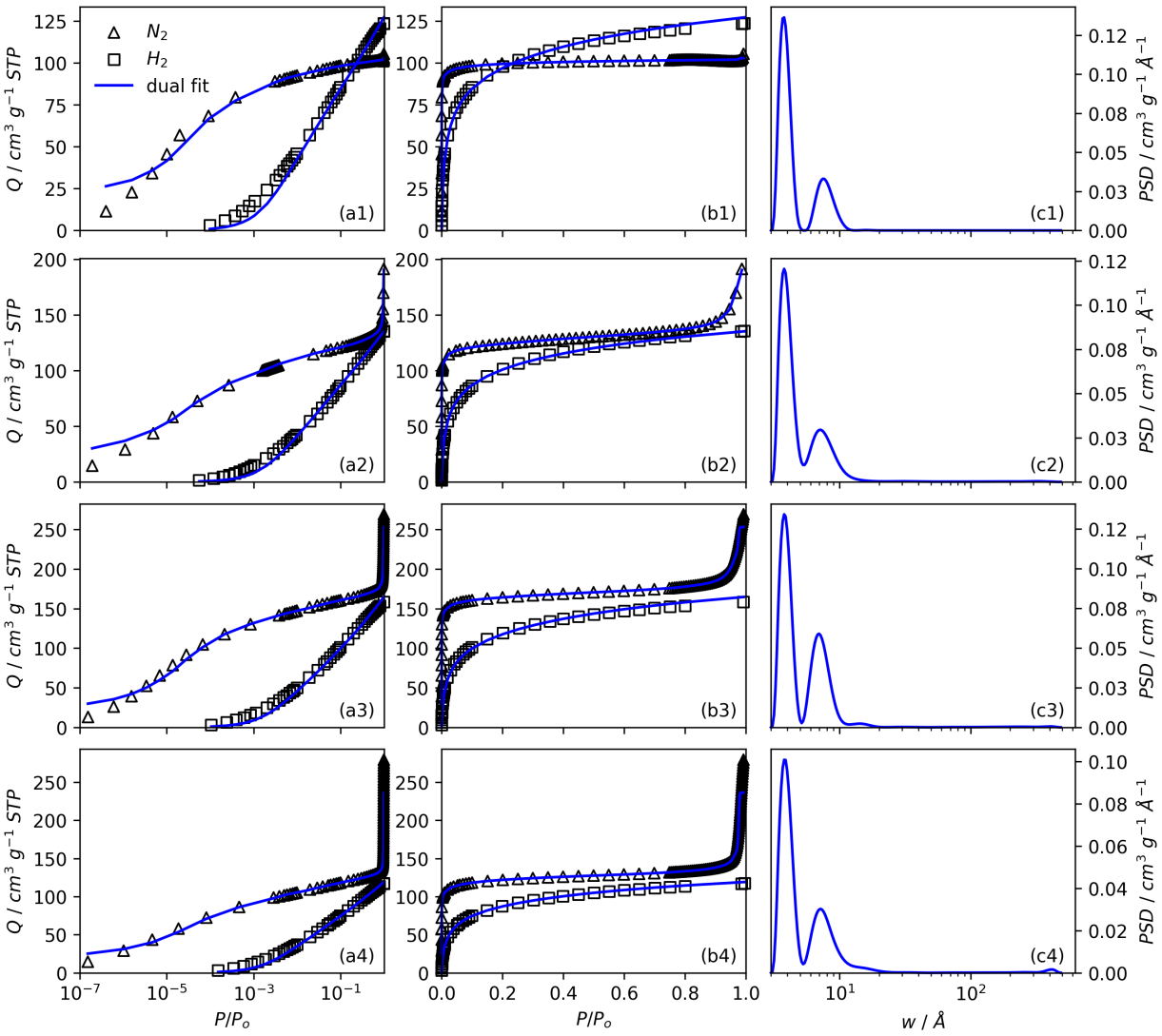

Figure S2.7 Dual fits to N_2, and H_2 isotherms with logarithmic (column a) and linear (column b) relative pressure scale, and resultant differential PSDs (column c) for samples NC0.0, NC0.7, NC0.9, and NC1.2 in order in rows (1-4).

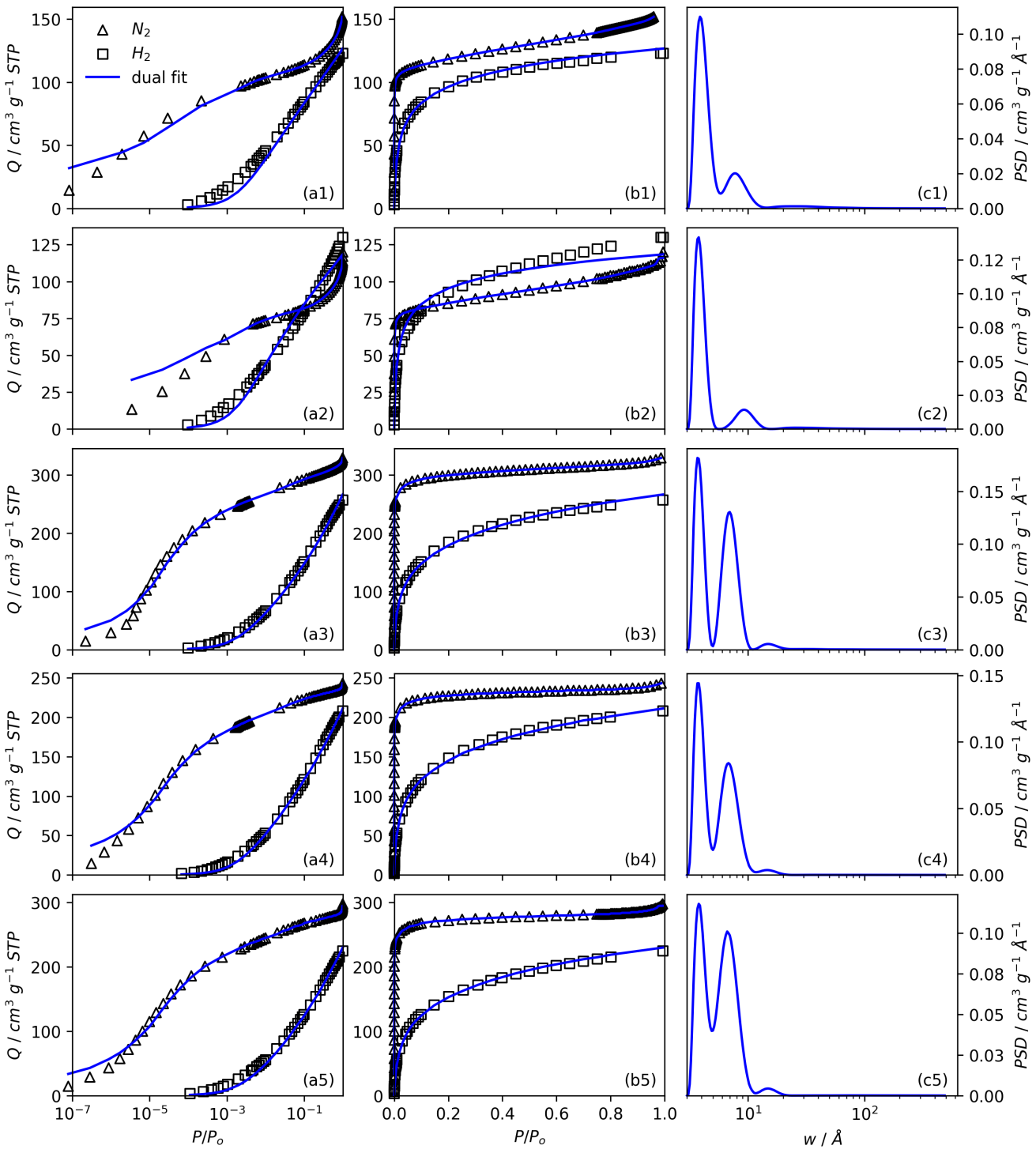

Figure S2.8 Dual fits to N_2, and H_2 isotherms isotherms with logarithmic (column a) and linear (column b) relative pressure scale, and resultant differential PSDs (column c) for samples SA0.0-250, SA0.0-300, SA0.5-200, SA0.5-250, SA0.5-300 in order in rows (1-5).

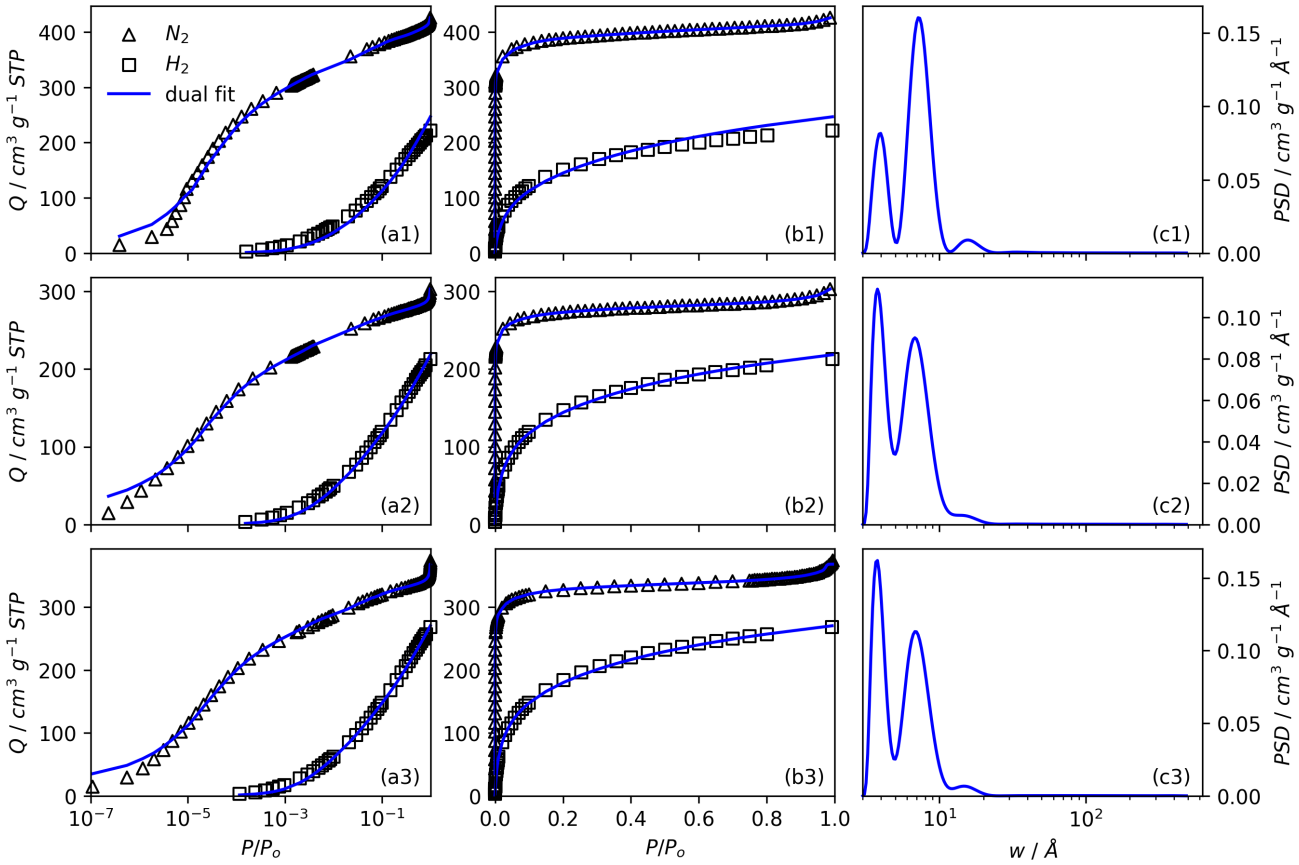

Figure S2.9 Dual fits to N_2, and H_2 isotherms with logarithmic (column a) and linear (column b) relative pressure scale, and resultant differential PSDs (column c) for samples SA1.0-200, SA1.0-250, SA1.0-300 in order in rows (1-3).

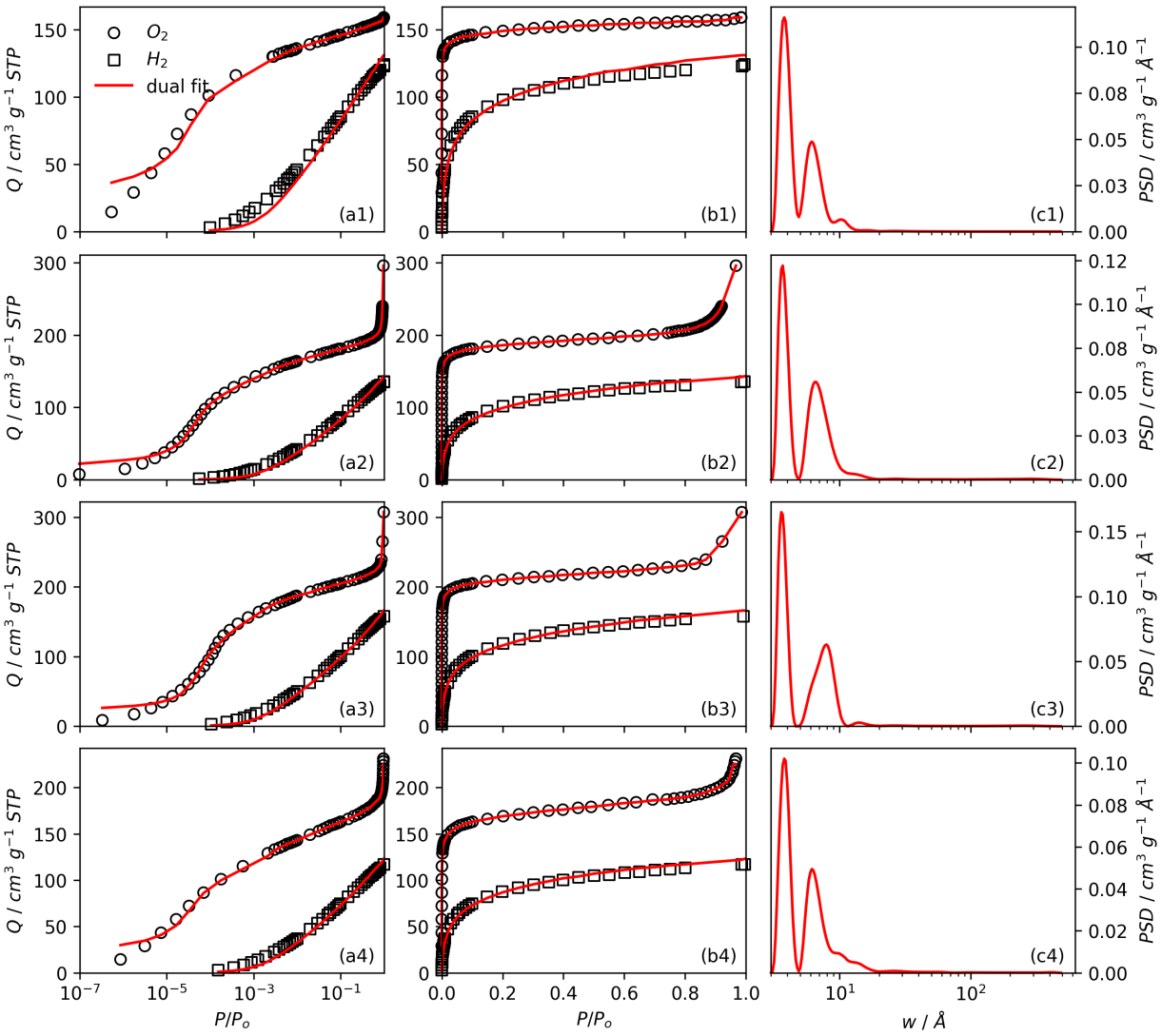

Figure S2.10 Dual fits to O_2, and H_2 isotherms with logarithmic (column a) and linear (column b) relative pressure scale, and resultant differential PSDs (column c) for samples NC0.0, NC0.7, NC0.9, and NC1.2 in order in rows (1-4).

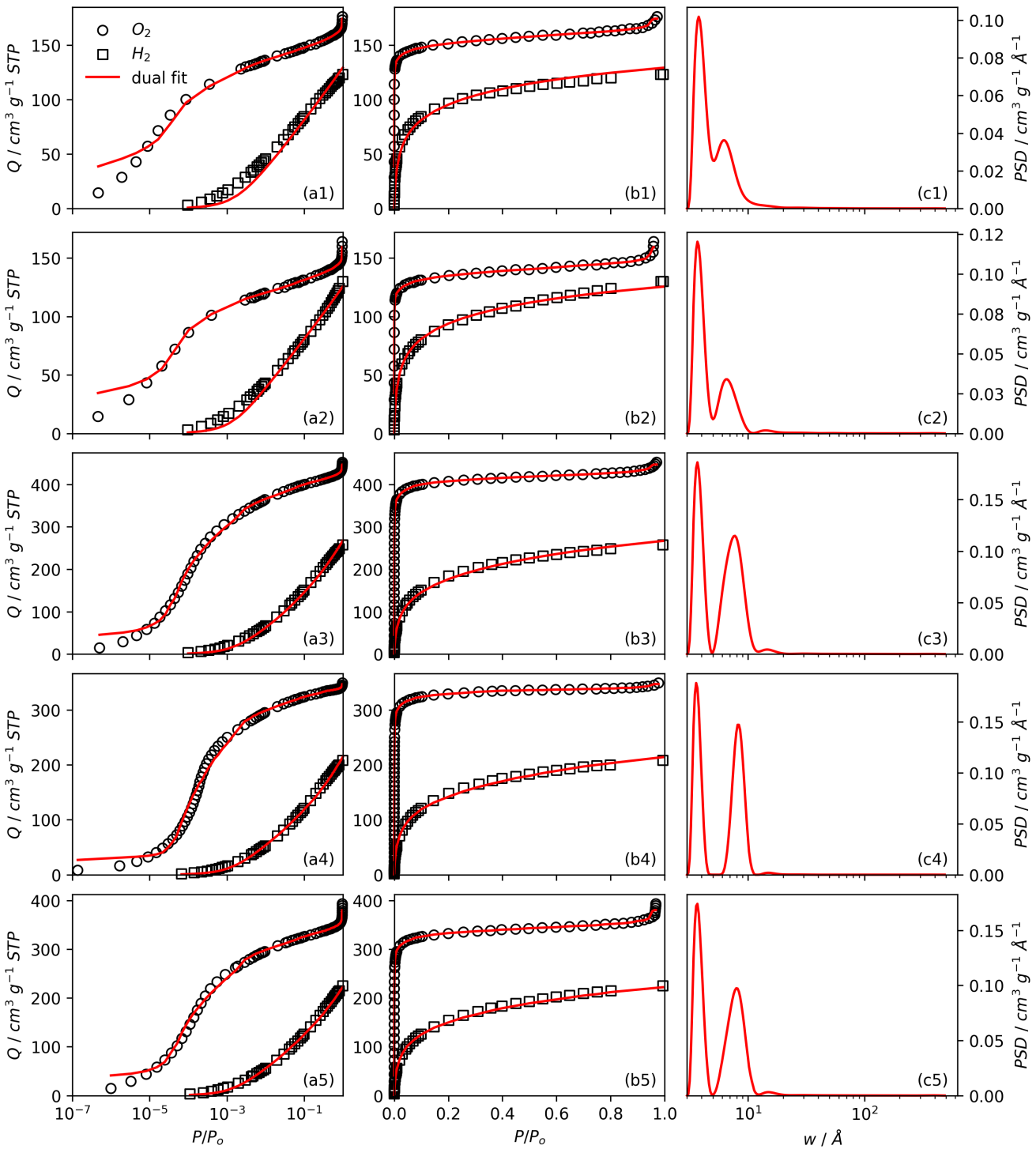

Figure S2.11 Dual fits to O_2, and H_2 isotherms isotherms with logarithmic (column a) and linear (column b) relative pressure scale, and resultant differential PSDs (column c) for samples SA0.0-250, SA0.0-300, SA0.5-200, SA0.5-250, SA0.5-300 in order in rows (1-5).

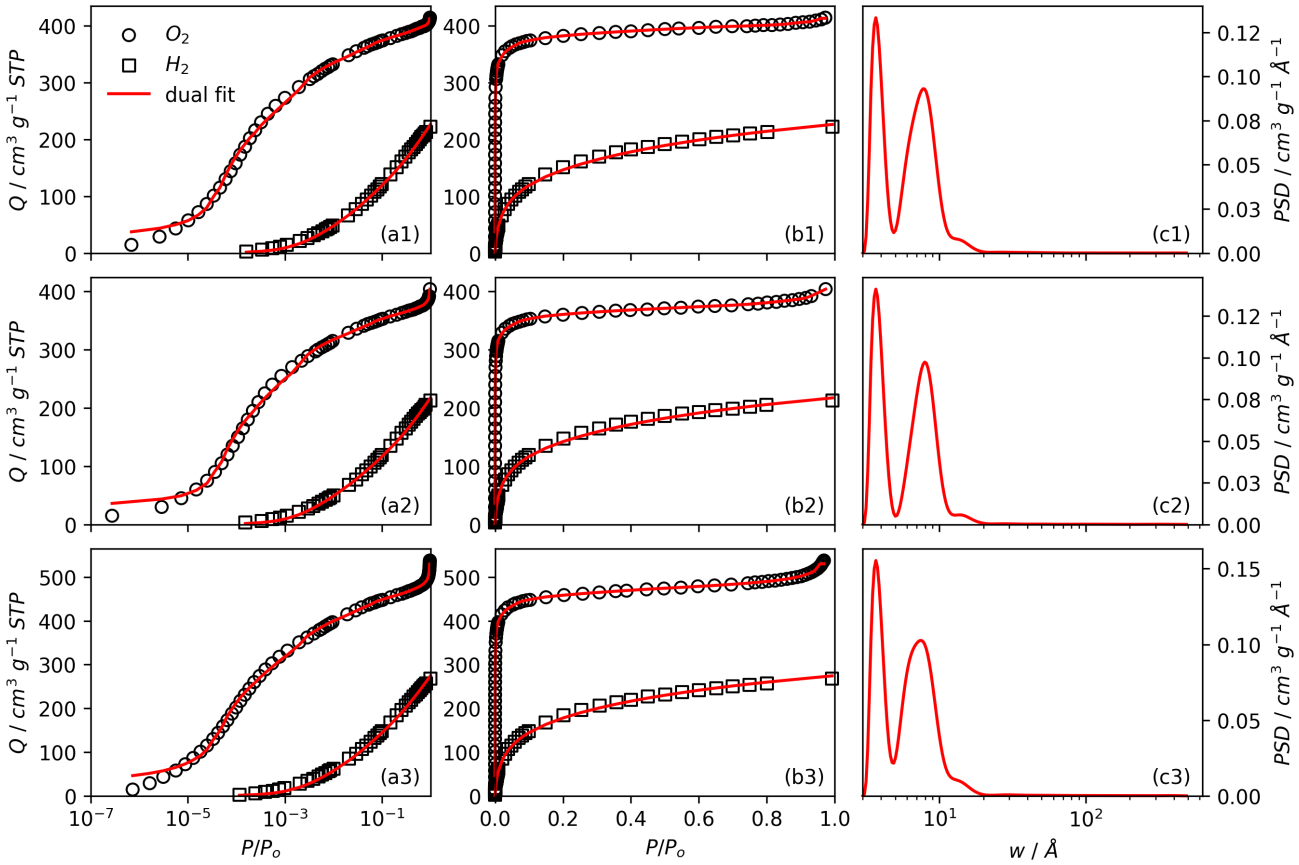

Figure S2.12 Dual fits to O_2, and H_2 isotherms with logarithmic (column a) and linear (column b) relative pressure scale, and resultant differential PSDs (column c) for samples SA1.0-200, SA1.0-250, SA1.0-300 in order in rows (1-3).

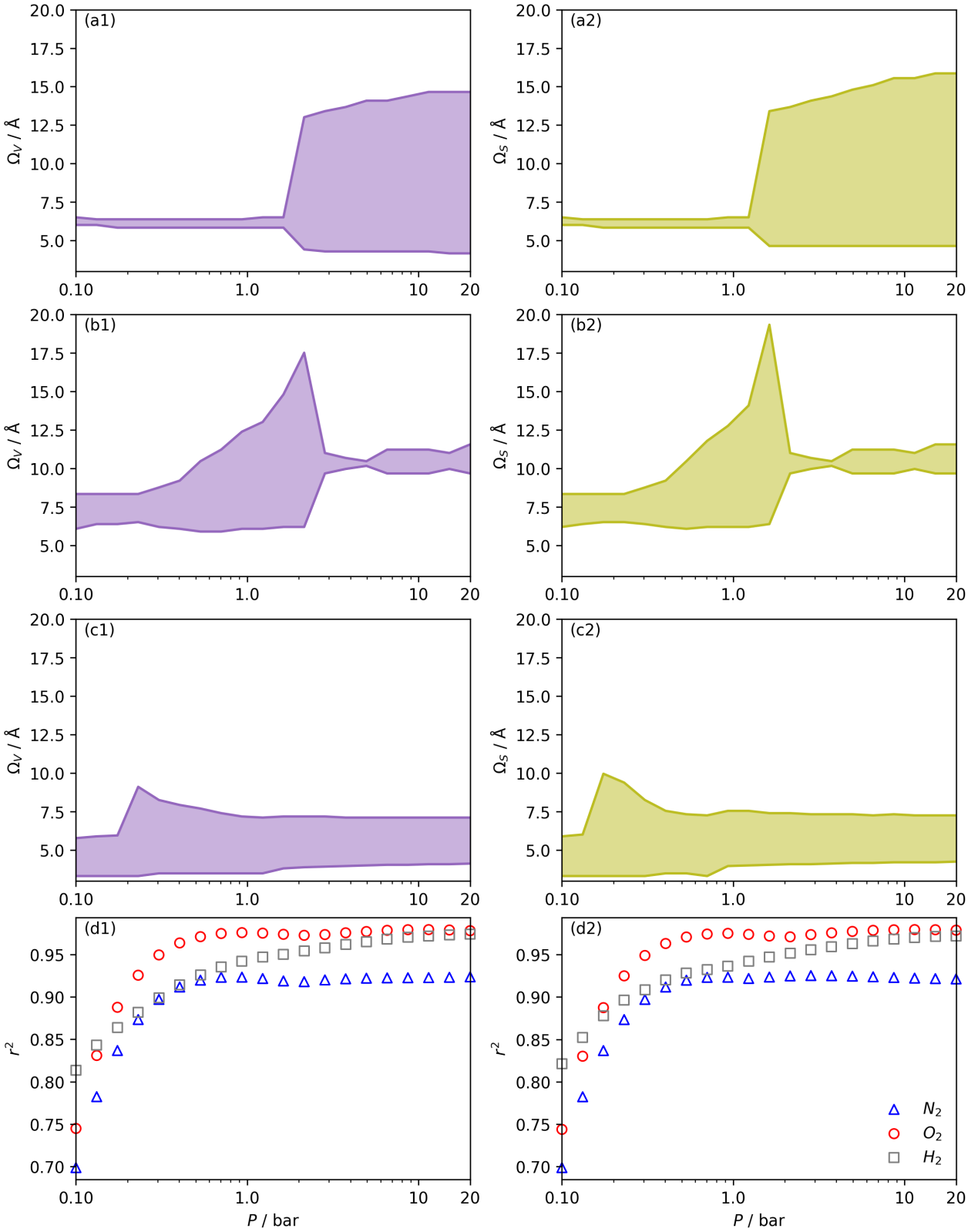

Figure S2.13 : Ω_V (column 1) and Ω_S (column 2) calculated using PSDs N_2 (row a), O_2 (row b), and H_2 (row c) isotherms as well as corresponding r^2 values (row d).

Notes and references

[1] L. S. Blankenship, J. Jagiello and R. Mokaya, *Available at SSRN 3946228*, 2022.

References

1. S. Biloé, V. Goetz and A. Guillot, *Carbon*, 2002, **40**, 1295–1308.
2. I. Cabria, M. J. López and J. A. Alonso, *Carbon*, 2007, **45**, 2649–2658.
3. S. Hlushak, *Physical Chemistry Chemical Physics*, 2018, **20**, 872–888.
4. S. Choi, M. A. Alkhabbaz, Y. G. Wang, R. M. Othman and M. Choi, *Carbon*, 2019, **141**, 143–153.
5. V. Presser, J. McDonough, S.-H. Yeon and Y. Gogotsi, *Energy & Environmental Science*, 2011, **4**, 3059–3066.
6. M. Sevilla, J. B. Parra and A. B. Fuertes, *ACS Applied Materials & Interfaces*, 2013, **5**, 6360–6368.
7. B. Adeniran and R. Mokaya, *Chemistry of Materials*, 2016, **28**, 994–1001.
8. N. P. Wickramaratne and M. Jaroniec, *Journal of Materials Chemistry A*, 2013, **1**, 112–116.
9. J. Jagiello and W. Betz, *Microporous and Mesoporous Materials*, 2008, **108**, 117–122.
10. J. Jagiello, J. Kenvin, A. Celzard and V. Fierro, *Carbon*, 2019, **144**, 206–215.
11. J. Jagiello, J. Kenvin, C. O. Ania, J. B. Parra, A. Celzard and V. Fierro, *Carbon*, 2020, **160**, 164–175.
12. M. Sevilla, N. Díez and A. B. Fuertes, *ChemSusChem*, 2021, **14**, 94–117.
13. J. Ludwinowicz and M. Jaroniec, *Carbon*, 2015, **94**, 673–679.
14. J. Singh, S. Basu and H. Bhunia, *Journal of the Taiwan Institute of Chemical Engineers*, 2019, **102**, 438–447.
15. D. Grau-Marin, J. Silvestre-Albero, E. O. Jardim, J. Jagiello, W. R. Betz and L. E. Peña, *Carbon*, 2020, **157**, 495–505.
16. K. R. Matranga, A. Stella, A. L. Myers and E. D. Glandt, *Separation*

Science and Technology, 1992, **27**, 1825–1836.

17. Z. Tan and K. E. Gubbins, *Journal of Physical Chemistry*, 1990, **94**, 6061–6069.
18. C. M. Simon, J. Kim, D. A. Gomez-Gualdron, J. S. Camp, Y. G. Chung, R. L. Martin, R. Mercado, M. W. Deem, D. Gunter and M. Haranczyk, *Energy & Environmental Science*, 2015, **8**, 1190–1199.
19. D. W. Breck, *Zeolite Molecular Sieves*, Wiley, New York, 1974.
20. B. E. Poling, J. M. Prausnitz and J. P. O'connell, *Properties of Gases and Liquids*, McGraw-Hill Education, 2001.
21. M. De la Casa-Lillo, F. Lamari-Darkrim, D. Cazorla-Amoros and A. Linares-Solano, *The Journal of Physical Chemistry B*, 2002, **106**, 10930–10934.
22. R. Clausius, *Annalen der Physik*, 1850, **155**, 368–397.
23. É. Clapeyron, *Journal de l'École Polytechnique*, 1834, **14**, 153–190.
24. P. B. Whittaker, X. Wang, K. Regenauer-Lieb and H. T. Chua, *Physical Chemistry Chemical Physics*, 2013, **15**, 473–482.
25. H. Li, J. Kang, F. Zhou, Z. Qiang and G. Li, *Journal of Loss Prevention in the Process Industries*, 2018, **55**, 437–449.

Chapter 8

Conclusions & Outlook

The work detailed in this thesis investigated the synthesis of turbostratic carbons to be utilised for CO_2 capture, firstly developing the understanding of carbons derived from Used Cigarette Filters (UCFs) (see chapter 4) based on the authors previous work detailed in **Publication V** and **Publication VI**. It was found that the removal of the wrapping paper on the Used Cigarette Filter (UCF) is likely an essential step in the production of carbons with the extremely high porosities *via* activation using KOH, and associated gravimetric H_2 capacities seen in **Publication VI**. Furthermore, retaining the wrapping paper in the precursor resulted in high levels of irremovable inorganic material left in the derived turbostratic carbons. The resultant hierarchically porous, medium surface area carbons were found to have reasonable CO_2 uptake capacity nonetheless and such materials may have further application in Pressure Swing Adsorption (PSA) applications. In addition, a series of carbons activated without the use of any external porogen were produced, and these materials *appear* to be highly ultramicroporous, though the analytic techniques used in the chapter are insufficient to yield precise and accurate data concerning porosity within

this pore width range.

Inspired by assertions that impregnated contaminant porogens in UCFs may provide a degree of porosity that is higher than expected from KOH activation alone, in chapter 5 this so-called impregnation technique was further explored. This was done *via* the hydrothermal impregnation of KOH into sawdust (SD) prior to pyrolytic activation, as well as by the pyrolysis of sodium carboxymethyl cellulose (NC). The relationship between porosity of the derived samples and their activation conditions was of great interest. In particular, highly ultramicroporous carbons can be synthesised *via* both methods explored in this chapter. Such porosity previously been shown to be useful for low-pressure CO_2 capture. However what is more interesting is the relationship between porosity of- and the synthetic conditions used- to form these novel carbons. In particular, while in general carbons derived from SD are essentially entirely microporous, at a sufficiently high KOH:SD ratio the derived material becomes almost entirely mesoporous. This change in PSD is also accompanied by an large reduction in density, resulting in an unprecedentedly diffuse turbostratic carbon. The NC-derived samples showed unusual trends in the relationship between porogen:precursor ratio and porosity, in that maximisation of porosity appears to occur for an Na:C atomic ratio of 1.2 (corresponding to a degree of substitution (DS) of the sodium carboxymethyl group of 0.9). As the precursor is polymeric with carboxyl sidechains, it can be expected that cross-links may form at some point during synthesis thus yielding porosity independently from the oxidative action of Na and Na-containing compounds. The aforementioned breakdown in porosity indicates that these two pore forming processes may be competitive; at higher Na:C ratios oxidative chemical activation destroys porosity previously produced *via* cross-link formation.

The synthesis-based chapters 4 and 5 give way to further routes of investigation with respect to routes to microporous carbons for small molecule adsorption. In particular, the reason for the difficulty in removal of inorganic contaminants in Used Cigarette Filter (UCF)-derived carbons ought to be further investigated, as the extensive washing steps used are common and have been found to be overwhelmingly successful in the community of researchers working on activated carbons. Indeed, the metals identified ought to be very water soluble. Routes to understanding the stubbornness of these species include use of other solvents to remove them, as well as in-depth electron microscopic techniques to understand if and whether the metal clusters are 'stuck' inside the pores. Additionally, understanding of the mechanisms of porogenesis in the materials described in chapter 5 ought to be fully elucidated, perhaps *via* thermal kinetic studies, in situ electron microscopy, and/or analysis of volatiles released during the pyrolytic processes.

In terms of analytical methods what is clear from both of the synthetic chapters is that the traditional method of porosimetry as derived from N_2 isotherms measured at $-196\,^{\circ}\mathrm{C}$ is insufficient, in that N_2 does not appear to easily diffuse into the ultramicropores present in many of the materials previously described. As such, chapter 6 details the investigation of alternative porosimetric probes, namely H_2 and O_2. While these probe molecules have been investigated prior to this work, this chapter showed that only the simultaneous fit of the 2D-NLDFT heterogeneous surface (2D-NLDFT-HS) kernel to both isotherms was able to give a precise and reasonable description of the subtle PSD broadening as associated with increased porogen concentration. This may be related to the fact that both O_2 and H_2 seem to have less trouble diffusing into these extremely small pores. Apart from this, H_2 has been confirmed to probe porosity that, as a result of restrictive

pore openings is not accessible to the larger O_2 and N_2 molecules. As the low pressure adsorption of small, environmentally-relevant molecules such as CO_2 is supposed to be associated with the presence of ultramicropores, the accurate understanding of porosity within such pores is vital and as such the work in chapter 6 ought to inform how porosity is measured in turbostratic carbons. In future these techniques should be exploited on a series of porous crystaline materials with varying PSDs, but with significant porosity which is poorly accessible to N_2 at $-196\,°C$. Crystallographic data can then be compared to porosities determined as a result of NLDFT kernel fitting to each of these isotherms and pairs thereof. This will give an indication of the accuracy of each of the isothermal porosimetric techniques which is not possible to achieve on the turbostratic materials studied in this work.

Chapter 7 seeks to thoroughly investigate the association of pore width with CO_2 uptake as a function of pressure. In order to meticulously investigate this relationship, a small piece of software known as the python Porosity Uptake Correlator (pyPUC) was produced. Starting with an experimental dataset of gravimetric CO_2 uptake isotherms and PSDs from a set of turbostratic carbons, pyPUC performs linear regressions between porosity of pores with some range of widths, and CO_2 uptake at a given pressure. This process is repeated for all pore width ranges and all CO_2 uptakes. As a result, a statistically optimal pore width range can be determined for uptake of CO_2 at a given pressure. It was confirmed that the optimum pore width range broadened with increasing pressure, but this seems to be more associated with an increase in the upper limit, that is at higher pressures CO_2 uptake becomes associated with larger and larger pores. However, past some pressure ultramicropores become insignificant to CO_2 uptake. As mentioned in the previous paragraph, N_2 porosime-

try is inadequate for probing the smallest of ultramicropores. pyPUC was also able to determine that the understanding of the relationship between low-pressure CO_2 uptake and ultramicroporosity is best described using dual isotherm O_2/H_2 porosimetry. That is, the r^2 values for correlations between uptake of CO_2 at $\sim$1 bar or less and the optimum pore size range are best using this porosimetric method. pyPUC has much more potential, in particular for the investigation of the poorly understood relationship between CH_4 adsorption and pore size. In addition, the software can easily be adapted to incorporate other variables such as surface chemistry and heat of adsorption into the understandings of the relationships determined.

In summary, this thesis presents multiple novel methods for the production of highly ultramicroporous turbostratic carbons, and investigates improvements to the porosimetric methodology used in their characterisation. Furthermore, a computational tool (pyPUC) has been created, which has helped in the thorough elucidation of the relationship between CO_2 uptake and pore size. This work raises interesting questions as to the nature of pore formation mechanisms in these materials, while pyPUC should provide a means and philosophy by which to investigate the adsorption capacity-porosity relationship in porous materials in general.

Appendices

Appendix A

Publication III: Modulating the porosity of carbons for improved adsorption of hydrogen, carbon dioxide, and methane: a review

Contribution of the author: The author designed and performed the literature review and wrote the manuscript.

Materials Advances

ROYAL SOCIETY OF CHEMISTRY

REVIEW

View Article Online
View Journal | View Issue

Check for updates

Cite this: *Mater. Adv.*, 2022, 3, 1905

Modulating the porosity of carbons for improved adsorption of hydrogen, carbon dioxide, and methane: a review

L. Scott Blankenship * and Robert Mokaya *

Received 30th September 2021,
Accepted 9th January 2022

DOI: 10.1039/d1ma00911g

rsc.li/materials-advances

Porous carbons provide a low-cost route to a highly stable material for the adsorption of various gases. In particular, activated carbons (ACs) and zeolite templated carbons (ZTCs) show promise in their ability to capture and store environmentally relevant small molecules such as hydrogen, carbon dioxide and methane. Indeed biogas upgrading and methane storage are already partially commercialised. While ZTCs offer precise control over porosity, ACs have the advantage of being easy to synthesise from a wide range of sources. This review examines state-of-the-art techniques to control the porosity of both ACs and ZTCs in order to fine-tune their ability towards the capture and storage of various gases under different pressure and temperature applications.

Open Access Article. Published on 12 January 2022. Downloaded on 3/24/2022 12:40:42 PM.
This article is licensed under a Creative Commons Attribution 3.0 Unported Licence.

1. Introduction

The current climate and ecological emergency threatens all life on planet earth, and is largely caused by incessant anthropogenic emissions of greenhouse gases. The resultant climate change, which is already causing extreme weather events and is threatening mass extinction, is well underway but the full extent of effects of the climate crisis are yet to come.[1,2] In order to keep within the temperature limits prescribed by the Paris Agreement,[3] it is necessary not only to drastically reduce global net greenhouse gas (GHG) emissions by reducing consumption and transitioning to 'green' energy sources but also to capture CO_2 and CH_4 in the interim.[3–6] Although bioremediation of

School of Chemistry, University of Nottingham, University Park, Nottingham, NG7 2RD, UK. E-mail: leo.blankenship@nottingham.ac.uk, r.mokaya@nottingham.ac.uk

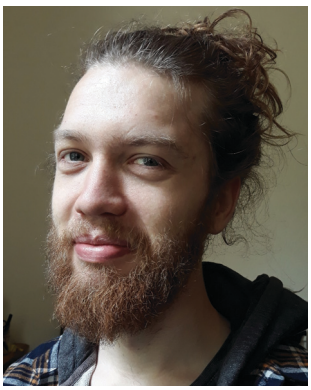

L. Scott Blankenship

L. Scott Blankenship is a PhD student in the Mokaya group at the University of Nottingham, and obtained his MSc in the same group in 2016 working on porous carbons from cigarette butts for H_2 storage and CO_2 capture. His research interests focus on critical evaluation of porosimetric methods for carbons and the ability of these methods to predict uptake of environmentally relevant small molecules.

Robert Mokaya

Robert Mokaya received his BSc in Chemistry from the University of Nairobi in 1988 after which he spent a year working for Unilever in Kenya. He was awarded his PhD from the University of Cambridge in 1992. In 1992, he was elected to a Research Fellowship at Trinity College, Cambridge and in 1996 was awarded an EPSRC Advanced Fellowship. He joined the School of Chemistry in Nottingham, as a lecturer in Materials Chemistry in 2000, where he is Professor of Materials Chemistry. His research interests are on the design, synthesis and characterisation of new forms of sustainable porous materials and the study of their structure–property relations. The research involves exploring fundamentally new synthesis methods that are simpler, cheaper, and more efficient and offer valorisation routes to materials with optimised properties for targeted sustainable energy applications.

© 2022 The Author(s). Published by the Royal Society of Chemistry

Open Access Article. Published on 12 January 2022. Downloaded on 3/24/2022 12:40:42 PM.
This article is licensed under a Creative Commons Attribution 3.0 Unported Licence.

carbon capturing ecosystems has a great role to play in the offsetting of GHG emissions, it is insufficiently expedient to keep up with the reduction in emissions necessitated by both the aforementioned Paris Climate Agreement and the UK's limited goal of achieving net zero emissions by 2050.[3,6–8]

These factors necessitate development of novel, low cost CO_2 capture technologies.[9] Additionally the global economy must rapidly transition away from fossil fuels as vehicular energy sources and towards cleaner, renewable fuels such as natural gas (CH_4) and H_2.[10–12] Although natural gas is not a carbon neutral fuel, it is produced sustainably from the breakdown of biomass and releases much less CO_2 and other pollutants than other fossil fuels.[13,14] As for H_2, the sole product of its combustion is water making it a carbon-neutral fuel at the point of use.[10] The difficulty with storing or capturing CO_2, CH_4 and H_2 is that they all exist in the gas phase under ambient conditions. As a result, the challenge becomes both economic and practical – how these gases can be stored and transported in a cost and space-efficient way.[10,14–22] Currently, industrial CO_2 capture is achieved principally through reaction with liquid amines in the presence of water to form aqueous ammonium bicarbonates,[23,24] while commercial technologies for the storage of natural gas/CH_4 and H_2 rely on compression or liquefaction.[10,14,18,20–22,25] The cost of liquid amine capture is principally a result of its relatively low CO_2 capacity as well as energy requirements for regeneration of the amine from the ammonium bicarbonate. Though compression or liquefaction of gaseous fuels does not come with the same regeneration issues present in chemical capture of CO_2, it is plagued by the high energy costs of maintaining the high pressures and/or low temperatures required.[14,20] In the case of compressed gases the weight of sufficiently robust containers needed to maintain these pressures is very high, leading to energy losses for on-board applications.[22]

Promising alternative methods of gas storage involve chemical (chemisorption) or physical (physisorption) adsorption onto a suitable solid material. Physisorption has the distinct advantage over chemisorption of facile regeneration of the adsorbate by decreasing pressure or increasing temperature. Microporous adsorbents such as Metal Organic Frameworks (MOFs),[26–28] porous polymers,[29] Porous Inorganic Membranes,[30] and zeolites[31–33] present possible storage solutions but have the disadvantage of relatively high cost of production and/or finite lifecycles due to thermal instability or undesirable reactivity with contaminants such as water. On the other hand, porous carbons provide a storage medium that is relatively inexpensive to produce and extremely thermally and chemically stable.[18,20,34] Furthermore, the porosity of carbons can be tailored to be selective for specific adsorbates and adsorption conditions.[20,35–37]

Porous sorbents are actually already beginning to see some commercial use in the capture/storage of small molecules. This is particularly evident for CH_4, which is already being used as an on-board fuel.[38–42] It is principally stored *via* compression (CNG) or liquefaction (LNG).[38,39] However, adsorbed natural gas (ANG) is now competitive with the CNG and LNG as a result of the much higher energy density than CNG, and is already commercially available.[43,44] As pressures required for ANG are significantly lower than those for CNG, ANG infrastructure is less costly.[38,40,45,46] Additionally, adsorption of CH_4 poses a much lower safety risk relative to compression and improves overall efficiency at point of use.[12,46] Due to its low cost, activated carbons are used as the adsorbents in on-board applications as well as at fuelling stations.[43,44] Additionally, porous carbons are in commercial use for the upgrading of biogas (typically $\sim$60% CH_4) by selective removal of H_2O, CO_2 and H_2S resulting in improved CH_4 concentration of over 98%.[44,47,48] The principal problem with porous materials for this application is imperfect selectivity resulting in so-called methane slip, wherein some methane is lost to the sorbent.[48–50] In theory this problem can be mitigated by finely tuning pore widths and/or surface chemistry.

Porous carbons fall into four main categories; activated carbons, carbonised frameworks, templated carbons, and carbide-derived carbons.[51] Of these, the simplest to produce are activated carbons, which in the case of so-called chemical activation, require simple heating of a carbonised (typically graphitic) material with an activating agent to generate pores. In fact, the initial carbonisation step can be performed simultaneously with the so-called activation step.[20,52] The perceived disadvantage of this technique is that the amorphous nature of the product means tuning of the pore size can be difficult. Framework carbonisation involves pyrolysis of an already porous organic material such as an aerogel or other polymer network.[53–55] Templating is one of the newer techniques and is performed by depositing a carbon rich material onto some inorganic template (typically silicas or zeolites) with the desired pore size and surface area, followed by heat treatment in order to form a graphenic crystalline structure within the template pores, before removing the template.[34,51,56] Finally carbide-derived carbons, which use metal carbides as starting material, allow for tuning of porosity at the atomic level. This is possible as suitable carbides are selected according to their lattice spacing, wherein removal of the metal counterion generates pure carbon with pore channels whose size is determined by the precursor's lattice geometry.[57–59] Broadly, porous carbons for small molecule gas adsorption should be microporous and have high surface area and pore volume.[18,60–63] Although it is possible to achieve porous carbons with such characteristics *via* any of the aforementioned routes, by far the most popular methods are activation and templating using zeolites and as such these form the subject of this review. For both of these processes, the challenge is tuning the porosity of resultant carbons to optimise uptake performance for specific adsorbates and/or adsorption conditions; in the case of activated carbons (ACs) this centres on techniques to narrow the pore size distribution (PSD),[20] whilst with zeolite templated carbons (ZTCs) improvements come *via* more improved replication of the template structure.[34,56]

Gas uptake and molecular selectivity of ZTCs and ACs can also be improved chemically by introducing, as dopants, moieties with affinities for the targeted adsorbate.[63–68] This review however, focuses on improvements in physisorption of small

© 2022 The Author(s). Published by the Royal Society of Chemistry

Open Access Article. Published on 12 January 2022. Downloaded on 3/24/2022 12:40:42 PM.
This article is licensed under a Creative Commons Attribution 3.0 Unported Licence.

gas molecules by porous carbons achieved by tailoring the size, shape, and abundance of pore channels available to the adsorbate. Any reference herein to doping of the carbon structure with heteroatoms is made in the context of the effect on pore structure.

2. Synthesis of porous carbons

Methods for synthesizing porous carbons can be split up into two broad groups; top-down or bottom-up. A top-down method takes an existing carbon or carbonaceous material and develops porosity in it by etching away material; this process is commonly known as activation.[20] Conversely, bottom-up methods consist of constructing the carbon structure from its building blocks in such a way that voids or pores are formed, often with the use of a porous template. Such templates include mesoporous silica,[69,70] micro-phase separated block copolymers[71] or even MOFs,[72,73] however perhaps the most well-known microporous templates are zeolites where the product of such a process is known as zeolite-templated carbon (ZTC).[34] Bottom-up synthesis can also occur in the absence of a template, for example *via* the direct carbonization of organic crystals.[74]

2.1. Activation of carbon-rich precursors

Activation, here meaning the development of porosity in a carbon precursor, can be achieved by either physical or chemical means. Physical activation is a two-step process whereby the precursor is first pyrolised at 400–900 °C in an inert atmosphere, in order to increase carbon content. Thereafter the sample is exposed to an oxidizing gas at 350–1000 °C in order to develop pores. Chemical activation however, can take place in a single step wherein the carbon precursor is mixed with an activating agent - also known as a porogen (such as alkali metal hydroxides, H_3PO_4, or $ZnCl_2$), then pyrolised at 450–900 °C.[20] Precursors can essentially be any organic matter, and include biomass such as wood,[75,76] fruit seeds,[35,77] grass,[78] and refined biopolymers.[79] The degree of activation, *i.e.* the extent of porosity development, can be improved by pre-carbonisation of the precursor.[80–82] Newer forms of carbon such as templated carbons, nanotubes, and carbide derived carbons (CDCs) have also been activated to improve their porosity.[83–88]

It should be noted that physical activation can be achieved without addition of an oxidising gas because volatile components of the precursor are converted to (among other things) oxidising gases on pyrolysis resulting in the development of small micropores. In the case of biomass carbonisation in the absence of a porogen, porosity and structure are maintained in the resulting so-called biochar material.[89–91]

2.1.1. Physical activation. As mentioned above, the first step in physical activation is pyrolysis of the precursor in an inert atmosphere (typically under nitrogen). This removes the majority of volatiles from the precursor as well as carbonizing it. By-products of the pyrolysis are burned off by the oxygen in the activating agent (CO_2, air or steam) during the gasification step, which results in opening of some larger, closed pores. Further pores in the micropore region are developed as the porogen burns off less stable parts of the carbon skeleton. The porosity of the resultant activated carbon is dependent on the composition of the precursor, choice of activating agent and temperature used at both steps. For a given activating agent-precursor pair, porosity development is generally improved by increasing activation temperature.[20,92–94] However, this comes with a broadening in the PSD, which is undesirable for gas uptake applications at low pressure.[63,95–97] Such broad porosity can nonetheless be useful in high pressure or so-called pressure-swing applications.[35,98–101]

Activation with CO_2 and steam generally result in higher yields than using air as a porogen. This is because the reaction between carbon and oxygen in the air is highly exothermic and leads to a much faster reaction, burning off more of the carbon.[20] This does however mean that much lower temperatures are required for activation using air, as compared to CO_2 and steam.[52,102,103] Steam and CO_2 are nonetheless the preferred physical activating agents due to the aforementioned problems with air.[20] Steam is generally characterised as the more reactive porogen of the two, requiring lower activation temperatures than CO_2.[92,104,105] There is however still some disagreement as to what type of porosity is developed by each activating agent.[105–108]

2.1.2. Chemical activation. Chemical activation is favoured for the production of porous carbons for use in small gas molecule storage as it results in high surface area carbons whose porosity is primarily in the micropore region. Furthermore, this microporosity can be tailored *via* experimental conditions to be within a narrow pore size range. In addition, the process is more efficient than physical activation as synthesis usually occurs in a single, low temperature step and results in higher carbon yields.[20,109]

Chemical activating agents can be divided into two groups according to their activation mechanism; the first group are dehydrating agents such as H_3PO_4 and $ZnCl_2$ wherein the dehydration of the carbonaceous structure, triggered by the action of the activating agent leads to the formation of cross-linkages.[110,111] This in turn triggers condensation of the structure around the activating compound and its hydrates. Pore size is thus limited by size of these compounds. Further, the breadth of the PSD is a function of the variation in molecular sizes of the activating agent and its hydrates. For example, activated carbons produced using $ZnCl_2$ have narrow PSDs as structural condensation occurs around $ZnCl_2$ and its hydrates which are of similar size.[112] On the other hand, H_3PO_4 is converted to molecules with a broader range of sizes such as $H_4P_2O_5$ and $H_{13}P_{11}O_{34}$ resulting in a heterogeneous PSD, regardless of activating conditions.[113]

Despite the ubiquity of KOH as a porogen in the literature, the mechanism of activation is a matter of some debate.[20,109,114–121] Nonetheless, there is a broad agreement that pore formation occurs *via* three principle processes:[20,109,114–116,118] (i) chemical activation wherein redox reactions between K compounds and the carbon framework occur; (ii) formation of the physical activating

Open Access Article. Published on 12 January 2022. Downloaded on 3/24/2022 12:40:42 PM.
This article is licensed under a Creative Commons Attribution 3.0 Unported Licence.

agents CO_2 and H_2O which induce gasification of carbon to further develop porosity; (iii) the intercalation of metallic K between graphitic sheets. Washing of the sample removes both intercalated K as well as K oxides and carbonates, resulting in a permanently porous carbon. There is inconsistent evidence on the exact nature and validity of processes (i) and (iii). For example, work by Linares-Solano indicates that (i) occurs directly *via* the oxidation of carbon by KOH (eqn (1)).[116,117]

$$6KOH + 2C \rightarrow 2K + 3H_2 + 2K_2CO_3 \quad (1)$$

On the other hand, Otowa *et al.* argue that KOH first dehydrates to form K_2O and H_2O (eqn (2)), and C is oxidised by H_2O (eqn (3) and (4)).[115]

$$2KOH \rightarrow K_2O + H_2O \quad (2)$$

$$C + H_2O \rightarrow CO + H_2 \quad (3)$$

$$CO + H_2O \rightarrow CO_2 + H_2 \quad (4)$$

As for (iii), some researchers accept that above 700 °C K_2CO_3 and K_2O is reduced by C to form metallic K,[20,116] and indeed there is some evidence that this reaction can occur and furthermore that K can intercalate with graphite.[122,123] However, the formation of metallic K is not observed industrially. It should also be noted that the mechanisms discussed above preclude the consideration of heteroatoms. There is evidence, for example that for nitrogen-rich precursors cyanide compounds can be produced during activation with KOH.[124,125] In the case of NaOH activation, the mechanism is believed to be similar (and just as ill-defined), however there is no evidence that Na can intercalate as in (iii).[117,119]

Chemical activation using KOH is noted for the distinct advantage of giving a higher degree of control over the PSD as compared with other activating agents.[20,79,126,127] Though PSDs for carbons derived using small amounts of KOH or NaOH are typically narrow, significant broadening occurs with increasing MOH/precursor ratio.[128–130] For applications in which high porosity materials with narrow PSDs are required, alkali metal carbonates and bicarbonates as well as oxalates show significant promise.[131–134] These porogens have been shown to be significantly less corrosive than their hydroxide counterparts, yet produce materials with significant surface area, particularly in the micropore region,[135–138] and are discussed in more detail in Section 4.1.1.

While oxidative chemical activation is heavily favoured in the literature due to its ability to produce carbons with extremely high surface areas, it comes with the disadvantage of resulting in significant loss of material. Dehydrating agents are non-destructive thus result in much higher yields. In addition, it has been shown that air, as opposed to an inert gas may be used in such scenarios, for example Fierro *et al.* produced carbons from lignin activated with H_3PO_4 at temperatures up to 600 °C.[139,140]

Pre-carbonisation methods. The porosity of carbons can be improved by subjecting the precursor to an initial carbonisation step before activation. This results in the partial graphitisation of the material and increases the carbon content, accompanied by a reduction in concentration of heteroatoms. This means that fewer oxidising gases are released upon activation resulting in more controlled activation and thus a narrower PSD, less pore collapse and generally higher surface area. Carbonaceous matter can exist in carbonised form such as coal, pitch or tar and can be converted to high surface area activated carbon in a single step.[141–143] Alternatively, biomass can be hydrothermally carbonised by heating in water under high pressure to generate carbonaceous matter composed of microspheres which possess a hydrophobic core and hydrophilic shell, of which the latter is more susceptible to chemical activation.[144–147] Another route is so-called air- or flash carbonisation, which is achieved by briefly interrupting the inert atmosphere used during pyrolysis by injection of air into the system.[35,80,81]

2.1.3. Microwave activation. Conventionally the thermal treatment(s) of precursors in a chemical and/or physical activation process is achieved *via* convective and conductive heating of the sample in a fixed bed. This can result in uneven heating of the sample, and thus inconsistency in pore structure across the derived AC. To mitigate this the heating is usually accomplished *via* a slow continuous ramp, and with a long isothermal period (the dwell time), which result in the activation lasting several hours. The use of microwave radiation as a heat source provides more even heating and thus much faster activated carbon synthesis; reaction times are on the order of a few minutes.[148] It has been shown that pyrolysis and/or activation using microwaves result in ACs with textural properties similar to those derived *via* conventional methods.[67,149,150]

2.1.4. Physicochemical activation. In some cases the porosity of ACs derived *via* chemical activation using dehydrating agents can be extended by physical activation. The initial dehydration step causes development of micropores, while subsequent treatment with steam or CO_2 produces larger pores.[52] This results in a broader and/or multimodal PSD,[151,152] which is particularly suited to methane/natural gas storage.

2.1.5. Carbon molecular sieves. Molecular sieves are a class of porous materials with very narrow PSDs, which make them useful in gas separation applications wherein species are separated according to their size.[153–157] These materials are derivatives of porous materials such as silicates and zeolites.[154,158,159] While activated carbons typically have heterogeneous PSDs, if they are synthesised or adapted to change pore entrance dimensions to a single pore size they are known as carbon molecular sieves (CMSs).[157,160] Prior to the explosion in ZTC research, templated carbons were often referred to as CMSs,[69] however the term is now restricted to non-templated carbons with narrow PSDs. On an industrial scale, CMSs are typically synthesised by depositing pyrolytic carbon at the mouth of the pores in activated carbons, resulting in uniform pore entrances.[160–162] This results in so-called bottle-neck pores, wherein the pore entrance is narrower than the main pore channel.[157] CMSs can also be synthesised directly by activation of an appropriate precursor(s) under precise conditions. Suitable porogens include nitric acid or oxygen and initial activation is followed by a final heating stage.[163] Suitable precursors

© 2022 The Author(s). Published by the Royal Society of Chemistry

Open Access Article. Published on 12 January 2022. Downloaded on 3/24/2022 12:40:42 PM.
This article is licensed under a Creative Commons Attribution 3.0 Unported Licence.

include polymers, some coals, and woody biomass such as peach stones or coconut shells.[156,157,161,163] Alternatively, pore entrance uniformity can be encouraged by mixing a precursor with a binder prior to pyrolysis.[164]

2.2. Templating onto porous zeolitic structures

Zeolites are three-dimensional uniform microporous crystalline framework structures. For aluminosilicates, the structure is based on silica networks where some of the Si^{4+} cations are replaced by Al^{3+}, resulting in an overall negative charge for the framework. Cations such as Na^+, H^+ or NH_4^+ reside within the framework pores to balance the charge.[154,165,166] More than 40 naturally occurring zeolites are known to exist,[167] and while theoretical zeolites number in the thousands[168] only *ca.* 200 have thus far been synthesised.[169] The aforementioned uniformity of zeolitic micropores means they are interesting in their own right as gas sorption and separation materials.[32,33,170] However, the chemical and thermal stability (under inert conditions) of some zeolites is lower than that of activated carbons. Interest in using zeolites as sacrificial templates for the preparation of porous carbons arises from a desire to improve the structural ordering of highly stable but totally amorphous porous carbon materials. ZTCs provide a route to uniformly porous graphenic microporous solids with porosity and thermochemical stability comparable to that of activated carbon.[171] In addition, this regularity in structure leads to greater scope for functionalisation of the carbon surface.[34,172]

These improved characteristics necessitate more precise synthesis conditions. ZTCs can be divided into three types according to how graphenic the overall structure is, which is connected to the degree of replication of the template's pore channels ranging from type-I where near complete template replication is achieved, to type-III where the pore structure bears little resemblance to its template and possesses a high degree of graphene stacking. Type-II ZTCs are formed when the template is partially replicated, but there is still a high degree of graphiticity due to deposition of carbon on the outer surface of the template.[34] The structural uniformity of the zeolite can only be conferred on the resultant ZTC (*i.e.* a type-I ZTC) when the template's pore structure is composed of large 3D channels.[173–175] Specifically, pore entrances should contain a minimum of 12 O atoms in the prototypical Si–O–Si ring which forms the zeolite channel opening to allow for uniform pore filling by the carbon monomer without risking pore blocking.[34,176] Smaller pores or low dimensional pore networks always result in a disordered, graphitic structure (type-III) more akin to activated carbons. As most natural zeolites have small pore entrances, they typically yield poorly ordered ZTCs. To achieve type-I ZTCs, sufficient carbon monomer must be inserted evenly into the zeolite pores and allowed to polymerise before carbonisation. Thus two heating stages are required to achieve discrete, uniform graphenic structures.[34] Carbonisation of the monomer without polymerisation can lead to partial uniformity with some graphene stacking (type-II) with a mixture of graphitic and graphenic ordering, while failure to achieve even distribution of monomer is likely to result in no replication of the template structure. As type-I ZTCs typically have the highest degree of porosity ($A_{BET} > 2100\ m^2\ g^{-1}$)[177] precise selection of zeolite, monomer, and activation conditions is vital for producing a ZTC with adventitious porosity for small molecule physisorption.

2.2.1. Liquid impregnation. Introduction of a carbonaceous precursor into zeolite pores can be achieved by simply inserting a carbon-rich liquid monomer into the channels. By heating the zeolite/monomer mixture, and with assistance from the catalytic action of the zeolite template, polymerisation occurs resulting in a zeolite–polymer composite. This is then carbonised by heating in an inert atmosphere. The most commonly used liquid monomer is furfuryl alcohol (FA),[88,174,178–182] due to its ease of insertion into pores.[34] However other monomers such as acrylonitrile,[174] saccharides,[183,184] and ethylene diamine[185] have also been studied as precursors. ZTCs derived *via* liquid impregnation (LI) typically poorly replicate the zeolite structure (resulting in a type-III structure) as it is difficult to insert sufficient precursor into the pores.[34] Dissolved polymers such as lignin,[186,187] and a co-polymer of sulfonic and maleic acids[188] have also been used as carbon precursors but the resultant ZTCs have relatively low surface area and poorly replicate the zeolite pore structure. This is likely a result of inadequate pore penetration due to the size of precursor molecules relative to that of the pore entrance.[34]

2.2.2. Chemical vapour deposition. In order to overcome the problem of inadequate pore penetration during ZTC synthesis presented by the liquid impregnation method, chemical vapour deposition (CVD) can be used.[34,171] Introduction of sufficient carbon into the pores is achieved by using a small, unsaturated organic molecule in the gas phase such as methane,[189] short-chain alkenes,[64,179,190–193] acetylene[194,195] or acetonitrile.[61,64,83,179,182,190,196–198] CVD must be conducted at a temperature below the decomposition temperature ($\sim$600 °C) of the carbon source in order to maximise pore channel structure replication in the ZTC. This initial step results in the zeolite-catalysed conversion of the CVD source into disconnected polyaromatic hydrocarbons (PAHs). A second heating step at elevated temperature ($>$800 °C) is needed to carbonise the PAHs and fully connect the pore network. Removal of the template without the second heat treatment step can result in a poorly connected (type-III) ZTC structure upon template removal.[34,56] Improvements in porosity have been reported by incorporating two temperatures stages into the CVD step.[190,195]

2.2.3. Two-step method. ZTCs may also be constructed using LI followed by CVD, which offers some improvement in porosity relative to using either step alone.[179,180] Porosity improvements are likely a result of more uniform pore filling by two or more carbon sources used in the steps.[34] FA is most commonly used as the LI precursor in this method as it provides good pore penetration. This is then followed by CVD using acetonitrile,[179,190,199] ethylene,[61,179,180,182,190] or other small unsaturated hydrocarbons.[200–203] Larger precursor molecules which would not normally produce good zeolite replication in an LI (such as lignin) or CVD (such as benzene) process can be employed in a combined process, resulting in improved

Open Access Article. Published on 12 January 2022. Downloaded on 3/24/2022 12:40:42 PM.
This article is licensed under a Creative Commons Attribution 3.0 Unported Licence.

textural characteristics relative to ZTCs produced *via* either CVD or LI alone.[187,204,205]

2.2.4. Template removal. In order to remove the zeolitic framework after the synthesis, it is typically necessary to wash with HF or some combination of HF washing and HCl reflux.[34,182,192,193,206] The use of HF is impractical for industrial synthesis due to safety issues. Hedin and co-workers found that template removal could be achieved with a combination of HCl and NaOH for a silicoaluminophosphate-templated carbon, however this is likely due to less chemical robustness compared to a pure aluminosilicate framework.[207] NaOH has been shown to be at least partially effective in desilicating zeolites, so does show some promise for removal of actual zeolite templates from ZTCs,[208] and has been attempted on a few occasions.[176,209–211] Moon *et al.* found that washing with hot NaOH followed by HCl resulted in complete removal of Al, but left residual Si in the resultant ZTCs.[210] Ryoo and co-workers found the ash content of the carbon could be reduced to as low as 2.0 wt% with a combination of NaOH and HCl washing. This result however is constrained to zeolite-beta which has a higher proportion of Si–O–Si bonds which are more easily dissolved in NaOH. On the other hand, zeolite-X and -Y with significantly higher Al content are more resistant to dissolution in NaOH and HCl. Even in the case of zeolite-beta templated carbon, an HF/HCl wash significantly outperforms NaOH and HCl, resulting in an ash content of 0.5 wt%.[211] Template dissolution with NaOH–HCl on the other hand produces more oxygen-rich carbons,[209,211] and may result in slight reductions in overall porosity of ZTCs relative to those washed in HF.[211]

3. Textural characteristics for gas storage applications

Desirable textural characteristics for gas storage are dependent on the adsorptive, temperature and pressure of interest. Fig. 1 and 2 show how different pressures can affect the optimal textural characteristics of carbons. A summary of relevant properties of common gaseous sorptives is shown in Table 1. In the literature, measurements are commonly taken at 25 °C for H_2, CO_2, and CH_4 while −196 and 0 °C are also typical for H_2 and CO_2 respectively.[14,16,20,212,213] A series of isotherms at various temperatures for a given adsorbate-sample pair may also be reported to allow determination of isosteric heats of adsorption.[214] The pressure range used in isotherm measurement may depend on sample porosity; adsorption will typically plateau at relatively low coverage for samples with low surface area thus the upper pressure used need not be very high. Typical reports include data up to ∼40 bar for CH_4 and CO_2, while H_2 uptake is more commonly measured up to ∼100 bar. Of particular interest is the adsorption at 1 bar, however lower pressure such as 0.15 bar are also used for selectivity calculations especially in CO_2 uptake studies. Increases in surface area and pore volume generally improve a sample's uptake of an adsorbate by supplying adsorbed molecules with more surface to interact with and greater volume to fill, respectively. This is however limited by pore size, which can differentiate an adsorbent as a good candidate for storing one gas but not another.[63,91,215–217] As such, more detailed measures of porosity such as pore size distribution (PSD) and average pore size are used. Furthermore, low pressure adsorption of CO_2, CH_4 and H_2 is dominated by micropores, and thus micropore surface area and volume is typically reported alongside the total values.[218]

3.1. Pore size

If pore width is less than the diameter of the adsorptive (see Table 1), adsorption will not occur within the pore – indeed even pores with diameters slightly greater than that of the molecule's kinetic diameter (d_k) can lead to extremely slow diffusion at low temperatures, meaning that equilibrium may take a long time (hours) to achieve.[52,225,226] Additionally, optimum pore size has an upper limit due to the improvements in adsorption from field overlap when pore walls are sufficiently close together.

For small molecules like H_2, CO_2, and CH_4 (d_k = 2.89, 3.30, and 3.80 Å respectively),[154,222,223] this means that highly microporous materials are the most suitable for physisorption (see Fig. 1). Optimal pore size for adsorption of a given molecule is proposed to be that which can hold two layers of the molecule.[212,217,227] Fig. 1 shows how average pore size affects

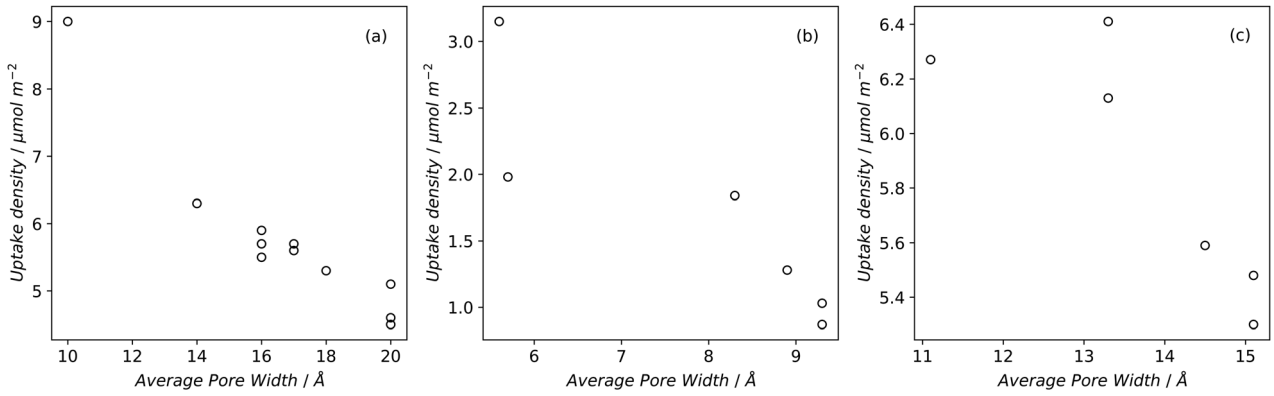

Fig. 1 Uptake densities of (a) H_2 at 1 bar and −196 °C, (b) CO_2 at 1 bar and 25 °C, and (c) CH_4 at 65 bar and 25 °C on carbons[79,194,219] as a function of average pore size.

© 2022 The Author(s). Published by the Royal Society of Chemistry

Open Access Article. Published on 12 January 2022. Downloaded on 3/24/2022 12:40:42 PM.
This article is licensed under a Creative Commons Attribution 3.0 Unported Licence.

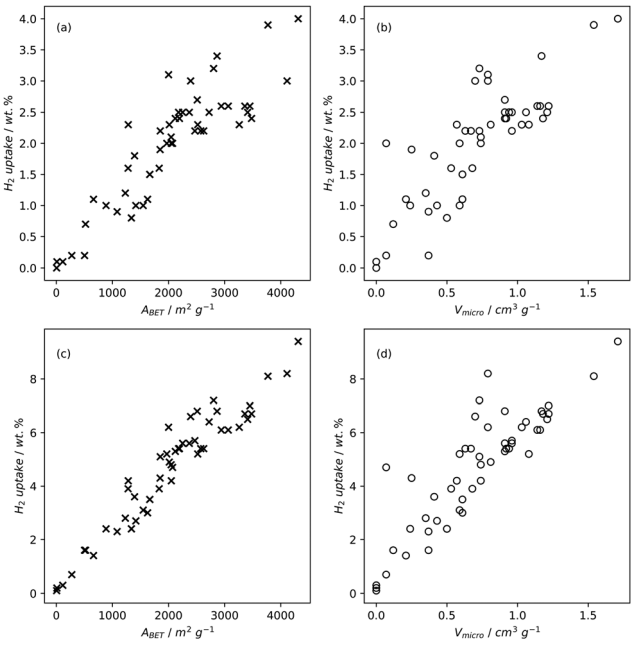

Fig. 2 H_2 uptake of carbons at −196 °C and 1 bar (a) and (b) or 20 bar (c) and (d) as a function of BET surface area (a) and (c) or micropore volume (b) and (d).[79,82,83,196,220,221]

Table 1 Physical properties of commonly stored gas molecules as well as relevant molecules for porosimetry measurements[154,222–224]

Species	d_k/Å	T_b/°C	μ
H_2	2.89	−252	0.260
CO_2	3.30	−78[a]	2.139
CH_4	3.80	−161	0.000
N_2	3.64	−196	0.697
O_2	3.46	−182	0.155
Ar	3.40	−186	—

d_k = kinetic diameter, T_b = boiling point, μ = quadrupole moment. [a] Sublimes.

the uptake density of gases under some standard adsorption conditions. For H_2 this means that ultramicropores are the dominant pore structure for storage at atmospheric pressure,[60] while optimum pore width is generally agreed upon to be 6 Å.[212,216] Maximum hydrogen uptakes can be achieved by samples wherein the PSD is narrow,[95] and centred around the optimum pore width; this is true at both cryogenic and ambient temperatures.[212,228] There is also evidence that hydrogen and methane preferentially adsorb on carbon slit pores rather than cylindrical pores,[229–231] which may give ACs an advantage over ZTCs.

To adsorb CO_2 under ambient conditions it is generally agreed that the best carbonaceous sorbents have the majority of their pores smaller than 8 Å, and distributed narrowly[62,63,96,97,219,232] (see Fig. 1) but slightly higher and lower limits have also been experimentally demonstrated.[233,234] This limit decreases with decreasing pressure – at 0.1 bar, pores of 5 Å have the biggest contribution to adsorption of CO_2.[97,227] This is particularly applicable for post-combustion industrial capture applications wherein it is necessary to remove CO_2 from a mixture of gases (~75% N_2). To achieve the selectivity necessary for such applications, adsorbents require ultramicropores as small as 3.5 Å to prevent the ingress of larger molecules.[235,236] At higher pressures the optimum pore size progressively increases into the supermicropore and small mesopore region.[62,97,136,234,237] At such pressures, the PSD can broaden without harming overall uptake.[66,126,227,238] In fact, high pressure CO_2 capture can be harmed by excessive microporosity as overall pore volume needs to be maximized for optimal molecular packing.[237]

Determination of the optimum pore size for methane storage appears to have yielded less conclusive results than that for H_2 and CO_2. Computational estimates range from 11 to 15 Å.[217,239,240] Through optimization experiments, Biloé *et al.* propose 15 Å as the optimum,[241] whereas other studies seem to suggest that optimal micropore width depends on whether the porous carbon is intended for gravimetric or volumetric storage.

3.2. Surface area

High pressure adsorption is much less dependent on pore size, and available surface area (A_{BET}) begins to dominate as a predictor of gas uptake capacity (Fig. 3e and f). In particular, Bénard and Chahine determined that cryogenic hydrogen storage capacity increases by approximately 1 wt% per 500 m^2 g^{-1}.[242] However, the degree of influence of A_{BET} on H_2 uptake posited in the eponymous Chahine rule has been recently disputed by Kusdhany and Lyth who found *via* a multivariate analysis that a 500 m^2 g^{-1} increase in surface area corresponds to at most a 0.24 wt% increase in hydrogen uptake.[243] Nonetheless high surface area remains an important factor in determining high pressure H_2 storage capacity in carbons, with the best performing carbons possessing surface areas approaching 4000 m^2 g^{-1}.[82,98,178,220,238,244–247] Similarly, in the case of CO_2 and CH_4 capture and storage, increased surface area is generally associated with improved gravimetric uptake.[14,35,131,132,194,248–255] However, depending on the prevailing pressure, CO_2 capture is much less dependent on surface area, and having pores of the appropriate size is more important.[132,244,252,256] In fact recent work by Jing Cui *et al.* suggests that excessive volumetric surface area results in poor selectivity of CO_2 over N_2, a metric which is vital in many industrial applications.[257] Furthermore, gravimetric surface area is becoming a less interesting variable for CH_4 storage because it does not correlate well to volumetric capacity.[18,35,258] As such, metrics like packing density and volumetric surface area (surface area density, see Fig. 1) are often cited in lieu of or as well as the traditional gravimetric value.[35,194,259]

3.3. Pore volume

Pore volume generally correlates to surface area, and thus increases in pore volume are typically associated with increases in gas adsorption capacity. Of course, the strength of the relationship between pore volume and surface area is affected by the size of the pores in question, *i.e.* an ultramicropore will contribute much less pore volume than a mesopore of identical

Open Access Article. Published on 12 January 2022. Downloaded on 3/24/2022 12:40:42 PM.
This article is licensed under a Creative Commons Attribution 3.0 Unported Licence.

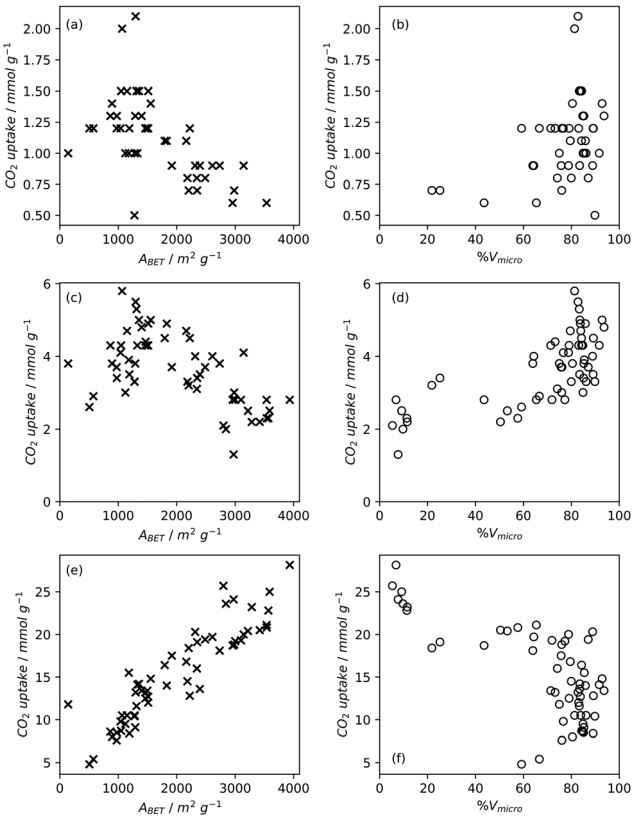

Fig. 3 Trends in BET surface area and percentage micropore volume with CO_2 uptake capacity of carbons[78,80,81,135,237,238,244,248] at 0.15 bar (a) and (b), 1 bar (c) and (d), and 20 bar (e) and (f).

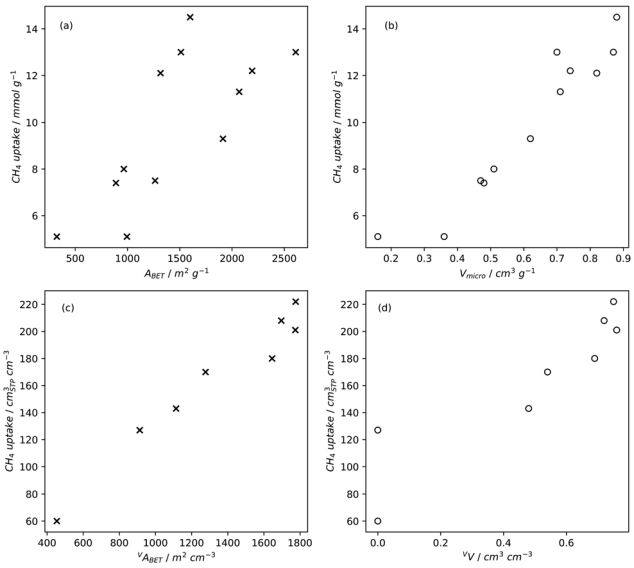

Fig. 4 Trends in CH_4 uptake with gravimetric (a) and (b) and volumetric (c) and (d) porosity of carbons[35,131,258] at 35 bar and 25 °C.

surface area.[20,234,260] If a sample is mostly microporous and has a high total pore volume, this indicates that there are lots of or very deep micropores within the sample. Such a sample is advantageous for small molecule adsorption, especially at lower pressures. As such, (percentage) micropore volume rather than total pore volume is likely a better predictor for H_2, CO_2 or CH_4 uptake (Fig. 2–4).[14,18,20,34,68,257,261]

3.4. Measuring porosity

Unlike for crystalline materials, the porosity of ZTCs and ACs cannot be easily determined using diffractive techniques such as XRD. Additionally, due to the size of pores needed for small molecule sorption, use of electron microscopy is not a particularly accurate technique for determining porosity. Thus, sorptometric porosimetry remains the main method for determining specific surface area, pore volume and pore size of carbons.

3.4.1. Choice of adsorptive. Sorptometry of carbons is typically performed by measuring nitrogen isotherms at −196 °C. While subcritical argon is recommended as the best adsorptive by the IUPAC,[218] such measurements are uncommon in the literature due to its impracticality and relatively highcost of such measurements with respect to using nitrogen. Unfortunately, cryogenic nitrogen isotherms are the source of two errors in pore width measurement. Firstly, nitrogen does not readily diffuse into so-called ultramicropores (of width <7 Å). This means that in order to attempt to measure these pores, extremely low relative pressures must be used, on the order of $\sim 10^{-8}$. However, under these conditions diffusion occurs extremely slowly, in fact equilibrium may not ever be achieved.[225,262] As a result, many studies have opted out of using low pressure nitrogen isotherms, but instead probe ultramicropores using CO_2 isotherms at 0 °C.[62,102,226,263–267] CO_2 isotherms do however have an upper detectable pore size limit under these conditions as condensation will not be achieved. Thus, the combination of these two isotherms can be used to produce a better picture of micropore sizes above 4 Å.

Secondly, nitrogen's relatively high quadrupole moment[224] can confound measurements on samples containing polar moieties as is the case for many activated carbons. Polar groups affect the orientation of nitrogen with respect to the surface – this results in the actual cross-sectional area of the molecule differing to that which is used in calculations of textural parameters such as A_{BET}. This is even more problematic for CO_2 as it is more polar than N_2.[224,268] As such, dual gas adsorption techniques may also employ O_2 and H_2 (at −196 °C) which both have lower quadrupole moments than N_2.[225,268,269] H_2 has the added advantage of being smaller than CO_2 thus improving the lower pore size limit to ~3 Å.[225]

3.4.2. Calculations

Classical. Historically, measures of porosity were determined *via* individual manipulations and/or calculations from the raw isotherm.

(i) Surface area: Stephen Brunauer, Paul Hugh Emmett, and Edward Teller expanded Langmuir theory to account for multilayer adsorption, which occurs at higher pressures and temperatures. The eponymous BET surface area, A_{BET}, is calculated by first determining the total quantity of gas adsorbed, Q, and from this calculating Q_m, the quantity of gas in the monolayer

© 2022 The Author(s). Published by the Royal Society of Chemistry

Open Access Article. Published on 12 January 2022. Downloaded on 3/24/2022 12:40:42 PM.
This article is licensed under a Creative Commons Attribution 3.0 Unported Licence.

using the following equation;

$$\frac{1}{Q\left(\frac{P_0}{P}-1\right)}=\frac{c-1}{Q_{\mathrm{m}}c}\left(\frac{P}{P_0}\right)+\frac{1}{Q_{\mathrm{m}}c}$$

where the BET constant, c, is derived from the heat of adsorption of the first and subsequent layers (E_1 and E_{L});

$$c=\mathrm{e}^{\frac{E_1-E_{\mathrm{L}}}{RT}}$$

A measured isotherm can be transformed in accordance with the BET equation allowing for the determination of Q_{m} from a linear portion of the plot, selected according to the Rouquerol criteria.[270,271] Thus A_{BET} is determined using the adsorption cross-section, σ, and mass of the adsorbate, a;

$$A_{\mathrm{BET}}=\frac{Q_{\mathrm{m}}N_{\mathrm{A}}\sigma}{a}$$

Despite its ubiquity, the theoretical backing of A_{BET} does not robustly describe the surface area of all materials, particularly in the case of materials having very small pores as so-called multilayer adsorption is not relevant here.[218,271] In addition, the model does not account for surface chemical or energetic heterogeneity, and as such σ may differ at different points on the surface.[218,225,272] As a result A_{BET} should not be considered a 'true' value for the surface area of porous carbons. Nevertheless if applied consistently and correctly, (*i.e.* selecting the relative pressure range as ascribed by the aforementioned Rouquerol criteria),[218,271] A_{BET} provides the 'apparent' surface area for microporous materials, which is a useful metric for comparing the porosity of different, related samples. This is in contrast to the much simpler typical criteria used to select the pressure region for determination of A_{BET} in mesoporous, macroporous or nonporous materials, wherein the range is typically between 0.05 and 0.30.

It should be noted however that manual application of the Rouquerol criteria can be extremely inconsistent when applied by different people. In a round-robin study, the Fairen-Rodriguez group found that the manually determined A_{BET} from the same isotherm could differ by more than 7000 $\mathrm{m^2\ g^{-1}}$. Furthermore, even when applied correctly the Rouquerol method can yield multiple acceptable pressure regions for an isotherm. They therefore propose an algorithmic approach to determine of the optimal Rouquerol range and thus the valid BET area.[273]

(ii) Pore volume: is typically measured using the quantity of gas adsorbed at the isothermal plateau and at relative pressure approaching 1, as by this point the pores are considered to be fully filled by the adsorbate. As this method only uses one point on the isotherm, it is known as the single-point pore volume calculation.[218] This method is not applicable to all isotherms, as some do not exhibit a plateau.

(iii) Microporosity: there are various classical methods used for this, the first of these being the t-plot method which relies upon comparison of the experimental isotherm with that of a standard adsorbent under the same analytical conditions.[274] This of course relies on an appropriate standard, which is not always available. Furthermore this method may give inaccurate micropore volumes for samples that contain significant mesoporosity,[275] in some cases yielding negative values for microporosity.[276] Further developments include the α_{S}, Dubinin–Astakhov (DA) and Dubinin–Radushkevich (DR) plots.[274,277] These methods utilise a transformation of the isotherm to yield a roughly linear plot. The slopes and intercepts of such plots can then be used to calculate micropore volume and surface area.

(iv) Pore size: methods are available for determination of a pore size distribution such as H–K (Horváth–Kawazoe) and BJH (Barrett, Joyner and Halenda) from an N_2 isotherm in the micropore and mesopore region, respectively. The former relies on the assumption that pores of some width fill at a certain relative pressure, which in turn is calculated using molecular potentials. The latter method uses the isotherm's desorption branch to relate the amount of N_2 removed from pores at decreasing relative pressure to pore width.[278,279] Whatever the method, PSDs can be displayed in cumulative or differential form and according to either surface area or pore volume. Once the PSD is achieved, determination of an average pore width is trivial.

Density functional theory. Classical models for pore structure determination rely on parameters including (but not limited to) the monolayer capacity of the adsorbent, as well as the adsorbate–adsorbent interaction. Additionally, they make use of potentially false assumptions such as that the adsorbate behaves as a two-dimensional ideal gas (in the case of the Horvath–Kawazoe model). Conversely, Density Functional Theory (DFT), when applied to porosity, makes use of statistical modelling of adsorbate–adsorbate and adsorbate–adsorbent interactions specific to a system determined by pore size, pore geometry, nature of the adsorptive and temperature. A set of theoretical isotherms is generated according to the specific variables of the system under examination, where each individual, theoretical isotherm is calculated for an idealized adsorbent having a single pore width. This library of calculated isotherms is known as the kernel, $N\left(\frac{P}{P_0},W\right)$ which can be used in conjunction with the experimental isotherm, $N\left(\frac{P}{P_0}\right)$ to yield a pore size distribution as a function of pore width, $f(W)$;[274]

$$N\left(\frac{P}{P_0}\right)=\int_{W_{\min}}^{W_{\max}}N\left(\frac{P}{P_0},W\right)f(W)\,\mathrm{d}W$$

This data can be displayed in terms of differential or cumulative pore volume and surface area, and as such can be used to determine textural quantities traditionally calculated *via* classical methods.[215,266] Recent reports indicate that gas uptake may be better predicted using porosity determined according to DFT rather than classical methods.[280,281] DFT methods have also been employed in recent years to combine isotherms determined using two separate gases to yield a single PSD.[91,225]

It is useful to compare measures of porosity derived using DFT methods to those using classical methods. In terms of pore volume, Jagiello *et al.* reported that both total and micropore

Open Access Article. Published on 12 January 2022. Downloaded on 3/24/2022 12:40:42 PM.
This article is licensed under a Creative Commons Attribution 3.0 Unported Licence.

volume of a set of biochars and activated carbons as determined using the single-point and DR methods respectively, were essentially the same as those found using DFT.[91] This was shown to also be true for micropore volumes.[282] Villarroel-Rocha *et al.* found broad agreement between values of micropore volume in microporous materials derived using the DR, t-plot, α_S and DFT methods.[275] However, this is not true in the application of these methods to all isotherms; DFT and t-plot methods show greater disagreement the further the isotherm deviates from type-I.[275,276]

3.5. Grain density

While gravimetric measures of porosity have historically been the metric associated with gas uptake increasingly, high volumetric capacity is desired in applications such as methane storage,[127,260,283] as well as CO_2 capture.[174,284,285] Various studies have shown that grain density is a good predictor of H_2, CH_4 and CO_2 capacity, provided that this is balanced with appropriate pore size as well as high surface area and pore volume.[35,81,143,178,182,194,255,284,286] Grain density, d may be calculated according to

$$d = \left(\frac{1}{\rho_s} + V_T\right)^{-1}$$

where ρ_s is the skeletal density determined *via* helium pycnometry and V_T is the total pore volume.[35] Alternatively it can be measured directly by packing the sample at high pressure.[127] Determination of grain density allows for the derivation of volumetric equivalents to surface area and pore volume, which are typically calculated gravimetrically. These can be used as further metrics to assess volumetric gas uptake (see Fig. 4).

4. Controlling porosity

While the achievement of reasonable porosity in carbons for small gas molecule adsorption is relatively well established, various methods for fine control over various textural parameters are under constant development. Of particular recent interest in the literature are methods to improve volumetric as opposed to gravimetric porosity so as to optimise volumetric capacity for applications such as on-board storage.

4.1. Activated carbons

4.1.1. Choice of activating agent. KOH is the primary reagent used for synthesis of activated carbons intended for physisorption of small molecules as it yields superior carbons with high surface area and pore volume, a high degree of microporosity and tuneable PSD.[20,79,127,220,233,249,287–289] Nonetheless, physical activating agents such as CO_2 and steam,[77,249,260,288,290] as well as other 'traditional' chemical agents such as $ZnCl_2$, H_3PO_4 and NaOH continue to be explored.[152,252,287–289,291,292] A summary of textural properties of carbons derived using a variety of activating agents is presented in Table 2. Recently Chao Ge *et al.* have produced moderate surface area (up to 865 $m^2\ g^{-1}$) carbons by CO_2-activation of polyurethane films at 1000 °C, with CO_2 capacity of *ca.* 3 mmol g^{-1} at 1 bar and 0 °C. It should be noted however that this uptake is not realistic, as post-combustion capture is unlikely to take place at 0 °C, so we can expect significantly less uptake at more realistic temperatures (>25 °C).[293] In addition, this uptake is likely significantly improved by the high N-content of this carbon. The uptake of the CO_2-activated carbon was dwarfed by NaOH- and KOH-activated samples reported in the same work, which have superior microporosity.[288] While KOH can produce extensive microporosity, for some applications this may not be as relevant; Yueqin Song *et al.* produced activated carbons from coconut shell charcoal using both KOH and H_3PO_4 as activating agents. Despite the KOH-activated sample having a surface area triple that of its H_3PO_4-activated counterpart, their gravimetric methane capacity at 1 bar and 10 °C was nearly identical at 4.1 and 4.0 mg g^{-1} respectively.[287] The narrow PSD associated with KOH-activation at KOH/precursor mass ratio <2 can also be achieved using $ZnCl_2$, however surface area and pore volume of such samples tend to be relatively low.[112,152] Indeed, the ultrahigh surface areas accompanied by extreme microporosity required for H_2 storage at high pressures (>40 bar) can only be readily achieved by activation with KOH. Conversely, the multiplicity of CO_2 adsorption applications under different pressure and temperature conditions means that a greater variety of textural characteristics are useful for CO_2 capture on activated carbons.[61,220,221,237,294] Thus, when 'alternative' chemical activating agents are reported that yield lower surface area materials, the suggested application is typically some form of CO_2 capture

Table 2 Porosity of recently reported carbons derived using a variety of porogens, and gravimetric gas uptakes where available

Porogen	Precursor[a]	A_{BET}[b]	V_t[c]	$\%V_{mic}$[d]	S[e]	U[f]	Ref.
CO_2	Graphite oxide	908	3.08	3	CO_2 (1, 0)	1.6	249
KOH	Cigarette butts[g]	4310	2.09	82	H_2 (20, −196)	9.4	82
K_2CO_3	Polyacrylonitrile	1250	0.64	89	CO_2 (1, 30)	2.4	252
$KHCO_3$	Glucose[g]	2210	0.97	84			138
Potassium oxalate	Sawdust[g]	1470	0.71	73	CO_2 (1, 25)	4.4	135
NaOH	Polyacrylonitrile	1020	0.57	89	CO_2 (1, 30)	2.2	252
$NaNH_2$	Polyacrylonitrile	833	0.36	94	CO_2 (1, 30)	1.8	252
H_3PO_4	Coconut shell	304			CH_4 (1, 10)	0.3	287

[a] Precursor description. [b] BET surface area ($m^2\ g^{-1}$). [c] Total pore volume ($cm^3\ g^{-1}$). [d] Percent microporosity by volume. [e] Adsorbate measured (values in brackets are pressure (bar) followed by temperature (°C)). [f] Uptake in mmol g^{-1} except for H_2, which is wt%. [g] Precursor was converted to hydrochar prior to activation.

© 2022 The Author(s). Published by the Royal Society of Chemistry

Open Access Article. Published on 12 January 2022. Downloaded on 3/24/2022 12:40:42 PM.
This article is licensed under a Creative Commons Attribution 3.0 Unported Licence.

(see Table 2).[75,135,232,252,288] As an example, a recent paper by Weiwei Shi and co-workers found that activating ammonium citrate with $CuCl_2$ generates carbons were with hierarchical pore structure, albeit almost exclusively (up to 94%) in the micropore region. The authors' hypothesis is that coordination between Cu^{2+} ions and organic moieties is one of the driving forces for porosity development. Reasonable CO_2 capacity of 4.21 mmol g^{-1} was achieved at 1 bar and 25 °C.[295]

The success of group 1 metal hydroxides as activating agents for highly microporous carbons has led to the exploitation of other hydroxides, as well as salts of potassium and sodium as porogens.[232,252,288,296,297] Theoretically a gentler activating agent, $Ca(OH)_2$-activation yields carbons with much lower surface areas and a lower degree of microporosity than KOH under identical conditions.[288] Taylor found that careful selection of conditions may produce carbons with pore volumes exceeding 1 cm^3 g^{-1}, with the majority of this coming from mesopores.[296] Although microporosity is low, activation at 800 °C yields carbons whose micropores are dominated by pores around 8 Å, thus achieving moderate CO_2 capacity of up to 2.3 mmol g^{-1} at 1 bar and 25 °C.[296] Similarly, Singh *et al.* reported that the activation of polyacrylonitrile with $NaNH_2$ yields carbons with low overall porosity development, but a higher concentration of pores centred at 7 Å when compared to carbons activated with NaOH under similar conditions. This indicates that when using $NaNH_2$ as an activating agent much of the porosity is likely formed *via* Na intercalation, rather than redox reactions – in contrast to what happen with NaOH as activating agent.[252]

While KOH has been identified as a uniquely superior activating agent, its corrosive nature qualifies it as an aggressive reagent in activated carbon synthesis, thus resulting in low yields. As the majority of the microporosity comes about *via* the intercalation of potassium ions into graphitic layers as opposed to corrosive action of the hydroxide counterion, gentler anions such as carbonate,[232,298] and bicarbonate,[138,299] have been shown to give improved yields, resulting in high surface area carbons with tuneable porosity. For example, Sevilla and Fuertes produced $KHCO_3$-activated carbons from glucose hydrochar with surface areas of 2000 m^2 g^{-1} with more than 80% microporosity. Porosity development is lower than that for an equivalent amount of KOH under similar conditions because the initial pore formation process – the oxidation of C by K_2CO_3 – requires temperatures in excess of 700 °C, while KOH can oxidise C at much lower temperatures.[138] On the other hand, Xia and co-workers use of an acetate counterion has shown that a contributing factor to pore formation may be hydrogen bonding between polar moieties within the biomass and the activating agents.[297]

Another promising 'gentle' potassium activating agent is potassium oxalate (PO).[131,135–137,300,301] The activation mechanism proceeds principally *via* gasification of K_2CO_3 at or below 800 °C, resulting in carbons that are almost exclusively microporous. Therefore activating with PO allows a high degree of control over sample porosity – Aljumialy and Mokaya found that pore volume of sawdust-derived carbons could be reliably increased within the micropore region by increasing activation temperature. Interestingly this improvement in overall porosity had little effect on pore sizes. When the activation temperature is increased to 900 °C, oxidative etching of the carbon surface begins,[135,136] which results in mesopore formation without the collapse of the previously formed micropores, producing carbons with a hierarchical pore network optimised for moderate pressure (20 bar) CO_2 storage (18 mmol g^{-1} excess uptake). The highly microporous (>90% microporosity) carbons produced at lower temperatures achieve CO_2 capacity of 4.3 mmol g^{-1} at room temperature and ambient pressure.[135] Lee *et al.* achieved similarly high degrees of microporosity (approaching 100%) in the PO activation of carbonized corn husks (CCH). Quite unusually, increasing quantities of PO lead to greater development of ultramicropores. Methane capacity was optimised (7.75 mmol g^{-1} at 35 bar and 25 °C) at PO/CCH ratio of 3 as a result of highest surface area as well as hierarchical pore structure including ultramicropores.[131]

Mixing method. Chemical activating agents may be combined with the precursor material either through physical mixing[35,135,255,302] or by impregnation with a dissolved agent.[75,288,290,295,303] The latter technique, so-called solution impregnation, is followed by a drying step to remove the solvent prior to activation. The perceived advantage of solution impregnation over solid mixing is that the activating agent is more evenly distributed, thus resulting in more consistent porosity throughout the material. Nevertheless, PSDs of carbons derived using the physical mixing technique show narrow PSDs indicating that an impregnation and drying step may not strictly be necessary.[80,82,135] There is, unfortunately, a dearth of literature comparing the porosity of carbons derived using the two techniques. However, in 2018 Boujibar *et al.* reported activated carbons synthesised using KOH and NaOH *via* both solution impregnation and physical mixing. In terms of surface area, the KOH-activated samples showed improvements of 20% when physical mixing was employed but these gains reduced the proportion of microporosity. Conversely, surface area of NaOH-activated samples were 25% greater using solution impregnation over physical mixing, though the former samples had a much broader PSD. Despite the differences in textural properties attained through these two mixing techniques, CO_2 uptake at 25 °C and 1 bar does not significantly differ between the two sample sets, implying that both impregnation and solid mixing can be effectively used to balance overall porosity development and level of microporosity for gas adsorption.[292]

Combined activating agents. While chemical activating agents provide highly microporous samples which are suited to H_2 storage and low pressure CO_2 capture, other applications such as high pressure CO_2 capture require so-called hierarchical or multimodal pore structures wherein most or all microporosity is retained but further porosity is generated in the mesopore region. Caturla *et al.* achieved this in 1991 by subjecting a $ZnCl_2$-activated carbon to physical activation using CO_2.[112] Using both a chemical and physical activating agent has become known as physicochemical activation. Since then other

Open Access Article. Published on 12 January 2022. Downloaded on 3/24/2022 12:40:42 PM.
This article is licensed under a Creative Commons Attribution 3.0 Unported Licence.

researchers have produced activated carbons *via* a simultaneous physicochemical method, wherein during the pyrolysis of a mixture of precursor and chemical activating agent the flow of inert gas is interrupted with a physical activating agent.[152,287,304,305] In fact, Hu and Srinivasan reported that simultaneous physicochemical activation using $ZnCl_2$ and CO_2 is more effective for formation of mesopores than an equivalent sequential activation.[304] KOH and H_3PO_4 have also been used as the chemical porogen in conjunction with CO_2 although it appears that using KOH makes the material more resistant to mesopore development.[305,306] Table 3 gives examples of the porosity of carbons derived through single and two step-activations.

Physicochemical activation is not limited to broadening of PSDs; for example Song *et al.* explored the sequential physicochemical activation of coconut shell charcoal using H_3PO_4 and steam and found that steam treatment at 800 °C produced carbons with twice the surface area of those activated with H_3PO_4 alone. In contrast to earlier carbons produced using $ZnCl_2$ and CO_2, the majority of new porosity development was in the micropore region, with 80% of surface area from pores of width 4.5–6.5 Å. This sample achieved 58% higher gravimetric CH_4 uptake at 1 bar and 10 °C compared to a conventionally activated equivalent.[287] Adlak *et al.* reported similar improvements in both overall surface area and microporosity for carbons activated using KOH and steam simultaneously. This could be a result of the dissolution of K compounds in steam, which results in greater mobility of the activating agent through the sample and thus further activation *via* intercalation.[290]

The porosity of carbon can also be modulated by adding a so-called mediator to the precursor-activating agent mixture. The mediator is a species that is not in itself an activating agent, but produces activating species as it breaks down during pyrolysis, which can then work in conjunction with the activating agent to produce multimodal porosity. An early example of a mediator is the use of melamine by Fuertes and Sevilla in the KOH-activation of hydrochars. Samples synthesised using melamine had higher surface areas than their conventionally activated counterparts, which came about through the development of mesopores. These mesopores purportedly originate from gasification by volatile nitrogen compounds released upon the decomposition of melamine.[307] Indeed, there are other notable instances of volatiles from nitrogenous compounds having an activating effect.[221,308] Further work revealed that surface areas above 3200 $m^2\ g^{-1}$ could be achieved by this method, with optimal porosity for cryogenic H_2 storage at 20 bar, and room temperature CO_2 capture at 40 bar, achieving uptakes of 7 wt% and 21 mmol g^{-1}, respectively.[244] By swapping KOH for the gentler PO, CO_2 uptake at 40 bar was improved to almost 40 mmol g^{-1} due to a broad, continuous PSD spanning the ultramicropore and small mesopore region.[136] More recently Hu *et al.* reported the use of sodium alginate as a mediator in conjunction with KOH to prevent the over-activation of carbons derived from a variety of biochars.[309] The pyrolysis of sodium alginate had previously been shown to produce non-porous carbons.[308] On pyrolysis the mediator broke down to produce Na_2O which appears to have restricted porosity development and limited the PSD to the micropore region accompanied by further development of ultramicropores. As a result, H_2 storage capacity at 1 bar and −196 °C was improved by up to 87% from 1.37 wt% to 2.56 wt%.[309]

Self-activation. In recent years, research interest has turned to precursors that can develop porosity *via* pyrolysis without the

Table 3 Comparison of porosity and gas uptake of activated carbons derived *via* activation in one or two activation steps

Precursor	Porogen[a]	A_{BET}[d]	V_t[e]	$\%V_{mic}$[f]	S[g]	U[h]	Ref.
Coal	$ZnCl_2$ (500)	1530	0.69	61			152
	$ZnCl_2$ (500) and CO_2 (950)[b]	1820	0.97	44			
Coconut shell	S (unknown)	875			CH_4 (10, 1)	0.2	287
	S, then KOH (600)[c]	961				0.3	
Coconut shell	S (unknown)	875			CH_4 (10, 1)	0.2	287
	S, then H_3PO_4 (500)[c]	304				0.3	
Oil palm shell	H_3PO_4 (450)	615	0.28	93	CH_4 (30, 1)	0.7	306
	H_3PO_4 (450), then CO_2 (855)[c]	642	0.28	93		1.1	
Neem wood[i]	KOH (800)	764	0.44	81			290
	KOH (800) and S (800)[b]	963	0.55	87			
Starch[j]	KOH (800)	3000	1.4	77			307
	KOH (800) and M (800)[b]	3280	2.4	45			
Sodium alginate	HNO_3 (750),	444	0.21		CO_2 (25, 1)	2.0	308
	HNO_3 (750) and H_3PO_4 (750)[b]	1740	1.6			4.5	
Cellulose[j]	KOH (700)	1280	0.68	84	H_2 (−196, 20)	4.2	
	KOH (700) then KOH (700)[c]	2470	1.18	81		5.7	
Sawdust	PO (800)	1270	0.52	96			136
	PO (800) and M (800)[b]	3090	1.8	66			
Melon seeds[i]	KOH (600)	1140	0.41	100	H_2 (−196, 1)	1.4	309
	KOH (600) and NaA (600)[b]	2310	0.89	96		2.6	

[a] First and second steps. Activation temperature (°C) in parenthesis, S = steam, M = melamine, PO = potassium oxalate, NaA = sodium alginate. [b] Simultaneous activation. [c] Sequential activation. [d] BET surface area ($m^2\ g^{-1}$). [e] Total pore volume ($cm^3\ g^{-1}$). [f] Percentage microporosity by volume. [g] Adsorbate gas (CH_4, CO_2 or H_2); values in parenthesis are measurement temperature (°C) and pressure (bar), respectively. [h] Gravimetric uptake in mmol g^{-1}, except for H_2, which is wt%. [i] Precursor was pyrolysed before porogenesis. [j] Precursor was hydrothermally carbonised before porogenesis.

© 2022 The Author(s). Published by the Royal Society of Chemistry

Open Access Article. Published on 12 January 2022. Downloaded on 3/24/2022 12:40:42 PM.
This article is licensed under a Creative Commons Attribution 3.0 Unported Licence.

assistance of an external activating agent. As previously mentioned, so-called biochar is derived through physical self-activation of biomass to produce microporous carbons,[89–91] through the release of oxidising gases such as CO_2 and H_2O upon biomass pyrolysis.[310,311] Under typical conditions, the bulk of these oxidising gases are removed from the sample due to a flow of N_2 or Ar before they can develop significant porosity. Xia and Shi found that long, harsh pyrolysis of kenaf core in a closed system allowed the oxidising gases to react more with the carbonised biomass to form pores, resulting in mesoporous carbons with surface areas approaching 2500 m^2 g^{-1}. Carbons with hierarchical pore structures were produced when temperature and dwell time were limited to 1000 °C and 10 h respectively.[312]

Precursors or additives with high nitrogen contents are often employed to produce N-doped carbons for use in CO_2 capture. However, nitrogen also has a part to play in porosity development in the mesopore region. Sevilla *et al.* found that polypyrrole-derived carbons gave higher than expected surface area for the activation conditions.[126] Later work confirmed that by increasing the N concentration by use of an additive, the porosity of microporous carbons could be extended into the mesopore region, resulting in higher H_2 and CO_2 storage capacity. This effect is presumed to come about due to the gasification of the carbonaceous structure by volatile N-compounds.[244,307] Similar effects have also been reported by Ariharan *et al.* for precursors containing phosphorous.[313,314]

Self-activation may also have had a part to play in the unusual temperature-porosity relationship of a series of cigarette butt-derived KOH-activated carbons. It is supposed that the unexpectedly high surface area (4300 m^2 g^{-1}) of highly microporous sample activated at 600 °C may be a result of metal contaminants within the cigarette butt that assist KOH in the activation process. Such textural properties resulted in unprecedented hydrogen storage capacity of 8.1 wt% at −196 °C and 20 bar.[82] This idea of activation by contaminants is supported by a 2018 study by Longxin Li *et al.* wherein carbons produced *via* the simultaneous physicochemical activation of demineralised coal achieved lower surface areas than and equivalent carbon from untreated coal.[152]

Organic salt carbonisation. Organic salts are an interesting class of so-called self-activating precursors for activated carbon production. To achieve self-activation, the cation must be a metal that can take part in chemical activation. Furthermore, the anion must be both sufficiently rich in carbon, and stable enough that it does not fully degrade before its cation can cause it to undergo activation. For example, while PO is interesting as a so-called gentle porogen, the oxalate ($C_2O_4^{2-}$) anion degrades to CO_3^{2-} before activation can be achieved, meaning that no residual carbon remains.[133] More bulky precursors such as K, Na, Ca, Mg, Fe, and Zn salts of citric acid have been successfully carbonised to yield carbons with surface areas of at least 500 m^2 g^{-1}.[315–320] Other notable examples include K, Na, and Ca gluconate,[315,321–323] Na and Ca alginate,[315] and potassium tartrate.[324] K salts of polymers such as poly(acrylamide-*co*-acrylic acid),[325] Na salts of several forms of poly(styrene sulfonate),[326–328] and even a Zn organic framework[329] have been carbonised in order to build on structural voids in the precursor.

Use of organic salts as self-activation precursors means that porosity of the carbons is easily tuneable simply by changing the anion or cation. For example, Sevilla and Fuertes found that while pyrolysis at 800 °C of potassium gluconate or citrate yields relatively high surface area and highly microporous carbons, the equivalent Ca salts produce a greater degree of mesoporosity in the resultant carbon.[315] Pyrolysis of Mg, Zn, and Fe salts also results in highly mesoporous carbons.[318–320] Indeed, mesoporous carbons derived from magnesium citrate and zinc glycolate have pore volumes in excess of 2.5 cm^3 g^{-1}.[318,330] The pore structure of carbons derived from Na salts often lie somewhere in the middle, typically having hierarchical (microporous plus meso- or macroporous) PSDs.[321,326–328,331] The identity of the cation can also affect pore shape, for example carbonisation of sodium gluconate produces unusually long, narrow slit-shaped pores, whereas pores in calcium gluconate derived carbons have a more cellular structure.[315,332] On the other hand, anion composition and structure seems to have a greater effect on large scale morphological features rather than the fine pore structure.[133] For example, while salts of smaller anions like gluconate and citrate can be used to produce regular, sheet-like structures under appropriate conditions, polymeric salts typically yield carbons with a much lower degree of structural regularity.[315,321,322,326,327,333,334]

Despite the easily tuneable porosity of organic salt-derived carbons, reports on their application as gas storage media are minimal. By far the dominant application of such materials appears to be as electrodes for supercapacitors,[315,316,319,320,330,334,335] however their use as (electro)-catalysts,[319,322,329] as well as ion storage[318,331] and battery[326,336] materials is well documented. This may be due to the fact that although microporous carbons can easily be formed from organic salts, the surface areas of such materials are typically quite low (<1500 m^2 g^{-1}). Of course some gas storage/capture applications require more hierarchical micro-mesoporous pore structure, but surface areas of such carbons still seem to be largely limited to no more than 2000 m^2 g^{-1}. A notable exception to this are some carbons synthesised by Sevilla *et al.* from potassium citrate, which when carbonised with urea at 750–800 °C yields a carbon with surface area of up to 3350 m^2 g^{-1} and pore volume >2.0 cm^3 g^{-1} which is relatively evenly divided between meso- and micropores.[335] Such a material would be an interesting candidate for CO_2 pressure swing adsorption (PSA) applications but unfortunately this wasn't examined by the authors. The sole instance of an organic salt-derived carbon being employed in gas storage/capture is that of potassium hydrogen phthalate (KHP). Uniquely narrow PSDs were achieved by researchers in the Mokaya group through gentle pyrolysis conditions producing carbons with a single micropore width. This is presumably the result of mechanistic differences when K^+ (as opposed to the harsher KOH) is the primary activating agent – that is, activation proceeds solely *via* intercalation of potassium ions into the pores. At temperatures above 800 °C, the PSD

Open Access Article. Published on 12 January 2022. Downloaded on 3/24/2022 12:40:42 PM.
This article is licensed under a Creative Commons Attribution 3.0 Unported Licence.

begins to broaden resulting in higher surface area samples with CO_2 capacities up to 4.5 mmol g^{-1} under ambient conditions.[296,337]

4.1.2. Precursor composition. It has been noted that the composition of the precursor, in particular the (atomic) O/C ratio, may have a role to play in pore development upon both chemical and physical activation. Precursors with higher O/C ratios are typically more susceptible to activation, and therefore may yield higher surface area carbons.[77,135] These increases in surface area are however accompanied by PSD broadening and pore collapse, meaning that improvements in microporosity and thus low pressure storage/capture of small molecules may be facilitated by starting materials with *lower* O/C ratios, known as activation-resistant precursors.[35,98] However, activation resistance may not be a direct function of precursor oxygen content; more complex factors such as the presence of specific oxygen containing moieties, the lignin content of ligno-cellulosic biomass, or the formation of highly stable composite structures during pyrolysis may confer activation resistance.[80,98,251,338] For example, it has been shown the high stability of pure lignin, conferred by aromatic structures, means that is does not readily form pores on pyrolysis without the use of an activating agent, whereas dehydration reactions between hydroxyl groups during the pyrolysis of cellulose and hemi-cellulose confer three-dimensional porosity on the resultant carbon.[338] Nonetheless it is possible to tailor pore sizes of carbons *via* careful selection of precursors according to their composition. For example, Pedicini *et al.* synthesised biochars from seaweed and wood chips and found that the O/C ratio of the former was approximately 50% higher than that of the latter. When activated with KOH, their surface areas were similar, however the carbons derived from wood chips had a much greater proportion of micropores.[76] Similarly, Park *et al.* reported that when 'upgrading' commercial activated carbons by further activation with KOH, the precursor with the higher O/C ratio produced higher surface area, more mesoporous carbons whilst lower O/C ratios lead to more microporous, low surface area carbons. They therefore concluded that precursors with higher O/C ratios are more suited to synthesis of carbons for high pressure CH_4 storage.[254] On the other hand Altwala and Mokaya investigated the textural properties and CH_4 storage capacity of carbons synthesised from air-carbonised date seed, having a very low O/C ratio of 0.21. By increasing the KOH : precursor weight ratio to 2 to 4, it was possible to retain much of the microporosity whilst doubling the surface area to over 2000 m^2 g^{-1}. The authors attributed the lack of so-called over-activation to the high activation resistance of carbonised date seeds. Porosity of carbons could be controlled *via* temperature or KOH : precursor ratio towards high gravimetric or volumetric methane capacity (25 °C and 35 bar) up to 11.4 mmol g^{-1} and 196 cm^3_{STP} cm^{-3}, respectively.[35]

The O/C ratio of a precursor can also be modulated according to pre-carbonisation conditions. For example, Zhen Zhang *et al.* synthesised a set of precursors by calcining glucose-derived hydrochar in air at temperatures between 200 and 300 °C, as well as calcining pure glucose at 300 °C, and also examined non-calcined hydrochar. These precursors differed most apparently due to the abundance of COOH moieties present on their surface (so-called ion exchange capacity) which varied from 0.22 to 3.92 mmol g^{-1}. This corresponds to overall O/C ratios in the range 0.37–0.45. The authors posit that the presence of COOH is significant for activation *via* aqueous solution impregnation with KOH, as the carboxyl group undergoes an ion-exchange reaction to form COOK. The closely bound K^+ can thus act as a more effective activating agent than if it were present in the form of KOH. It was found that the content of ultramicropores was optimised for the activated carbon derived from hydrochar calcined at 300 °C, having an ion exchange capacity of 3.92 (O/C ratio 0.45). This sample showed the highest ambient (25 °C, 1 bar) CO_2 uptake of 4.3 mmol g^{-1}.[251]

This does not however mean that a pre-carbonisation or calcination step automatically improves a precursor's ability to form carbons with favourable porosity for small molecule adsorption. Balahmar *et al.* found that pre-treatment of precursors by hydrothermal carbonisation had either marginal or negative effects on the porosity of KOH-activated carbons derived from a variety of biomasses.[339] This may be a function of decreasing O/C ratio and thus increasing resistance to activation.

A simple way to change precursor composition is simply to mix two precursors with significantly different compositions. An example of this is the mixing of polypyrrole (PPY) with sawdust hydrochar (H) or raw sawdust (SD) which have an O/C ratio of 0.672, 0.483 and 0.773, respectively (see Fig. 5). Researchers in the Mokaya group determined that a greater degree of control over porosity could be achieved by activating the mixed precursor than by activating any of the three alone.[98,135,221,237] For samples activated with KOH, porosity was mainly developed in the mesopore region. Increasing concentrations of H in a PPY–H mixture results in decreased mesoporosity, which is attributed to the decrease in O/C ratio; more specifically the mesoporosity is a function of the amount of PPY in the mixture whereas the mesopore size is increased with increasing PPY : H ratio.[98] However, the same does not apply to carbons synthesised by from mixtures of PPY and SD, wherein increased O/C ratio actually results in higher a higher degree of microporosity and lower porosity over all. This is attributed to stabilising interactions between aromatic moieties on PPY and SD which confer resistance to activation.[98] On the other hand, using a gentler activating agent (potassium oxalate) results in more hierarchical meso–microporous carbons, with optimised pore structure for high pressure CO_2 capture.[135] The appropriate selection of Ppy : H ratio, activating agent and activation conditions can be used to produce carbons with a variety of porosities and textural characteristics suited to applications ranging from low pressure CO_2 capture to high pressure H_2 storage.[98,135]

4.1.3. Compactivation. Compactivation, also known as mechanochemical activation is a process first reported in 2015 by the Mokaya group, wherein a solid–solid mixture of precursor and activating agent is compressed into a pellet prior

© 2022 The Author(s). Published by the Royal Society of Chemistry

Open Access Article. Published on 12 January 2022. Downloaded on 3/24/2022 12:40:42 PM.
This article is licensed under a Creative Commons Attribution 3.0 Unported Licence.

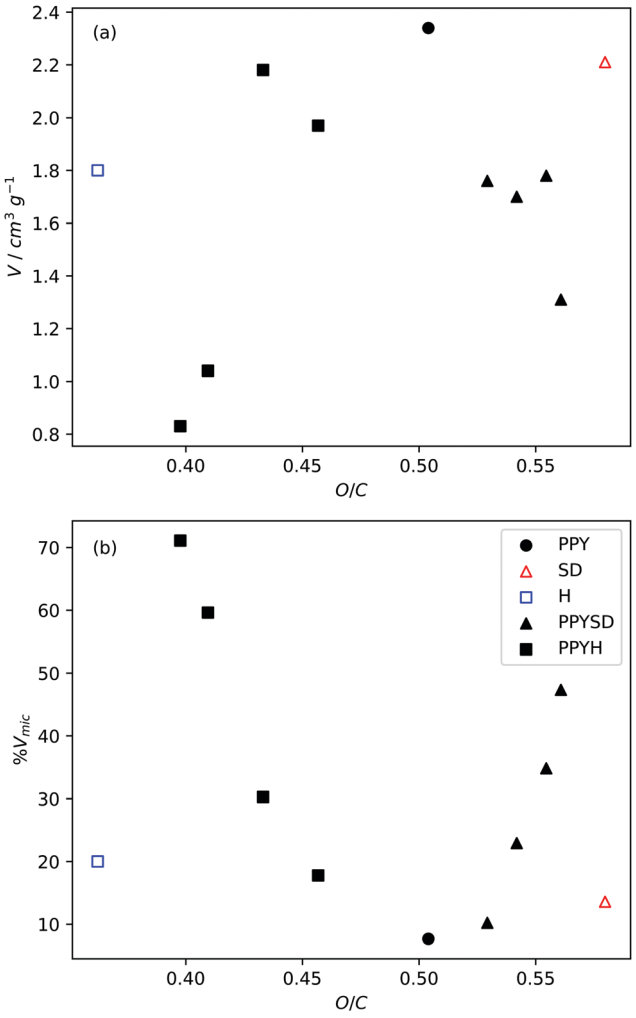

Fig. 5 Variation of pore volume and micropore percentage (by volume) with precursor O/C ratio as controlled by mixing in different quantities the precursors polypyrrole (PPY), sawdust (SD) and sawdust hydrochar (H). Adapted from work by Balahmar *et al.* O/C ratio. All samples activated at 800 °C for 1 h.[98] O/C ratio determined using weighted sums of the O/C contents of PPY, H, and SD.

to activation. The rationale of this step is to increase atomic proximity between the precursor and activating agents, in order to increase activating agent efficiency thus producing higher surface area carbons without broadening the PSD. In addition, carbons with relatively high surface areas and pore volumes can be produced at unusually low activation temperatures.[238,248] Table 4 compares the porosity and gas uptake capacity of materials derived through conventional activation and compactivation. Although a variety of precursors have been tested for compactivation, thus far materials have only been reported where KOH is used as an activating agent. Compactivated samples thus show superior CO_2 and H_2 capacity over similar conventionally activated carbons at pressures up to 50 bar.[237,238,248] Interestingly due to the high packing density of compactivated carbons, improvements in CO_2 uptake are more obvious from a volumetric perspective. For example, a compactivated carbon derived from polypyrrole using KOH at a ratio of 4 and activation temperature of 800 °C achieved a CO_2 uptake of 48 g L^{-1} at 1 bar and 25 °C; an improvement of 37% over its conventionally activated counterpart. This increase is more than triple that of the improvement in gravimetric uptake.[237] The porosity of compactivated carbons remains highly tuneable, with carbons being produced for either high or low pressure CO_2 capture by simply modulating activation temperature.[81]

In 2018 Rambau *et al.* reported mesoporous compactivated carbons from used tyre-derived char, however surface areas of the reported carbons do not approach those in other studies under similar conditions.[340] This may be a result of the char's relatively high carbon content and associated resistance to activation. An alternative explanation is that the compaction pressure was limited to 10 MPa whereas other studies used up to 740 MPa. Despite the clear advantages of compactivation for carbons for gas storage/capture applications there has been very little published on the topic in the past few years. As such, there is as yet no information on the effect of compaction pressure and duration on the porosity of synthesised carbons.

4.2. Zeolite templated carbons

While the synthesis of ZTCs continues to be a popular area of research,[34,172,193,341–344] articles reporting their application in the adsorption of CO_2, H_2 or CH_4 have dwindled in the past

Table 4 Comparison of porosity and gas uptake of carbons derived through conventional activation or compactivation. Values in italics are for compactivated samples

Precursor	T^a	d^b	$A_{BET}{}^c$	V^d	${}^vA_{BET}{}^e$	${}^vV^f$	Pore size^g	${}^gU^h$	${}^vU^i$	S^j	Ref.
Sawdust	600	0.94	866	0.46	814	0.43	6.8	4.3	178	CO_2 (1, 25)	248
		0.95	*1066*	*0.59*	*1013*	*0.56*	*5.9*	*5.8*	*242*		
Polypyrrole	600	0.92	976	0.47	898	0.43	6.8	3.4	136	CO_2 (1, 25)	238
		0.85	*1297*	*0.64*	*1102*	*0.54*	*5.9*	*5.5*	*206*		
Polypyrrole	800	0.32	3589	2.71	1148	0.87	28	45	638	CO_2 (50, 25)	237
		0.38	*3945*	*2.92*	*1499*	*1.11*	*34*	*54*	*928*		
Flash-carbonised wood	700	0.89	1280	0.65	1139	0.58	6.5	2.2	129	CO_2 (1, 25)	81
		0.78	*2315*	*1.08*	*1806*	*0.84*	*7.0*	*4.0*	*137*		
Waste tyres	800		775	0.41			5.8	1.1		H_2 (1, −196)	340

[a] Activation temperature (°C). [b] Packing density (g cm^{-3}). [c] BET surface area (m^2 g^{-1}). [d] Total pore volume (cm^3 g^{-1}). [e] Volumetric BET surface area (m^2 cm^{-3}). [f] Volumetric pore volume (cm^3 cm^{-3}). [g] Pore size taken from centre of most prominent peak in PSD. [h] Gravimetric uptake, in mmol g^{-1} for CO_2 and wt% for H_2. [i] Volumetric uptake (g dm^{-3}). [j] Adsorbate gas (CO_2 or H_2); values in parenthesis are pressure (bar) and temperature (°C).

Open Access Article. Published on 12 January 2022. Downloaded on 3/24/2022 12:40:42 PM.
This article is licensed under a Creative Commons Attribution 3.0 Unported Licence.

three years. In fact since 2018 there exist only nine journal articles on the subject of capture/storage of these molecules in ZTCs.[194,256,257,345–350] Furthermore, of these papers two are based on simulations of hypothetical optimized ZTCs.[257,345] While these provide insights into what an optimal ZTC structure might be for these applications, they do not provide novel methods for modulating ZTC porosity.[257,345] This may be due to a consensus within the community that the more facile synthesis of ACs leads to materials whose pore geometry is more suitable for small molecule sorption. Nonetheless the templating approach provides interesting and unique opportunities for modulation of porosity for use in storage of H_2 as well as CO_2 capture. In the case of CH_4 however, ZTCs have severe limitations on their volumetric storage capacity meaning that they are less feasible as ANG sorbents,[34,240,351] although there has been a recent noteworthy attempt to improve volumetric porosity of ZTCs to this end.[194]

4.2.1. Choice of reagents. It has long been established that replication of the zeolite template and thus maximisation of ZTC porosity requires that the carbon source can easily diffuse into pore channels. As such the choice of potential carbon sources is narrowed to small, volatile, unsaturated organics in the case of carbon introduction *via* CVD[64,179,189–192,195,197,198] while for LI, furfuryl alcohol is the reagent of choice.[88,174,178–182] For example, in 2010 Xia *et al.* reported on the effects of the use of various carbon sources on textural outcomes and template replications using a combination of both CVD and LI techniques. Structural replication and porosity were maximised by templating of zeolite-Y using ethylene in a two-step CVD synthesis. Consequently this carbon with A_{BET} of 2164 $m^2\ g^{-1}$, >90% microporosity and a narrow PSD achieved the highest cryogenic (−196 °C) H_2 storage capacity in the sample set of 4.9 and 1.9 wt% at 20 and 1 bar, respectively. Carbons derived *via* a combination of LI and CVD could approach similar levels of overall porosity and H_2 capacity as the aforementioned sample, but at the cost of PSD broadening and less faithful replication of the zeolitic structure.[190] Table 5 illustrates the effects of the use of different templates, carbon sources, and carbon introduction methods on ZTC porosity.

In recent years attempts have been made to use alternative carbon sources such as sucrose. In order to be used for LI the disaccharide must be dissolved. Wijiyanti *et al.* produced a ZTC with moderate surface area (932 $m^2\ g^{-1}$) and pore volume (0.97 $cm^3\ g^{-1}$) with hierarchical porosity using sucrose dissolved in H_2SO_4, resulting in a material which allows rapid ingress of H_2 (at 30–50 °C and 1 bar) into the porous structure.[346] While the bulk of the literature has focused on using pristine carbon sources in synthesis of ZTCs, Musyoka *et al.* found that a 'dirty' source, namely the pyrolysis gases from used tyres can be used as a CVD vapour (see Table 5). The vapour is composed primarily of small aromatic molecules. When performed following LI templation with furfuryl alcohol on zeolite-13X, the resulting carbons exhibited higher porosity (3254 $m^2\ g^{-1}$ and 91% microporosity) compared to those derived using ethylene in the second (CVD) step. Indeed, carbons produced using tyre pyrolysis vapour as a CVD source exhibit a narrower PSD than those conventionally-produced ZTCs. High H_2 storage capacity of 2.5 wt% was achieved at −196 °C and 1 bar.[348] Although H_2 adsorption was not measured above atmospheric pressure, both the ZTC textural characteristics and the trajectory of the reported isotherm indicate this carbon may be suited to higher pressure applications.

The introduction of nitrogen into the structure of ZTCs is meant to improve adsorption of small molecules due to improved adsorbate-adsorbent interactions – typically this is performed by using a nitrogen-rich carbon source.[179,253,353,354] Such methods also tend to have the side-effect of changing the porosity of the ZTC. For example, Dewi and Widiastuti found

Table 5 Summaries of synthetic procedures, porosity and H_2 uptake capacity for selected ZTCs

Template	Carbonisation[a]		A_{BET}[b]	V[c]	H_2 uptake conditions[d]	H_2 uptake[e] wt%	Ref.
	Step 1	Step 2					
NaY	FA (LI, 700)	PP (CVD, 900)	3590		[f]−196, 24	5.5	245
13X	FA (LI, 700)	ET (CVD, 900)	3330	1.66 (1.18)	−196, 20	7.3	178
Y	ET (CVD, 900)		2000	1.11 (0.83)	−196, 1	1.8	190
Y	ET (CVD, 900)	ET (CVD, 900)	2160	1.26 (0.92)	−196, 1	1.9	190
Y	FA (LI, 900)		860	0.93 (0.24)	−196, 1	0.7	190
Y	FA (LI, 900)	ET (CVD, 900)	1940	1.18 (0.73)	−196, 1	1.6	190
Y	Sucrose (LI, 800)		930	0.97 (0.30)	30, 1	0.5	346
Y	Sucrose (LI, 800)		1250	0.95 (0.09)	30, 1	1.7	352
Y	Sucrose/AN (LI, 800)		1670	2.28 (0.55)	31, 1	3.9	352
13X	FA (LI, 700)	Tyre pyrolysis vapour (CVD, 900)	3250	1.72 (1.61)	−196, 1	2.5	348
13X	FA (LI, 700)	ET (CVD, 900)	3340	1.88 (1.72)	−196, 1	1.9	348
Clinoptilolite	1 : 5 glucose/urea (LI, 900)		66	0.32 (0.00)			350
Clinoptilolite	2 : 5 glucose/urea (LI, 900)		151	0.36 (0.03)			350
Y	ET (CVD, 790)		1930	0.97[f] (0.73)			193
Y, surfactant templated	ET (CVD, 790)		2140	1.59[f] (0.74)			193

[a] Carbon source, followed by carbonisation method and, in parenthesis the carbonisation technique (LI or CVD) and temperature (°C); FA = furfuryl alcohol, ET = ethylene, PP = polypropylene, AN = acetonitrile. [b] BET surface area ($m^2\ g^{-1}$). [c] Pore volume ($cm^3\ g^{-1}$); values in parenthesis are micropore volume. [d] Temperature (°C) and pressure (bar) at which H_2 uptake was measured. [e] H_2 uptake capacity (wt%). [f] No total pore volume reported, thus sum of V_{micro} and V_{meso} is used.

© 2022 The Author(s). Published by the Royal Society of Chemistry

Open Access Article. Published on 12 January 2022. Downloaded on 3/24/2022 12:40:42 PM.
This article is licensed under a Creative Commons Attribution 3.0 Unported Licence.

that mixing small amounts of acetonitrile into a sucrose solution prior to its use as an LI carbon source on zeolite-Y resulted in a ZTC with increased surface area (1250 to 1670 $m^2\ g^{-1}$) and increased microporosity from 5 to 24%. However, with increasing concentrations of the nitrogen dopant, overall surface area falls to 867 $m^2\ g^{-1}$ along with absolute microporosity.[352] Similarly, Rangel-Sequeda *et al.* have recently shown that increasing the amount of urea in a urea-glucose mixture resulted in higher surface area carbons when the mixture was used as an LI agent on the natural zeolite (clinoptilolite) template.[350] While the former did measure H_2 storage capacity and the latter CO_2 capture, it is impossible to disentangle the effects of improved porosity and chemical doping on the improved uptakes.

Template modification. A major stumbling block with the use of microporous zeolites as hard templates for carbons is that if the structure is replicated well, the PSD will invariably be unimodal. This lack of pore hierarchy can limit the gas storage/capture capacity of such ZTCs due to slow ingress into pores. Similarly, problems can arise in the synthesis of ZTCs if the carbon source cannot easily enter the narrow channels.[355,356] Mesopores can be created in zeolites (while retaining microporosity) by the use of surfactant-templating wherein the material is steamed in order to partially remove aluminium from the framework[357] thus yielding hierarchical templates. Aumond *et al.* achieved ZTCs with approximately equal micropore and mesopore volume by CVD using ethylene on a surfactant-templated zeolite-Y. The product showed an increase in total pore volume from 0.97 to 1.59 $cm^3\ g^{-1}$ relative to a ZTC derived by templating on non-treated zeolite.[193] Although not measured, such a material is an interesting candidate for CO_2 pressure swing adsorption applications.

4.2.2. Post-synthetic treatment. In some cases, the porosity of ZTCs can be modified after synthesis. This can be achieved by forming composites with some other material, however by definition the composite's porosity is then a result of the structures of both the ZTC and the other material.[358,359] On the other hand, Choi *et al.* found that through thermal treatment of ZTCs, a contraction in the width of micropores is produced, associated with loss of structural hydrogen, improved packing density and decreased gravimetric porosity. Consequently, volumetric methane capacity (65 bar, 25 °C) was improved by 7% from 164 to 176 $cm^3_{STP}\ cm^{-3}$ on a ZTC synthesised using BEA as a template, following heat treatment at 600 °C.[194] Other thermal, chemical and pressure treatments can lead to greater improvements in porosity and therefore improved gas uptakes.

Densification. Densification, also known as compaction or pelletisation is a process used to improve the volumetric storage of small molecules on carbons by compressing the skeletal structure *i.e.* increasing the packing density. As early as 2005, Celzard and Fierro found that increasing the apparent density of AC powders resulted in an approximately proportional improvement in volumetric methane capacity at 35 bar and 20 °C. Increases in apparent density did however lead to reductions in gravimetric uptake, thus densification pressure should be optimised.[360] Early attempts to increase density of ZTCs utilised so-called hot densification wherein pressures up to 147 MPa and temperatures up to 300 °C were used in order to convert the diffuse ZTC powder into a dense, compact pellet.[258,361] While studying the hot densification (300 °C) of a ZTC derived from zeolite-Y (Na-form), Hou *et al.* found that although gravimetric surface area decreased with increasing compaction pressure, the opposite trend was found when surface area is measured volumetrically.[361] Similarly Guan *et al.* found that hot densification of a ZTC halved gravimetric measures of porosity, while doubling their volumetric counterparts. As a result, volumetric CH_4 storage capacity (at 35 bar and 25 °C) was improved from 60 to 127 $cm^3_{STP}\ cm^{-3}$ for the pristine and compacted ZTC, respectively.[258] Gravimetric porosity generally decreases following densification, but to varying degrees depending on the compaction conditions and nature of the ZTC.[178,182,362] However, a report from Almasoudi *et al.* indicates that if compaction pressure is sufficiently low (370 MPa), gravimetric surface area can increase alongside volumetric porosity resulting in improved gravimetric and volumetric H_2 capacity.[363] As for pore size, compaction generally leads to the development of further microporosity and/or shifting of the PSD and average pore size towards the ultramicropores region as pores contract under pressure,[178,361,363] which may result in improved low pressure gas uptake. Fig. 6 illustrates the effect of densification pressure on various measures of porosity.

More recently, work by Balahmar *et al.* compared the result of compacting a ZTC to the compaction of the zeolite scaffold prior to templation (so-called pre-compaction) on the textural characteristics and H_2 and CO_2 storage capacities of the resultant ZTCs. Materials were synthesised on zeolite-13X or -Y templates using CVD of acetonitrile. It was found that pre-compaction actually increased gravimetric porosity in terms of both surface area and pore volume as compared with the conventional ZTC. Furthermore, packing density increased by over 50% from 0.53 to 0.82 g cm^{-3}. This resulted in simultaneous improvement to gravimetric (11.6 to 13.1 mmol g^{-1}) and volumetric (271 to 473 v/v) CO_2 uptake at moderate pressure (20 bar and 25 °C). Conversely, post-compaction had almost no effect on gravimetric storage and showed only mild improvements volumetrically.[182] A recent paper by Gabe *et al.* detailed the optimisation of densification conditions for a ZTC mixed with reduced graphene oxide. The authors found that volumetric H_2 storage was doubled at all pressures from 0 to 100 bar, when the zeolite-Y-derived carbon was subjected to compaction at 150 °C and 145 MPa. The densified composite also has the advantage of being extremely mechanically robust.[364]

Activation. The porosity of templated carbons can be expanded *via* chemical or physical activation; for example the porosity of mesoporous carbons formed when using a silica template can be expanded into the micropore region on activation with KOH or CO_2.[61,365,366] With the advent of microporous templated carbons based on zeolites, researchers have attempted activation to both improve absolute, overall

Open Access Article. Published on 12 January 2022. Downloaded on 3/24/2022 12:40:42 PM.
This article is licensed under a Creative Commons Attribution 3.0 Unported Licence.

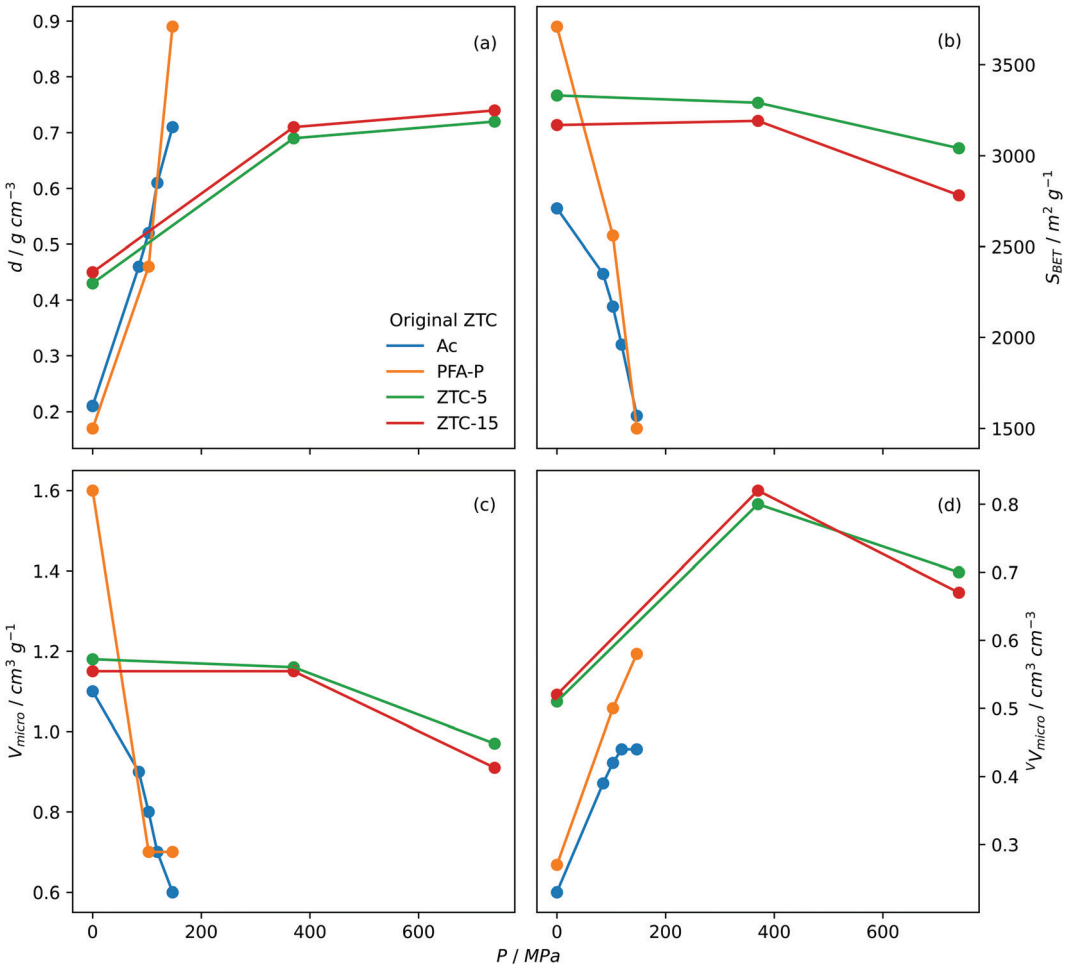

Fig. 6 Trends in (a) packing density, (b) BET surface area, (c) gravimetric micropore volume and (d) volumetric micropore volume of densified ZTCs with densification pressure. Ac and PFA-P both templated on Na-zeolite Y with Ac synthesized *via* acetylene CVD and PFA-P *via* polyfurfuryl alcohol LI followed by propylene CVD. Densification performed at 300 °C.[361] ZTC-5 and ZTC-15 synthesized *via* polyfurfuryl alcohol LI followed by ethylene CVD on zeolite 13X. 5 and 15 refer to the ramp rate used in the first carbonisation step.[178]

microporosity and extend porosity into the mesopore region. The activating agent of choice has become KOH as unlike CO_2 it can improve overall porosity without destroying the intricate network of micropores already present in the ZTC.[83,88,367] Inevitably, activation of ZTCs leads to destruction of much of the crystal structure meaning that the narrow PSDs which ZTCs are prized for are not present in activated-ZTCs,[34] although work by Anggarini *et al.* suggests that *increased* ordering can be achieved *via* activation with $ZnCl_2$.[368] Relatively aggressive KOH-activation (700–800 °C, 4 : 1 w/w) leads to doubling or even tripling of overall surface area according to work done in the Mokaya group. At the same time much, but not all of the original microporosity is retained.[83,88,199] However, it is not yet clear to what extent the initial porosity of the ZTC influences that of the activated ZTC. For example, KOH activated carbons with surface areas around 3000 $m^2\ g^{-1}$ can be produced from ZTCs with initial surface area as low as 367 $m^2\ g^{-1}$ and as high as 1670 $m^2\ g^{-1}$.[83,367] In fact, in one case ZTCs with the highest initial porosity show the smallest improvements following activation.[88] This unclear relationship is probably a result of entangled variables such as ZTC structural type and elemental composition.[34,77,135] The benefit of activation of ZTCs is somewhat questionable as the highest surface area achieved through this technique is only around 3350 $m^2\ g^{-1}$, significantly less than the record for conventionally activated carbons[82] or indeed non-activated ZTCs.[369]

Nevertheless, activation of ZTCs can lead to nearly doubling of cryogenic hydrogen storage capacity at 20 bar.[83,88] On the other hand improvements are not nearly as significant for applications wherein pore size, rather than overall surface area or porosity is the more significant factor in determining gas uptake. For example, Almasoudi *et al.* showed that despite improvements in overall surface area upon KOH-activation of a carbon derived from the templation of furfuryl alcohol on a zeolitic imidazole framework, ambient gravimetric CO_2 capacity could not be improved by more than 23%. Even more striking are accompanying decreases (up to 78%) in CO_2 uptake density. This is attributed to significant destruction of micropores during the activation process.[199] More recently Susanti and Widiastuti reported KOH-activation of a zeolite-Y

© 2022 The Author(s). Published by the Royal Society of Chemistry

templated carbon (ZTC-Y) synthesised *via* LI. They report that improvement in CO_2 (ambient pressure, 30 °C) capture capacity is optimised at a KOH : ZTC-Y ratio of 1.5 from 0.24 mmol g^{-1} to 0.62 mmol g^{-1}. Interestingly, activation of ZTC-Y is accompanied by a reduction in total surface area and simultaneous decrease in average pore width. This lends further credence to the vital role of pore size in such applications.[256]

5. Summary and outlook

Experimental control over the porosity of ZTCs and ACs is now well established, with a variety of routes to high surface area carbons possessing either unimodal or hierarchical porosities. As a result, it is possible to achieve carbons with consistently appropriate porosity for good gravimetric uptake of gases under a variety of conditions. For example, there are multiple routes to the narrow PSDs with high surface area useful in H_2 storage. For cyclic CO_2 capture applications, hierarchical carbons with moderate porosity can be formed both *via* the templation or activation routes. Paradoxically, of the three sorptives examined in this review, CH_4 while the most commercially developed has seen the lowest degree of development in so far as determination of optimal porosity for sorption on carbons. As such, works on porosity modulation for this particular application are limited.

Materials with high volumetric capacity are significantly under-investigated, a metric which is particularly relevant to CH_4 storage. While there have been some significant and interesting methods used to improve packing density and volumetric porosity of carbons *via* post-synthetic methods or by altering experimental conditions, work in this area is fairly limited and seems to be restricted to a handful of research groups. In particular, techniques such as compaction and densification have showed a lot of promise but the full effects of the balance of variables such as compaction time, pressure and temperature are yet to be examined – in stark contrast to well-established techniques like KOH-activation.

ACs show more promise than ZTCs as, despite their amorphous structure, it is at least as facile to control their porosity for any given application. Furthermore, conditions and reagents for AC synthesis typically require less precision than those needed for ZTCs resulting in reduced costs and the ability to use abundant and low value recycled materials. Besides for many applications, the exquisitely uniform porosity found in ZTCs is not necessary, and indeed the dearth of literature surrounding CH_4 adsorption on ZTCs reflects this. Their greatest utility appears to be in hydrogen storage where extremely homogenous pore widths are required. Further work is needed to determine whether good ZTC carbon sources can be generated from waste materials, and to determine the simplest routes to good ZTC porosity.

Author contributions

L. Scott Blankenship: Investigation, Visualisation, Writing – original draft. Robert Mokaya: Conceptualization, Funding acquisition, Supervision, Writing – review & editing.

Conflicts of interest

There are no conflicts to declare.

Acknowledgements

We are thankful to the EPSRC (Low-Dimensional Materials & Interfaces DTP) for a studentship for LSB. RM thanks the Royal Society for a Royal Society Wolfson Research Merit Award.

Notes and references

1 V. Ramanathan and Y. Xu, *Proc. Natl. Acad. Sci. U. S. A.*, 2010, **107**, 8055–8062.
2 V. Masson-Delmotte, P. Zhai, H.-O. Pörtner, D. C. Roberts, J. Skea, P. R. Shukla, A. Pirani, W. Moufouma-Okia, C. Péan and R. Pidcock, *Global warming of 1.5 °C: Summary for policy makers*, 2018.
3 C.-F. Schleussner, J. Rogelj, M. Schaeffer, T. Lissner, R. Licker, E. M. Fischer, R. Knutti, A. Levermann, K. Frieler and W. Hare, *Nat. Clim. Change*, 2016, **6**, 827–835.
4 T. Kuramochi, A. Ramírez, W. Turkenburg and A. Faaij, *Prog. Energy Combust. Sci.*, 2012, **38**, 87–112.
5 C.-C. Lin, R.-X. He and W.-Y. Liu, *Energies*, 2018, **11**, 3432.
6 G. P. Peters, R. M. Andrew, J. G. Canadell, S. Fuss, R. B. Jackson, J. I. Korsbakken, C. Le Quéré and N. Nakicenovic, *Nat. Clim. Change*, 2017, **7**, 118–122.
7 R. Clémençon, *J. Environ. Dev.*, 2016, **25**, 3–24.
8 UK becomes first major economy to pass net zero emissions law, https://www.gov.uk/government/news/uk-becomes-first-major-economy-to-pass-net-zero-emissions-law, accessed 23rd of March, 2021.
9 S. Choi, J. H. Drese and C. W. Jones, *ChemSusChem*, 2009, **2**, 796–854.
10 U. Eberle, B. Müller and R. Von Helmolt, *Energy Environ. Sci.*, 2012, **5**, 8780–8798.
11 M. S. Dresselhaus and I. L. Thomas, *Nature*, 2001, **414**, 332–337.
12 K. V. Kumar, K. Preuss, M.-M. Titirici and F. Rodríguez-Reinoso, *Chem. Rev.*, 2017, **117**, 1796–1825.
13 I. Angelidaki, L. Treu, P. Tsapekos, G. Luo, S. Campanaro, H. Wenzel and P. G. Kougias, *Biotechnol. Adv.*, 2018, **36**, 452–466.
14 T. A. Makal, J.-R. Li, W. Lu and H.-C. Zhou, *Chem. Soc. Rev.*, 2012, **41**, 7761–7779.
15 D. M. D'Alessandro, B. Smit and J. R. Long, *Angew. Chem., Int. Ed.*, 2010, **49**, 6058–6082.
16 Q. Wang, J. Luo, Z. Zhong and A. Borgna, *Energy Environ. Sci.*, 2011, **4**, 42–55.
17 M. Cozier, *Greenhouse Gases: Sci. Technol.*, 2019, **9**, 1084–1086.
18 D. Lozano-Castello, J. Alcaniz-Monge, M. De la Casa-Lillo, D. Cazorla-Amoros and A. Linares-Solano, *Fuel*, 2002, **81**, 1777–1803.

Open Access Article. Published on 12 January 2022. Downloaded on 3/24/2022 12:40:42 PM. This article is licensed under a Creative Commons Attribution 3.0 Unported Licence.

Open Access Article. Published on 12 January 2022. Downloaded on 3/24/2022 12:40:42 PM.
This article is licensed under a Creative Commons Attribution 3.0 Unported Licence.

19 J. Romanos, S. Sweany, T. Rash, L. Firlej, B. Kuchta, J. Idrobo and P. Pfeifer, *Adsorpt. Sci. Technol.*, 2014, **32**, 681–691.
20 M. Sevilla and R. Mokaya, *Energy Environ. Sci.*, 2014, **7**, 1250–1280.
21 L. Schlapbach and A. Züttel, *Mater. Sustainable Energy*, 2011, 265–270.
22 R. E. Morris and P. S. Wheatley, *Angew. Chem., Int. Ed.*, 2008, **47**, 4966–4981.
23 Z. Liang, K. Fu, R. Idem and P. Tontiwachwuthikul, *Chin. J. Chem. Eng.*, 2016, **24**, 278–288.
24 K. S. Fisher, K. Searcy, G. T. Rochelle, S. Ziaii and C. Schubert, *Advanced Amine Solvent Formulations and Process Integration for Near-term CO2 Capture Success*, Trimeric Corporation, 2007.
25 P. Pfeifer, L. Aston, M. Banks, S. Barker, J. Burress, S. Carter, J. Coleman, S. Crockett, C. Faulhaber and J. Flavin, *Chaos*, 2007, **17**, 41108.
26 Y. He, W. Zhou, G. Qian and B. Chen, *Chem. Soc. Rev.*, 2014, **43**, 5657–5678.
27 D. Farrusseng, *Metal-organic Frameworks: Applications from Catalysis to Gas Storage*, John Wiley & Sons, 2011.
28 M. Ding, R. W. Flaig, H.-L. Jiang and O. M. Yaghi, *Chem. Soc. Rev.*, 2019, **48**, 2783–2828.
29 J.-Y. Lee, C. D. Wood, D. Bradshaw, M. J. Rosseinsky and A. I. Cooper, *Chem. Commun.*, 2006, 2670–2672.
30 M. Pera-Titus, *Chem. Rev.*, 2014, **114**, 1413–1492.
31 R. V. Siriwardane, M.-S. Shen, E. P. Fisher and J. Losch, *Energy Fuels*, 2005, **19**, 1153–1159.
32 J. Weitkamp, M. Fritz and S. Ernst, *Zeolites as media for hydrogen storage*, Elsevier, Montreal, 1992.
33 R. Krishna and J. M. van Baten, *J. Membr. Sci.*, 2010, **360**, 323–333.
34 H. Nishihara and T. Kyotani, *Chem. Commun.*, 2018, **54**, 5648–5673.
35 A. Altwala and R. Mokaya, *Energy Environ. Sci.*, 2020, **13**, 2967–2978.
36 C. Xu and M. Stromme, *Nanomaterials*, 2019, **9**, 103.
37 I. Toda, H. Toda, H. Akasaka, S. Ohshio, S. Himeno and H. Saitoh, *J. Ceram. Soc. Jpn.*, 2013, **121**, 464–466.
38 S. Alhasan, R. Carriveau and D.-K. Ting, *Int. J. Environ. Studies*, 2016, **73**, 343–356.
39 iNatGas, The Natural Gas Industry Solutions, https://inatgas.com/, accessed 12th December, 2021.
40 Natural Gas Fueling Infrastructure Development, https://afdc.energy.gov/fuels/natural_gas_infrastructure.html, accessed 21st December, 2021.
41 G. Basich and T. Dao, CNG Use Expands Among Government Agencies, https://www.government-fleet.com/152834/cng-use-expands-among-government-agencies, accessed 21st December, 2021.
42 Shell, Liquefied Natural Gas (LNG), https://www.shell.com/energy-and-innovation/natural-gas/liquefied-natural-gas-lng.html, accessed 21st December, 2021.
43 Ingevity, Adsorbed Natural Gas, https://www.ingevity.com/markets/adsorbed-natural-gas/, accessed 21st December, 2021.
44 Daigas, Biogas purification and adsorption storage system, https://www.daigasgps.co.jp/en/service/engineering/energy/biogas_stocksystem/, accessed 21st December, 2021.
45 M. Smith and J. Gonzales, *Costs associated with compressed natural gas vehicle fueling infrastructure*, National Renewable Energy Lab. (NREL), Golden, CO (United States), 2014.
46 A. Y. Tsivadze, O. E. Aksyutin, A. G. Ishkov, I. E. Men'shchikov, A. A. Fomkin, A. V. Shkolin, E. V. Khozina and V. A. Grachev, *Russ. Chem. Rev.*, 2018, **87**, 950–983.
47 P. Greene, Basics of Biogas Upgrading, https://www.biocycle.net/basics-biogas-upgrading/, accessed 21st December, 2021.
48 F. Bauer, T. Persson, C. Hulteberg and D. Tamm, *Biofuels, Bioprod. Biorefin.*, 2013, **7**, 499–511.
49 T. Kvist and N. Aryal, *Waste Manage.*, 2019, **87**, 295–300.
50 A. McLeod, B. Jefferson and E. J. McAdam, *Water Res.*, 2013, **47**, 3688–3695.
51 J. Lee, J. Kim and T. Hyeon, *Adv. Mater.*, 2006, **18**, 2073–2094.
52 F. Rodriguez-Reinoso and M. Molina-Sabio, *Carbon*, 1992, **30**, 1111–1118.
53 J. Ozaki, N. Endo, W. Ohizumi, K. Igarashi and M. Nakahara, *Carbon*, 1997, **35**, 1031–1033.
54 N. Patel, K. Okabe and A. Oya, *Carbon*, 2002, **40**, 315–320.
55 R. Pekala and D. Schaefer, *Macromolecules*, 1993, **26**, 5487–5493.
56 H. Nishihara, K. Imai, H. Itoi, K. Nomura, K. Takai and T. Kyotani, *Tanso*, 2017, **2017**, 169–174.
57 V. Presser, M. Heon and Y. Gogotsi, *Adv. Funct. Mater.*, 2011, **21**, 810–833.
58 Y. Korenblit and G. Yushin, in *Carbon Nanomaterials*, ed. Y. Gogotsi and V. Presser, 2nd edn, 2014, ch. 11, pp. 303–330.
59 W. Gu and G. Yushin, *Wiley Interdiscip. Rev.: Energy Environ.*, 2014, **3**, 424–473.
60 N. Texier-Mandoki, J. Dentzer, T. Piquero, S. Saadallah, P. David and C. Vix-Guterl, *Carbon*, 2004, **42**, 2744–2747.
61 E. Masika and R. Mokaya, *J. Phys. Chem. C*, 2012, **116**, 25734–25740.
62 C. F. Martín, M. G. Plaza, J. Pis, F. Rubiera, C. Pevida and T. Centeno, *Sep. Purif. Technol.*, 2010, **74**, 225–229.
63 M. Sevilla, J. B. Parra and A. B. Fuertes, *ACS Appl. Mater. Interfaces*, 2013, **5**, 6360–6368.
64 Z. Yang, Y. Xia, X. Sun and R. Mokaya, *J. Phys. Chem. B*, 2006, **110**, 18424–18431.
65 Y. Li, S. Wang, B. Wang, Y. Wang and J. Wei, *Nanomaterials*, 2020, **10**, 174.
66 B. Adeniran and R. Mokaya, *Chem. Mater.*, 2016, **28**, 994–1001.
67 S. E. Moradi, *Korean J. Chem. Eng.*, 2014, **31**, 1651–1655.
68 A. I. Sultana, N. Saha and M. T. Reza, *Sustainability*, 2021, **13**, 1947.
69 R. Ryoo, S. H. Joo and S. Jun, *J. Phys. Chem. B*, 1999, **103**, 7743–7746.
70 S. Oh and K. Kim, *Chem. Commun.*, 1999, 2177–2178.
71 C. Liang, K. Hong, G. A. Guiochon, J. W. Mays and S. Dai, *Angew. Chem., Int. Ed.*, 2004, **43**, 5785–5789.

© 2022 The Author(s). Published by the Royal Society of Chemistry

Open Access Article. Published on 12 January 2022. Downloaded on 3/24/2022 12:40:42 PM.
This article is licensed under a Creative Commons Attribution 3.0 Unported Licence.

72 B. Liu, H. Shioyama, T. Akita and Q. Xu, *J. Am. Chem. Soc.*, 2008, **130**, 5390–5391.
73 L. Radhakrishnan, J. Reboul, S. Furukawa, P. Srinivasu, S. Kitagawa and Y. Yamauchi, *Chem. Mater.*, 2011, **23**, 1225–1231.
74 H. Nishihara, T. Hirota, K. Matsuura, M. Ohwada, N. Hoshino, T. Akutagawa, T. Higuchi, H. Jinnai, Y. Koseki and H. Kasai, *Nat. Commun.*, 2017, **8**, 1–9.
75 M. L. Botome, P. Poletto, J. Junges, D. Perondi, A. Dettmer and M. Godinho, *Chem. Eng. J.*, 2017, **321**, 614–621.
76 R. Pedicini, S. Maisano, V. Chiodo, G. Conte, A. Policicchio and R. G. Agostino, *Int. J. Hydrogen Energy*, 2020, **45**, 14038–14047.
77 A. E. Ogungbenro, D. V. Quang, K. A. Al-Ali, L. F. Vega and M. R. M. Abu-Zahra, *J. Environ. Chem. Eng.*, 2018, **6**, 4245–4252.
78 H. M. Coromina, D. A. Walsh and R. Mokaya, *J. Mater. Chem. A*, 2016, **4**, 280–289.
79 M. Sevilla, A. B. Fuertes and R. Mokaya, *Energy Environ. Sci.*, 2011, **4**, 1400–1410.
80 E. A. Hirst, A. Taylor and R. Mokaya, *J. Mater. Chem. A*, 2018, **6**, 12393–12403.
81 E. Haffner-Staton, N. Balahmar and R. Mokaya, *J. Mater. Chem. A*, 2016, **4**, 13324–13335.
82 L. S. Blankenship and R. Mokaya, *Energy Environ. Sci.*, 2017, **10**, 2552–2562.
83 M. Sevilla, N. Alam and R. Mokaya, *J. Phys. Chem. C*, 2010, **114**, 11314–11319.
84 M. Sevilla, R. Foulston and R. Mokaya, *Energy Environ. Sci.*, 2010, **3**, 223–227.
85 M. Sevilla and R. Mokaya, *J. Mater. Chem.*, 2011, **21**, 4727–4732.
86 S.-Y. Lee and S.-J. Park, *J. Solid State Chem.*, 2010, **183**, 2951–2956.
87 S.-Y. Lee and S.-J. Park, *Adv. Mater. Res.*, 2010, **123**, 695–698.
88 A. Almasoudi and R. Mokaya, *J. Mater. Chem.*, 2012, **22**, 146–152.
89 A. Downie, A. Crosky and P. Munroe, in *Biochar for Environmental Management: Science and Technology*, ed. J. Lehman and S. Joseph, 2009, ch. 2, p. 14.
90 K. Weber and P. Quicker, *Fuel*, 2018, **217**, 240–261.
91 J. Jagiello, J. Kenvin, A. Celzard and V. Fierro, *Carbon*, 2019, **144**, 206–215.
92 J. F. González, J. M. Encinar, C. M. González-García, E. Sabio, A. Ramiro, J. L. Canito and J. Gañán, *Appl. Surf. Sci.*, 2006, **252**, 5999–6004.
93 J. Ganan, J. Gonzalez, C. Gonzalez-Garcia, A. Ramiro, E. Sabio and S. Roman, *Appl. Surf. Sci.*, 2006, **252**, 5988–5992.
94 S. Osswald, C. Portet, Y. Gogotsi, G. Laudisio, J. Singer, J. Fischer, V. Sokolov, J. Kukushkina and A. Kravchik, *J. Solid State Chem.*, 2009, **182**, 1733–1741.
95 R. Ströbel, L. Jörissen, T. Schliermann, V. Trapp, W. Schütz, K. Bohmhammel, G. Wolf and J. Garche, *J. Power Sources*, 1999, **84**, 221–224.
96 N. P. Wickramaratne and M. Jaroniec, *J. Mater. Chem. A*, 2013, **1**, 112–116.
97 V. Presser, J. McDonough, S.-H. Yeon and Y. Gogotsi, *Energy Environ. Sci.*, 2011, **4**, 3059–3066.
98 N. Balahmar and R. Mokaya, *J. Mater. Chem. A*, 2019, **7**, 17466–17479.
99 M. G. Plaza, S. Garcia, F. Rubiera, J. J. Pis and C. Pevida, *Chem. Eng. J.*, 2010, **163**, 41–47.
100 H. An, B. Feng and S. Su, *Int. J. Greenhouse Gas Control*, 2011, **5**, 16–25.
101 G. Sdanghi, R. L. Canevesi, A. Celzard, M. Thommes and V. Fierro, *Carbon*, 2020, **6**, 46.
102 B. Feng and S. K. Bhatia, *Carbon*, 2003, **41**, 507–523.
103 E. A. Dawson, G. Parkes, P. A. Barnes and M. J. Chinn, *Carbon*, 2003, **41**, 571–578.
104 S. K. Ryu, H. Jin, D. Gondy, N. Pusset and P. Ehrburger, *Carbon*, 1993, **31**, 841–842.
105 F. Rodriguez-Reinoso, M. Molina-Sabio and M. González, *Carbon*, 1995, **33**, 15–23.
106 C.-F. Chang, C.-Y. Chang and W.-T. Tsai, *J. Colloid Interface Sci.*, 2000, **232**, 45–49.
107 M. M. Johns, W. E. Marshall and C. A. Toles, *J. Chem. Technol. Biotechnol.*, 1999, **74**, 1037–1044.
108 S. Román, J. F. González, C. M. González-García and F. Zamora, *Fuel Process. Technol.*, 2008, **89**, 715–720.
109 H. Wang, Q. Gao and J. Hu, *J. Am. Chem. Soc.*, 2009, **131**, 7016–7022.
110 M. Jagtoyen and F. Derbyshire, *Carbon*, 1998, **36**, 1085–1097.
111 T. K. Das, S. Banerjee, P. Sharma, V. Sudarsan and P. U. Sastry, *Int. J. Hydrogen Energy*, 2018, **43**, 8385–8394.
112 F. Caturla, M. Molina-Sabio and F. Rodriguez-Reinoso, *Carbon*, 1991, **29**, 999–1007.
113 M. Molina-Sabio and F. Rodrıguez-Reinoso, *Colloids Surf., A*, 2004, **241**, 15–25.
114 J. Wang and S. Kaskel, *J. Mater. Chem.*, 2012, **22**, 23710–23725.
115 T. Otowa, R. Tanibata and M. Itoh, *Gas Sep. Purif.*, 1993, **7**, 241–245.
116 D. Lozano-Castello, J. Calo, D. Cazorla-Amoros and A. Linares-Solano, *Carbon*, 2007, **45**, 2529–2536.
117 E. Raymundo-Pinero, P. Azaïs, T. Cacciaguerra, D. Cazorla-Amorós, A. Linares-Solano and F. Béguin, *Carbon*, 2005, **43**, 786–795.
118 W. Qiao, S.-H. Yoon and I. Mochida, *Energy Fuels*, 2006, **20**, 1680–1684.
119 M. Lillo-Ródenas, D. Cazorla-Amorós and A. Linares-Solano, *Carbon*, 2003, **41**, 267–275.
120 M. Lillo-Ródenas, J. Juan-Juan, D. Cazorla-Amorós and A. Linares-Solano, *Carbon*, 2004, **42**, 1371–1375.
121 Y. Yamashita and K. Ouchi, *Carbon*, 1982, **20**, 41–45.
122 S. Kelemen and C. Mims, *Surf. Sci.*, 1983, **133**, 71–88.
123 R. Xue and Z. Shen, *Carbon*, 2003, **41**, 1862–1864.
124 E. Fuente, R. R. Gil, R. P. Giron, M. A. Lillo-Ródenas, M. A. Montes-Moran, M. J. Martin and A. Linares-Solano, *Carbon*, 2010, **48**, 1032–1037.

© 2022 The Author(s). Published by the Royal Society of Chemistry

Open Access Article. Published on 12 January 2022. Downloaded on 3/24/2022 12:40:42 PM.
This article is licensed under a Creative Commons Attribution 3.0 Unported Licence.

125 N. Tsubouchi, M. Nishio and Y. Mochizuki, *Appl. Surf. Sci.*, 2016, **371**, 301–306.
126 M. Sevilla, P. Valle-Vigón and A. B. Fuertes, *Adv. Funct. Mater.*, 2011, **21**, 2781–2787.
127 D. Lozano-Castello, D. Cazorla-Amoros, A. Linares-Solano and D. F. Quinn, *Carbon*, 2002, **40**, 989–1002.
128 W. Zhao, V. Fierro, C. Zlotea, E. Aylon, M. Izquierdo, M. Latroche and A. Celzard, *Int. J. Hydrogen Energy*, 2011, **36**, 11746–11751.
129 W. Zhao, V. Fierro, C. Zlotea, E. Aylon, M. Izquierdo, M. Latroche and A. Celzard, *Int. J. Hydrogen Energy*, 2011, **36**, 5431–5434.
130 W. Zhao, V. Fierro, N. Fernández-Huerta, M. Izquierdo and A. Celzard, *Int. J. Hydrogen Energy*, 2012, **37**, 14278–14284.
131 J.-H. Lee and S.-J. Park, *J. Nanosci. Nanotechnol.*, 2020, **20**, 7124–7129.
132 J. Ludwinowicz and M. Jaroniec, *Carbon*, 2015, **82**, 297–303.
133 M. Sevilla, N. Díez and A. B. Fuertes, *ChemSusChem*, 2021, **14**, 94–117.
134 J. V. Guerrera, J. N. Burrow, J. E. Eichler, M. Z. Rahman, M. V. Namireddy, K. A. Friedman, S. S. Coffman, D. C. Calabro and C. B. Mullins, *Energy Fuels*, 2020, **34**, 6101–6112.
135 A. M. Aljumialy and R. Mokaya, *Mater. Adv.*, 2020, **1**, 3267–3280.
136 M. Sevilla, A. S. M. Al-Jumialy, A. B. Fuertes and R. Mokaya, *ACS Appl. Mater. Interfaces*, 2018, **10**, 1623–1633.
137 M. Sevilla, G. A. Ferrero and A. B. Fuertes, *Carbon*, 2017, **114**, 50–58.
138 M. Sevilla and A. B. Fuertes, *ChemSusChem*, 2016, **9**, 1880–1888.
139 V. Fierro, V. Torné-Fernández and A. Celzard, *Microporous Mesoporous Mater.*, 2006, **92**, 243–250.
140 V. Fierro, V. Torné-Fernández, A. Celzard and D. Montané, *J. Hazard. Mater.*, 2007, **149**, 126–133.
141 A. S. Oberoi, J. Andrews, A. L. Chaffee and L. Ciddor, *Int. J. Hydrogen Energy*, 2016, **41**, 23099–23108.
142 N. M. Musyoka, M. Wdowin, K. M. Rambau, W. Franus, R. Panek, J. Madej and D. Czarna-Juszkiewicz, *Renewable Energy*, 2020, **155**, 1264–1271.
143 J. Liu, X. Liu, Y. Sun, C. Sun, H. Liu, L. A. Stevens, K. Li and C. E. Snape, *Adv. Sustainable Syst.*, 2018, **2**, 1700115.
144 L.-P. Xiao, Z.-J. Shi, F. Xu and R.-C. Sun, *Bioresour. Technol.*, 2012, **118**, 619–623.
145 M. Sevilla and A. B. Fuertes, *Chem. – Eur. J.*, 2009, **15**, 4195–4203.
146 M. Sevilla, J. A. Maciá-Agulló and A. B. Fuertes, *Biomass Bioenergy*, 2011, **35**, 3152–3159.
147 M.-M. Titirici and M. Antonietti, *Chem. Soc. Rev.*, 2010, **39**, 103–116.
148 W. Ao, J. Fu, X. Mao, Q. Kang, C. Ran, Y. Liu, H. Zhang, Z. Gao, J. Li and G. Liu, *Renewable Sustainable Energy Rev.*, 2018, **92**, 958–979.
149 M. Fernanda Gonzalez-Navarro, L. Giraldo and J. Carlos Moreno-Pirajan, *J. Anal. Appl. Pyrolysis*, 2014, **107**, 82–86.
150 X. Fang, G. Li, J. Li, H. Jin, J. Li, V. Jegatheesan, S. Li, H. Wang and M. Yang, *Desalin. Water Treat.*, 2017, **96**, 120–127.
151 P. Veerakumar, T. Maiyalagan, B. G. S. Raj, K. Guruprasad, Z. Jiang and K.-C. Lin, *Arabian J. Chem.*, 2020, **13**, 2995–3007.
152 L. Li, F. Sun, J. Gao, L. Wang, X. Pi and G. Zhao, *RSC Adv.*, 2018, **8**, 14488–14499.
153 J. Y. Lin, *Science*, 2016, **353**, 121–122.
154 D. W. Breck, *Zeolite molecular sieves*, Wiley, New York, 1974.
155 D. Bastani, N. Esmaeili and M. Asadollahi, *J. Ind. Eng. Chem.*, 2013, **19**, 375–393.
156 H. C. Foley, in *Perspectives in Molecular Sieve Science*, ed. W. H. Flank and T. E. Whyte, American Chemical Society, 1988, ch. 21, pp. 335–360.
157 P. Serp, in *Comprehensive Inorganic Chemistry II*, ed. J. Reedijk and K. Poeppelmeier, Elsevier, 2nd edn, 2013, vol. 7, ch. 13, pp. 323–369.
158 J. S. Beck and J. C. Vartuli, *Curr. Opin. Solid State Mater. Sci.*, 1996, **1**, 76–87.
159 A. Dyer, *An introduction to zeolite molecular sieves*, Wiley, United States, 1988.
160 H. Marsh and F. Rodriguez-Reinoso, *Activated Carbon*, Elsevier Science Ltd., Oxford, UK, 2006, pp. 243–321.
161 A. R. Mohamed, M. Mohammadi and G. N. Darzi, *Renewable Sustainable Energy Rev.*, 2010, **14**, 1591–1599.
162 T. Horikawa, J. i. Hayashi and K. Muroyama, *Carbon*, 2002, **40**, 709–714.
163 C. Gomez-de-Salazar, A. Sepúlveda-Escribano and F. Rodrıguez-Reinoso, *Carbon*, 2000, **38**, 1889–1892.
164 G. Bello, R. García, R. Arriagada, A. Sepulveda-Escribano and F. Rodrıguez-Reinoso, *Microporous Mesoporous Mater.*, 2002, **56**, 139–145.
165 T. Maesen, in *Introduction to Zeolite Science and Practice*, ed. J. Čejka, H. van Bekkum, A. Corma and F. Schüth, Elsevier, Amsterdam, 3rd edn, 2007, ch. 1, pp. 1–12.
166 J. Liu and J. Yu, in *Zeolites and Zeolite-Like Materials*, ed. B. F. Sels and L. M. Kustov, Elsevier, 2016, ch. 1, pp. 1–25.
167 D. Barthelmy, Minerals Arranged by the New Dana Classification, http://webmineral.com/danaclass.shtml, accessed 16th March, 2021.
168 D. J. Earl and M. W. Deem, *Ind. Eng. Chem. Res.*, 2006, **45**, 5449–5454.
169 C. Baerlocher, L. B. McCusker, W. M. Meier and D. Olson, Database of Zeolite Structures, http://www.iza-structure.org/databases/, accessed March 16th, 2021.
170 N. Kosinov, J. Gascon, F. Kapteijn and E. J. Hensen, *J. Membr. Sci.*, 2016, **499**, 65–79.
171 B. Sakintuna and Y. Yürüm, *Ind. Eng. Chem. Res.*, 2005, **44**, 2893–2902.
172 J. Miao, Z. L. Lang, T. Y. Xue, Y. Li, Y. W. Li, J. J. Cheng, H. Zhang and Z. K. Tang, *Adv. Sci.*, 2020, **7**, 32.
173 J. Rodriguez-Mirasol, T. Cordero, A. L. Radovic and J. Rodriguez, *Chem. Mater.*, 1998, **10**, 550–558.

© 2022 The Author(s). Published by the Royal Society of Chemistry

Open Access Article. Published on 12 January 2022. Downloaded on 3/24/2022 12:40:42 PM.
This article is licensed under a Creative Commons Attribution 3.0 Unported Licence.

174 T. Kyotani, T. Nagai, S. Inoue and A. Tomita, *Chem. Mater.*, 1997, **9**, 609–615.
175 S. A. Johnson, E. S. Brigham, P. J. Ollivier and T. E. Mallouk, *Chem. Mater.*, 1997, **9**, 2448–2458.
176 K. Kim, M. Choi and R. Ryoo, *Carbon*, 2013, **60**, 175–185.
177 H. Nishihara and T. Kyotani, in *Novel Carbon Adsorbents*, ed. J. Tascón, Elsevier, London, 2012.
178 E. Masika and R. Mokaya, *Energy Environ. Sci.*, 2014, **7**, 427–434.
179 Y. Xia, G. S. Walker, D. M. Grant and R. Mokaya, *J. Am. Chem. Soc.*, 2009, **131**, 16493–16499.
180 N. Alam and R. Mokaya, *Energy Environ. Sci.*, 2010, **3**, 1773–1781.
181 N. Alam and R. Mokaya, *Microporous Mesoporous Mater.*, 2011, **142**, 716–724.
182 N. Balahmar, A. M. Lowbridge and R. Mokaya, *J. Mater. Chem. A*, 2016, **4**, 14254–14266.
183 C. Guan, F. Su, X. Zhao and K. Wang, *Sep. Purif. Technol.*, 2008, **64**, 124–126.
184 J. Shi, W. Li and D. Li, *Colloids Surf., A*, 2015, **485**, 11–17.
185 R. M. Freire, A. H. de Morais Batista, A. G. de Souza Filho, J. M. Filho, G. D. Saraiva and A. C. Oliveira, *Catal. Lett.*, 2009, **131**, 135–145.
186 R. Ruiz-Rosas, M. J. Valero-Romero, D. Salinas-Torres, J. Rodríguez-Mirasol, T. Cordero, E. Morallon and D. Cazorla-Amorós, *ChemSusChem*, 2014, **7**, 1458–1467.
187 M. Valero-Romero, E. Márquez-Franco, J. Bedia, J. Rodríguez-Mirasol and T. Cordero, *Microporous Mesoporous Mater.*, 2014, **196**, 68–78.
188 M. Seredych and T. J. Bandosz, *Langmuir*, 2007, **23**, 6033–6041.
189 Y. Lv, Z. Wu, Y. Fang, X. Qian, A. M. Asiri, B. Tu and D. Zhao, *Appl. Mater.*, 2014, **2**, 113302.
190 Y. Xia, Z. Yang and R. Mokaya, *Chem. Vap. Deposition*, 2010, **16**, 322–328.
191 T. Kyotani, Z. Ma and A. Tomita, *Carbon*, 2003, **41**, 1451–1459.
192 L. Chen, R. K. Singh and P. Webley, *Microporous Mesoporous Mater.*, 2007, **102**, 159–170.
193 T. Aumond, J. Rousseau, Y. Pouilloux, L. Pinard and A. Sachse, *Carbon Trends*, 2021, **2**, 100014.
194 S. Choi, M. A. Alkhabbaz, Y. G. Wang, R. M. Othman and M. Choi, *Carbon*, 2019, **141**, 143–153.
195 P. X. Hou, T. Yamazaki, H. Orikasa and T. Kyotani, *Carbon*, 2005, **43**, 2624–2627.
196 N. Alam and R. Mokaya, *Microporous Mesoporous Mater.*, 2011, **144**, 140–147.
197 Z. Yang, Y. Xia and R. Mokaya, *J. Am. Chem. Soc.*, 2007, **129**, 1673–1679.
198 A. Pacuła and R. Mokaya, *J. Phys. Chem. C*, 2008, **112**, 2764–2769.
199 A. Almasoudi and R. Mokaya, *Microporous Mesoporous Mater.*, 2014, **195**, 258–265.
200 C. Ducrot-Boisgontier, J. Parmentier, A. Faour, J. L. Patarin and G. D. Pirngruber, *Energy Fuels*, 2010, **24**, 3595–3602.
201 Z. Ma, T. Kyotani and A. Tomita, *Chem. Commun.*, 2000, 2365–2366.
202 H.-K. Youn, J. Kim, G. Chandrasekar, H. Jin and W.-S. Ahn, *Mater. Lett.*, 2011, **65**, 1772–1774.
203 P.-X. Hou, H. Orikasa, T. Yamazaki, K. Matsuoka, A. Tomita, N. Setoyama, Y. Fukushima and T. Kyotani, *Chem. Mater.*, 2005, **17**, 5187–5193.
204 F. Su, J. Zeng, Y. Yu, L. Lv, J. Y. Lee and X. Zhao, *Carbon*, 2005, **43**, 2366–2373.
205 J. Wang, Z. Liu, X. Dong, C.-E. Hsiung, Y. Zhu, L. Liu and Y. Han, *J. Mater. Chem. A*, 2017, **5**, 6860–6865.
206 R. J. Konwar and M. De, *Microporous Mesoporous Mater.*, 2013, **175**, 16–24.
207 Y. Li, X. Wang, T. Thersleff, G. Svensson and N. Hedin, *ACS Omega*, 2019, **4**, 9889–9895.
208 M.-C. Silaghi, C. Chizallet and P. Raybaud, *Microporous Mesoporous Mater.*, 2014, **191**, 82–96.
209 K. Kim, T. Lee, Y. Kwon, Y. Seo, J. Song, J. K. Park, H. Lee, J. Y. Park, H. Ihee and S. J. Cho, *Nature*, 2016, **535**, 131–135.
210 G.-H. Moon, A. Bähr and H. Tüysüz, *Chem. Mater.*, 2018, **30**, 3779–3788.
211 H. Park, S. K. Terhorst, R. K. Bera and R. Ryoo, *Carbon*, 2019, **155**, 570–579.
212 M. De la Casa-Lillo, F. Lamari-Darkrim, D. Cazorla-Amoros and A. Linares-Solano, *J. Phys. Chem. B*, 2002, **106**, 10930–10934.
213 S. S. Samantaray, S. R. Mangisetti and S. Ramaprabhu, *J. Alloys Compd.*, 2019, **789**, 800–804.
214 J. B. Condon, *Surface Area and Porosity Determination by Phisisorption Measurements and Theory*, 2006, ch. 2, pp. 29–53.
215 J. Jagiello and M. Thommes, *Carbon*, 2004, **42**, 1227–1232.
216 I. Cabria, M. J. López and J. A. Alonso, *Carbon*, 2007, **45**, 2649–2658.
217 K. R. Matranga, A. Stella, A. L. Myers and E. D. Glandt, *Sep. Sci. Technol.*, 1992, **27**, 1825–1836.
218 M. Thommes, K. Kaneko, A. V. Neimark, J. P. Olivier, F. Rodriguez-Reinoso, J. Rouquerol and K. S. Sing, *Pure Appl. Chem.*, 2015, **87**, 1051–1069.
219 J. Li, B. Michalkiewicz, J. Min, C. Ma, X. Chen, J. Gong, E. Mijowska and T. Tang, *Chem. Eng. J.*, 2019, **360**, 250–259.
220 L. S. Blankenship, N. Balahmar and R. Mokaya, *Nat. Commun.*, 2017, **8**, 1–12.
221 M. Sevilla, R. Mokaya and A. B. Fuertes, *Energy Environ. Sci.*, 2011, **4**, 2930–2936.
222 D. R. Lide, *Handbook of Chemistry and Physics*, CRC Press, United States, 88th edn, 2007.
223 B. E. Poling, J. M. Prausnitz and J. P. O'connell, *Properties of gases and liquids*, McGraw-Hill Education, 2001.
224 C. Graham, D. A. Imrie and R. E. Raab, *Mol. Phys.*, 1998, **93**, 49–56.
225 J. Jagiello, J. Kenvin, C. O. Ania, J. B. Parra, A. Celzard and V. Fierro, *Carbon*, 2020, **160**, 164–175.
226 J. Jagiello, C. Ania, J. B. Parra and C. Cook, *Carbon*, 2015, **91**, 330–337.
227 S. Reljic, E. Jardim, C. Cuadrado-Collados, M. Bayona, M. Martinez-Escandell, J. Silvestre-Albero and F. Rodríguez-

Open Access Article. Published on 12 January 2022. Downloaded on 3/24/2022 12:40:42 PM.
This article is licensed under a Creative Commons Attribution 3.0 Unported Licence.

Reinoso, *Porous Materials: Theory and Its Application for Environmental Remediation*, 2021, pp. 139–152.
228 M. Jordá-Beneyto, F. Suárez-García, D. Lozano-Castello, D. Cazorla-Amorós and A. Linares-Solano, *Carbon*, 2007, **45**, 293–303.
229 M. Rzepka, P. Lamp and M. De la Casa-Lillo, *J. Phys. Chem. B*, 1998, **102**, 10894–10898.
230 L. Zhou, Y. Zhou and Y. Sun, *Int. J. Hydrogen Energy*, 2004, **29**, 475–479.
231 S. Hlushak, *Phys. Chem. Chem. Phys.*, 2018, **20**, 872–888.
232 J. Srenscek-Nazzal and K. Kielbasa, *Appl. Surf. Sci.*, 2019, **494**, 137–151.
233 J. Ludwinowicz and M. Jaroniec, *Carbon*, 2015, **94**, 673–679.
234 M. E. Casco, M. Martínez-Escandell, J. Silvestre-Albero and F. Rodríguez-Reinoso, *Carbon*, 2014, **67**, 230–235.
235 K. Sumida, D. L. Rogow, J. A. Mason, T. M. McDonald, E. D. Bloch, Z. R. Herm, T.-H. Bae and J. R. Long, *Chem. Rev.*, 2012, **112**, 724–781.
236 J.-R. Li, R. J. Kuppler and H.-C. Zhou, *Chem. Soc. Rev.*, 2009, **38**, 1477–1504.
237 M. Cox and R. Mokaya, *Sustainable Energy Fuels*, 2017, **1**, 1414–1424.
238 B. Adeniran and R. Mokaya, *Nano Energy*, 2015, **16**, 173–185.
239 Z. Tan and K. E. Gubbins, *J. Phys. Chem.*, 1990, **94**, 6061–6069.
240 C. M. Simon, J. Kim, D. A. Gomez-Gualdron, J. S. Camp, Y. G. Chung, R. L. Martin, R. Mercado, M. W. Deem, D. Gunter and M. Haranczyk, *Energy Environ. Sci.*, 2015, **8**, 1190–1199.
241 S. Biloé, V. Goetz and A. Guillot, *Carbon*, 2002, **40**, 1295–1308.
242 P. Bénard and R. Chahine, *Scr. Mater.*, 2007, **56**, 803–808.
243 M. I. M. Kusdhany and S. M. Lyth, *Carbon*, 2021, **179**, 190–201.
244 M. Sevilla, W. Sangchoom, N. Balahmar, A. B. Fuertes and R. Mokaya, *ACS Sustainable Chem. Eng.*, 2016, **4**, 4710–4716.
245 N. P. Stadie, J. J. Vajo, R. W. Cumberland, A. A. Wilson, C. C. Ahn and B. Fultz, *Langmuir*, 2012, **28**, 10057–10063.
246 A. J. Lachawiec Jr and R. T. Yang, *Langmuir*, 2008, **24**, 6159–6165.
247 H. Nishihara, P.-X. Hou, L.-X. Li, M. Ito, M. Uchiyama, T. Kaburagi, A. Ikura, J. Katamura, T. Kawarada, K. Mizuuchi and T. Kyotani, *J. Phys. Chem. C*, 2009, **113**, 3189–3196.
248 N. Balahmar, A. C. Mitchell and R. Mokaya, *Adv. Energy Mater.*, 2015, **5**, 1500867.
249 K. Xia, R. Xiong, Y. Chen, D. Liu, Q. Tian, Q. Gao, B. Han and C. Zhou, *Colloids Surf., A*, 2021, 126640.
250 X. Ma, R. Chen, K. Zhou, Q. Wu, H. Li, Z. Zeng and L. Li, *ACS Sustainable Chem. Eng.*, 2020, **8**, 11721–11728.
251 Z. Zhang, D. Luo, G. Lui, G. Li, G. Jiang, Z. P. Cano, Y.-P. Deng, X. Du, S. Yin, Y. Chen, M. Zhang, Z. Yan and Z. Chen, *Carbon*, 2019, **143**, 531–541.
252 J. Singh, S. Basu and H. Bhunia, *J. Taiwan Inst. Chem. Eng.*, 2019, **102**, 438–447.
253 L. Wang and R. T. Yang, *J. Phys. Chem. C*, 2012, **116**, 1099–1106.
254 J. E. Park, G. B. Lee, S. Y. Hwang, J. H. Kim, B. U. Hong, H. Kim and S. Kim, *Appl. Sci.*, 2018, **8**, 1596.
255 N. Byamba-Ochir, W. G. Shim, M. S. Balathanigaimani and H. Moon, *Appl. Energy*, 2017, **190**, 257–265.
256 I. Susanti and N. Widiastuti, *Malaysian J. Fundament. Appl. Sci.*, 2019, **15**, 249–253.
257 J. Cui, K. Zhang, X. Zhang and Y. Lee, *Microporous Mesoporous Mater.*, 2020, **295**, 109947.
258 C. Guan, L. S. Loo, K. Wang and C. Yang, *Energy Convers. Manage.*, 2011, **52**, 1258–1262.
259 L. Giraldo and J. C. Moreno-Piraján, *Mater. Sci. Appl.*, 2011, **2**, 331.
260 I. Men'shchikov, A. Shiryaev, A. Shkolin, V. Vysotskii, E. Khozina and A. Fomkin, *Korean J. Chem. Eng.*, 2021, **38**, 276–291.
261 Z. Zhang, Z. P. Cano, D. Luo, H. Dou, A. Yu and Z. Chen, *J. Mater. Chem. A*, 2019, **7**, 20985–21003.
262 F. Rodriguez-Reinoso, J. de, D. Lopez-Gonzalez and C. Berenguer, *Carbon*, 1982, **20**, 513–518.
263 W. Hao, E. Björkman, M. Lilliestråle and N. Hedin, *Appl. Energy*, 2013, **112**, 526–532.
264 J. Jagiello, *Langmuir*, 1994, **10**, 2778–2785.
265 J. Garrido, A. Linares-Solano, J. Martin-Martinez, M. Molina-Sabio, F. Rodriguez-Reinoso and R. Torregrosa, *Langmuir*, 1987, **3**, 76–81.
266 D. Grau-Marin, J. Silvestre-Albero, E. O. Jardim, J. Jagiello, W. R. Betz and L. E. Peña, *Carbon*, 2020, **157**, 495–505.
267 D. Lozano-Castelló, D. Cazorla-Amorós and A. Linares-Solano, *Carbon*, 2004, **42**, 1233–1242.
268 R. H. Orcutt, *J. Chem. Phys.*, 1963, **39**, 605–608.
269 V. W. Couling and S. S. Ntombela, *Chem. Phys. Lett.*, 2014, **614**, 41–44.
270 S. Brunauer, P. H. Emmett and E. Teller, *J. Am. Chem. Soc.*, 1938, **60**, 309–319.
271 J. Rouquerol, P. Llewellyn and F. Rouquerol, *Stud. Surf. Sci. Catal.*, 2007, **160**, 49–56.
272 J. Rouquerol, F. Rouquerol, P. Llewellyn, G. Maurin and K. S. Sing, *Adsorption by powders and porous solids: principles, methodology and applications*, Academic Press, 2013.
273 J. Osterrieth, J. Rampersad, D. G. Madden, N. Rampal, L. Skoric, B. Connolly, M. Allendorf, V. Stavila, J. Snider, R. Ameloot, J. Marreiros, C. O. Ania, D. C. S. Azevedo, E. Vilarrasa-García, B. F. Santos, X.-H. Bu, X. Zang, H. Bunzen, N. Champness, S. L. Griffin, B. Chen, R.-B. Lin, B. Coasne, S. M. Cohen, J. C. Moreton, Y. J. Colon, L. Chen, R. Clowes, F.-X. Coudert, Y. Cui, B. Hou, D. D'Alessandro, P. W. Doheny, M. Dinca, C. Sun, C. Doonan, M. Huxley, J. D. Evans, P. Falcaro, R. Riccò, O. K. Farha, K. B. Idrees, T. Islamoglu, P. Feng, H. Yang, R. Forgan, D. Bara, S. Furukawa, E. Sanchez, J. Gascon, S. Telalovic, S. K. Ghosha, S. Mukherjee, M. R. Hill, M. M. Sadiq, P. Horcajada, P. Salcedo-Abraira, K. Kaneko, R. Kukobat, J. Kenvin, S. Keskin, S. Kitagawa, K. Otake, R. P. Lively, S. J. A. DeWitt, P. L. Llewellyn,

© 2022 The Author(s). Published by the Royal Society of Chemistry

Open Access Article. Published on 12 January 2022. Downloaded on 3/24/2022 12:40:42 PM.
This article is licensed under a Creative Commons Attribution 3.0 Unported Licence.

B. Lotsch, S. T. Emmerling, A. Pütz, C. Martí-Gastaldo, N. Muñoz, J. Garcia-Martinez, N. Linares, D. Maspoch, J. A. Suarez, P. Moghadam, R. Oktavian, R. Morris, P. Wheatley, J. Navarro, C. Petit, D. Danaci, M. Rosseinsky, A. Katsoulidis, M. Schroder, X. Han, S. Yang, C. Serre, G. Mouchaham, D. Sholl, R. Thyagarajan, D. Siderius, R. Q. Snurr, R. B. Goncalves, S. G. Telfer, S. J. Lee, V. Ting, J. Rowlandson, T. Uemura, T. Iiyuka, M. V. D. Veen, D. Rega, V. Vanspeybroeck, A. Lamaire, S. Rogge, K. Walton, L. W. Bingel, S. Wuttke, J. Andreo, O. Yaghi, B. Zhang, C. Yavuz, T. Nguyen, F. Zamora, C. Montoro, H.-C. Zhou, K. Angelo and D. Fairen-Jimenez, unpublished work.

274 A. Marczewski, Adsorption Glossary, 2002.

275 J. Villarroel-Rocha, D. Barrera, A. A. G. Blanco, M. E. R. Jalil and K. Sapag, *Adsorpt. Sci. Technol.*, 2013, **31**, 165–183.

276 M. Occelli, J. Olivier, J. Perdigon-Melon and A. Auroux, *Langmuir*, 2002, **18**, 9816–9823.

277 M. M. Dubinin and V. A. Astakhov, in *Molecular Sieve Zeolites-II*, ed. E. M. Flanigen and L. B. Sand, ACS Publications, United States, 1971, ch. 44, pp. 69–85.

278 G. Horváth and K. Kawazoe, *J. Chem. Eng. Jpn.*, 1983, **16**, 470–475.

279 E. P. Barrett, L. G. Joyner and P. P. Halenda, *J. Am. Chem. Soc.*, 1951, **73**, 373–380.

280 P. Ramirez-Vidal, R. L. Canevesi, G. Sdanghi, S. Schaefer, G. Maranzana, A. Celzard and V. Fierro, *ACS Appl. Mater. Interfaces*, 2021, **13**, 12562–12574.

281 J. Jagiello and M. Thommes, *International Conference on Carbon for Energy Storage and Environment Protection*, Orleans, France, 2005.

282 M. Kwiatkowski and D. Kalderis, *Carbon Lett.*, 2020, **30**, 325–329.

283 T. Tian, Z. Zeng, D. Vulpe, M. E. Casco, G. Divitini, P. A. Midgley, J. Silvestre-Albero, J.-C. Tan, P. Z. Moghadam and D. Fairen-Jimenez, *Nat. Mater.*, 2018, **17**, 174–179.

284 J. Marco-Lozar, J. Juan-Juan, F. Suárez-García, D. Cazorla-Amorós and A. Linares-Solano, *Int. J. Hydrogen Energy*, 2012, **37**, 2370–2381.

285 J. Marco-Lozar, M. Kunowsky, F. Suarez-Garcia, J. Carruthers and A. Linares-Solano, *Energy Environ. Sci.*, 2012, **5**, 9833–9842.

286 J. Juan-Juan, J. Marco-Lozar, F. Suárez-García, D. Cazorla-Amorós and A. Linares-Solano, *Carbon*, 2010, **48**, 2906–2909.

287 Y. Song, X. Zhou and J. A. Wang, *Energy Sources, Part A*, 2021, **43**, 1337–1347.

288 C. Ge, D. Lian, S. Cui, J. Gao and J. Lu, *Processes*, 2019, **7**, 592.

289 E. Mehrvarz, A. A. Ghoreyshi and M. Jahanshahi, *Front. Chem. Sci. Eng.*, 2017, **11**, 252–265.

290 K. Adlak, R. Chandra, V. K. Vijay and K. K. Pant, *J. Anal. Appl. Pyrolysis*, 2021, 105102.

291 P. Wang, G. Zhang, W. Chen, Q. Chen, H. Jiao, L. Liu, X. Wang and X. Deng, *ACS Omega*, 2020, **5**, 23460–23467.

292 O. Boujibar, A. Souikny, F. Ghamouss, O. Achak, M. Dahbi and T. Chafik, *J. Environ. Chem. Eng.*, 2018, **6**, 1995–2002.

293 E. García-Díez, S. Schaefer, A. Sanchez-Sanchez, A. Celzard, V. Fierro, M. M. Maroto-Valer and S. García, *ACS Appl. Mater. Interfaces*, 2019, **11**, 36789–36799.

294 X. Liu, C. Zhang, Z. Geng and M. Cai, *Microporous Mesoporous Mater.*, 2014, **194**, 60–65.

295 W. Shi, Q. Zhang, S. Liu, S. Su, B. Chang and B. Yang, *J. Colloid Interface Sci.*, 2021, **600**, 670–680.

296 A. Taylor, PhD thesis, University of Nottingham, 2019.

297 M. Xia, W. Chen, J. Wu, Y. Chen, H. Yang, X. Chen, D. Zhu and H. Chen, *Fuel*, 2021, **291**, 120185.

298 X.-F. Wang, L. Xiong, J.-J. Zhong, L. Jin, J.-L. Yan, B. Mu, Y.-G. Zhang and S.-L. Song, *Ind. Eng. Chem. Res.*, 2020, **59**, 18106–18114.

299 J. Deng, T. Xiong, F. Xu, M. Li, C. Han, Y. Gong, H. Wang and Y. Wang, *Green Chem.*, 2015, **17**, 4053–4060.

300 J.-S. Wei, S. Wan, P. Zhang, H. Ding, X.-B. Chen, H.-M. Xiong, S. Gao and X. Wei, *New J. Chem.*, 2018, **42**, 6763–6769.

301 J. Wang, Q. Yang, W. Yang, H. Pei, L. Zhang, T. Zhang, N. Hu, Y. Suo and J. Wang, *J. Mater. Chem. A*, 2018, **6**, 16690–16698.

302 A. Rehman, Y.-J. Heo, G. Nazir and S.-J. Park, *Carbon*, 2021, **172**, 71–82.

303 Z. Han, H. Yu, C. Li and S. Zhou, *Appl. Surf. Sci.*, 2021, **544**, 148963.

304 Z. Hu and M. P. Srinivasan, *Microporous Mesoporous Mater.*, 2001, **43**, 267–275.

305 Z. Hu, H. Guo, M. Srinivasan and N. Yaming, *Sep. Purif. Technol.*, 2003, **31**, 47–52.

306 A. Arami-Niya, W. M. A. W. Daud, F. S. Mjalli, F. Abnisa and M. S. Shafeeyan, *Chem. Eng. Res. Des.*, 2012, **90**, 776–784.

307 A. B. Fuertes and M. Sevilla, *Carbon*, 2015, **94**, 41–52.

308 X. Ma, Y. Li, M. Cao and C. Hu, *J. Mater. Chem. A*, 2014, **2**, 4819–4826.

309 W. Hu, W. Zhang, M. Zheng, Y. Xiao, H. Dong, Y. Liang, H. Hu and Y. Liu, *Int. J. Hydrogen Energy*, 2021, **46**, 896–905.

310 C. Bommier, R. Xu, W. Wang, X. Wang, D. Wen, J. Lu and X. Ji, *Nano Energy*, 2015, **13**, 709–717.

311 H. Yang, R. Yan, H. Chen, D. H. Lee and C. Zheng, *Fuel*, 2007, **86**, 1781–1788.

312 C. Xia and S. Q. Shi, *Green Chem.*, 2016, **18**, 2063–2071.

313 A. Ariharan, K. Ramesh, R. Vinayagamoorthi, M. S. Rani, B. Viswanathan, S. Ramaprabhu and V. Nandhakumar, *J. Energy Storage*, 2021, **35**, 102185.

314 A. Ariharan, B. Viswanathan and V. Nandhakumar, *Indian J. Chem., Sect. A: Inorg., Bio-inorg., Phys., Theor. Anal. Chem.*, 2016, **55**, 649–656.

315 M. Sevilla and A. B. Fuertes, *J. Mater. Chem. A*, 2013, **1**, 13738–13741.

316 W. Yang, W. Yang, F. Ding, L. Sang, Z. Ma and G. Shao, *Carbon*, 2017, **111**, 419–427.

317 M. Sevilla and A. B. Fuertes, *ACS Nano*, 2014, **8**, 5069–5078.

318 T. Tsumura, A. Arikawa, T. Kinumoto, Y. Arai, T. Morishita, H. Orikasa, M. Inagaki and M. Toyoda, *Mater. Chem. Phys.*, 2014, **147**, 1175–1182.

© 2022 The Author(s). Published by the Royal Society of Chemistry

Open Access Article. Published on 12 January 2022. Downloaded on 3/24/2022 12:40:42 PM.
This article is licensed under a Creative Commons Attribution 3.0 Unported Licence.

319 G. A. Ferrero, A. B. Fuertes, M. Sevilla and M.-M. Titirici, *Carbon*, 2016, **106**, 179–187.
320 G. Ferrero, M. Sevilla and A. Fuertes, *Carbon*, 2015, **88**, 239–251.
321 A. B. Fuertes and M. Sevilla, *ACS Appl. Mater. Interfaces*, 2015, **7**, 4344–4353.
322 T. Yang, W. Li, M. Su, Y. Liu and M. Liu, *New J. Chem.*, 2020, **44**, 7968–7975.
323 A. Fuertes, G. Ferrero and M. Sevilla, *J. Mater. Chem. A*, 2014, **2**, 14439–14448.
324 H. Luo, Y. Yang, X. Zhao, J. Zhang and Y. Chen, *Electrochim. Acta*, 2015, **169**, 13–21.
325 D. Puthusseri, V. Aravindan, S. Madhavi and S. Ogale, *Energy Environ. Sci.*, 2014, **7**, 728–735.
326 A. D. Roberts, X. Li and H. Zhang, *Carbon*, 2015, **95**, 268–278.
327 P. Yadav, A. Banerjee, S. Unni, J. Jog, S. Kurungot and S. Ogale, *ChemSusChem*, 2012, **5**, 2159–2164.
328 D. Hines, A. Bagreev and T. J. Bandosz, *Langmuir*, 2004, **20**, 3388–3397.
329 L. Tong, L.-L. Zhang, Y.-C. Wang, L.-Y. Wan, Q.-Q. Yan, C. Hua, C.-J. Jiao, Z.-Y. Zhou, Y.-W. Ding and B. Liu, *ACS Appl. Mater. Interfaces*, 2020, **12**, 25211–25220.
330 W. Li, F. Zhang, Y. Dou, Z. Wu, H. Liu, X. Qian, D. Gu, Y. Xia, B. Tu and D. Zhao, *Adv. Energy Mater.*, 2011, **1**, 382–386.
331 B. Yang, J. Chen, S. Lei, R. Guo, H. Li, S. Shi and X. Yan, *Adv. Energy Mater.*, 2018, **8**, 1702409.
332 Y. Wang, H. Wang, H. Wang, M. Zhang, X. Liang, K. Xia and Y. Zhang, *ACS Appl. Mater. Interfaces*, 2019, **11**, 20272–20280.
333 N. Wang, Y. Wang, X. Xu, T. Liao, Y. Du, Z. Bai and S. Dou, *ACS Appl. Mater. Interfaces*, 2018, **10**, 9353–9361.
334 J. K. Guo, J. Liu and L. B. Kong, *ChemElectroChem*, 2020, **7**, 2592–2598.
335 M. Sevilla, G. A. Ferrero, N. Diez and A. B. Fuertes, *Carbon*, 2018, **131**, 193–200.
336 D. Li, X. Ren, Q. Ai, Q. Sun, L. Zhu, Y. Liu, Z. Liang, R. Peng, P. Si and J. Lou, *Adv. Energy Mater.*, 2018, **8**, 1802386.
337 B. Adeniran, E. Masika and R. Mokaya, *J. Mater. Chem. A*, 2014, **2**, 14696–14710.
338 J. Deng, T. Xiong, H. Wang, A. Zheng and Y. Wang, *ACS Sustainable Chem. Eng.*, 2016, **4**, 3750–3756.
339 N. Balahmar, A. S. Al-Jumialy and R. Mokaya, *J. Mater. Chem. A*, 2017, **5**, 12330–12339.
340 K. M. Rambau, N. M. Musyoka, N. Manyala, J. Ren and H. W. Langmi, *Mater. Today: Proc.*, 2018, **5**, 10505–10513.
341 E. E. Taylor, K. Garman and N. P. Stadie, *Chem. Mater.*, 2020, **32**, 2742–2752.
342 R. K. Bera, H. Park, S. H. Ko and R. Ryoo, *RSC Adv.*, 2020, **10**, 32290–32295.
343 H. Park, J. Bang, S. W. Han, R. K. Bera, K. Kim and R. Ryoo, *Microporous Mesoporous Mater.*, 2021, **318**, 111038.
344 R. S. Ambekar, E. F. Oliveira, B. Kushwaha, V. Pal, L. D. Machado, S. M. Sajadi, R. H. Baughman, P. M. Ajayan, A. K. Roy and D. S. Galvao, *Addit. Manuf.*, 2021, **37**, 101628.
345 H. Tanaka, T. Seto, H. Nishihara, T. Kyotani and M. T. Miyahara, *Carbon*, 2021, **175**, 609.
346 R. Wijiyanti, T. Gunawan, N. S. Nasri, Z. A. Karim, A. F. Ismail and N. Widiastuti, *Indones. J. Chem.*, 2020, **20**, 29–42.
347 D. Tiwari, H. Bhunia and P. K. Bajpai, *J. Indian Chem. Soc.*, 2018, **95**, 247–252.
348 N. M. Musyoka, K. M. Rambau, N. Manyala, J. W. Ren, H. W. Langmi and M. K. Mathe, *J. Environ. Sci. Health, Part A: Toxic/Hazard. Subst. Environ. Eng.*, 2018, **53**, 1022–1028.
349 T. Gunawan, R. Wijiyanti and N. Widiastuti, *RSC Adv.*, 2018, **8**, 41594–41602.
350 J. Rangel-Sequeda, M. Loredo-Cancino, V. I. A. Maté, J. A. D. Dobladez, D. A. De Haro-Del Rio, J. J. Salazar-Rábago and E. Soto-Regalado, *Water, Air, Soil Pollut.*, 2021, **232**, 1–18.
351 N. P. Stadie, M. Murialdo, C. C. Ahn and B. Fultz, *J. Am. Chem. Soc.*, 2013, **135**, 990–993.
352 S. T. J. Dewi and N. Widiastuti, in *3rd International Seminar on Chemistry: Green Chemistry and Its Role for Sustainability*, ed. Y. Kusumawati, S. Fatmawati, A. S. Purnomo, F. Kurniawan and H. Juwono, Amer Inst Physics, Melville, 2018, vol. 2049.
353 C. Xue, H. Zhu, T. Xu, E. Wang, B. Xiao, X. Liu, X. Hao and G. Guan, *RSC Adv.*, 2017, **7**, 24195–24203.
354 X. Ma, L. Li, R. Chen, C. Wang, H. Li and H. Li, *Chem. – Asian J.*, 2018, **13**, 2069–2076.
355 A. Garsuch, O. Klepel, R. R. Sattler, C. Berger and R. Gläser, *Carbon*, 2006, **44**, 593–596.
356 R. Baur and R. Krishna, *Catal. Today*, 2005, **105**, 173–179.
357 A. Sachse and J. Garcia-Martinez, *Chem. Mater.*, 2017, **29**, 3827–3853.
358 P. Annamalai, N. M. Musyoka, J. W. Ren, H. W. Langmi, M. Mathe, D. Bessarabov and L. F. Petrik, *Res. Chem. Intermed.*, 2017, **43**, 4095–4102.
359 M. Mazaj, M. Bjelica, E. Žagar, N. Z. Logar and S. Kovačič, *ChemSusChem*, 2020, **13**, 2089–2097.
360 A. Celzard and V. Fierro, *Energy Fuels*, 2005, **19**, 573–583.
361 P.-X. Hou, H. Orikasa, H. Itoi, H. Nishihara and T. Kyotani, *Carbon*, 2007, **45**, 2011–2016.
362 J. Shao, X. Xiao, X. Fan, X. Huang, B. Zhai, S. Li, H. Ge, Q. Wang and L. Chen, *Nano Energy*, 2015, **15**, 244–255.
363 A. Almasoudi and R. Mokaya, *J. Mater. Chem. A*, 2014, **2**, 10960–10968.
364 A. Gabe, M. Ouzzine, E. E. Taylor, N. P. Stadie, N. Uchiyama, T. Kanai, Y. Nishina, H. Tanaka, Z.-Z. Pan and T. Kyotani, *J. Mater. Chem. A*, 2021, **9**, 7503–7507.
365 J. Jiang, Q. Gao, K. Xia and J. Hu, *Microporous Mesoporous Mater.*, 2009, **118**, 28–34.
366 K. Xia, Q. Gao, S. Song, C. Wu, J. Jiang, J. Hu and L. Gao, *Int. J. Hydrogen Energy*, 2008, **33**, 116–123.
367 H. Wang, Q. Gao and J. Hu, *Microporous Mesoporous Mater.*, 2010, **131**, 89–96.
368 U. Anggarini, E. Agustina and N. Widiastuti, *Indones. J. Chem.*, 2015, **15**, 315–318.
369 K. Matsuoka, Y. Yamagishi, T. Yamazaki, N. Setoyama, A. Tomita and T. Kyotani, *Carbon*, 2005, **43**, 876–879.

© 2022 The Author(s). Published by the Royal Society of Chemistry

Appendix B

Compositional Analyses

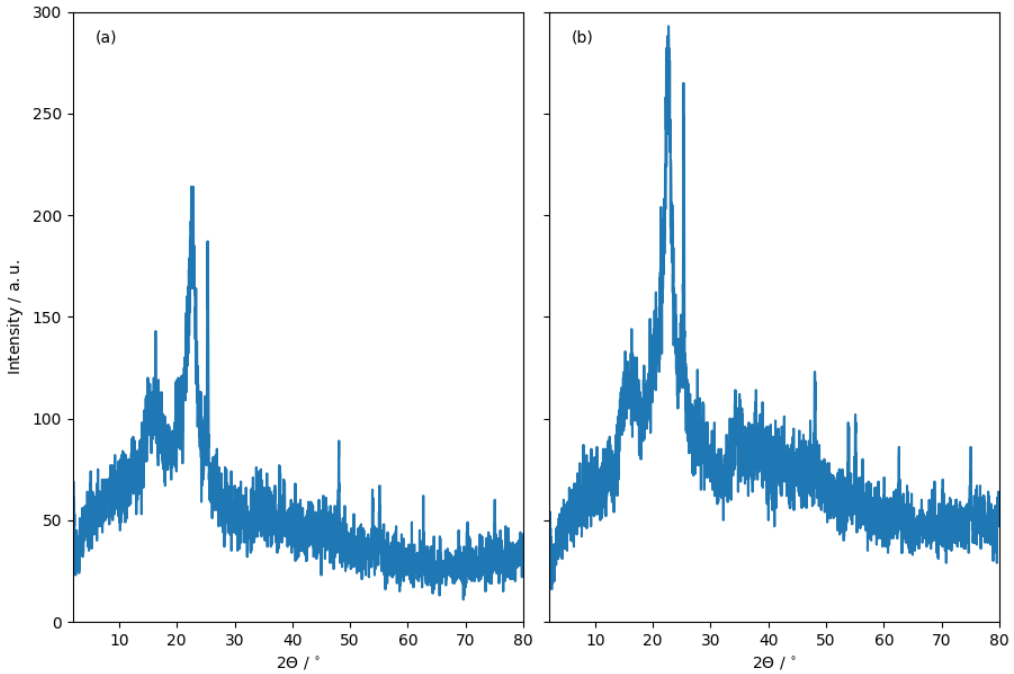

Figure B.1: P-XRD spectra for samples hC-hydrochar (a) and hD-hydrochar (b).

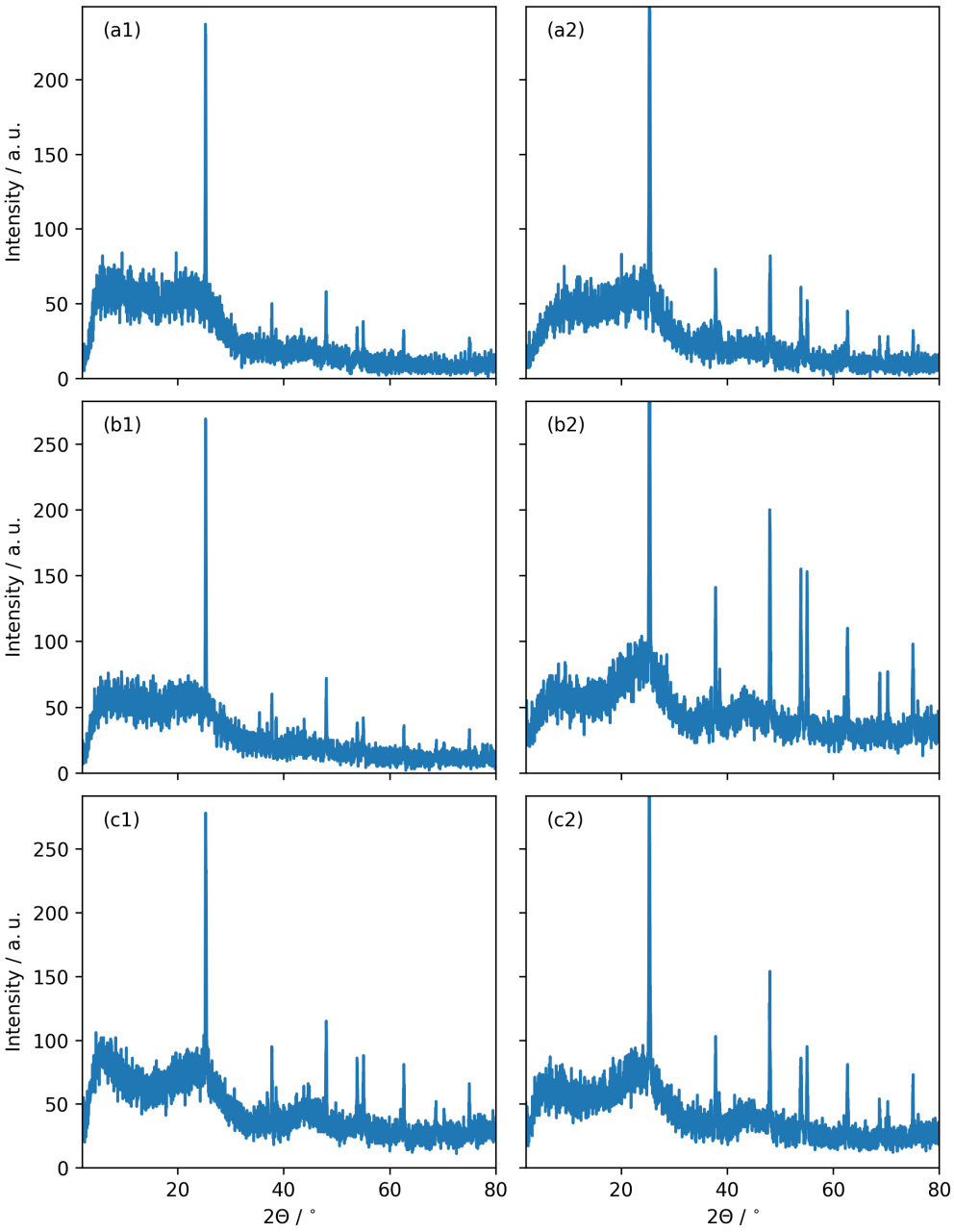

Figure B.2: P-XRD spectra for samples hC-0600 (a1), hC-0600′ (a2), hC-0700 (b1), hC-0700′ (b2), hC-0800 (c1), hC-0800′ (c2).

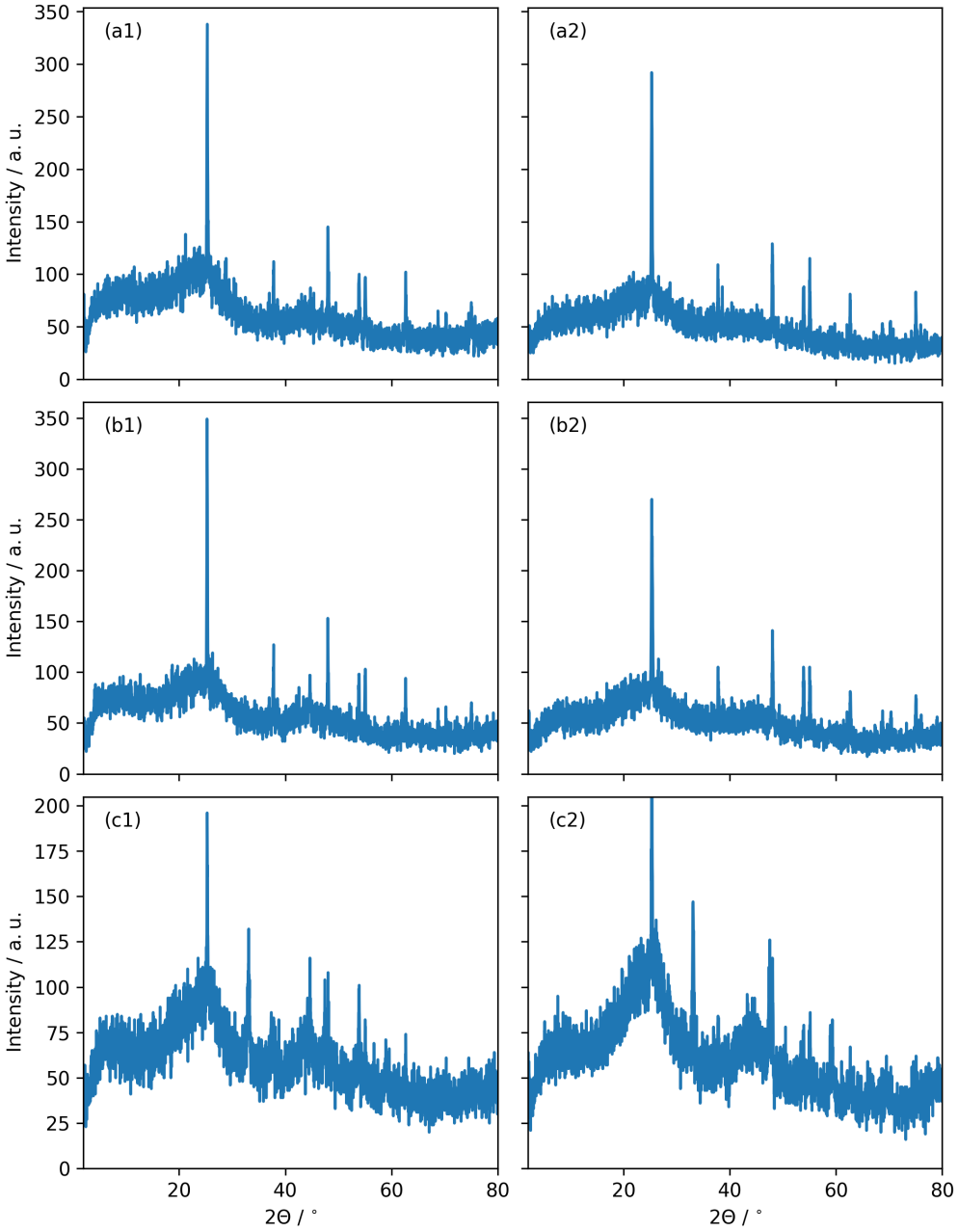

Figure B.3: P-XRD spectra for samples hD-0600 (a1), hD-0600′ (a2), hD-0700 (b1), hD-0700′ (b2), hD-0800 (c1), hD-0800′ (c2).

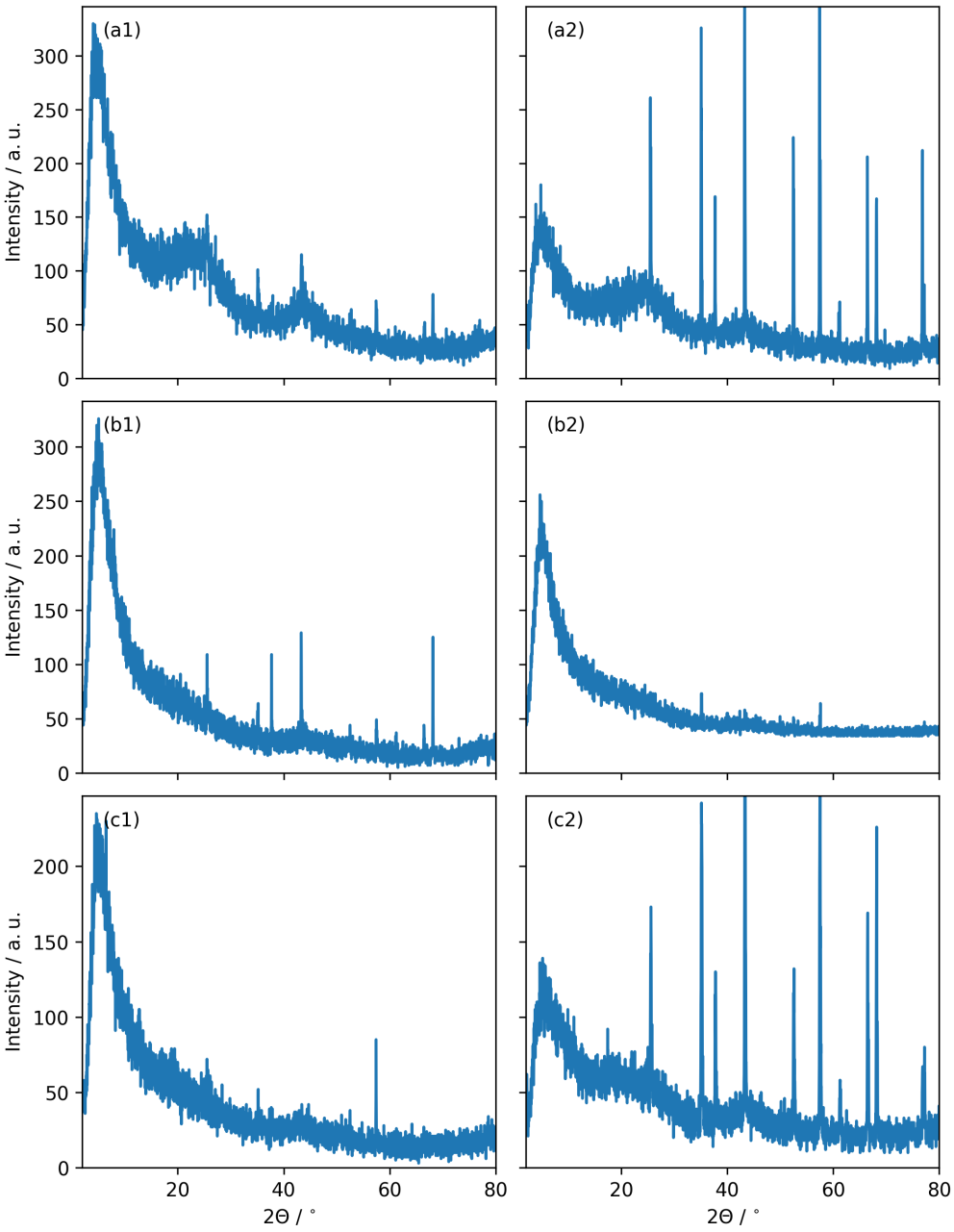

Figure B.4: P-XRD spectra for samples hC-4600 (a1), hD-4600 (a2), hC-4700 (b1), hD-4700 (b2), hC-4800 (c1), hD-4800 (c2).

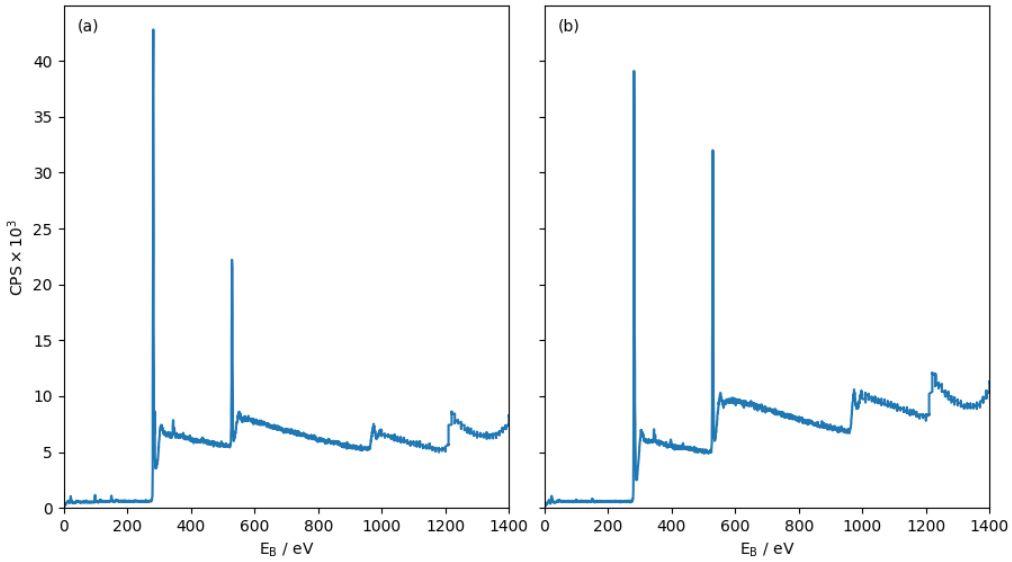

Figure B.5: XPS spectra for samples hD-0700 (a) and hD-hydrochar (b).

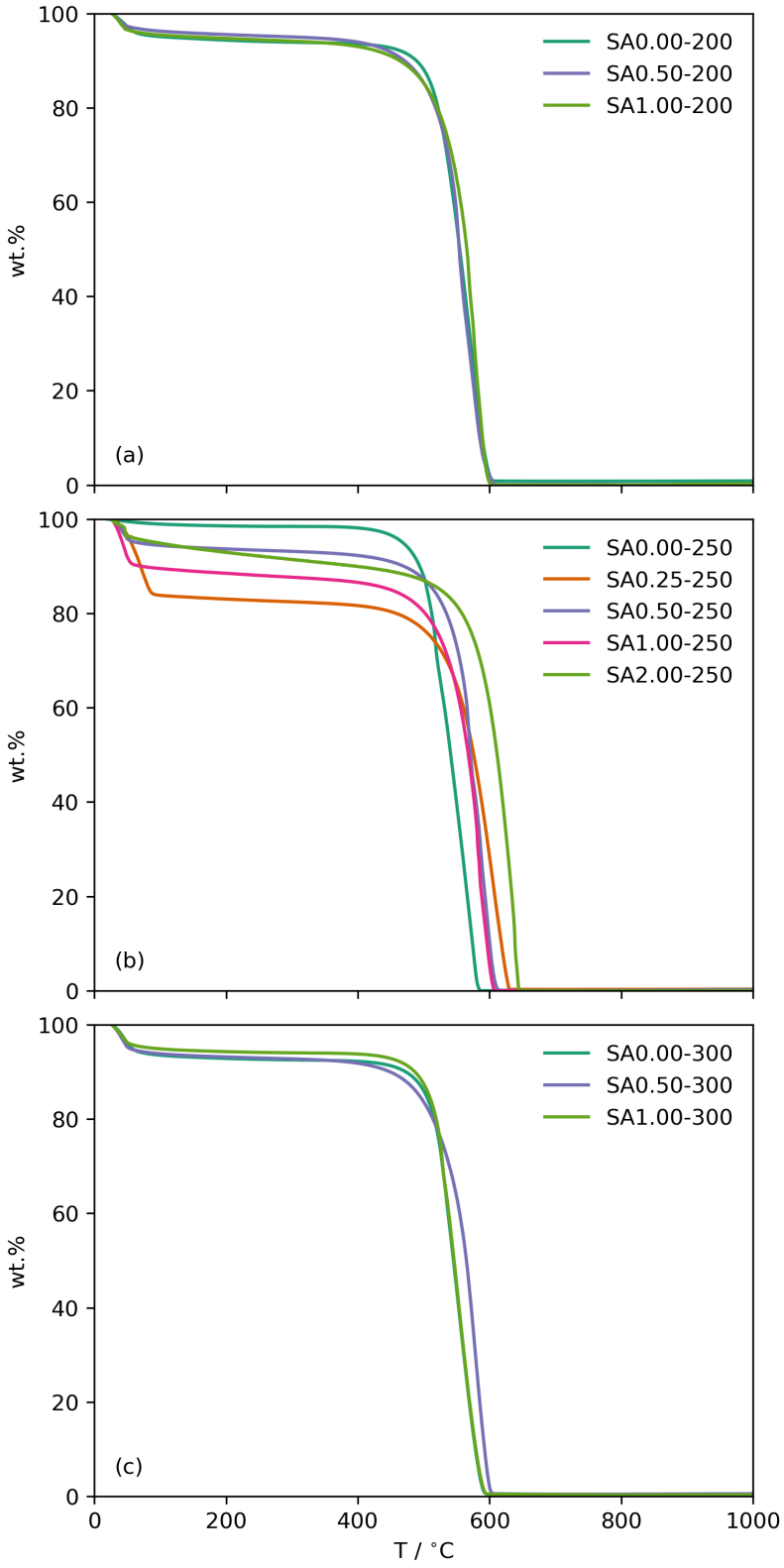

Figure B.6: TGA curves for SD*x.xx-HHH* samples.

Appendix C

Porosimetry

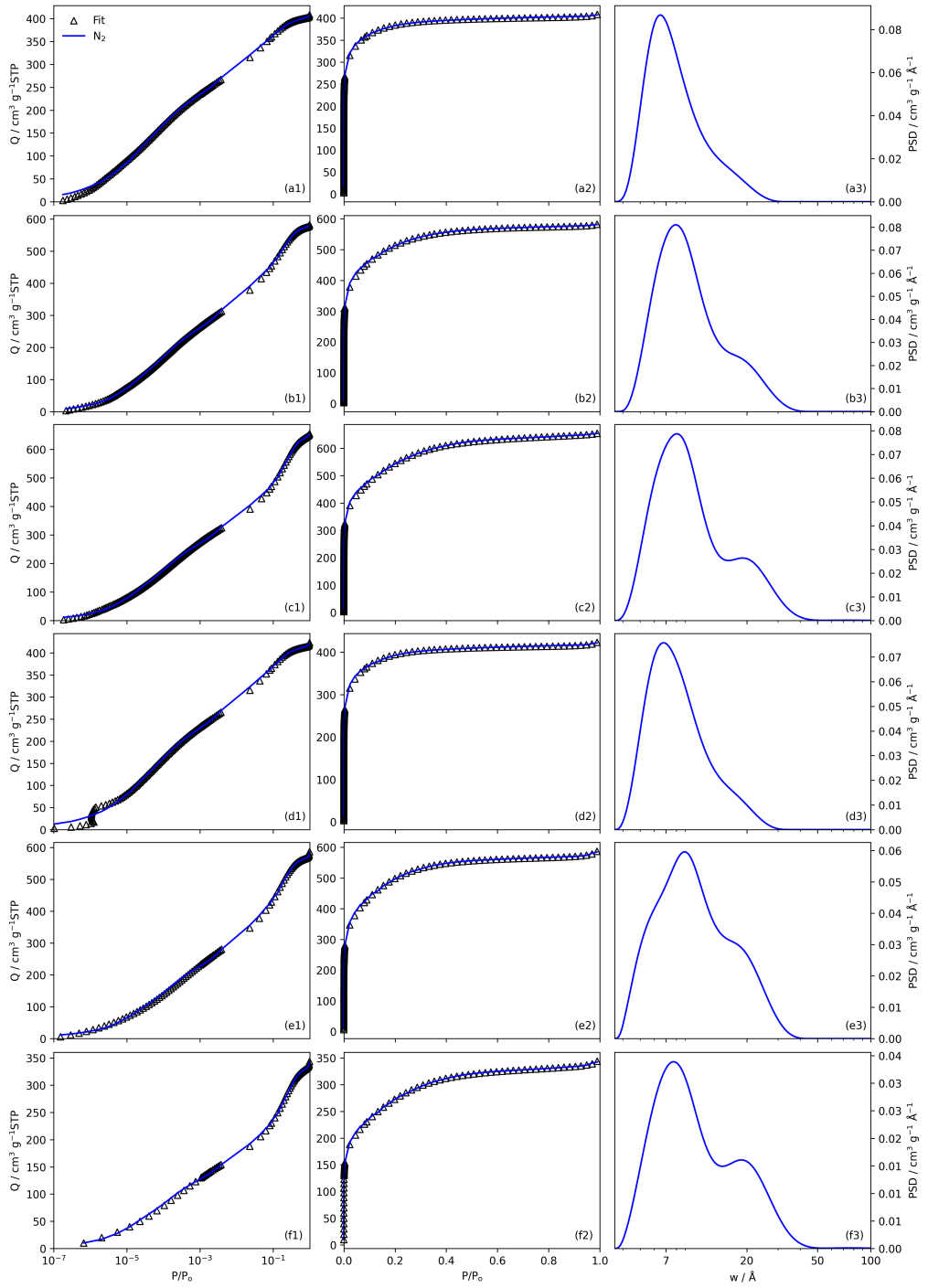

Figure C.1: Fits to N_2 isotherms with logarithmic (a) and linear (b) relative pressure scale, and resultant differential PSDs (c) for samples hC-4600, hC-4700, hC-4800, hD-4600, hD-4700, hD-4800 in order in rows (1-6).

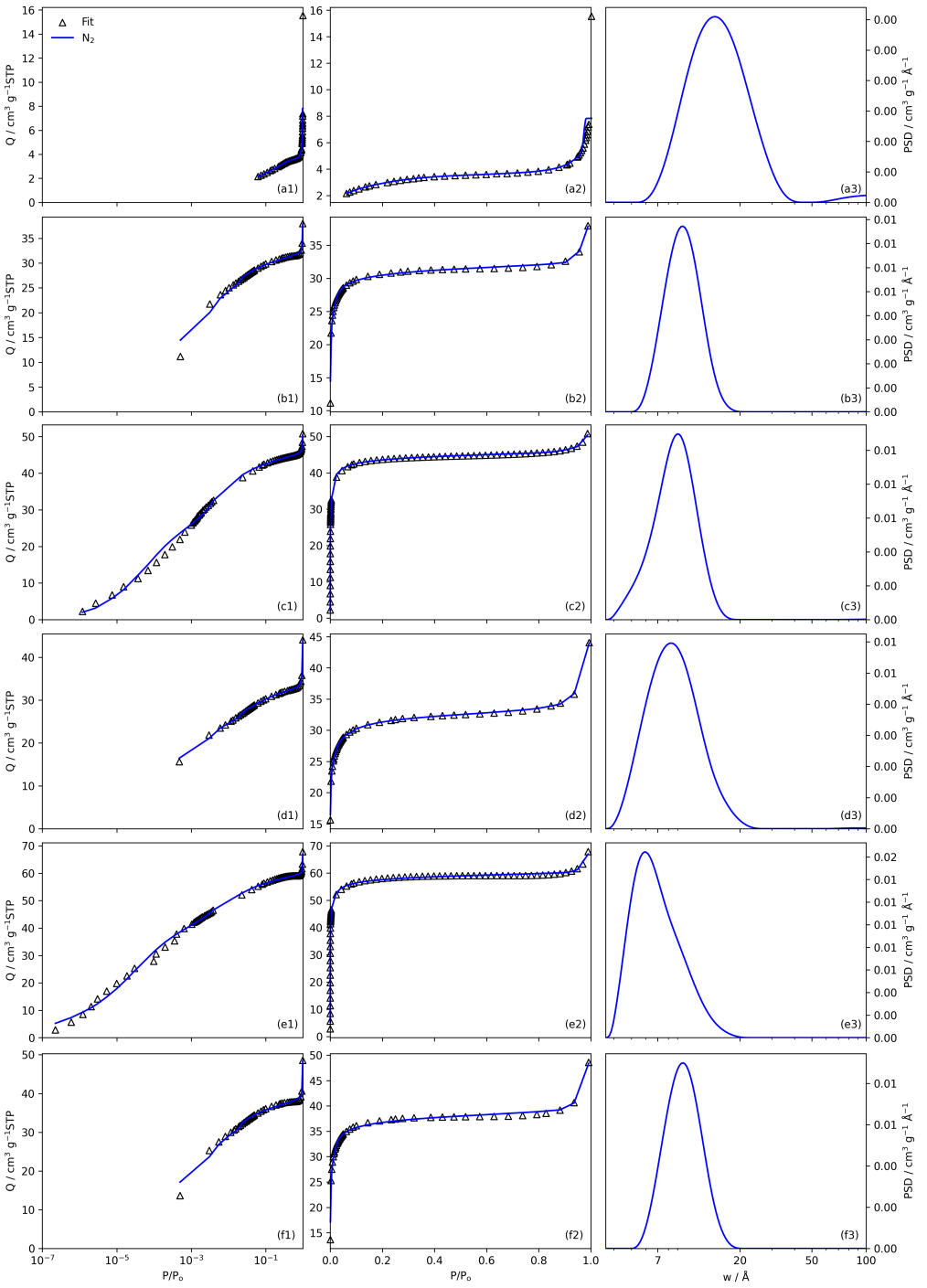

Figure C.2: Fits to N_2 isotherms with logarithmic (a) and linear (b) relative pressure scale, and resultant differential PSDs (c) for samples hD-0600, hD-0700, hD-0800, hD-0600′, hD-0700′, and hD-0800′ in order in rows (1-6).

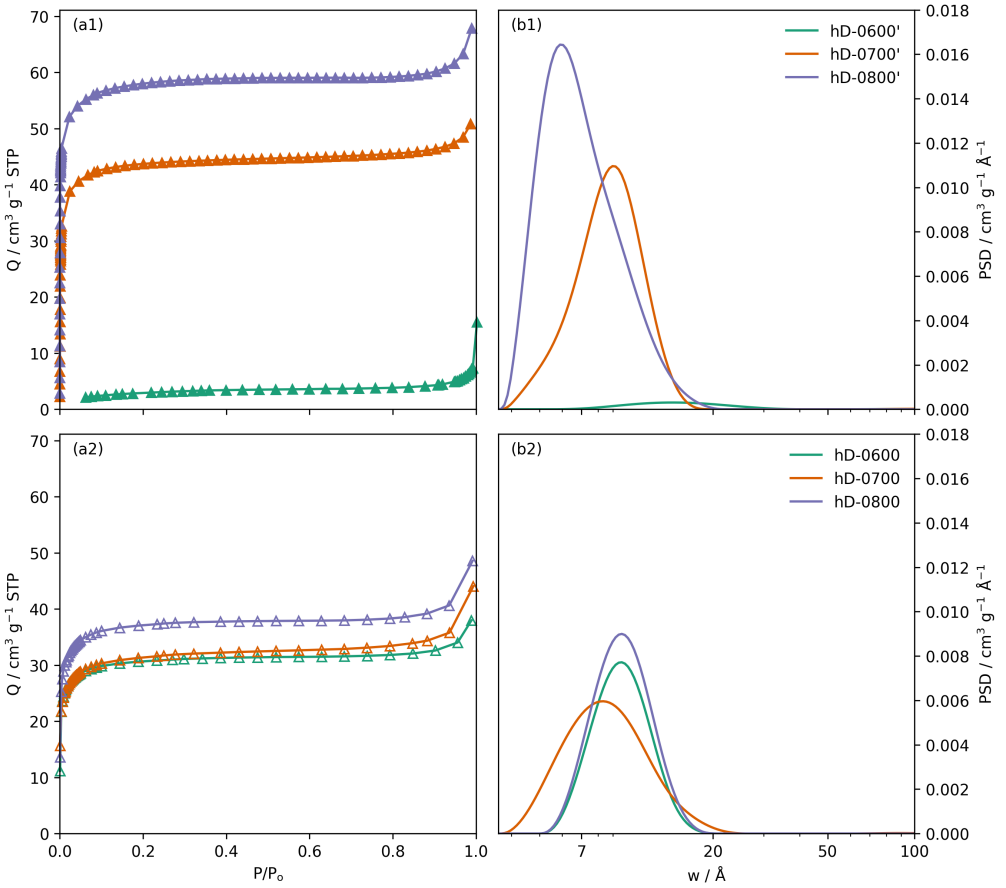

Figure C.3: Isotherms and resultant PSDs for samples hD-0TTT and hD-0TTT'.

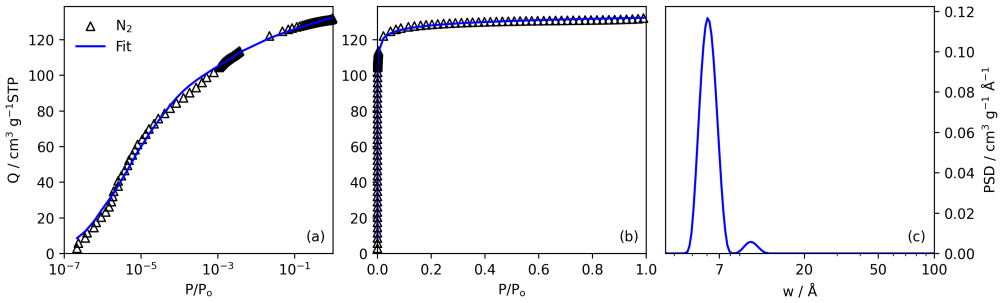

Figure C.4: Fits to N_2 isotherms with logarithmic (a) and linear (b) relative pressure scale, and resultant differential PSDs (c) for the cellulose acetate derived sample CA-0800.

Table C.1: Porosity of CA-0800

$\mathbf{A_{BET}}$ / $\mathbf{m^2\ g^{-1}}$	Pore volume / $\mathbf{cm^3\ g^{-1}}$	Pore size / Å
522 (491)	0.20 (0.19)	6

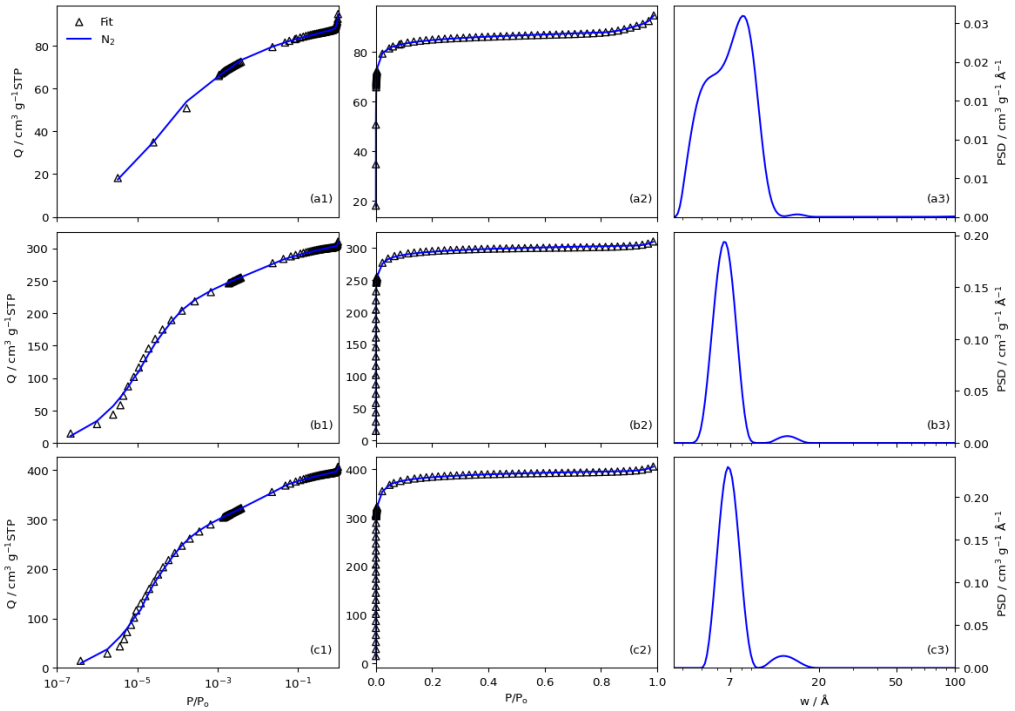

Figure C.5: Fits to N_2 isotherms with logarithmic (a) and linear (b) relative pressure scale, and resultant differential PSDs (c) for samples SA0.00-200, SA0.50-200, and SA1.00-200 in order in rows (1-3).

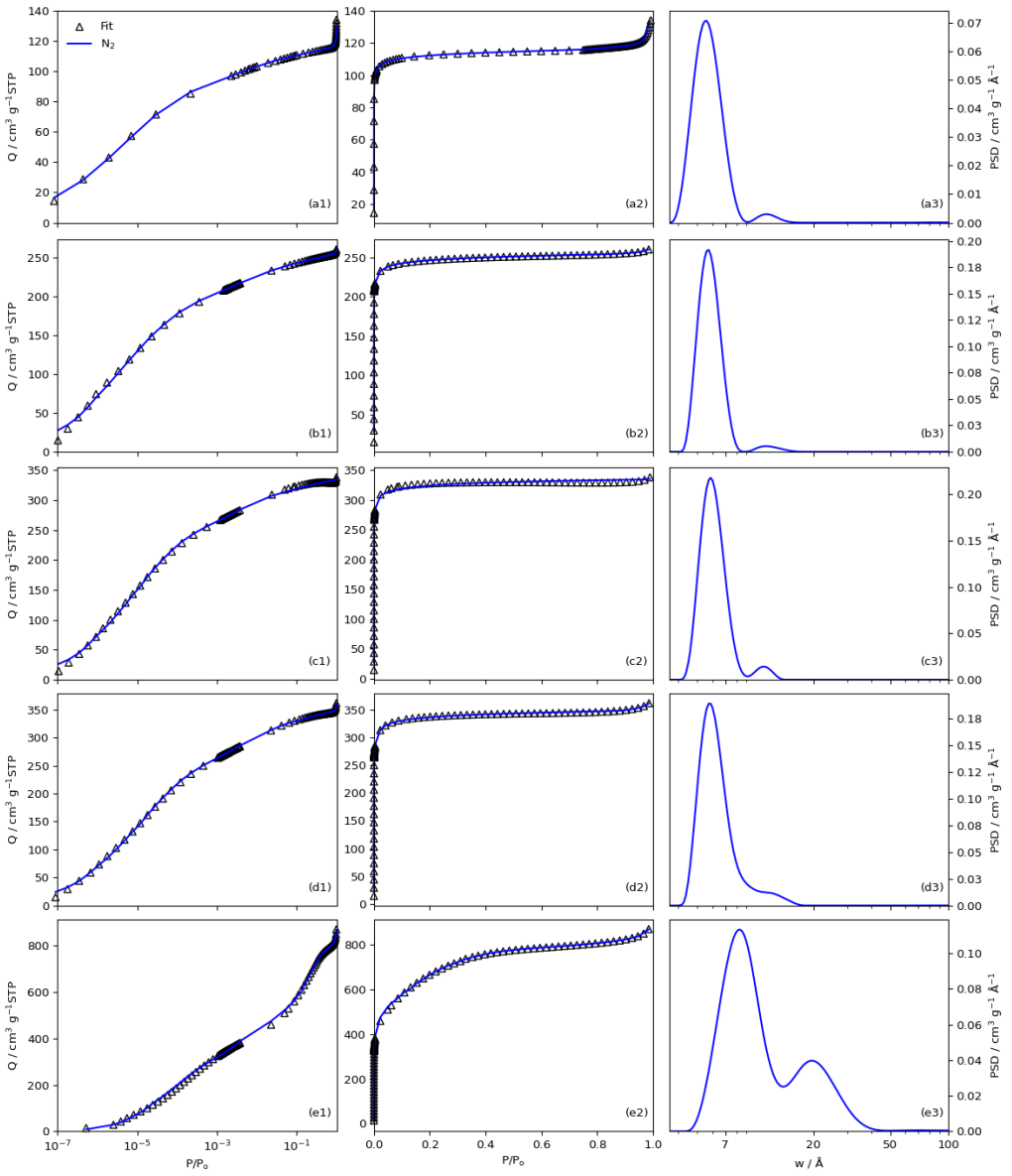

Figure C.6: Fits to N_2 isotherms with logarithmic (a) and linear (b) relative pressure scale, and resultant differential PSDs (c) for samples SA0.00-250, SA0.25-250, SA0.50-250, SA1.0-250, and SA2.00-250 in order in rows (1-5).

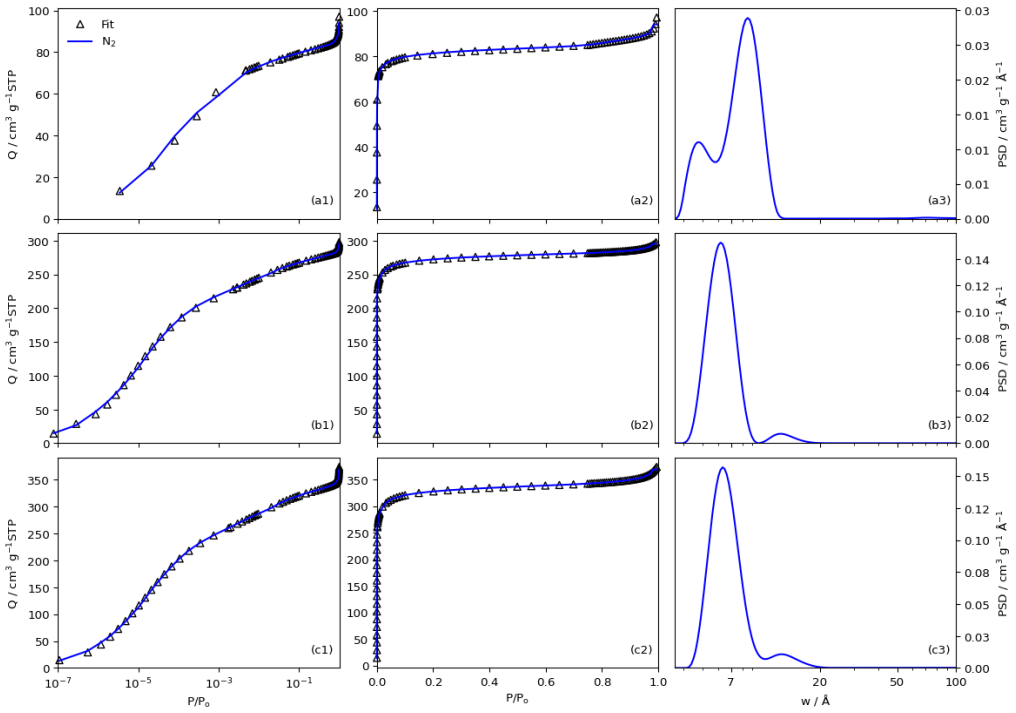

Figure C.7: Fits to N_2 isotherms with logarithmic (a) and linear (b) relative pressure scale, and resultant differential PSDs (c) for samples SA0.00-300, SA0.50-300, and SA1.00-300 in order in rows (1-3).

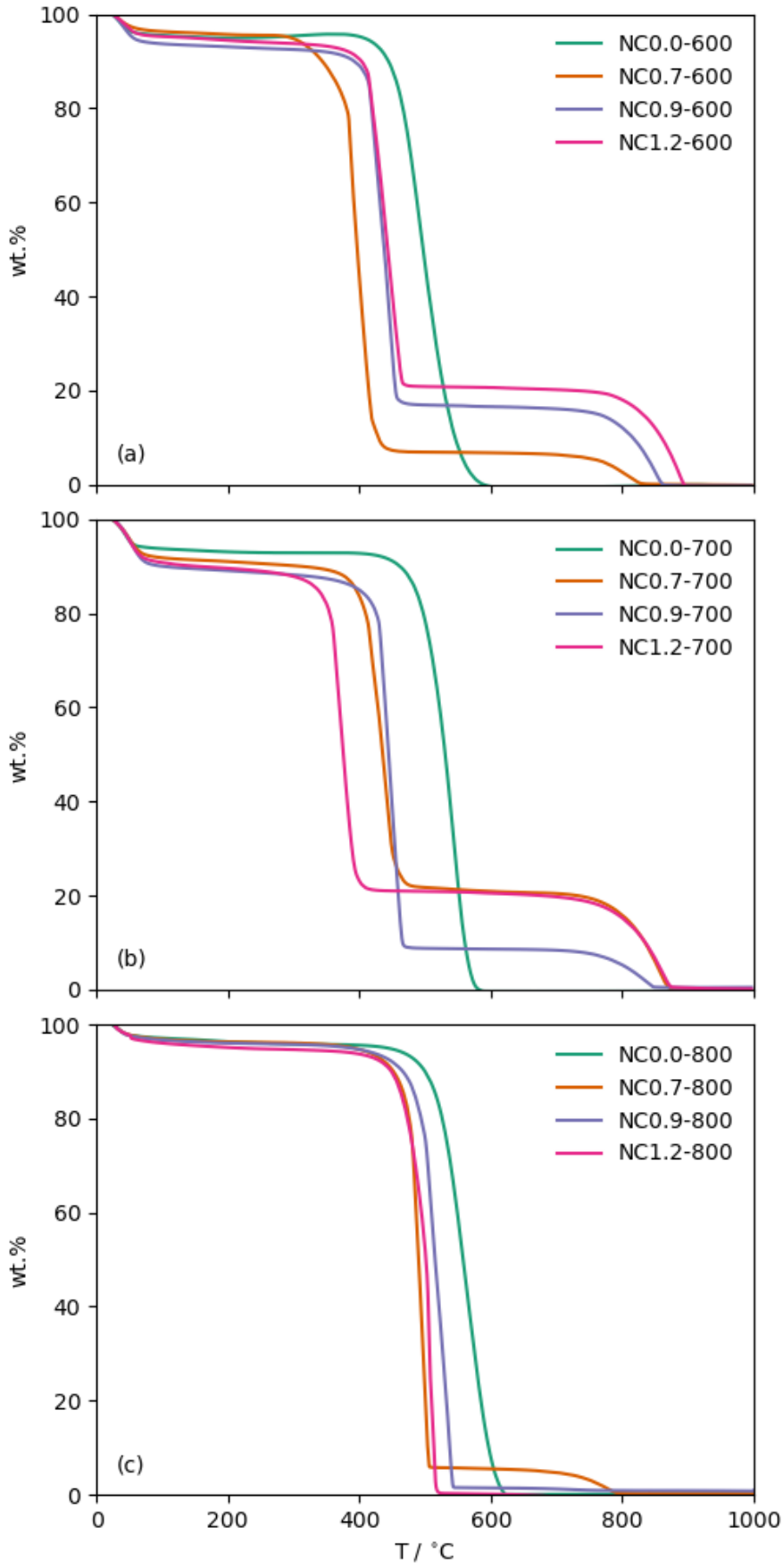

Figure C.8: Unadjusted TGA curves for NC$x.x$-TTT samples.

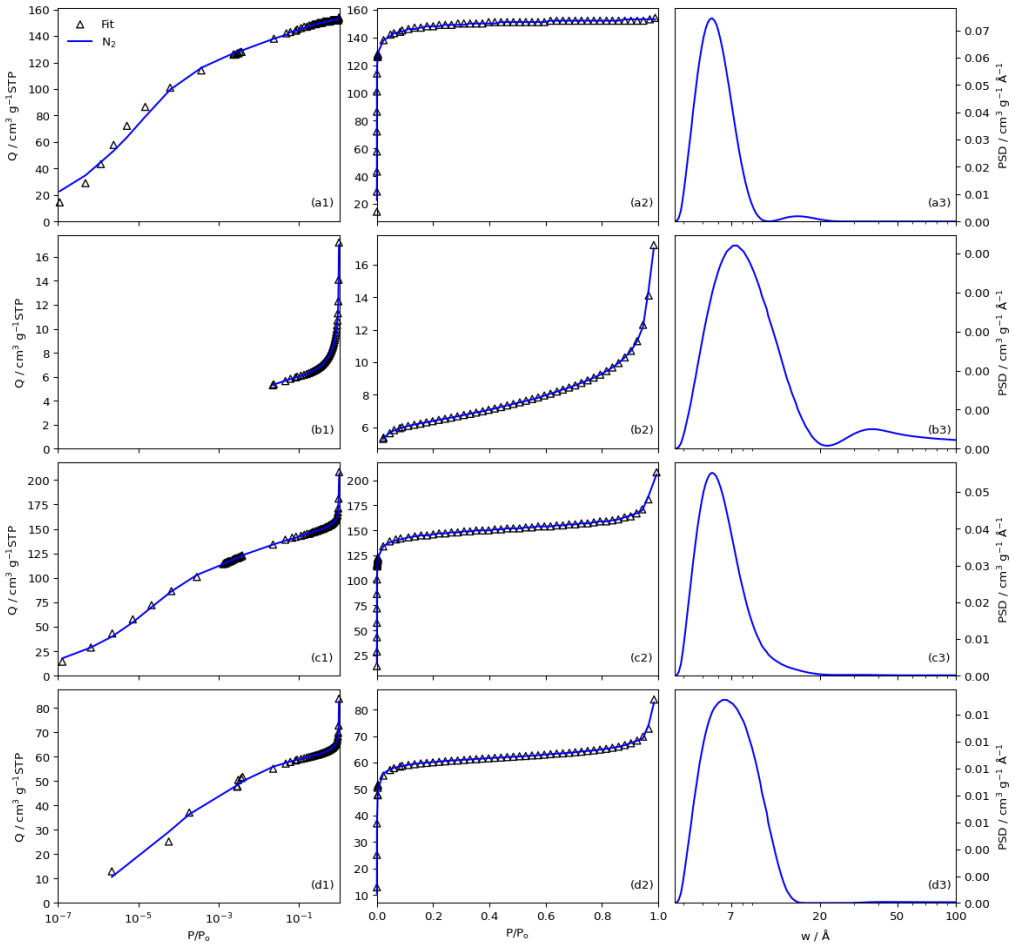

Figure C.9: Fits to N_2 isotherms with logarithmic (a) and linear (b) relative pressure scale, and resultant differential PSDs (c) for samples NC0.0-600, NC0.7-600, NC0.9-600, and NC1.2-600 in order in rows (1-4).

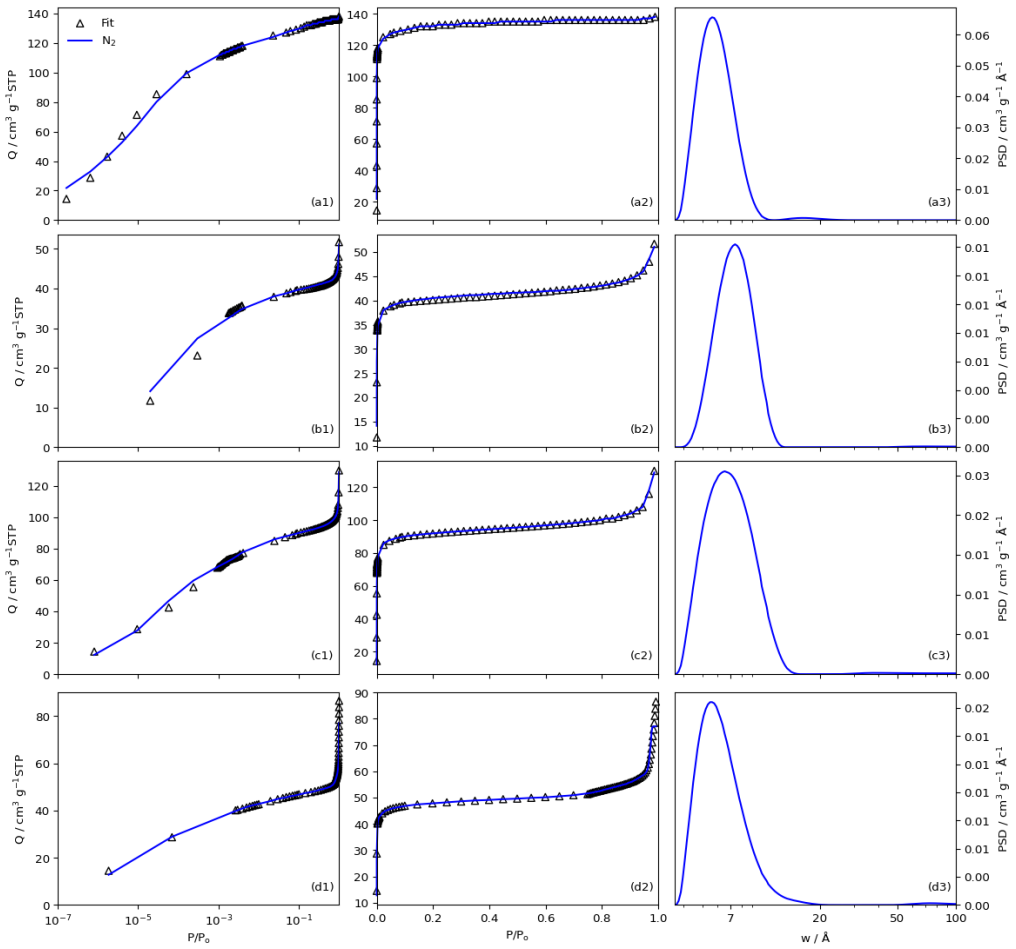

Figure C.10: Fits to N_2 isotherms with logarithmic (a) and linear (b) relative pressure scale, and resultant differential PSDs (c) for samples NC0.0-700, NC0.7-700, NC0.9-700, and NC1.2-700 in order in rows (1-4).

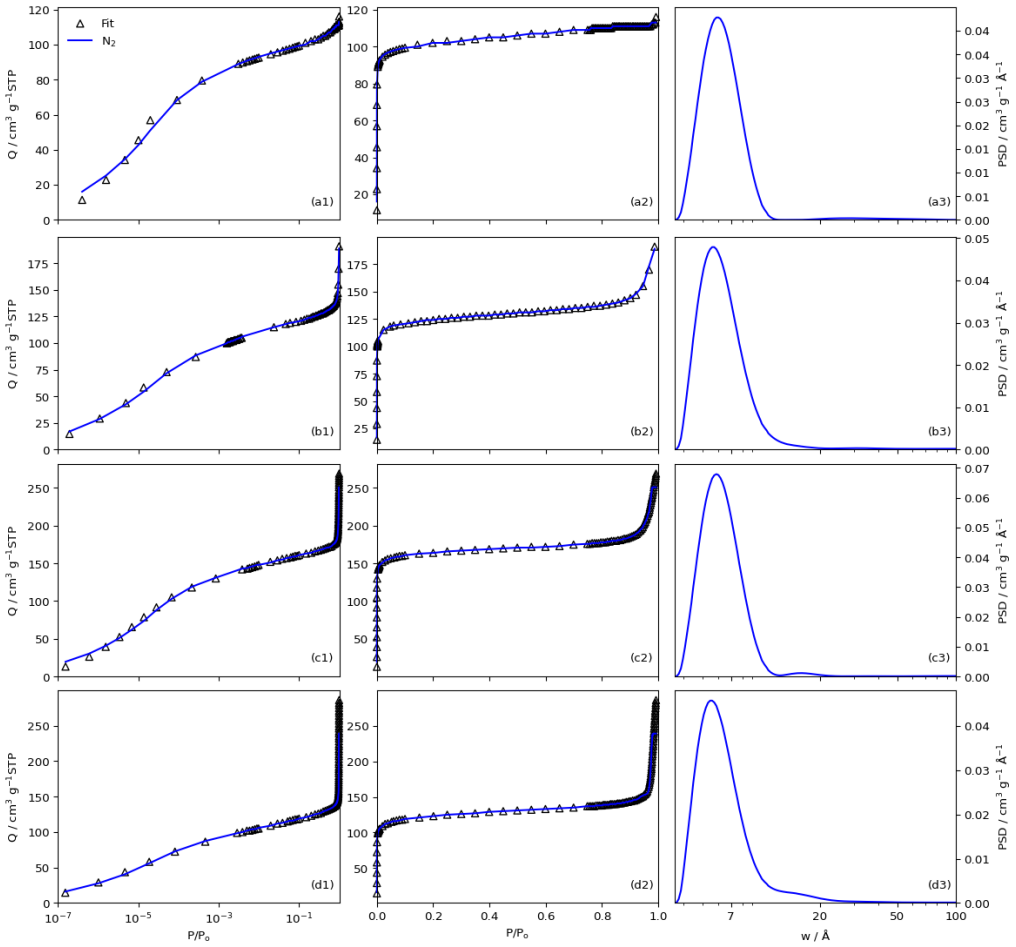

Figure C.11: Fits to N_2 isotherms with logarithmic (a) and linear (b) relative pressure scale, and resultant differential PSDs (c) for samples NC0.0-800, NC0.7-800, NC0.9-800, and NC1.2-800 in order in rows (1-4).

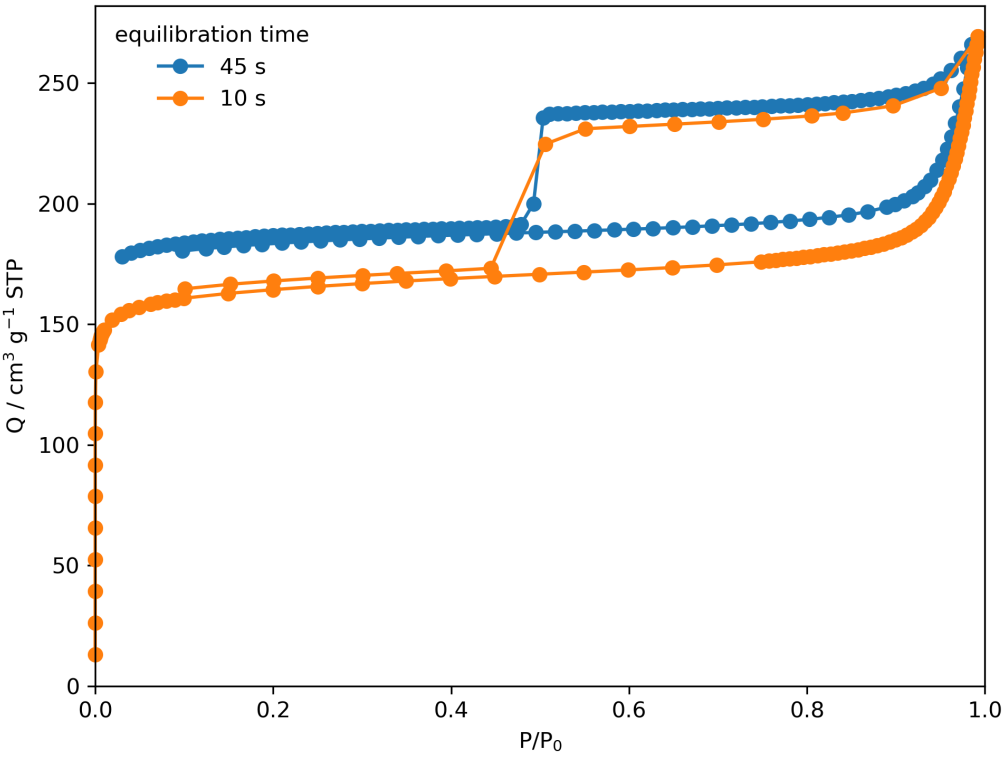

Figure C.12: Demonstration of the permanence of the hysteresis loop for N_2 isotherms on NC samples (NC0.9-800 in this case) even when isotherm is given longer to equilibrate during the desorption branch. Small discrepancies in the adsorption branch are likely due to errors in measurement of sample mass.

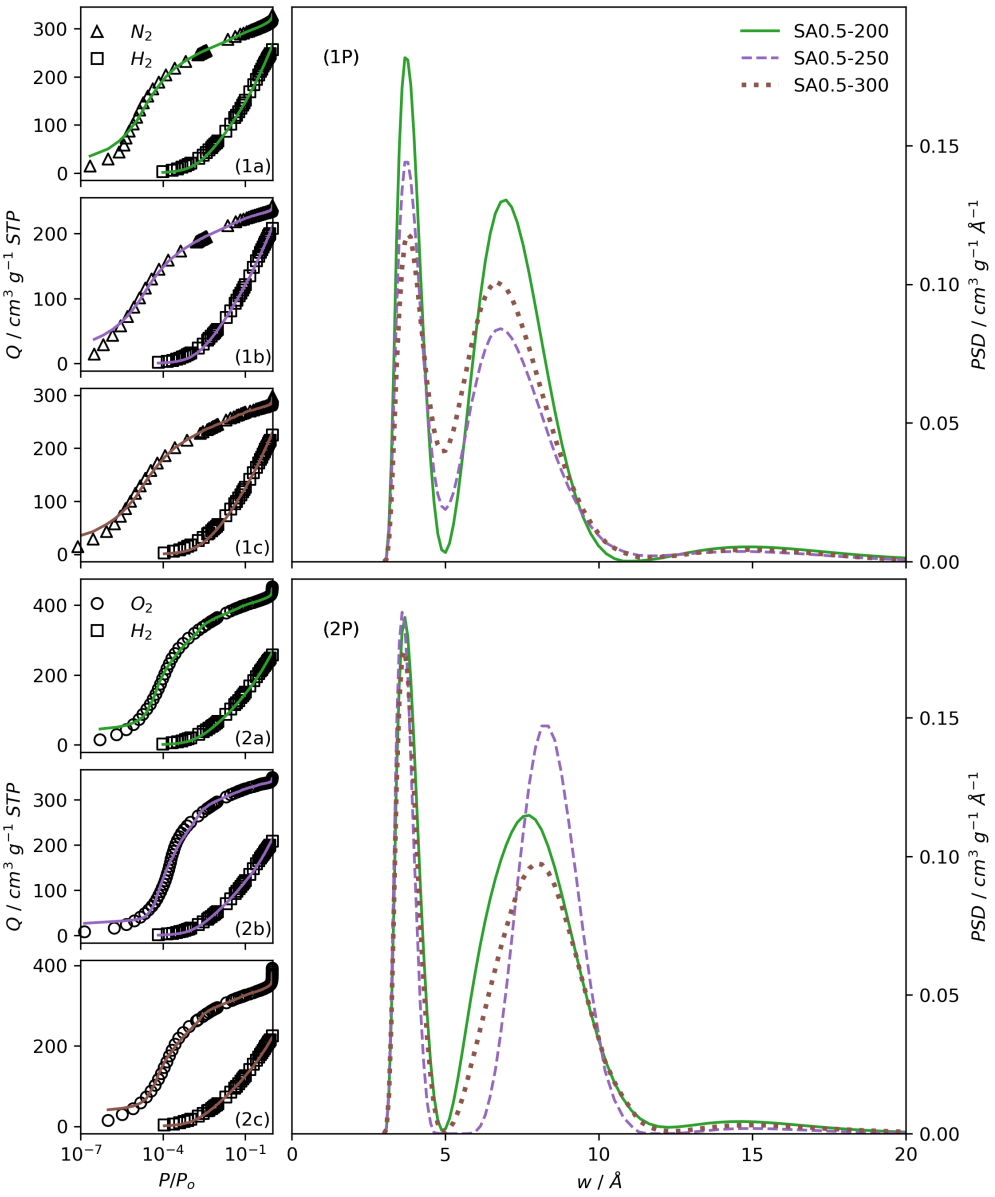

Figure C.13: Changes in porosity with hydrothermal carbonisation temperature for SA0.5-TTT carbons. Compared according to dual fit N_2/H_2 (1) and O_2/H_2 (2) porosimetry.

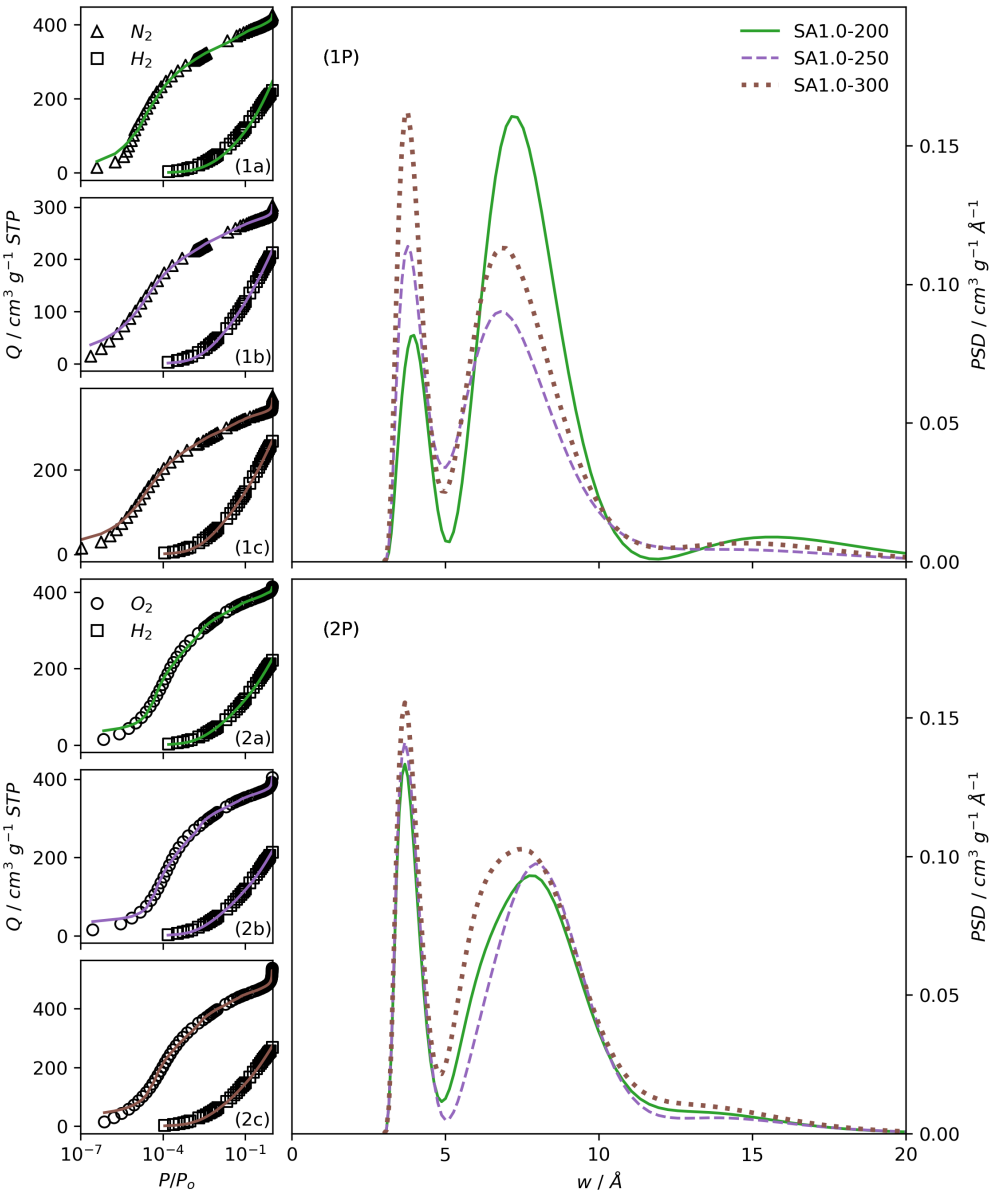

Figure C.14: Changes in porosity with hydrothermal carbonisation temperature for SA1.0-TTT carbons. Compared according to dual fit N_2/H_2 (1) and O_2/H_2 (2) porosimetry.

Appendix D

Software

```
Loading DataFrame generated at 15:09 on 22-01-26
-------------------------------------------------

Project name = 0000_example, Sorptive = co2, T = 298 K
Models used = ['Langmuir', 'DSLangmuir',
               'TSLangmuir', 'GAB',
               'Freundlich', 'DR', 'Toth'],
Number of isotherms = 4
Pressure range = 1.0 - 4.0 bar, with increment 1.0
```

Figure D.1: An example of the report generated after processing experimental uptake isotherms with pyPUC.

```
Parameter DataFrame generated at 15:08 on 22-01-26
---------------------------------------------------

Project name = 0000_example, Sorptives = n2h2,
Number of PSDs = 4, calculated for surface area.
Using pore widths between 4.0 and 7.0 A with a
minimum increment of 1.0 A
```

Figure D.2: An example of the report generated after processing experimental PSDs with pyPUC.